FORSCHUNGSZENTRUM JÜLICH GmbH

Institut für Nuklearchemie

Cosmic and Solar Radiation Induced Suprathermal Processes in Titan's Atmosphere

A.-M. El-Sagheer Mansour H. Abd Elkhalk K. Roessler

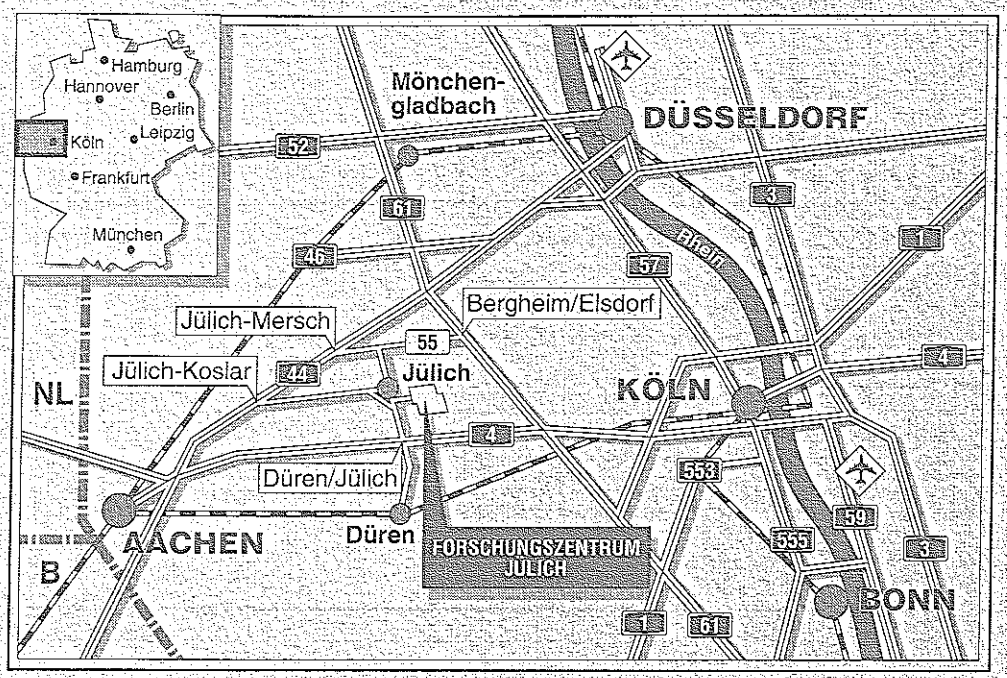

Berichte des Forschungszentrums Jülich ; 3002
ISSN 0944-2952
Institut für Nuklearchemie Jül-3002

Zu beziehen durch: Forschungszentrum Jülich GmbH · Zentralbibliothek
D-52425 Jülich · Bundesrepublik Deutschland
Telefon: 02461/61-6102 · Telefax: 02461/61-6103 · Telex: 833556-70 kfa d

Cosmic and Solar Radiation Induced Suprathermal Processes in Titan's Atmosphere

A.-M. El-Sagheer Mansour[1] H. Abd Elkhalk[1] K. Roessler

[1] Physics Department, Science Faculty, Suez Canal University, Ismailiya, Egypt

CONTENTS

Summary

A theoretical study was made on the interaction of energetic H, He, C, and Fe ions from solar wind and cosmic rays with the atmosphere of Titan, a satellite of planet Saturn. It was based on computer simulation of binary collisions with the program *MARLOWE* in a kind of Monte Carlo calculation.
Two main issues were treated:

1. The production of energetic secondary atoms with energies exceeding 0.5 eV by knock on processes and the range of the primary ions in a model lattice containing the atmospheric components N_2, Ar, and CH_4 in three mixtures: I (98%, 0%, 2%), II (82%, 12%, 6%), and III (65%, 25%, 10%) at 1.6 bar.

2. The application of this model calculation to Titan's atmosphere using the range of primaries and the barometric formula in a 10 km bin arrangement. A distribution profile of secondary N, C, and H atoms resulted, depending on the kind and energy of primary ions. It was folded with the average solar and cosmic rays flux at Titan resulting in a profile of suprathermal atoms. This is important to evaluate the chance for the extremely fast hot or suprathermal chemical reactions (i.e. in thermal non-equilibrium) and their competition with classical ion-molecule reactions in thermal equilibrium.

MARLOWE had to be modified for the application to gas phase and high energy collisions ($E \geq 10^6$ eV). The latter was achieved by introducing the Bethe-Bloch formalism and relativistic corrections to inelastic loss calculation. The study showed that heavy primary particles (C, Fe) produce very high numbers of secondaries (e.g. 10^8 Fe in target I : 69774; 10^8 H : 306 only). This counterbalances their low abundance in space radiation in view of chemical effects. A very interesting result was that light primaries with 10^8 eV and heavy ones even up to 10^{10} eV dissipate their energy mainly within Titan's atmosphere and do not reach the solid surface. For a 98% N_2 + 2% CH_4 mixture the column density of all hot atoms generated by space particle radiation from H to Fe was calculated to about $2 \cdot 10^9$ cm^{-2} s^{-1}. An important contribution of these hot atoms can be expected locally in the actual atmosphere. On a global scale in the change from a primordial to the existing atmosphere during the lifetime of the solar system, the number density of these suprathermal atoms amounted to about

$2 \cdot 10^{26}$ cm^{-2}, i.e. the total column density of the atmosphere which implies that each atom once had been a suprathermal atom.

The study was complemented by an experimental approach. Hot chemical reactions of secondary atoms were studied by 32 MeV $^3He^{2+}$ ions from Jülich compact cyclotron impinging into a gas target with pure CH_4 and mixtures of 90% N_2 + 10% CH_4, and 98% N_2 + 2% CH_4 at 1.6 bar. The nuclear reaction $^{12}C(^3He,^4He)^{11}C$ created radioactive ^{11}C recoils which labeled typical hot products. These could be analyzed by radiogaschromatography. Formation of unsaturated compounds C_2H_2 and C_2H_4 and nitrogen containing molecules such as HCN, CH_3CN and CH_3NH_2 was strong at low doses ($D > 10^{-2}$ eV per target molecule), whereas at higher doses the formation of CH_4 and C_2H_6 predominated. The abundance of nitrogen compounds labeled by ^{11}C was however, relatively very low. Carbon seems to react preferentially with carbon compounds (and oxygen), nitrogen with nitrogen compounds and in particular with N_2. Thus, the formation of carbon-nitrogen compounds is not favored, a result which is reflected in the atmospheric composition of Titan.

CHAPTER 1

INTRODUCTION

1.1 Titan and its atmosphere

Titan, the moon of planet Saturn is the second largest satellite in the solar system (Ganymed's radius is only 70 km wider) and is considerably larger than planet Mercury. It is the attracting much attention by the astrophysical community, since it is the only satellite with an atmosphere similar to that of the Earth. It is an interesting object for planetary chemistry, prebiotic chemistry and exobiology [1.1-4].

Its dense atmosphere, dominantly nitrogen but with a substantial component of methane, makes it unique. Its surface and possible clouds are hidden by a dense, uniform dark orange haze. Basic properties of Titan are summarized in Table 1.1. Many of these data were obtained by the close pass of Voyager 1 on 12 November 1980, cf. Fig. 1.1.

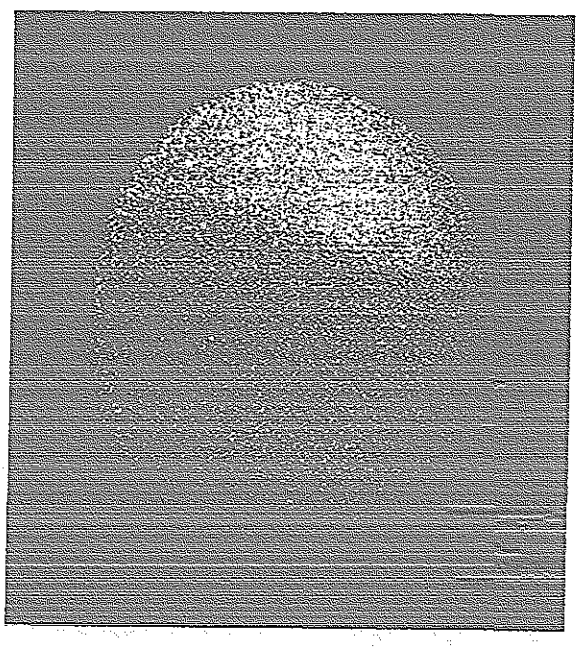

Fig. 1.1 : Image of Titan taken by Voyager I wide angle camera. Outstanding features are high altitude haze, detached polar hood, and a north-south asymmetry in the albedo, from [1.2].

The considerable history of pre-Voyager observations has been discussed in two NASA workshop reports [1.5,6] and several reviews [1.7-9]. and Limb darkening implying the presence of an atmosphere was observed visually already early [1.10]. Near-infrared methane bands were discovered by Kuiper [1.11,12]. These early observations were enormously extended by the Voyager 1 encounter. The key methods were near infrared spectroscopy, thermal-infrared radiometry, radio wave measurements, polarimetry, and ultraviolet spectroscopy from Earth

orbit. Lewis [1.13] made the influential realization that the low mean density implies an interior composition much richer in ices than that of the terrestrial planets, despite the many rarallels between Titan and these bodies. He also suggested that the atmosphere might be rich in nitrogen from photolysis of ammonia. Models based on this idea were presented in [1.14,15]. Ambiguous spectral evidence was interpreted as implying a large amount of transparent gas (nitrogen or argon) in addition to the observed methane [1.15,16], but there were alternative interpretations [1.17].

Table 1.1 : Properties of Titan, from [1.1].

Surface radius, R_T	2575 km
Mass, M	1.346×10^{26} g (0.022 M_{Earth})
GM	8.976×10^{18} cm^3 s^{-2}
Surface gravity, g_s	1.346 m s^{-2}
Mean density	1.881 g cm^{-3}
Rock / ice ratio (by mass)	~ 52 : 48
Distance from Saturn	1.226×10^6 km (20.3 R_{Saturn})
from Sun	9.546 A.U.
Orbit period	15.95 d
Orbit around Sun	30 a
Obliquity	26 °7 (assumed)
Temperature, K	
Surface	94
Effective	86
Tropopause (42 km)	71.4
Stratopause (200 km)	170
Exobase (1600 km)	186 ± 20
Band albedo	0.20
Solar flux	1.1 % of Earth's
Surface pressure	1496 ± 20 mbar *

* The present discussion is between 1.5 and 1.6 bar.

The assumed chemical composition of Titan's atmosphere is shown in Table 1.2. The amount of methane, obtained from its near-infrared absorption, implies that dissociation is occurring, driven by solar radiation with wavelengths < 1400 Å. The products are hydrogen and free radicals such as CH_2. The hydrogen mixing ratio stabilizes at 0.2 %, and reaches a steady state with escape. The radicals initiate the buildup of heavier hydrocarbons, many of which eventually condense to form particles. This chain of processes plausibly explains many of the observed molecules and the dark haze. Production of nitrogen compounds such as HCN requires dissociation of N_2 which is caused primarily by electron impact or other ionospheric processes such as recombinations.

Electrons may come from the solar wind, the magnetosphere, or photoionization with excess energy, cf. chapter 1.2.

Table 1.2 : Atmospheric composition of Titan below 0.1 mbar as inferred from infrared data [1.1].

Gas		Band	Position cm^{-1}	Mole Fraction
Nitrogen	N_2			0.65 - 0.98
Argon	Ar			0 - 0.25 (?)
Methane	CH_4	ν_4	1304	0.02 - 0.10
Hydrogen	H_2	S_0	360	2×10^{-3}
		S_1	600	
Carbon-monoxide	CO	$(3\text{-}0)X^1\Sigma^+$	6350	6×10^{-5} - 1.5×10^{-4}
Ethane	C_2H_6	ν_9	821	2×10^{-5}
Propane	C_3H_8	ν_4	748	4×10^{-6}
Acetylene	C_2H_2	ν_5	729	2×10^{-6}
Ethylene	C_2H_4	ν_7	950	4×10^{-7}
Hydrogen-cyanide	HCN	ν_2	712	2×10^{-7}
Methyl-acetylene	C_3H_4	ν_9	633	3×10^{-8}
		ν_{10}	328	
Diacetylene	C_4H_2	ν_8	628	$\sim10^{-8}$ - 10^{-7}
		ν_9	220	
Cyano-acetylene	HC_3N	ν_5	663	$\sim10^{-8}$ - 10^{-7}
		ν_6	499	
Cyanogen	C_2N_2	ν_5	233	$\sim10^{-8}$ - 10^{-7}
Carbon-dioxide	CO_2	ν_2	667	1.5×10^{-9}

The outer atmosphere was observed in considerable detail by the ultraviolet spectrometer (UVS) on Voyager 1. This instrument gave the only direct evidence that N_2 is the major constituent, although the mean mass of 28.0 amu strongly implies the same thing. The temperature of 186 K assures that hydrogen and helium will escape freely at a rate limited by diffusion from below. This rate is readily calculated, and for H_2 it is compatible with the observed mixing ratio and the proposed source by photolysis of methane. The escaping gas is probably a mixture of H and H_2 ; it goes into orbit about Saturn, forming a torus. The Lyman α radiation scattered by the atoms was observed by both Voyager 1. It extends from 8 to 25 R_S (Saturn radii), enveloping Titan's orbit at 20 R_S. Its vertical thickness is 14 R_S. The lifetime of atoms in the torus is estimated at to 3 years, so the required source strength is ~ 3 x 10^{27} atoms s^{-1}. The supply from Titan is 8 x 10^{27} atoms s^{-1}, but both estimates are rather uncertain and the disagreement is tolerable.

There are several popular representations of the atmosphere of Titan, one of which is reported in Fig 1.2, an elaborate, but quite speculative view, from [1.18]. It can be seen, that the atmosphere is composed by CH_4-N_2 clouds, and rain, organic molecules, C_2H_6 fogs, absorption layers, and organic polymeric

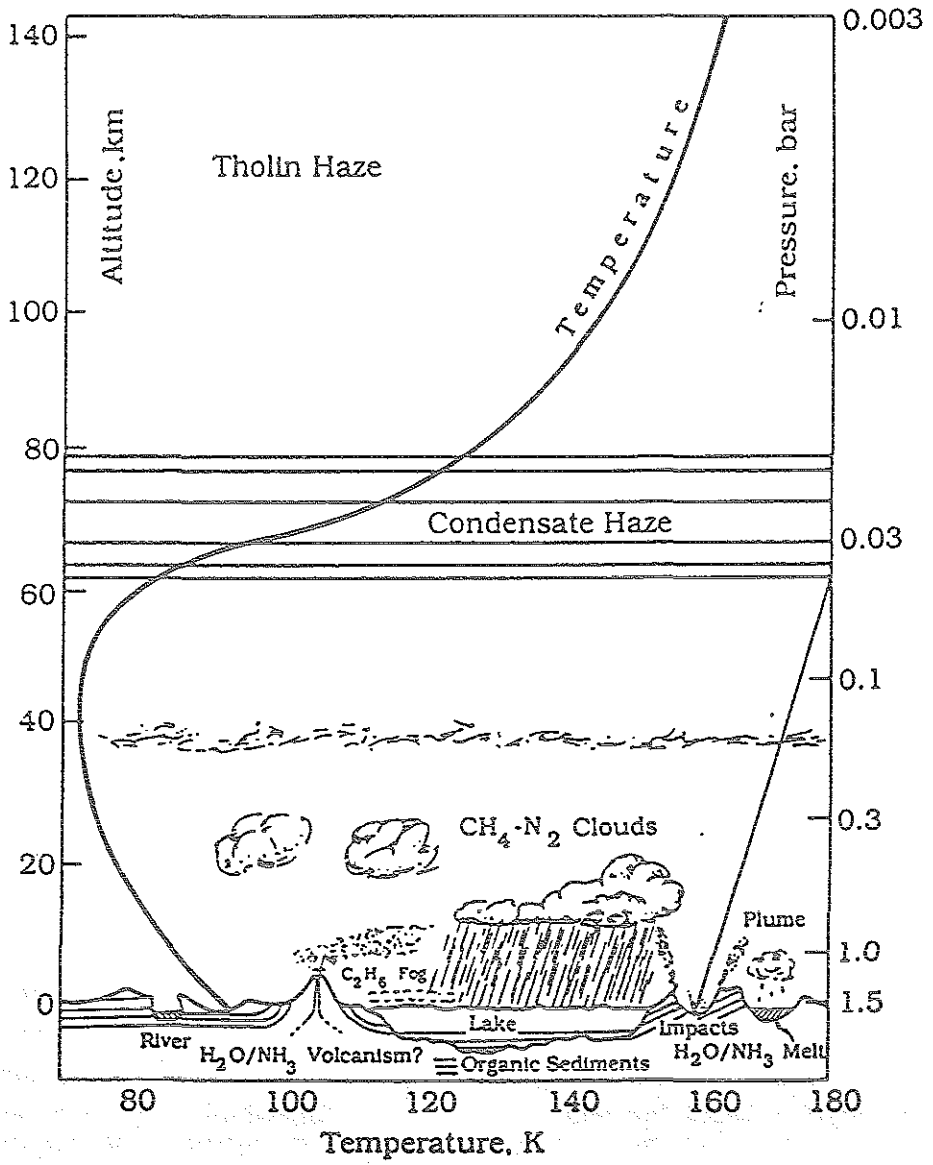

Fig. 1.2 : Schematic representation of Titan's atmosphere and potential surface, including stratospheric hazes of organic polymers (tholins) and condensed organic gases produced by UV and charged particle initiated chemistry; tropospheric clouds composed of a binary $CH_4 + N_2$ condensate, $CH_4 + N_2$ rain, C_2H_6-lakes and rivers, organic sediments, and aqueous ejecta from volcanism, from [1.18].

grains. The surface may be composed from H_2O-NH_3 ices, organic sediments, rivers, lakes and oceans of C_2H_6 and other organic liquids, and plumes from volcanoes.

There is a general uncertainty about many parameters, such as e.g. the exact boundaries of the abundance of molecules. Neither there is clear-cut evidence whether Ar is present at all. The actual discussion of main chemical composition of the atmosphere can be characterized by the extreme values : 98% N_2 + 2% CH_4 and 65% N_2 + 25% Ar + 10% CH_4, where the true value is supposed to be nearer to the first than to the latter one. The composition may also change a lot with the altitude.

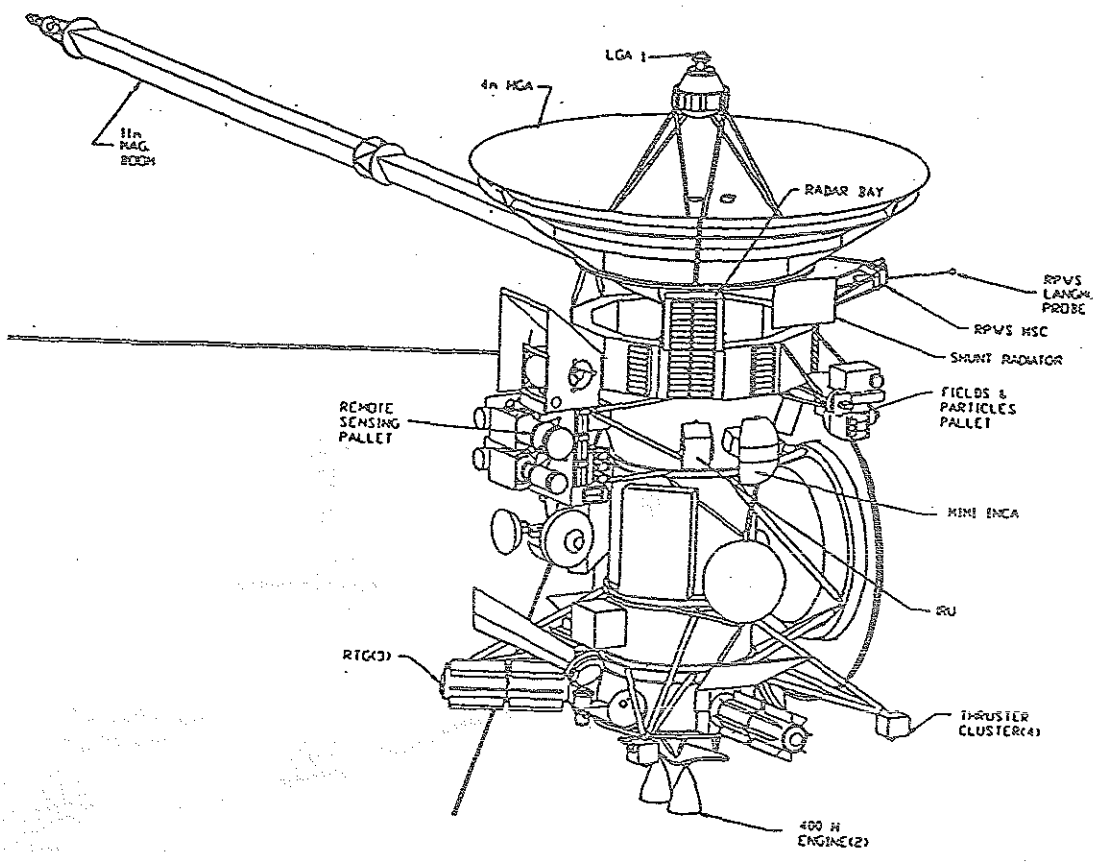

Fig. 1.3 : The CASSINI spacecraft in its cruise configuration; HUYGENS probe is on the near side of the apparatus in the lower right part.

To overcome the present uncertainties is the driving force to prepare the CASSINI mission Fig. 1.3, which will be launched eventually in 3-6 October 1997.
The primary goal of CASSINI, is to conduct a thorough second-phase exploration of the Saturnine system. It is designed to carry out a more extensive exploration and to address some specific scientific objectives which were identified as the result of previous work. There are five high-level scientific objectives for the CASSINI mission [1.19]:

1- The general composition and physical state of Saturn's atmosphere.
2- The chemical composition and physical state of Titan's atmosphere and surface.
3- The chemical composition and physical state of icy Saturnine satellites.
4- The chemical composition and physical state of Saturn's rings.
5- The structure and physical dynamics of the Saturnine magnetosphere.

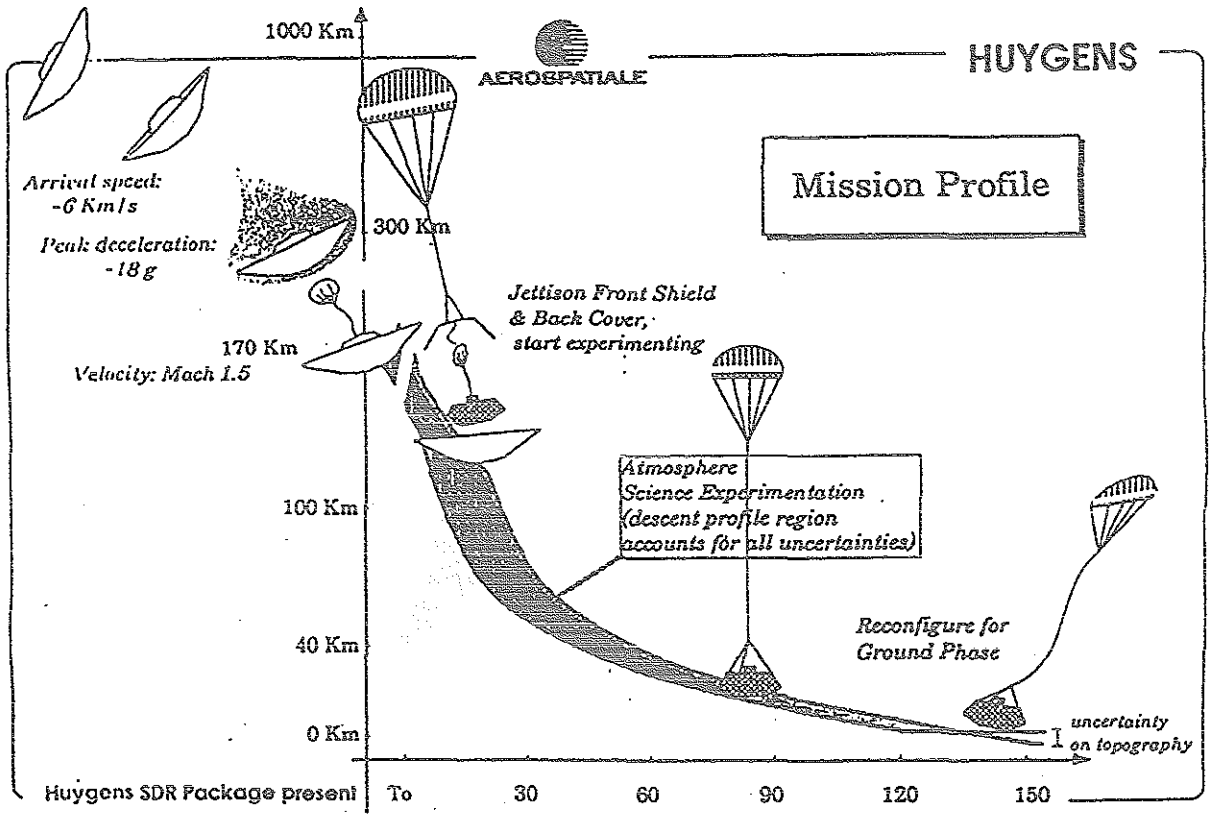

Fig 1.4 : The thrusting of HUYGENS probe into Titan's atmosphere, from Aerospatiale.

The second issue will be performed in particular by the HUYGENS probe [1.20] which will be thrusted in June 2005 into Titan's atmosphere to land on the surface, Fig 1.4. It will contain an aerosol collector pyrolyzer (ACP), a descent imager spectralradiometer (DISR), a Doppler wind experiment (DWE), a gas chromatograph with a mass spectrometer (GCMS), the HUYGENS atmospheric structure instrument (HASI) and the surface science package (SSP). It will determine the abundance of atmospheric constituents (e.g. noble gases and isotope ratios), observe vertical and horizontal distribution of trace gases, search for complex organic molecules, investigate energy sources for atmospheric chemistry, model the photochemistry of the stratosphere, study formation and composition of aerosols, investigate upper atmosphere (e.g. as material source for Saturn's magnetosphere), perform atmospheric wind measurements, determine physical state , topography, and composition of the surface.

1.2 Thermal structure and density profile

The currently accepted thermal profile of Titan is shown in Fig 1.5. The refraction of radiowaves at 13 cm and 3.6 cm by the atmosphere of Titan has been analyzed to yield an atmospheric temperature of ± 0.7 K at the surface, assuming a pure N_2 atmosphere. The lapse rate, i.e. the rate at which temperature in an atmosphere decreases with respect to altitude, is found up to 3.5 km altitude to be 1.38 ± 0.1 K km^{-1}, which is entirely consistent with a 100 % N_2 atmosphere as discussed below, cf. [1.2].
The dry adiabatic lapse rate for an ideal gas is given by :

$$\Gamma_d = g / C_p \qquad (1.1)$$

where :

g = 1.354 ms^{-1} at Titan's surface, and
C_p = 1069 J kg^{-1} K^{-1} the specific heat of N_2.
Thus, Γ_d = 1.27 K km^{-1} at Titan's surface.

However, N_2 is close to phase transition on Titan, it does not behave like an ideal gas [1.2]. Taking into consideration the van der Waals corrections due to intermolecular forces and molecular compressibility [1.21] a lapse rate of 1.40 K km^{-1} was derived for Titan's surface, which is in agreement with the measured value of 1.38 K km^{-1}.

The radio measurements, however, yield only the scale height information, cf. [1.2]. Thus, they provide only $T/\overline{m}$, i.e., the ratio of temperature (T) to the mean molecular weight ($\overline{m}$). Knowledge of either T or $\overline{m}$ is essential to infer atmospheric properties from the data. In principal, the radio data can be normalized against the infrared data, since infrared opacities are used to determine the temperature at some reference level.

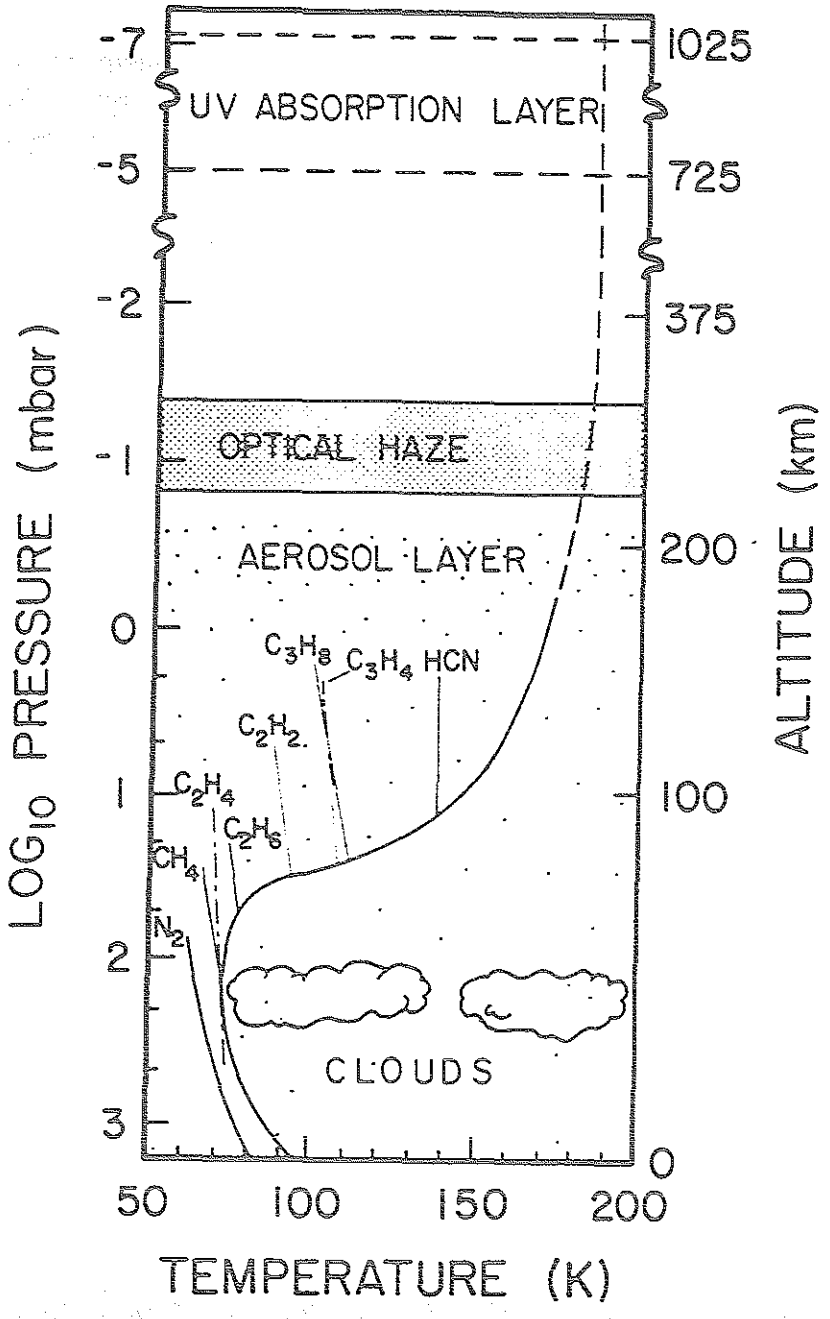

Fig. 1.5 : Thermal structure of Titan's atmosphere, from [1.2].

In practice, however, infrared measurements at Titan were capable of yielding only a wide range of possible temperatures for the following reasons. Most of the infrared opacity at Titan results from CH_4, whose abundance has not been determined directly. Any indirect measure of the CH_4 abundance applies to the region above the clouds, and models assume uniform vertical mixing of CH_4 in the stratosphere. Using a wavelength region (200-400 cm^{-1}) which does not critically depend on the nature of opacity sources, a lower limit of 94 ± 0.4 K

was determined for air temperature immediately above the surface (the surface in this model is 0.5 K warmer). The upper limit is highly uncertain, with a maximum value of 98 K, and a nominal acceptable value of 95 K [1.23].

Despite large uncertainties, the infrared data can be satisfactorily normalized to the above cited radio measurements, yielding the same value for the atmospheric surface temperature of 94 K. This implies a mean molecular weight of ~ 28, i.e., the atmosphere is composed of essentially pure N_2. Small quantities of CH_4 and Ar at the surface can be tolerated within the limits of these measurements.

By modeling the dependence on temperature of the shape of the 1304 cm^{-1} band, and the emission levels at 1304 cm^{-1} and 1260 cm^{-1}, Samuelson et al. [1.23] have obtained a temperature profile in the 0.1 - 5 mb range. Both infrared and the radio data yield temperature of 170 ± 15 K at the stratopause which is located around the 1 mb level.

Like Jupiter and Saturn, Titan has an "information gap" region in the middle atmosphere (200 km to 1250 km or 0.1 mb to 5 nb) where no temperature measurements are available. At a radial distance of 3840 km and beyond, the Voyager ultraviolet spectrometer measured the column abundances of N_2, CH_4, and C_2H_2 in a solar occultation experiment [1.24]. The column abundances can be used to provide scale heights, and subsequently temperatures. The angular diameter of the Sun projected into the atmosphere of Titan was 3 km during Voyager 1 entry occultation, and 17 km during exit, both values being considerably less than the atmospheric scale height (65 km) at these altitudes. The observed transmission characteristics are consistent with the principal absorbers being N_2 for $\lambda < 800$ Å, and CH_4 and C_2H_2 for $\lambda > 800$ Å [1.24]. The measurements yielded the following values for the exospheric temperature in the equatorial region (3°N), 196 K near the morning terminator, 176 K near the evening terminator. Thus a globally averaged value for the exospheric temperature on Titan is 186 ± 20 K.

The N_2 density at the upper end of the "information gap" region, (R = 3840 km), is found from the solar occultation experiment to be 2.7×10^8 cm^{-3}. In order to reconcile it with the atmospheric density near the lower end, (R = 2750 km, 4.5×10^{16} cm^{-3}), it is imperative that the mean temperature between 2750 km and 3840 km radii be 165 K. Since the stratopause (R = 2775 km) temperature is 170 K, and exosphere (R = 3840 km) temperature is 186 K, a temperature of 165 K in this height range would imply considerable structure in the thermal profile. This is not unreasonable considering the presence of aerosols of all sizes over an extensive height range on Titan. A working model of the atmospheric number density can then be constructed in the following manner, cf. also Table 1.3.

For 2575 km < R < 2750 km, use the measured n and T [1.22].
For 2575 km < R < 3840 km, use the hydrostatic law of densities with :
n (2750 km) = 4.5×1016 cm^{-3}, T (2750 km) = 165 K and constant up to 3840 km.
For R > 3840 km, use again the hydrostatic law, but with :

n (3840 km) 2.7×10^{18} cm^{-3}, as derived in the previous step, and T = 186 K, the average exospheric temperature.
The hydrostatic law of densities is given below :

$$n(R_2) = n(R_1)\left(\frac{T_1}{T_2}\right)\exp\left[-\int_{R_1}^{R_2} dR / H(R)\right] \qquad (1.2)$$

where H (R) is the scale height :

$$H(R) = k\frac{T(R)}{\overline{m}g(R)} \quad . \qquad (1.3)$$

with T = const. between 2750 km and 3840 km, $\overline{m}$ = 28 AMU for an essentially N_2 atmosphere, the scale height simply becomes a function of gravity, which varies with R as :

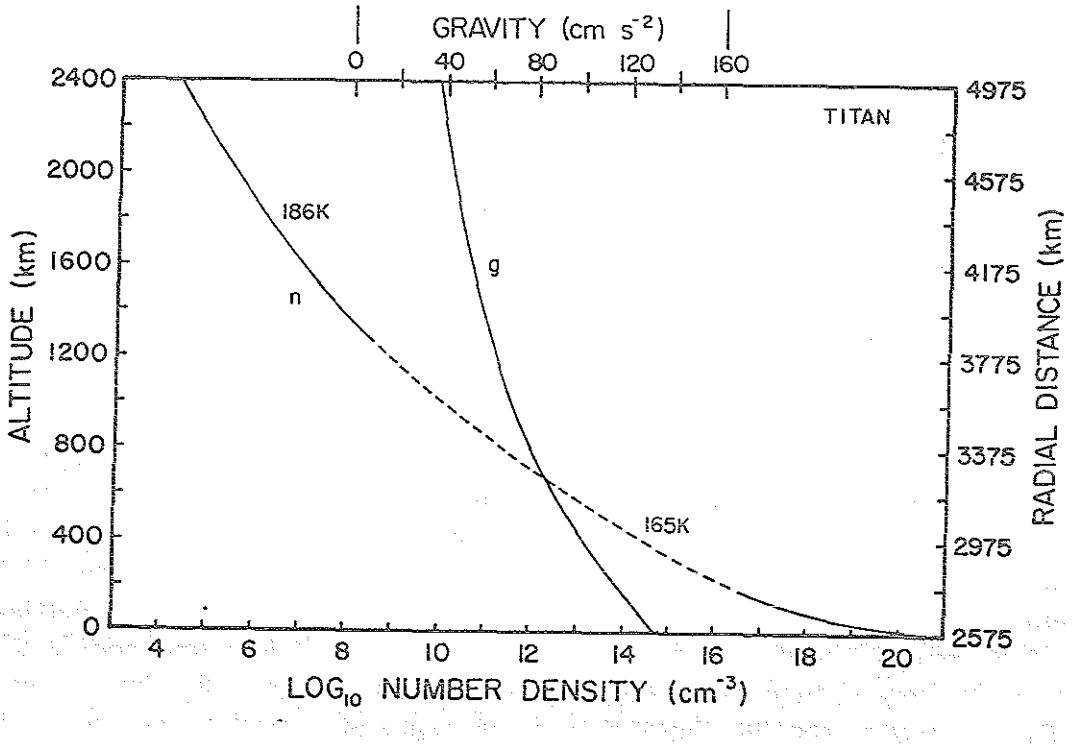

Fig. 1.6 : Variation of the atmospheric number density and gravity of Titan with height. Interpolation between the lower atmospheric measurements by the infrared and radio techniques and the upper atmospheric measurements by UV occultation is shown by broken line, from [1.2].

Table 1.3 : Atmospheric properties of Titan, from [1.2], based on data from [1.22,25,26].

property	value
surface	
pressure	1496±20 mb
temperature	94±0.7 K
effective temperature	86 K
measured lapse rate	
0 - 3.5 km	1.38±0.1K km^{-1}
3.5 km	0.9±0.1K km^{-1}
42 km	0
tropopause	
hight	42km
pressure	127mb
temperature	71.4±0.5 K
stratopause	
hight	200 km
pressure	0.7 mb
temperature	170±15 K
homopause	
height	925±70 km
number density	2.7×10^{10} cm^{-3}
eddy diffusion coefficient	$1.0\pm2.7\times10^{8}$ cm^{-2} s^{-1}
exosphere	
temperature	
evening terminator	176±20 K
morning terminator	196±20 K
critical level	1600 km
number density at critical level	9.3×10^{6} cm^{-3}
incident solar flux	1.1×10^{-2} of flux at 1 A.U.

$$g(R) = g(R_1)(R_1/R)^2. \qquad (1.4)$$

With the above assumption, Eq. (1.2) becomes the barometric formula [1.2] :

$$n(R_2) = n(R_1)\exp\left[-\left(\frac{R_1}{4(R_1)} - \frac{R_2}{4(R_2)}\right)\right]. \qquad (1.5)$$

The same expression holds for R > 3840 km, except T = 186 K in Eq. (1.3), but with H(R) to mean the scale height of atom / molecule in question.

The resulting model atmosphere is shown in Fig 1.6. It should be regarded only as an engineering model until thermal structure measurements in the middle atmosphere are available, e.g. from an entry probe such as the one under

consideration for the CASSINI project in the future. For this work the relationships given in Fig. 1.6 will be the base of the calculations, neglecting more detailed structures, chemical composition and special layers such as clouds, hazes, etc.

1.3 Solar and cosmic radiation at Titan

Table 1.4 lists some of radiation sources in the solar system [1.27], cf. also [1.28-30]. The values at 10 A.U. are typical for Saturn, i.e. also for Titan.

Table 1.4 : Radiation sources in solar system, from [1.27]..

type	species	energies eV	direction	flux, $cm^{-2}s^{-1}$ at 1 A.U.	at 10 A.U.
solar UV-photons SUV	hν	4–7	from sun	$2 \cdot 10^{16}$	$2 \cdot 10^{13}$
		7–11	from sun	$2 \cdot 10^{12}$	$2 \cdot 10^{10}$
interstellar medium ISM	50% H 45% He 2% C, N, O etc	10–10^2	directed	$6.5 \cdot 10^6$	$6.5 \cdot 10^5$
solar wind SW	95% H^+ 4% He^{2+} 0.1% C^{6+} etc	10^3–10^5	from sun	$2–3 \cdot 10^8$	$2–3 \cdot 10^8$
solar flares SF	95% H^+ 5% He^{2+} etc	$<10^6$	from sun	$4 \cdot 10^2$	4
T-Tauri winds TT	H^+ He^{2+} etc	$<10^6$	from sun	10^{10}	10^8
nuclear reaction recoils NR	almost all elements	10–10^8	isotropic		
solar cosmic rays SCR	H^+ He^{2+} C^{6+} etc	10^6–10^7	from sun		
anomalous cosmic rays ACR	H^+ He^{2+} O^{6+}	10^7–10^8	almost isotropic		
galactic cosmic rays GCR	H^+ He^{2+} etc	$>10^8$	isotropic		

The rubrics on the lower right part are left open, since reliable data are somewhat difficult to obtain. Table 1.5 reports the solar wind fluxes for objects in the solar system.

Table 1.5 : Solar wind fluxes for objects in the solar system, from [1.31].

Object in space	Distance to sun A.U.	Flux of solar wind ions $cm^{-2}c^{-1}$
Mercury	0.387	$2 \cdot 10^9$
P/Halley at perihelion	0.587	$1.3 \cdot 10^9$
Venus	0.723	10^9
Earth	1.000	$2 - 3 \cdot 10^8$
Mars	1.524	10^8
Asteroids	3.5	$2 \cdot 10^7$
Jupiter + moons	5.202	10^7
Saturn + moons	9.555	$3 \cdot 10^6$
Uranus	19.21	$7 \cdot 10^5$
Neptune	30.109	$3 - 4 \cdot 10^5$
P/Halley at aphelion	≈ 35	$2 \cdot 10^5$

Titan in addition is hit by ions with energies in between 10^3 to 10^5 eV from its plasma tail, and accelerated ions from Saturn with energies ranging from 10^4 to 10^5 eV. The contribution of low energetic cosmic rays is somewhat difficult to estimate. The MeV component should show a flux of about 10 particles cm^{-2} s^{-1} [1.28], however it mixes with ions from solar flares and should be much bigger as a Sun. The famous energy dependence of cosmic H, He, C + O, and Fe ions from [1.33] is plotted in Fig. 1.7.

The abundance of the elements is given e.g. in [1.33-35], cf. Table 1.6. In this work the curve of relative abundance versus nuclear charge number in Fig. 1.8 [1.33] is considered.

This work in its chapter 4 uses the flux distribution for protons given in Fig. 1.9 from [1.36]. It shows the flux for solar wind, flares etc., and cosmic ray protons as a function of energy. The broad curve (by the present author) represents something like a conservative average over all the contributions to proton radiation at 1 A.U. (Earth), the dashed curve the same for Titan's position in the solar system.

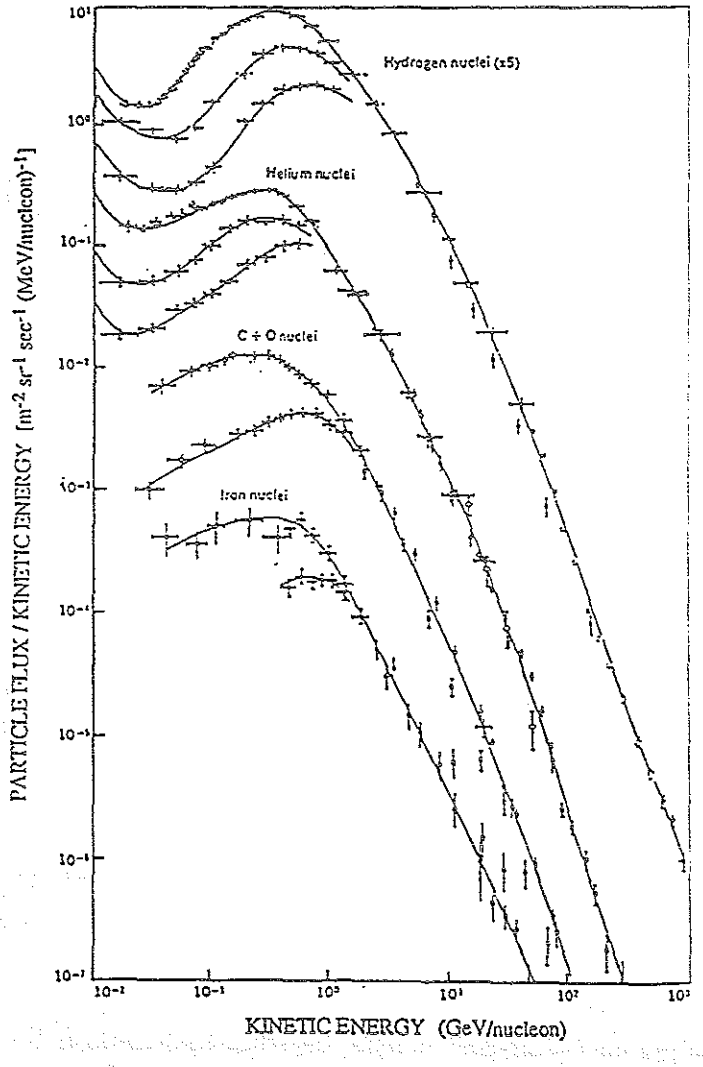

Fig. 1.7 : Energy dependence of cosmic rays fluxes (different curves are due to solar minimum (the higher ones) and solar maximum interaction (the lower ones), from [1.33].

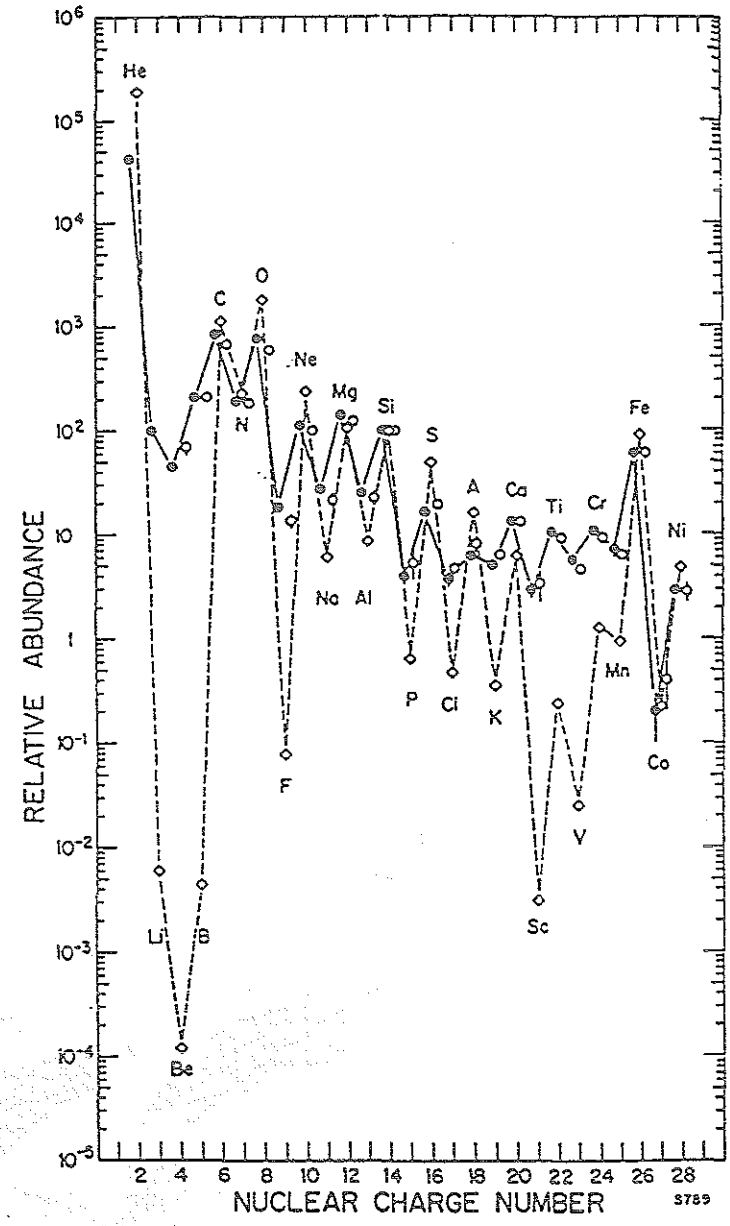

Fig. 1.8 : Relative abundance of elements in cosmic rays versus the nuclear charge number, from [1.33].

Table 1.6 : Abundance of elements [1.33,34]

element	cosmic abundance	cosmic rays	solar system
H	1		
He	1.2×10^{-1}	1.15×10^{4}	1.8×10^{5}
C	3.7×10^{-4}	4.65×10^{2}	1.11×10^{3}
N	1.17×10^{-4}	20	2.31×10^{2}
O	6.76×10^{-4}	5.25×10^{2}	1.84×10^{3}
Ne	6.3×10^{-4}	6.2×10	2.6×10^{2}
Na	1.3×10^{-6}	9	6
Mg	3.4×10^{-5}	1.1×10^{2}	1.06×10^{2}
Al	(-)	14	8.5
Si	3.2×10^{-5}	10^{2}	10^{2}
S	2.8×10^{-5}	14	50
Ar	(-)	4	10.6
Ca	1.6×10^{-6}	7	6.25
Fe	2.6×10^{-5}	9.2×10^{2}	90
Ni	(-)	4.8	4.8

It has to be emphasized that this work only considers the collisional components of stopping of infalling particle radiation at energies up to 10^8 eV. At higher energies, also nuclear reactions are possible, such as e.g. the formation of electrons, hadrons, muons and pions, cf. Fig. 1.10, which contribute to radiation effects, but will not be treated here.

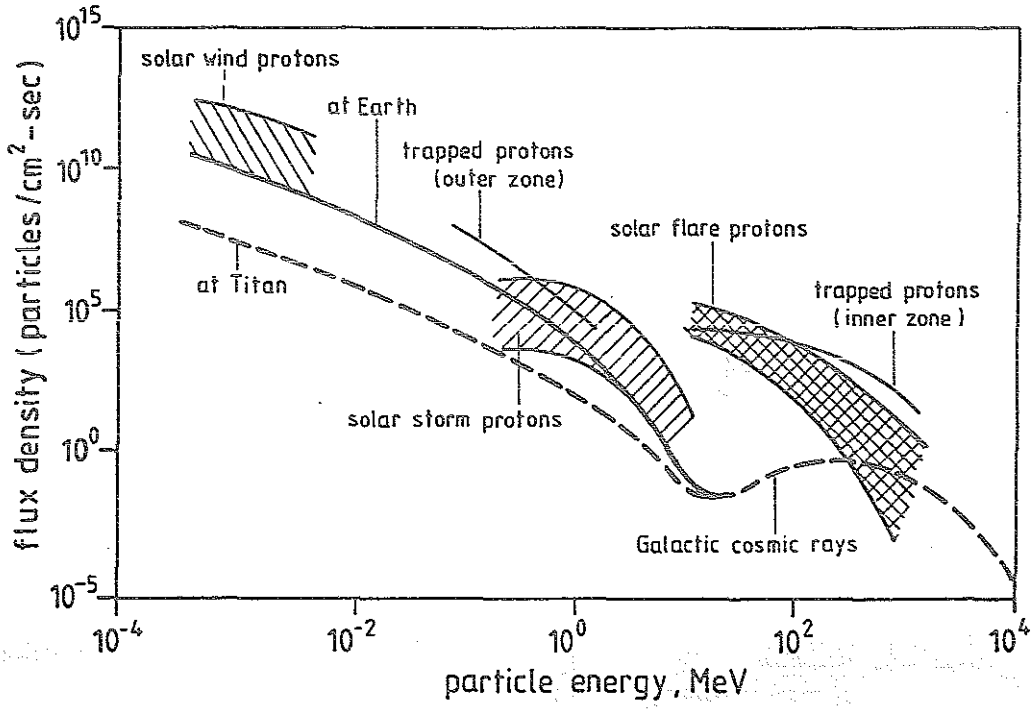

Fig. 1.9 : Space proton radiation, from [1.36].

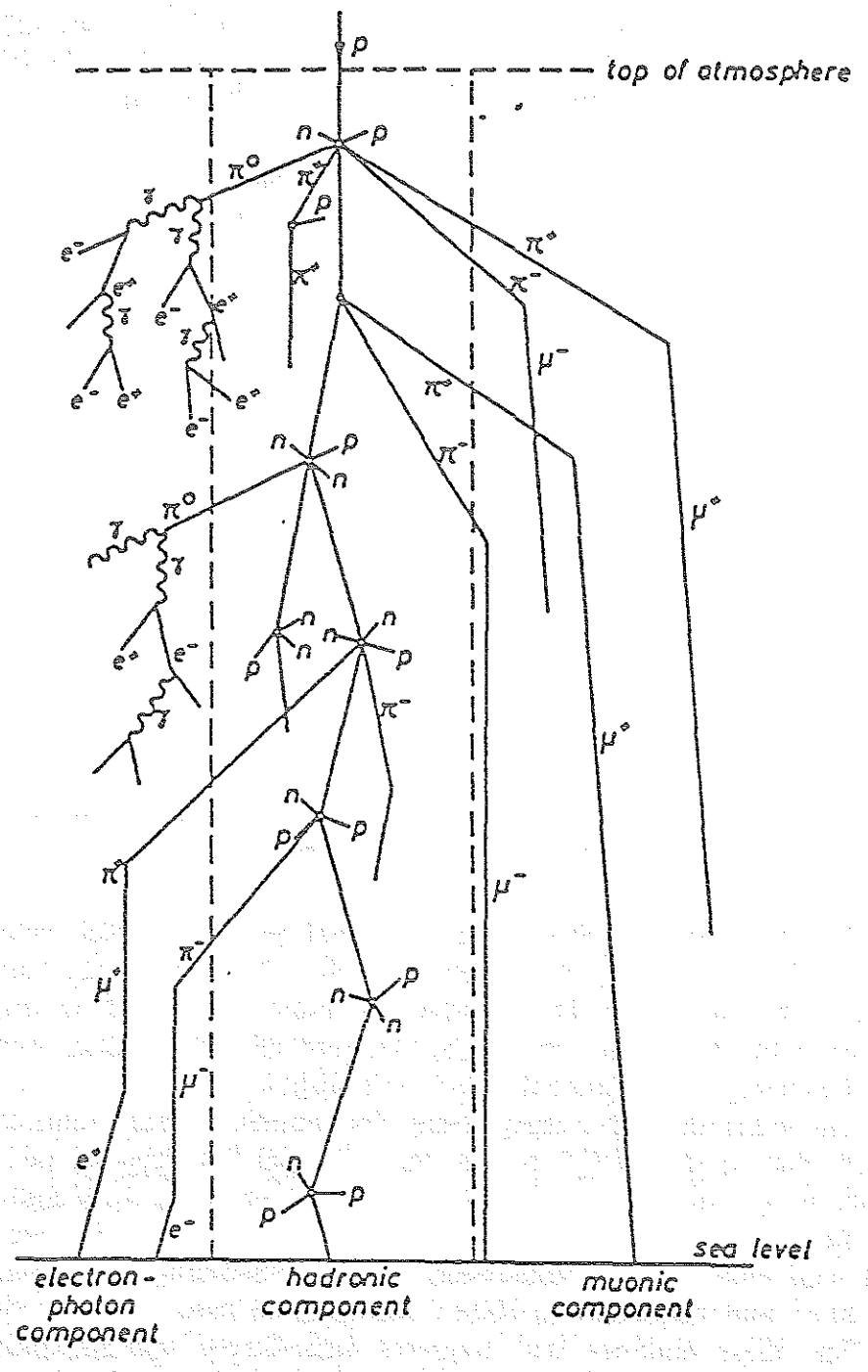

Fig 1.10 : Formation of secondaries by nuclear reactions of high energies ($\geq 10^9$ eV), from [1.36]

1.4 Radiation and suprathermal chemistry

Suprathermal ions and atoms are not in thermal equilibrium with their surrounding. This is the general case for energies exceeding some 0.5 eV. Atoms escaping planetary atmospheres with energies of 0.3 to 0.5 eV are called (hot). This term, even if very often used, is somewhat misleading since by definition a temperature can not be attributed to single particles. The equation: 1 eV = 10^4 K holds when a group of atoms or ions possesses this energy (e.g., in a hot grain) since heat is a collective phenomenon. The typical hot atom penetrates into a surrounding which is cold in comparison to its own high energy. Fig. 1.11 shows that hot species can easily overcome activation energy thresholds of reactions.

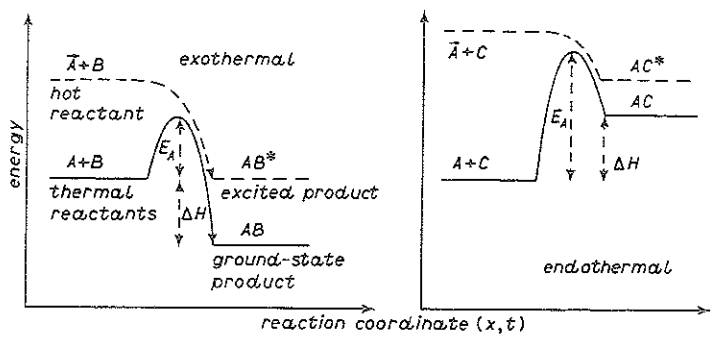

Fig. 1.11 : Schematic view of energetic of thermal and hot reactions in exo- and endo othermal- thermal processes [1.28].

A very important aspect of suprathermal reactions is their velocity. They can be much faster than thermal ones since the activation energy barrier can be overcome in one single attack. Another important factor in suprathermal chemistry is that hot atoms can also be electronically excited and, thus, add their excitation energy to overcome the reaction threshold.

The lower and upper energy limits for suprathermal reactions are given by the facts that a) the energy barrier for a typical hot process, i.e., a slightly endothermic reaction, has to be overcome (in order of 1 - 3 eV and that b) the new bond of the molecule to be formed must be stable at least for one vibrational period. This limits the maximum energy for bond formation for the gas phase to about 20 eV and to some 50 to 100 eV for the solid state. Molecules which carry more than these energies will fragment inmediately and the projectile will continue its trajectory. Chemical interactions of this kind should rather be regarded as polarization effects and should be attributed to inelastic loss phenomena.

Fig 1.12 displays an energy scale of interactions of a high energy projectile entering a solid with 1 MeV down to thermalization at the end of its trajectory.

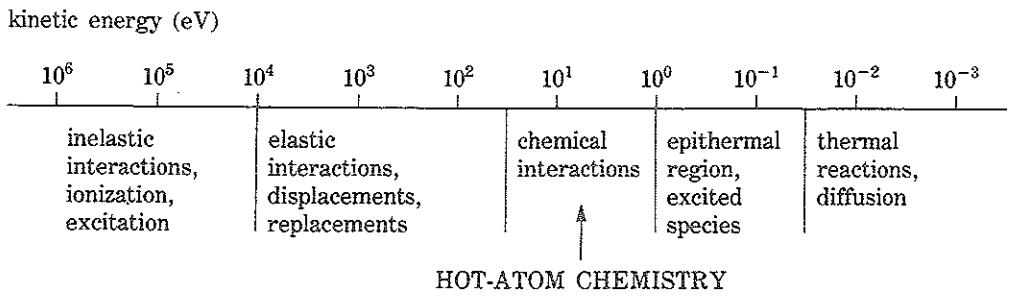

Fig 1.12 : Energy scale of interactions of suprathermal species, from [1.39].

The nonequilibrium character of hot-reaction kinetics prevents the application of simple energy distribution functions such as Maxwell Boltzmann equation. These reactions are very fast and in general performed by few isolated reactions only such as in the case of nuclear recoil. A short review on the state of the art of hot-atom kinetics is given here.

The classical Arrhenius equation for reaction kinetics of binary collisions in thermal equilibrium is written:

$$k(T) = A \cdot \exp\left[E_A / kT\right], \qquad (1.6)$$

where k(T) is the temperature-dependent velocity constant, A the pre-exponential factor, E_A the activation energy, k the Boltzmann constant and T the temperature. The pre-exponential factor A is :

$$A = \sqrt{2}\,\pi\,\sigma^2\,\overline{\omega}\,N \qquad (1.7)$$

where the δ signifies the reaction cross-section. σ^2 should better be written as $(\sigma_1+\sigma_2)^2$, the gas kinetic diameters of the reaction partners. This terms becomes relatively high for ion-molecule interactions. $\overline{\omega}$ signifies the average velocity, i.e. in the thermal case the temperature. It is this term which is effected by the high velocity of the suprathermal atom. N is the number density of the target and, thus, high for solids. The activation energy E_A is in general considered as the energy threshold to be crossed by the relative translational motion of the reaction partners. This is, however, a simplification since the reaction probability depends also on the inner (electronic excitation) energy and the geometrical configuration. The mean velocity constant can also be expressed as :

$$k(T) = \int_0^\infty f(T, V)\, \sigma(V)\, dV \qquad (1.8)$$

where f (T,V) signifies the velocity distribution and σ (V) is the cross- section. k(T) can be formulated in a general way in terms of energy E as :

$$k(T) = \left[\left(\frac{2}{kT}\right)^{3/2}\left(\frac{1}{\pi\mu}\right)^{1/2}\int_0^\infty E\sigma(E)\left\{\frac{E_0 - E}{kT}\right\}dE\right]\exp\left[-E_0/kT\right] \qquad (1.9)$$

where σ(E) is the energy-dependent cross section. Fig. 1.13 shows the overlap of Maxwell-Boltzmann (thermal) energy distribution with typical cross-section curve.

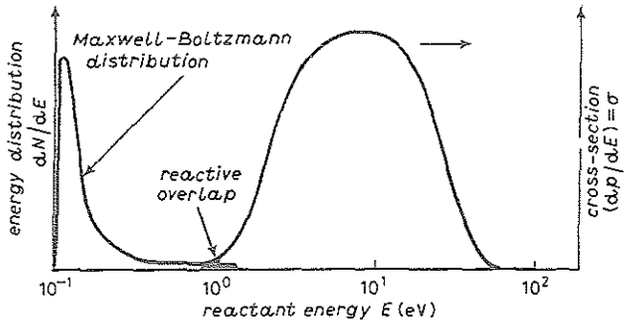

Fig. 1.13 : Thermal reaction characteristics (Maxwell-Boltzmann).

Fig. 1.14 shows the same situation for a hot atom which has been created with an energy of 2 eV (e.g., by photodissociation) and an atom which has started with higher energies (> 100 eV). One has to consider that the hot atoms loose their kinetic energy in a few collisions irreversibly.

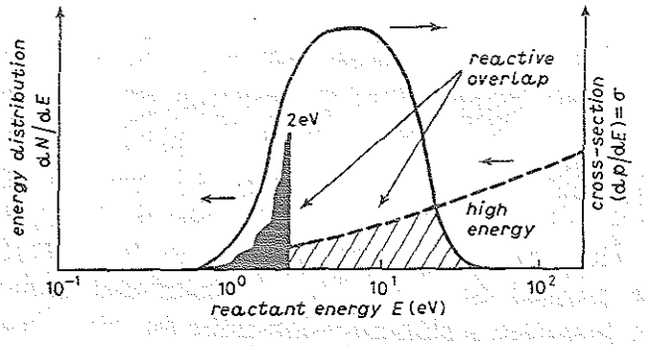

Fig. 1.14 : Suprathermal-reaction characteristics for hot atoms starting with 2 eV and > 100 eV.

A typical view of the hitherto existing overestimation of the role of UV-photons for radiation chemistry in Titan's atmosphere is given in Table 1.7, from [1.37]. It shows a compilation of energy sources available for organic synthetic processes known to operate at radial distance < 3900 km in Titan atmosphere. The energy sources are listed in rank order of decreasing altitude. The penultimate entry in the Table covers the case that ultraviolet photons at wavelengths as long as 2200 Å can be gainfully employed in higher organic synthesis with a quantum yield ~ 0.1. Even neglecting this possibility, we see that ultraviolet photolysis is taken here as by far the most effective mechanism for organic synthesis in the atmosphere of Titan, with charged particles from the Saturnian magnetosphere running a distance second. Photodissocciation occurs mainly in the 10^{-7} to 10^{-5} mbar pressure level, pressures so low that a reaction vessel several thousand km in diameter would be required to achieve photodissociation optical depth unity.

Table 1.7 : Energy sources and rates of organic synthesis on Titan (r < 3900), from [1.37].

Energy Source	Altitude of Peak Dissociation (from Center of Titan) (km)	Pressure Level of Peak Dissociation (mbar)	Dissociation Rate ($cm^{-2}\ s^{-1}$)	Synthesis Rate of Organic Molecules, Integrated Over the History of Titan ($g\ cm^{-2}$)
N_2 photolysis, $\lambda \leq 800$ Å	3700	10^{-7}	1.2×10^9	3×10^{3} [b]
Interplanetary electrons	3550	10^{-6}	6×10^7	20
CH_4 photolysis, $\lambda \leq 1550$ Å (mainly H Lyman-α)	3500	10^{-6}	4×10^9	10^4
Saturn magnetosphere, energetic electrons	3300	3×10^{-5}	5×10^8	10^2
Saturn magnetosphere, energetic protons	3150	5×10^{-3}	4×10^7	10
Photolysis, higher organics, $\lambda > 1550$ Å, $\phi \sim 0.1$	2850	10^{-1}	2×10^{11}	5×10^5
Cosmic rays	2650	20	2×10^8	50

The role of particle irradiation is in general underestimated, first because the fluxes of infalling particles are not fully known, second because the specific reaction of energetic particles are ignored. Table 1.8 shows the manifold of sources for suprathermal (hot) species with energies exceeding 0.5 eV in space.

Table 1.8 : Sources for hot species in space [1.40].

source	primary energy eV	approx. penetration into solids µm
photodissociation by UV photons	1 - 5	surface
dissociative recombination of photolytically produced ions	1 - 5	surface
collision of space craft with rest gas	3 - 10	surface
motion relative to the interstellar medium	10^1 - 10^2	surface
nuclear β-decay	1 - 10^1	surface
nuclear α-decay	10^5	some 10^{-2}
nuclear reactions	10^2 - 10^8	10^{-5} - 10^1
shock waves in the interstellar medium	10^1 - 10^3	10^{-6} - 10^{-4}
discharges, lightenings	10^2 - 10^4	10^{-5} - 10^{-3}
solar (stellar) wind	10^3 - 10^5	10^{-4} - 10^{-2}
ion torus (Io)	10^3 - 10^5	10^{-4} - some 10^{-2}
pick-up-ions	10^4 - 10^5	10^{-3} - 10^{-2}
T-Tauri winds	10^6	10^{-1} - 10^0
cosmic rays	10^3 - 10^{23}	10^{-4} - > 10^8

A recent approach to non-equilibrium kinetics of hot atoms used the method of inversed Laplace transformation of thermal rate constants to obtain energy dependent cross sections and hot reaction rates [1.41, 42].Table 1.9 shows that the hydrogen abstraction in H_2O and CH_4 gas proceeds many orders of magnitude faster with hot hydrogen of 1 eV kinetic energy than with species in thermal equilibrium at 293 K.

Table 1.9: Comparison of hot and thermal reaction rate constants for H-abstraction reactions in the gas phase, according to [1.40].

reaction	$E_{threshold}$, eV	k_{hot} (1eV H) $cm^3\ s^{-1}$	$k_{thermal}$ (293 K) $cm^3\ s^{-1}$
$H + H_2O \rightarrow HO + H_2$	0.883	$1.7 \cdot 10^{-11}$	$9.6 \cdot 10^{-26}$
$H + CH_4 \rightarrow CH_3 + H_2$	0.51	$5 \cdot 10^{-11}$	$2.5 \cdot 10^{-19}$

Hot reaction rates seem to be in order of those for the corresponding ion-molecule reaction. Since in space neutral species are much more abundant than ions, hot atom chemistry constitutes an important part of all chemical processes. A specific application of UAC to Titan is given in [1.32].

Suprathermal chemical reactions of hot hydrogen (tritium), carbon and nitrogen atoms in gases and solids are reviewed in [1.39, 1.43,44], cf. also tables in [1.32]. The reactions of recoil ^{11}C atoms were studied in gaseous CH_4 [1.44 - 47], C_2H_4 [1.46, 1.48,49], C_2H_6 and C_3H_8 [1.50, 51]. In all these experiments the formation of high yields of unsaturated compounds and of more complex products by chain elongation was observed. One of the most prominent

mechanisms was carbon atom, CH or CH_2 insertion into C-H bonds. Experiments in the solid state of CH_4, C_2H_2 and C_2H_4 were reported by [1.47, 1.50, 1.52 - 59]. Reactions of carbon atoms with N_2 have been studied by [1.46, 1.60,61], the most prominent product besides CO (reaction with O_2 impurities) was CN or HCN. Photolysis of ICN yielded CN which reacted in methane atmosphere to CH_3CN [1.62]. Hot nitrogen atom reactions in CH_4 yielded NH_3, N_2, HCN, NO, CH_3CN, CH_3NH_2, $C_2H_5NH_2$ [1.63-1.65], cf. also [1.32]. Experiments with hot carbon in CH_4 gas mixtures were reported for CH_4/O_2 [1.66], CH_4/NH_3, CH_4/H_2O and $CH_4/H_2O/NH_3$ gas mixtures [1.67]. Most important for the problems of this work are the studies of carbon recoil in CH_4 or alkane mixtures with N_2 [1.68, 69]. The only primary carbon-nitrogen compound observed was HCN, formed at higher kinetic energies, i.e. by hot carbon atoms. It could also be shown that the HCN yield dropped with the radiation dose from 22.7% at $D^* = 2 \cdot 2 \cdot 10^{-3}$ to 4.65% at $D^* = 6 \cdot 6 \cdot 10^{-2}$ eV/molecule [1.68].

Among the many publications on radiation chemistry of gaseous methane and mixtures those by γ-rays [1.70, 71] and protons [1.72] shall be cited here, cf. also Tables 2.8 and 2.9 in [1.59].

A global overview on classical photochemistry and chemistry in Titan's atmosphere was given by [1.18, 1.73-76]; specific interest is given to the generation of carbon-nitrogen compounds in view of their importance for evaluation of potential life forms.

1.5 The aims of the work

The chemical effects of particle radiation have often been underestimated with respect to that of photon radiation. If considering, however, the contribution of hot atom reactions by suprathermal particles, the relatively low energy distribution of photodissociation products may often not reach the reaction cross sections to compete with thermal ion-molecule interactions induced by photolysis. At Titan all solar radiation is diminished by a factor of 10^{-2} with respect to the conditions on Earth. Thus, the isotropic cosmic rays will play a comparatively greater role as on Earth.

It is the aim of this work to provide some physical data on the collisional production of suprathermal particles by space radiation in Titan's atmosphere, in order to enable a future evaluation of suprathermal chemical reactions. Since actually, in the pre-HUYGENS probe period, informations on radiation flux and atmospheric composition are very limited, it should not be attempted to present a final description. The procedure should be a more modular one, working with simplified assumptions on the basis of our present knowledge, however step by step, that a substantial part of the results can be modified easily when new data will be obtained from future missions.

The collisional interactions of ions and neutrals from ISM, Titan's plasma tail, Saturn, solar wind, solar flares, solar cosmic rays, anomalous cosmic rays and galactic cosmic rays with energies ranging from 10 to 10^8 eV with Titan's atmosphere via knock-on processes will be studied to evaluate the chance for

potential suprathermal processes. The number of suprathermal atoms which are generated with kinetic energies ≥ 0.5 eV will be calculated by computer code MARLOWE (M.T. Robinson, ORNL) which works in a Monte-Carlo mode on the basis of binary collision approximation. Both, elastic (nuclear) and inelastic (electronic) interactions are regarded. Hot atoms are produced mainly by knock-on processes, i.e. elastic collisions. As typical representatives for the particle component of space radiation, the ions H, He, C, and Fe are selected. Since it is assumed on the basis of the collisional behaviour of high energetic light ions, that H and He with 10^8 eV are already in the relativistic regime and will not produce secondaries, the calculations shall be carried out for all energy decades from 10 to a maximum energy of 10^8 eV. It will be checked for the heavier ions such as C and Fe, whether they still are able to generate hot atoms at these energies. For the higher energetic light particles the Lindhard-Scharff-Schiott procedure for calculating inelastic (electronic) collisional loss must be substituted by a more quantum mechanical approach including corrections for relativistic effects.

Three mixtures are selected as typical representatives of Titan's atmosphere in the limits of the actual discussion: a) 98 % N_2 + 2 % CH_4, b) 82 % N_2 + 12 % Ar + 6 % CH_4, and c) 63 % N_2 + 25 % Ar + 12 % CH_4. The numerical calculation is carried out in solid model lattices based on an artifical cubic N_2 arrangement with statistical Ar, C, and H "impurities" bound to the lattice with their typical chemical bond energies in thermodynamic equilibrium. The calculation is aimed to yield the range of primaries, the production of hot atoms by collisions along the trajectory and their energy distribution. The model lattices and the interaction parameters are chosen in a way that they can easily be "translated" to the gaseous state. Special effects of the collisional behaviour in multi-component targets with their modulated pathways of energy transfer will be described.

The second part of the approach is the application to Titan's atmosphere which changes dynamically with altitude. Any special structures such as hazes, clouds, aerosol layers, demixing zones etc. shall be neglected in this very general approach. From the three targets calculated the two most probable ones: 98 % N_2 + 2 % CH_4 and 82 % N_2 + 12 % Ar + 6 % CH_4 are selected. The calculation is based on the column density in the solid model lattice and the number density of Titan's atmosphere in 10 km bins. The ranges of primary particles and the distribution profile of hot atoms will be evaluated. In (98 % N_2 + 2 % CH_4) mixture the production of hot atoms is calculated as a result of the infall of all cosmic particles (up to Fe) in a column density function with averaged flux and elemental composition data. Potential stopping in the magnetosphere and at internal boundary layers for lower energetic particles is neglected here, however, the lowest energy considered is 10^3 eV. It should be mentioned, that not only ions may penetrate into Titan's atmosphere but also neutrals from secondary reactions and charge neutralization processes. The modular procedure based on a full calculation of hot species in the condensed model atmospheres, enables an easy change of parameters and recalculation of the data.

Even if the application of these data on hot atom profiles in Titan's atmosphere to potential suprathermal, chemical reactions is the proper task of physicochemical kineticists, it is thought, that an even somewhat preliminary experiment on the interaction of fast ions with a typical gas mixture might be an interesting complementary approach to the calculations. 32 MeV $^3He^{2+}$ ions from the Jülich compact cyclotron CV 28 will interact with three gas targets containing N_2 and CH_4 at 1.6 bar (Titan's surface pressure): a) pure CH_4, b) 90 % N_2 + 10 % CH_4, and c) 98 % N_2 + 2 % CH_4. The temperature is 295 K. Dose effects for D* = 0.0022 to 0.88 eV per target molecule will be studied. The formation of products will be followed by gaschromatography, in particular with a radioactivity detector. The nuclear reaction $^{12}C(^3He,^4He)^{11}C$ generates ^{11}C with a half-life of T = 20.3 min and a primary energy of 4.6 MeV. Then it is gradually stopped in the pressure gas target to undergo hot chemical reactions. Measuring the ^{11}C radioactivity distribution means to follow specifically hot carbon atoms such as generated in Titan's atmosphere, an elegant application of nuclear chemistry.

The detailed numerical calculation of altitude profiles on hot atoms and the preliminary experiment on the chemical action of one of them, are aimed to provide more insight into the chemical processes of one of the most interesting bodies in our solar system.

CHAPTER 2

PRODUCTION OF HOT ATOMS BY COLLISIONS THEORETICAL APPROACH

2.1 General description of *MARLOWE* program

Computer simulation of the slowing down of energetic atoms by a series of elastic and inelastic collisions, thereby displacing the target atoms (secondaries) and creating a collision cascade, is a domain of theoretical solid state physics [2.1]. The processes include erosion of the target (sputtering), changes in its physical properties (radiation damage) or chemical composition (hot atom chemistry). The theory of displacement cascades and their analytical treatment [2.2,2.3] were however for quite a time devoted to metallic substrates only . Computer simulation techniques were first introduced into studies of low energy radiation damage events by Vineyard et al. [2.4,2.5] who studied small crystallites of a few hundred atoms bound together by e.g. Lennard-Jones potentials, with boundary restraints to represent imbedding in a larger lattice. This model has been applied to bcc-and fcc-metals [2.4,2.6] and to sputtering [2.7]. The alternative procedure was to construct the trajectory of a moving particle as a series of isolated collisions [2.8,2.9] an approximation which is useful in particular at high energies. The more elaborate models included electronic excitation. Since isolation of the collisions was difficult to obtain at low energies, a more developed program was presented 1972 by Robinson and Torrens: *MARLOWE* [2.10,2.11]. This code follows the primary and secondary projectiles through a series of binary atomic collisions, where always the currently fastest particle is calculated. It is a kind of Monte Carlo calculation which simulates slowing down and scattering of energetic ions in solid targets. It was developed for determining ion range, angular distribution and damage concentration of backscattered and penetrating ions. A high degree of accuracy is achieved mainly by applying an analytical formula for determining nuclear scattering angles, and by suitably expanding the distance between collisions at high energies. This Monte Carlo program is used to calculate the range distributions of a variety of ion / target combinations.

Several ion transport procedures based on the Monte Carlo method have been reported [2.11-13] Aside from considering crystalline or amorphous targets, their major differences lie in their treatment of elastic or nuclear scattering. Only Oen, Robinson et al. [2.11,2.12] treated this scattering in a precise manner by numerically evaluating the classical scattering integral for realistic interatomic potentials. Other authors base their formalisms on either the momentum approximation extended to large angles or fitted, truncated Coulomb potentials to obtain analytical representations of the scattering integral.

The *MARLOWE* method consists of following a large number of individual ion or particle (histories) in a target. Each history begins with a given energy, position, and direction. The particle is assumed to change direction as a result of binary nuclear collisions. The energy is reduced as a result of nuclear and electronic (inelastic) energy losses and a history is terminated either when the energy drops below a pre-specified value or when the particle's position is outside the target. The target may be an ordered single crystal or amorphous with atoms at random location. Here the directional properties of the crystal lattice are ignored. This method is applicable to a wide range of incident energies, approximately 0.1 keV to several MeV, depending on the masses involved. The lower limit is due to the inclusion of binary collisions only, while the upper limit results from the neglect of relativistic effects. Also, nuclear reactions are not included. The efficiency for dealing with high energy particles has been increased by introducing an energy dependent free-flight-path between collisions, which is longer at high energies and is steadily reduced in the course of slowing down.

The development of the cascade in time was simulated by always computing the next collision of the fastest particle currently in the cascade. This procedure was altered only when a sequence of replacement collisions was detected. Since the target receives nearly all of the projectile energy, it is followed immediately.

The basic mechanism of stopping particles such as protons or heavier ions in matter is the energy loss due to nuclear and electronic collisions. At high energies or velocities ions are slowed down mainly by electronic collisions (electronic stopping) where as at low energies nuclear collisions are dominating (nuclear stopping). Thus a fast projectile will in the first part of its history suffer mainly electronic losses where as in the final part, towards the end of its range, it will be slowed down predominantly by nuclear losses. There exists rule of thumb : the electronic loss will be greater than the nuclear one, when the energy of projectile in keV is equal or exceeds the mass in a.m.u.

The nuclear and electronic energy losses or stopping powers are in principle assumed to be independent. Thus, particles loose energy in discrete amounts in nuclear collisions and more continuously by electronic interactions. For low energies, where nuclear scattering and energy loss is particularly important, the program utilizes the above mentioned analytical scheme based on solid-state interatomic potentials as will be described in chapter 2.1.1. The electronic energy loss will also be described in chapter 2.1.3.

Printout control parameters select either a detailed information about each individual interaction or just a statistical analysis from a number of single events including lattice dependent data (e.g. number of collisions, number of atoms involved, number of vacancies, number of interstitial atoms, replacement reactions) as well as a detailed energy balance for all atoms of the cascade.

2.1.1 Treatment of binary collisions

The binary collision approximation is the basis of a large number of computer simulation programs. True binary collisions between atoms have been studied in the past in the field of atomic collisions in the gas phase. The movement of an atom in a solid can be treated as a series of successive binary collisions.

It is assumed in the computational model that the particles move along straight-line segments, these being the asymptotes of their paths in the laboratory (L) system. The trajectories of two particles interacting according to a conservative central repulsive force are shown in Fig 2.1 which defines several terms of interest. The equations of motion which describe these trajectories can be manipulated in the usual manner [2.1,2.14] to yield the barycentric scattering angle θ :

$$\theta = \pi - 2p\int_R^\infty dr\left[r^2 g(r)\right]^{-1} \tag{2.1}$$

and the time integral T :

$$T = \left(R^2 - p^2\right)^{1/2} - \int_R^\infty dr\left[\left(g(r)\right)^{-1} - \left(1 - \frac{p^2}{r^2}\right)^{-1/2}\right] \tag{2.2}$$

where :

$$g(r) = \left[1 - p^2/r^2 - V(r)/E_r\right]^{1/2} \tag{2.3}$$

with :

p	impact parameter,
E_r	relative kinetic energy,
r	variable interatomic separation,
V(r)	potential of interatomic force, and
R	apsis of the collision defined by $g_{(r)} = 0$.

The relative kinetic energy is :

$$E_r = AE_0 / (1+A) \tag{2.4}$$

where E_0 is the incident kinetic energy of the projectile and A is the ratio of the mass of the target (scattering atom) to that of the projectile (scattered atom). The integrals in Eqs. 2.1 and 2.2 are evaluated by four-point Gauss-Mehler [2.15, 16] quadrature. The scattering angles ϑ and θ of the projectile and the target in L system are :

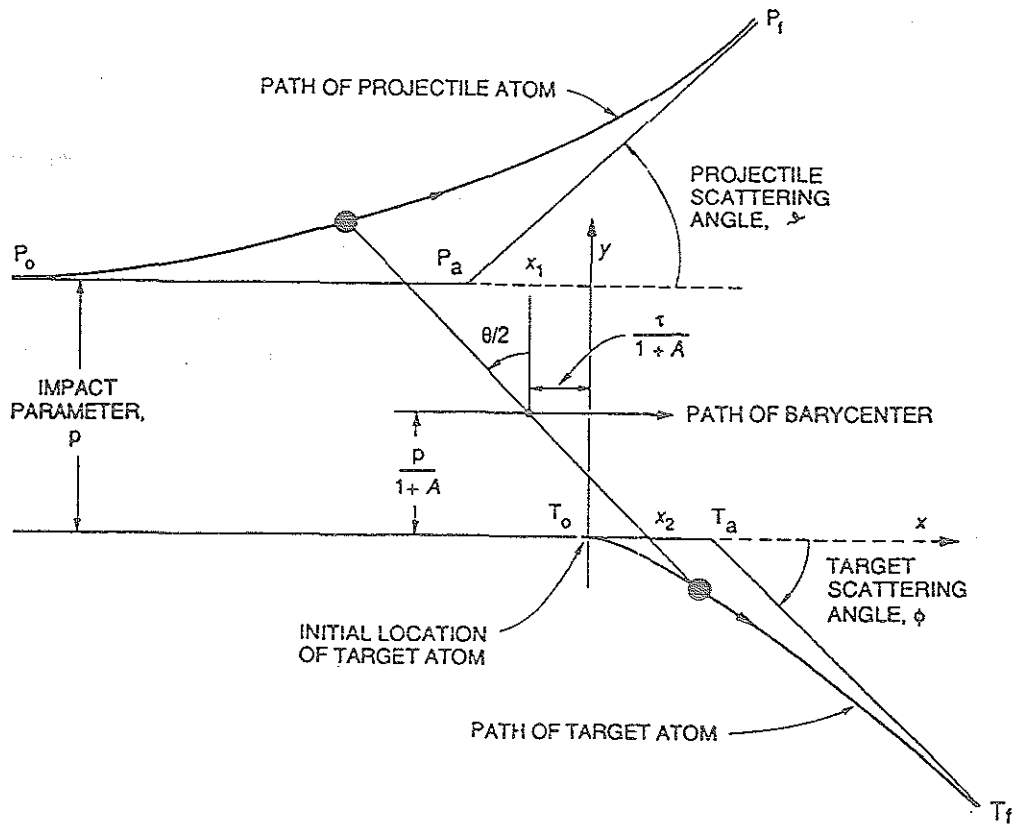

Fig. 2.1 : Trajectories of two particles interacting according to a conservative central repulsive force in the L system. The positions of the particles and of the barycenter are shown at the apsis of the collision.

$$\tan\vartheta = Af\sin\theta/(1+Af\cos\theta) \qquad (2.5)$$

and

$$\tan\Phi = f\sin\theta/(1-f\cos\theta) \qquad (2.6)$$

where:

$$f = (1-Q/E_r)^{1/2} \qquad (2.7)$$

and Q is the energy lost by electron excitation. The energy transferred to the target atom in the collision is :

$$T = \left[f\sin^2\frac{1}{2}\theta + \frac{1}{4}(1-f)^2\right]T_m \qquad (2.8)$$

where the maximum transferred energy is :

$$T_m = 4E_r/(1+A)\,. \qquad (2.9)$$

The energy E_1 of the projectile after scattering is :

$$E_1 = E_\circ - T - Q. \tag{2.10}$$

The differential scattering cross-section is defined as :

$$\sigma(\theta)d\theta = \frac{2\pi dp}{\sin\theta} \tag{2.11}$$

where $\sigma(\theta)d\theta$ describes the probability that particles in a uniform beam incident upon the scattering center will be deflected into the angular range $d\theta$ at θ. The differential scattering cross section may also be defined as :

$$d\sigma = \frac{\sigma(\theta)dT}{T_m} \tag{2.12}$$

which describes the probability that the projectiles will lose energy in range dT at T.

The basic idea to calculate the linear range R_L of a projectile starting with energy $E_\circ$ can be obtained from the stopping power :

$$R_L(E_\circ) = \int_0^{E_\circ} \frac{dE_1}{(-dE_1/dR)} = \frac{1}{n}\int_0^{E_\circ} \frac{dE_1}{S(E_1)} \tag{2.13}$$

where $S(E_1)$ is called the stopping cross section (per scattering centre).

$$S(E_1) = \frac{1}{n}\frac{dE_1}{dR}\int T\sigma(T, E_1)dT, \tag{2.14}$$

where n is the density of scattering centres (atomic density) of the crystal and σ the total elastic scatering cross section, T is the energy transfer to target particle, E_1 energy of the projectile and R is the path length.

In *MARLOWE*, the particles move along straight-line segments from one laboratory deflection point to the next. Note that although the inelastic energy loss does not enter the barycentric equations of motion, it does affect the kinematics of the collision through Eq. 2.7. The program contains three options with respect to the inelastic loss .These may be omitted altogether (Q = 0 and f = 1), they may be included in the energy loss, but omitted from the kinematics (Q $\neq$ 0, but f = 1), or they may be included in both of them.

2.1.2 Interatomic potential

When two atoms approach each other very closely, the interaction potential must approach the Coulomb repulsion between the two nuclei, but at larger separations the nuclear charges will be partially screened by the atomic electrons. The difficult general problem of selecting an interaction potential function for various application is discussed elsewhere [2.2, 17, 18] . Proper treatment of the high-energy region dictates the use of a screened Coulomb potential :

$$V_{(r)} = \left(\frac{Z_1 Z_2 e^2}{r}\right)\Phi\left(\frac{r}{a_{12}}\right). \qquad (2.15)$$

Z_1, Z_2 are the nuclear charges of the projectile and target,
$\Phi(x)$ is a suitable screening function, and
a_{12} is a screening length which depends on the properties of the collision partners.

While *MARLOWE* is constructed to allow fairly easy alteration of the potential function, all calculations to date have used the Molière approximation [2.19] to the Thomas-Fermi screening function :

$$\Phi(x) = 0.35y + 0.55y^4 + 0.10y^{20} \qquad (2.16)$$

where : $y = e^{-0.3x}$.

Firsov [2.20] on the basis of approximate numerical solution of the Thomas-Fermi diatomic molecule problem, has suggested the formula :

$$a_{12} = \left(\frac{9}{128}\pi^2\right)^{1/3} a_B \left(Z_1^{1/2} + Z_2^{1/2}\right)^{-2/3} \qquad (2.17)$$

where a_B = 0.526 Å is the Bohr radius. This screening length is optionally available in the program. It is possible to use screening lengths deduced in other ways.

At this point the theoretical model describes the elastic energy loss at lower velocities $v_1 << Z_1 v_o$, where $v_o = e^2/\hbar$ is the orbital velocity of the electron in the hydrogen atoms and the screening of the projectile's atomic nucleus by electrons present in the undisturbed atoms plays a role.

At sufficiently high energies the projectile, however, may be deprived of many if not all of its electrons. This will alter the screening of the nuclear charge of the projectile. In previous work by Westmeier and Roessler [2.21, 22] two values for Z were used : Z, the charge of the nucleus and Z', the number of electrons of the atom which changed with its velocity according to an empirical formula, cf. also [2.23, 24]. It had been shown, that even for very heavy atoms

which have a lot of electrons to loose, the effect on the nuclear stopping power is not too strong [2.21]. The effect on light, high energetic particles in *MARLOWE* is discussed in [1.59], cf. also [2.25]. In this work the effects of projectile electronic charges to elastic loss are neglected at lower energies.

2.1.3 Inelastic loss functions

Energy losses of a projectile due to electronic collisions come about not only by energy transfers to target electrons (resulting in excitation and ionization of target atoms) but also by the loss of own electrons (stripping) and by exchange of an own electron with one of the target electrons (charge exchange). In such processes the projectile has to expend kinetic energy for the removal of bound electrons. This can lead to a change in kinematics.

Firsov [2.20] proposed a model where the electron clouds of colliding atoms overlap, assuming a collision time long enough for complete mixing of the electrons in the overlap region. The momentum transfer in this mixing process allows the determination of the electronic energy loss. An approximation Thomas-Fermi description and the impulse approximation for the motion of the nuclei lead to the following formula for the energy loss Q as a function of impact parameter p and kinetic energy E:

$$Q(p,E) = \frac{\alpha_{12} E^{1/2}}{(1+\beta_{12} s)^5} \text{ [eV]} \qquad (2.18)$$

where α_{12} and β_{12} are numerical constants. The basic idea for the derivation of Eq. 2.18 is as follows. Firsov`s description leads to $Q \propto \int \phi^2 \, dx$ where ϕ is the screening function. The use of an asymptotic Thomas-Fermi approximation [2.26] involves that $\phi \propto x^{-3}$ gives $Q \propto x^{-5}$. The actual denominator just remedies the singularity at x = 0. The constants α_{12}, and β_{12} are given by :

$$\alpha_{12} = 0.61 \frac{2\hbar}{\pi a_B} \left(\frac{2}{M_1}\right)^{1/2} \left(\frac{9\pi^2}{128}\right)^{1/3} (Z_1 + Z_2)^{1/3} \qquad (2.19)$$

$$= 0.06685 \frac{(Z_1 + Z_2)^{1/3}}{M_1^{1/2}} \text{ [eV]}^{1/2} \text{ ,and:}$$

$$\beta_{12} = \left(\frac{0.285}{2a_B}\right) \left(\frac{9\pi^2}{128}\right)^{-1/3} (Z_1 + Z_2)^{1/3} \qquad (2.20)$$

$$= 0.3043 (Z_1 + Z_2)^{1/3} \text{ [Å}^{-1}\text{]}$$

where :

M_1 is the projectile's mass and,
Z_1 its electronic charge, and
Z_2 is the electronic charge of the target atom.

The constants α_{12} and β_{12} have been determined by numerical integration. Eq. 2.16 has an upper limit of validity for the energy E :

$$E < \overline{E} = \frac{1}{2} M_1 v_F^{\,2} = 24.97 Z_1^{\,4/3} M_1 \ [\mathrm{keV}] \qquad (2.21)$$

with the Fermi velocity $v_F = v_B Z_1^{\,2/3}$
and Bohr velocity $v_B = e^2/\hbar$.

The stopping cross-section S_e then becomes :

$$S_e = 2\pi \int_0^{p_{max}} p\,Q(p,E)\,dp \ . \qquad (2.22)$$

As a correction to use of the impulse approximation in the derivation of (2.18), Robinson applying the idea that $\phi \propto e^{-X}$ might be a better approach than Firsov`s, proposed a different formula for the electronic energy loss, Q_{OR} (Oen Robinson) [2.27]:

$$Q_{OR}(p,E) = \frac{d_1^2}{2} \frac{K E^{-1/2}}{\pi a^2} \exp\left[-d_1 R(p,E)/a\right] \qquad (2.23)$$

where :

d_1 is a potential parameter,
a is a screening length,
R is the distance of closed approach (apsis), and
K is a constant defined in (2.26), the exponential term of which describes the electron density around the atom.

The stopping cross section for high energies, where $R(p,E) \approx p$, becomes :

$$\begin{aligned} S_{OR}(E) &= 2\pi \int_0^{p_{max}} p Q_{OR}(p,E) dp \\ &= 2\pi \frac{d_1^2}{2} \frac{K E^{-1/2}}{\pi a^2} \left(\frac{a}{d_1}\right)^2 (-k+1) \qquad (2.24) \\ &= K E^{1/2} (1-k), \end{aligned}$$

where :

$$k = \left(1 + \frac{d_1 p_{max}}{a}\right) e^{-d_1 p_{max}/a} < 0.1. \qquad (2.25)$$

The factor K is that proposed by Lindhard et al. [2.28, 29] for the continuous stopping, where the electron gas in a solid behaves like a viscous medium for the moving ion. Lindhard and Scharff gave a formula for the inelastic stopping cross-section S_{LS} :

$$S_{LS}(E) = 8\pi\sqrt{2}a_B\hbar\frac{Z_1^{7/6}Z_2}{\left(Z_1^{2/3}+Z_2^{2/3}\right)^{3/2}}\sqrt{\frac{E_1}{M_1}},$$
$$= K\sqrt{E} = 1.21\frac{Z_1^{7/6}Z_2}{\left(Z_1^{2/3}+Z_2^{2/3}\right)^{3/2}}\sqrt{\frac{E_1}{M_1}}. \qquad (2.26)$$

They used the electronic response for the derivation of Eq. 2.19 and 2.20. The fitting parameter C_k is often introduced to account for Z_2 oscillations in the inelastic stopping, so that :

$$S_{LS}(E) = C_k K\sqrt{E} \qquad (2.27)$$

where C_k varies between 0.67 and 2.4 .

The difference between the stopping cross-section of Lindhard-Scharff and Oen-Robinson increases with decreasing energy, exhibiting a lower loss for the Oen-Robinson model. At low energies, in the eV range, the Oen-Robinson inelastic loss can be up to a factor of 10 lower than the continuos Lindhard-Scharff energy loss. It should be mentioned that the Firsov-based derivations fit better the case of insulator targets with localized electrons and the Lindhard-Scharff approach applies better to metallic target with electronic continous.

Inelastic energy losses are included in the program using a modification of a model proposed by Firsov, as described above in Eq. 2.23 and 2.24.

2.1.4 Crystal description and cascade development

A principal advantage of the binary collision approximation is that it requires only a small amount of information to describe the target crystal. In *MARLOWE* a list is made of the positions of several atoms in the crystal, using one of the lattice atoms as the origin of the Cartesian coordinate system. A list of first and second nearest neighbors is determined and use is made of the transitional symmetry of the crystal. Searching of lists containing only first nearest neighbors is faster, than of those containing also second nearest neighbors, but the latter has to be performed often because of the probability of finding no suitable collision partner.

The search procedure for finding the next collision partner is illustrated in Fig. 2.2 From the point D_{i-1}, where the last change in direction of the asymptote occurred, the atom is moving in the director λ_o (unit vector). The search in the neighbor list finds the target atom T_i. Then the distance ζ and the impact parameter p are determined by :

$\zeta = \lambda_o \cdot \Delta x$, and (2.28)

$p^2 = (\Delta x \cdot \times \lambda_o)^2$ (2.29)

where Δx is the distance from T_i to D_{i-1}, to avoid the target atom T_{i-1} being chosen again as a collision partner.

The following equation is set :

$\zeta > \zeta_{min} \geq 0$. (2.30)

If p is larger than a preset maximum impact parameter p_{max}, the target atom T_i is considered to be too far away to cause any reasonable deflection of the moving atom or energy transfer to the target atom T_i. If $p < p_{max}$, the new directions can be found from Fig 2.2 :

$(\zeta+\zeta`) \lambda_o - \Delta x = \lambda'_1$, and

(2.31)

$(\zeta-\zeta``) \lambda_o + \lambda'_2 = \Delta x$, with

$\tan \vartheta_1 = p / \zeta`$, $\tan \vartheta_2 = p / \zeta``$,

$\sin \vartheta_1 = p / |\lambda'_1|$, $\sin \vartheta_2 = p / |\lambda'_2|$.

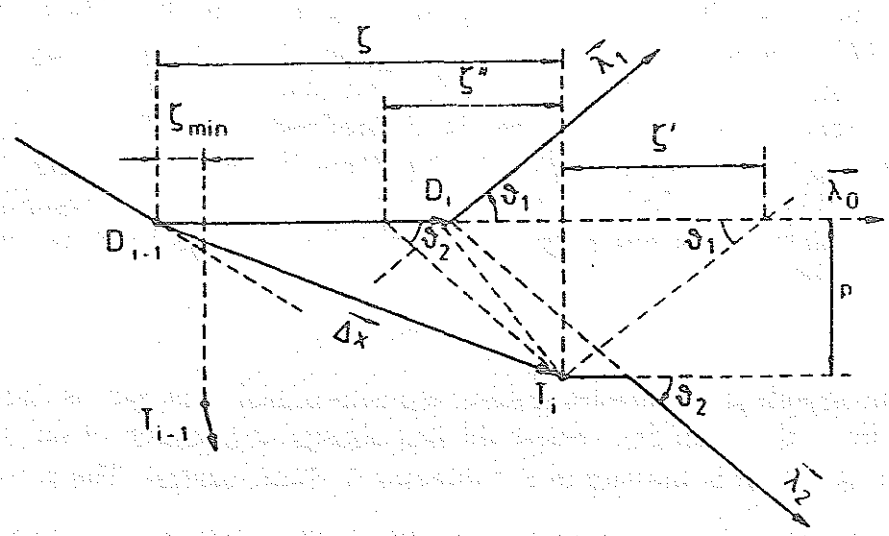

Fig 2.2 : Schematic drawing illustrating the search procedure for the next collision partner in *MARLOWE* .

One obtains the new directions (unit vectors):

$$\lambda_1 = \left(\cos\vartheta_1 + \frac{\xi}{p}\sin\vartheta_1\right)\lambda_o - \left(\frac{1}{p}\sin\vartheta_1\right)\Delta x,$$
$$\lambda_2 = \left(\cos\vartheta_2 - \frac{\xi}{p}\sin\vartheta_2\right)\lambda_o + \left(\frac{1}{p}\sin\vartheta_2\right)\Delta x \quad . \tag{2.32}$$

Now the whole procedure is repeated to find the next collision partner and directions. The value of p_{max} must be larger than a minimum value that depends on the crystal. The value of ζ_{min} has to be found by trial and error; it is usually taken as one-tenth of a lattice unit.

At this point another complication arises. It may happen that more than one target atom meets the criteria of Eqs.2.30 and 2.32. If i indicates these target atoms along the trajectory, then for each of these potential collision partners the following values are calculated, see also Fig 2.3 and the expressions in it :

$$\Delta\zeta_{1i} = \zeta_i - \zeta_1 \quad . \tag{2.33}$$

These collisions are regarded as simultaneous collisions if :

$$\Delta\zeta_{1i} < \zeta_m \quad . \tag{2.34}$$

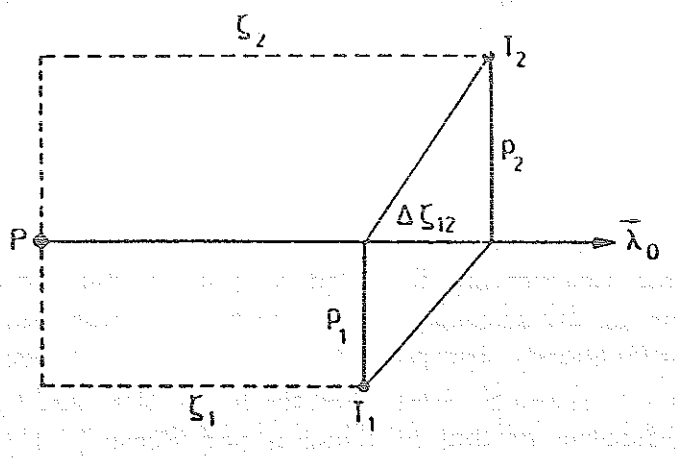

Fig 2.3 : Schematic drawing illustrating the conditions for simultaneous collisions.

For all atoms which obey the conditions of Eq. 2.34 the collision is treated as usual in the center-of mass system. These simultaneous collisions are mainly important at low energies and the procedure described is one possible approximation.

Thermal vibrations can be included but correlations between neighboring atoms` displacements are not considered. Since thermal vibrations are slow compared to the time of a collision they lead to randomly displaced target atom positions.

The development of the cascade in time was simulated by always computing the next collision of the fastest particle currently in the cascade. This procedure was altered only when a sequence of replacement collisons was detected. Since the target atom receives nearly all of the projectile energy, it followed immediately.

Printout control parameters select either a detailed imformation about each individual interaction or just a statistical analysis from a number of single events including lattice dependent data (e.g. number of collisions, number of atoms involved, number of vacancies, number of interstitial atoms, replacement reactions) as well as a detailed balance for all atoms of the cascade.

2.1.5 Displacement model

Seitz [2.30] introduced the important idea that a target atom is ejected permanently from a lattice site only if it receives a kinetic energy in excess of a sharp displacement threshold E_d, usually about 25 eV. The model of *MARLOWE* allows considerable flexibility in defining this threshold, with a view to studying its influence on the results of the calculations. Consider a collision from which the original projectile energy with kinetic energy E_1, after transferring kinetic energy T to the target atom, cf. Eqs. 2.8 and 2.10. The target may be required at the same time to overcome a binding energy $E_b \leq E_d$ Then it is added to the cascade with kinetic energy E_2 :

$$E_2 = T - E_b. \qquad (2.35)$$

The atoms in the cascade are followed as long as their energies exceed a preassigned value E_c, the so-called cutoff energy. No limitation is placed on the relation between E_c and E_d. The projectile is deemed to replace the target on its lattice site when $T > E_d$ and E_1 is less than the lesser of E_c and E_d. This definition is a slight modification of that of Kinchin and Pease [2.31]. If the arriving projectile is of the correct chemical type to occupy the vacated lattice site, the replacement is termed proper, otherwise it is improper. No attempt is made to force stopped projectiles to occupy particular locations. Both interstitial and replacing atoms are left at the turning points of the collisions in which their energies pass below E_c. This procedure is argued from the fact that these abandoned particles still have kinetic energy which they must dissipate before they adopt well-defined positions. The time required for this energy dissipation

exceeds the time needed to generate the cascade A corollary of this argument is that interactions between cascade particles should be omitted.

2.1.6 Calculation of hot atoms

Atoms which are displaced by energy transfer exceeding the threshold and then possessing a kinetic energy higher than the cutoff energy 0.5 eV, are classified by the program as "new cascade atom". Their number ordered with respect to the different kinds of atoms in a lattice and their energy distribution in a half-decade grid (e.g. 0.5 to 1.0; 1.0 to 5.0; 5.0 to 10 eV, etc.) can be obtained changing some output parameters in the *MARLOWE* subroutine DETAIL. The problem in the listing based on "new cascade atoms" is that it includes the starting particles of side cascades and the knock-ons likewise, i.e. it reports an integral over the whole temporal development of the cascade. This becomes only critical for the energy distribution of hot atoms after their last displacive action, i.e. before slowing down to undergo chemical reaction. The problem is discussed in more detail in chapter 3.5.

2.2 Application to high energy collision in gas phase

When applying a program such as *MARLOWE*, which is conceived for calculations in the solid state and for not too high primary energies up to about 1 MeV and relatively heavy projectiles, to the gas phase and high energy collisions, the right parameters have to be chosen in the program as well as alterations have to be made with respect to the inelastic energy transfer modes.

2.2.1 Description of the model lattice

MARLOWE needs a complete description of the lattice structure of the stopper medium with atom positions in orthorhombic coordinates and information about the individual species such as their mass, atomic charge and binding energies. An unusual method of lattice representation permits a very fast searching algorithm to find the next interaction partner after each collision, *MARLOWE* does not require the description of one crystallographic unit-cell which is duplicated in the direction of the projectile motion.

Our model lattice is an artificial simple cubic arrangement of N atoms as shown in Fig. 2.4. Ar and CH_4 are included as single atoms (Ar, C, 4H) via the MIXT subprogram to simulate Titan's atmospheric composition corresponding to the actual discussion: two extreme mixtures, one without Ar (I) and one with a large amount of Ar and CH_4 (III), and an intermediate mixture (II), see Table 2.1.

Table 2.1 : Targets for three atmospheric compositions.

target	assumed comp., Mole % N_2	CH_4	Ar	*MARLOWE*-MIXT, % N	C	H	Ar
I	98	2	0	95	1	4	0
II	82	6	12	79	3	12	6
III	65	10	25	63	5	20	12

A general lattice constant of 2.5 Å was chosen for the cubic model lattice. It should be mentioned that this procedure does not include full N_2 and CH_4 molecules. In the next subchapter it will be shown how the chemical bond energies are included in the program. Thermal vibrations are not treated.

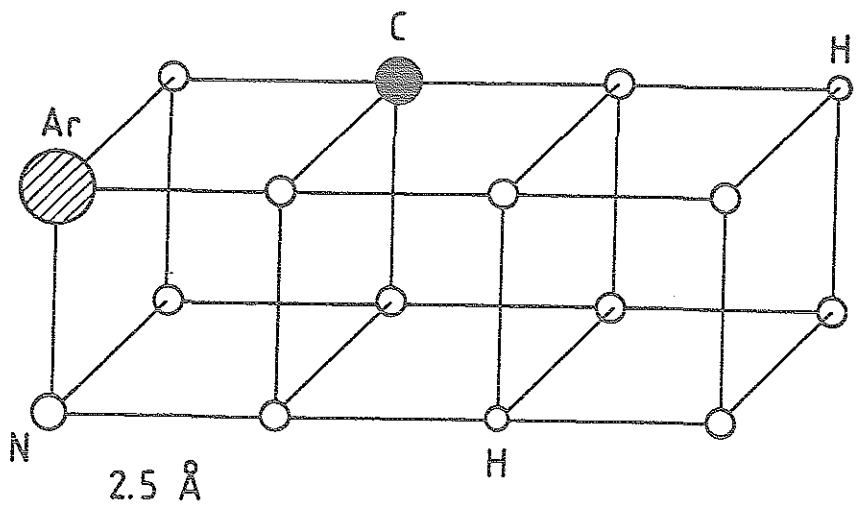

Fig 2.4 : Model lattice of cubic N containing Ar and CH_4 .

2.2.2 Conversion to gas phase

The *MARLOWE* program is originally conceived for solids; some parameters have to be modified when applying it to gas systems, First, simultaneous collisions with next neighbors have to be suppressed, since they do not happen in the relatively diluted gas phase. To achieve this, the *MARLOWE* input data for DSIM, the maximum distance permitted between two simultaneous collisions was set very small to 0.001 a_o (0.0025 Å).

Second, the structure of the target crystal was randomly disordered by the subprogram POLY = T,T to simulate an amorphous structure by changing the orientation of the three Carthesian axes, i.e. rotating slightly the arrangement of neighbors using the random number generator.

To simulate the chemical bonds the values for the displacement thresholds of the single atoms in the lattice were those of the bond energies of the molecules in thermodynamical equilibrium: N_2 : 9.5 eV, CH in CH_4 : 4.4 eV and C in CH_4 : 17.6 eV [cf. Table 2.2]. Ar as a free atom possesses only a low E_d = 0.5 eV. This value is deliberately not 0 in order to avoid the set into motion of particles with kinetic energy below E_c. Fig 2.5 illustrates the situation for the model lattice : the bond energies are substituted by those of the displacement threshold E_d. This procedure is justified from the fact, that the calculation is aimed to give data on formation of single energetic atoms. Nevertheless a certain amount of energy transferred is lost by bond breakage. Since this is a non-equilibrium process the values of binding loss energy E_b will be lower than those in thermal equilibrium. Thus, they are set somewhat smaller than those for E_d. but still relatively high, close to the full bond energy. This is meaningful for the case of gas phase molecules. In solids E_b values are in general much smaller because the lattice structure weakens the individual covalent bond energies. The cutoff energy E_c, at which the calculation is stopped, is set relatively low to 0.5 eV.

Table 2.2 : Energies of bonds as simulated by lattice displacement thresholds E_d and binding loss energies E_b .

element	E_d, displ. thresh., eV	E_b, bind. loss, eV	E_c,cutoff energy, eV
N	9.5	9.0	0.5
Ar	0.5	0.5	0.5
C	17.6	17.1	0.5
H	4.4	3.9	0.5

The fourth important item is blowing up of the solid model lattice in three dimensions to yield the concentration of the gas phase. In the present approach this is achieved by applying the barometric formula and the number density function. The chances of interaction of projectile and target atoms are, thus, diminished and consequently the range increased. It has to be considered that the potentials might be somewhat different in the gaseous state for isolated atoms (molecules). Potentials in the gas phase may stretch farther out than those in the solids. *MARLOWE* in particular cuts off any interactions in a distance with its search radius of 0.7 $a_o \approx 1.75$ Å. This was discussed by Ziegler [2.32] for the charge / electron density of isolated Al atoms and those in a solid arrangement. The differences are only visible at higher distances (> 1 Å), but are not very significant for the whole stopping process. In his Handbook Tables [2.32] the total stopping of light and heavier ions in Xe (mass 54) is not too different for the solid and the gas phase approach. Thus, it seems possible to use a density function to describe the effects of dilution. It should also be remembered that the first approach to describe collision dynamics was performed for isolated, gaseous atoms and that the solid state application was only a modification of the first theories. By the above described choice of *MARLOWE* parameters some of the typical solid state character of the calculations was modified a priori.

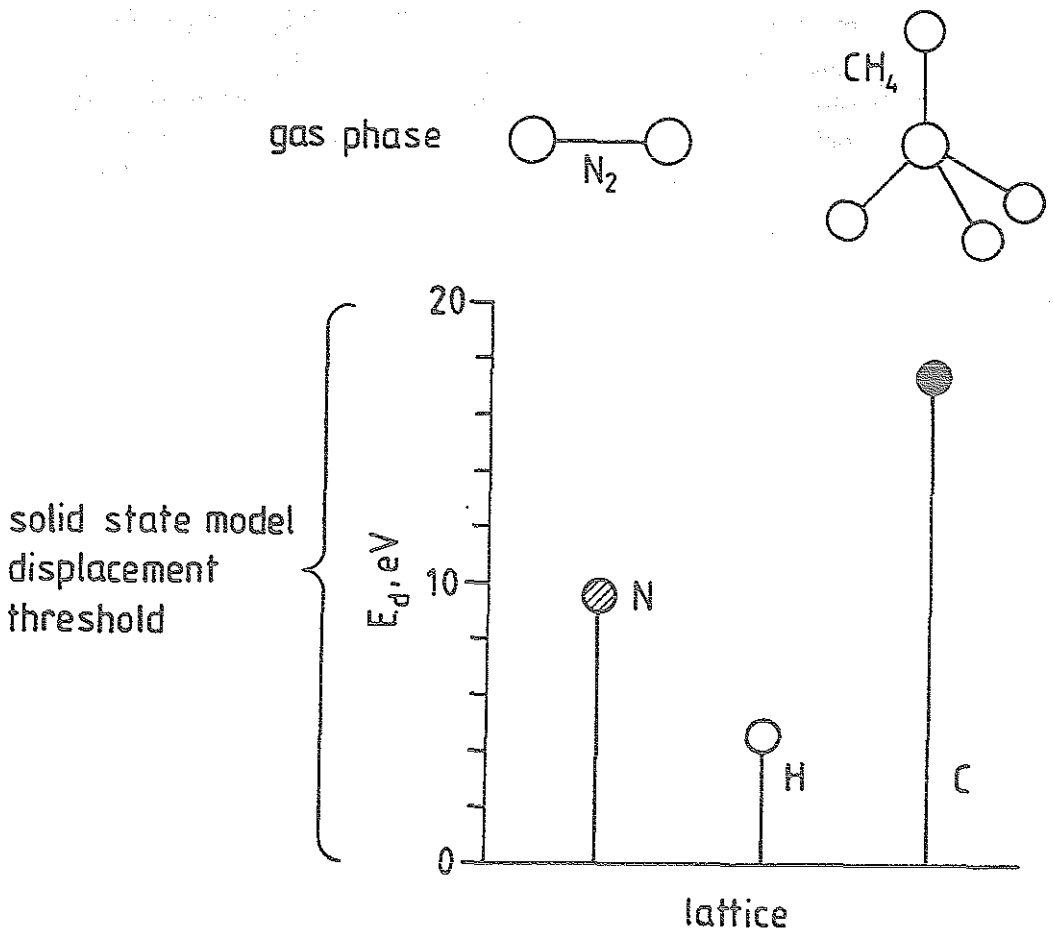

Fig 2.5 : Representation of energy bonds in the model lattice.

Last not least the inelastic interactions are here reduced in a quite natural way from transfer to electronic continuum to isolated binary cases. This enables the evaluation of electronic energy transfer per collision, which plays an important role in this work, cf. chapter 3.6.

The actual procedure to calculate in a denser medium and dilute to the gas state is a generally followed procedure, cf. e.g.[2.32-35] and it is the only one to include the dynamics of a steadily densifying atmosphere with respect to the impinging species. It has, however, the tendency to overestimate the collisional interactions. The search radius of 1.75 Å is quite big compared to the model lattice dimensions. Specifically at high gas dilutions the chances of interaction drop. Thus, the formation of secondaries can be regarded as some what too optimistic; the ranges, on the other hand, may be too short. These effects are to a certain degree counterbalanced by two facts. The freely moving gas will to a certain degree be more opaque than the diluted solid state with its regular atomic arrangements even in the POLY = T,T mode. Second, the calculation for a homogeneous gas does not include concentration in special atmospheric zones,

sudden jumps in density and in particular the presence of mist, aerosols and icy grains. With the currently very limited knowledge on Titan's atmospheric structures, it is not possible to include all details in the evaluations. The reason, that the numerical results are reported in extension, is to enable later refinements of the data treatment, when CASSINI mission has provided more insight.

2.2.3 Electronic stopping at high energies

The electronic charging of the projectile due to loss of electrons at higher energies can not be neglected for the inelastic loss process. Likewise relativistic effects may occur at very high energies. The model for inelastic loss in *MARLOWE* in chapter 2.1.3 is thus not applicable to light projectiles at high energies. Both Thomson [2.36] and Darwin [2.37] treated energy loss as the energy transferred by a moving charged particle to a free electron. Since such a collision without shielding has an infinite energy loss cross-section, they were both led into the problem of specifying maximum impact parameters based on atomic densities. Bohr based his study of electronic stopping cross-sections on a model which considered the target to be a collection of harmonic oscillators whose frequencies were determined by optical absorption data [2.38].

Thereafter several attempts were made by Bethe [2.39, 40] and Moller [2.41], and others [2.42 - 45] and finally by Bloch [2.46 - 48] to include quantum mechanics into this problem. Bloch found that Bohr`s distant collision theory was quantum-mechanically correct as the mean energy loss averaged over all electronic transitions. For high energies ($E_1 >> \bar{E}$), Bloch has given a treatment of stopping where the differential cross-section for a process in which the ion transfers a given energy to the atomic electrons is essentially given by the square of the matrix element of Coulomb interaction between the appropriate initial and final states. Summing over all possible differential cross sections, weighted with the corresponding energy loss, one obtains Eq. 2.36, the so-called Bethe-Bloch formula for the stopping power at high energies :

$$S_e = \frac{4\pi Z_1^{\,2} Z_2^{\,2} e^4}{M_e M_2 v_{in}^{\,2}} B \qquad (2.36)$$

where :

Z_1 , Z_2	represent the atomic number of projectile and target,
e	the electron charge (e^2 = 14.4 eVÅ),
M_e , M_2	mass of electron and target atom,
v_{in}	the velocity of the projectile, and
B	the stopping number which can be written as :

$$B = Z_2 \ln\left(\frac{2M_e v_{in}^2}{I}\right). \qquad (2.37)$$

The mean excitation energy I was calculated by Bloch [2.48]. He applied a dynamical treatment to a Thomas-Fermi statistical model of target atoms, see Fano [2.49] and Table 2.3 for current estimates of I.

Table 2.3 : Mean excitation energy I for the main elements representing Titan's atmosphere .

Substance	Z	I(eV)	reference
H (molecular)	1	19 (theory)	[2.50]
		18.3 +2.6	[2.51]
H (in compounds)		15 - 18	[2.52]
C (graphite)	6	81	[2.52]
C (in compounds)		77 - 80	[2.52]
N (molecular)	7	88	[2.52]
N (in compounds)		79 - 102	[2.52]
Ar	18	190	[2.53]

The relativistic correction which enhances the stopping becomes important only at very large velocities since the maximum velocity of the projectile is :

$$v_{in} \approx Z_1^{2/3} v_o \qquad (2.38)$$

with Bohr velocity $v_B = e^2/\hbar = 2.18*10^6$ ms^{-1}. Eqs. 2.34-2.35 have been extended to relativistic velocities ($v_{in} / c = \beta \approx 1$) where c is the light velocity $2.998*10^8$ ms^{-1}. Table 2.4 gives numerical values for some projectiles with different primary energies according to :

$$E = \frac{M_o c^2}{\left[1-\left(v_{in}/c\right)^2\right]} = M_o c^2 + E_{in} \text{ , and} \qquad (2.39)$$

$$\beta = {}^{v_{in}}\!/_{c} = \sqrt{1 - \frac{1}{\left[E_{in}/M_{\circ}c^2\right] + 1}} \quad . \tag{2.40}$$

where :

β is the relativistic velocity of the projectile
E_{in} is the projectile energy, and
$M_{\circ}$ is the rest mass .

Table 2.4 : Relative velocities β using Eq.2.40 for different projectiles.

projectile	1keV	10keV	0.1MeV	1MeV	10MeV	100MeV
H	0.001	0.003	0.010	0.0330	0.103	0.310
He		0.0016	0.005	0.016	0.052	0.163
C		0.001	0.003	0.009	0.030	0.094
Fe			0.0014	0.004	0.014	0.044

Thus, the stopping number becomes :

$$B = Z_2\left[\ln\left(\frac{2M_e V_{in}}{I}\right) - \left\{\ln\left(1-\beta^2\right) - \beta^2\right\}\right] \tag{2.41}$$

The relativistic correction which enhances the stopping becomes important only at very high velocities since it is proportional to β^4 for small β.

MARLOWE program does not include the relativistic corrections for light and high energies projectile, therefore one has to change the parameter FK(I,J) in order that it calculates the stopping cross-section by Bethe Bloch Eq. 2.36:

$$FK(I,J) = \frac{S}{\sqrt{E_{kin}}} \; [eV^{1/2} \cdot Å^2]. \tag{2.42}$$

Table 2.5 reports the calculated data which were applied in *MARLOWE* program, where (I,J) are the type numbers of projectile and target atoms, respectively.

Table 2.5 : FK(I,J) parameters for different target elements .

projectile→target elements	1MeV	10MeV	100MeV
H →N	0.08247	0.00508	0.00026
→Ar	0.14926	0.01111	0.00062
→C	0.07472	0.00415	0.00023
→H	0.01979	0.00099	0.00005
He→N	0.59178	0.05703	0.00309
→Ar	0.45995	0.11484	0.00692
→C	0.57508	0.05087	0.00271
→H	0.21989	0.01220	0.00057
C →N		1.04560	0.06709
→Ar		1.82920	0.14481
→C		0.95120	0.05932
→H		0.25890	0.01311

The electron number of projectile and of target atom Z_1 and Z_2 influences the screening length a_{12} in Eq. 2.15 and consequently the elastic and inelastic energy transfer. The mean equilibrium charge Z* of a projectile with the speed v_1 and atomic number Z_1 can be calculated according to Fleischer [2.54] :

$$Z^* = Z_1\left[1-\exp\left\{-130v_1/\left(cZ_1^{2/3}\right)\right\}\right]. \qquad (2.43)$$

The mean equilibrium charges Z* of some projectiles are shown in Table 2.6.

Table 2.6 : Z^* for the some projectiles according to Eq. 2.43.

projectile	0.1keV	1keV	10keV	0.1MeV	1MeV	10MeV
H	0.00	0.09	0.32	0.72	0.98	1.00
He	0.00	0.00	0.25	0.67	1.50	1.97
C	0.00	0.00	0.23	0.67	1.80	4.20

The values found by Kitagawa semiempirically differ by ± 5-10 % from those of Fleischer. The influence of the energy and with it of the ionization of the projectile on the screening length a_{12} is shown in Table 2.7 for different projectile energies.

Table 2.7 : The screening length a_{12} of some projectiles in target elements .

projectile→target element	0.1MeV	1MeV	10MeV	100MeV
H →N	1.486	0.237	0.245	0.245
→Ar	2.235	2.053	0.179	0.179
→C	1.395	1.213	0.258	0.258
→H	0.505	0.066	0.468	0.468
He→N		0.209	0.235	0.245
→Ar		0.161	0.174	0.179
→C		0.218	0.246	0.258
→H		0.328	0.421	0.468
C →N		0.670	0.186	0.245
→Ar		0.138	0.149	0.179
→C		0.172	0.193	0.258
→H		0.290	0.277	0.468

2.2.4 Stripe calculations

The range of particles with energies up to 10^4 eV as well as the generation of energetic secondary atoms and their energy distribution are calculated in full cascade mode (PRIM = F,F) down to the cut off energy of 0.5 eV averaging over 10^4 individual cascades. For higher primary energies this procedure becomes too

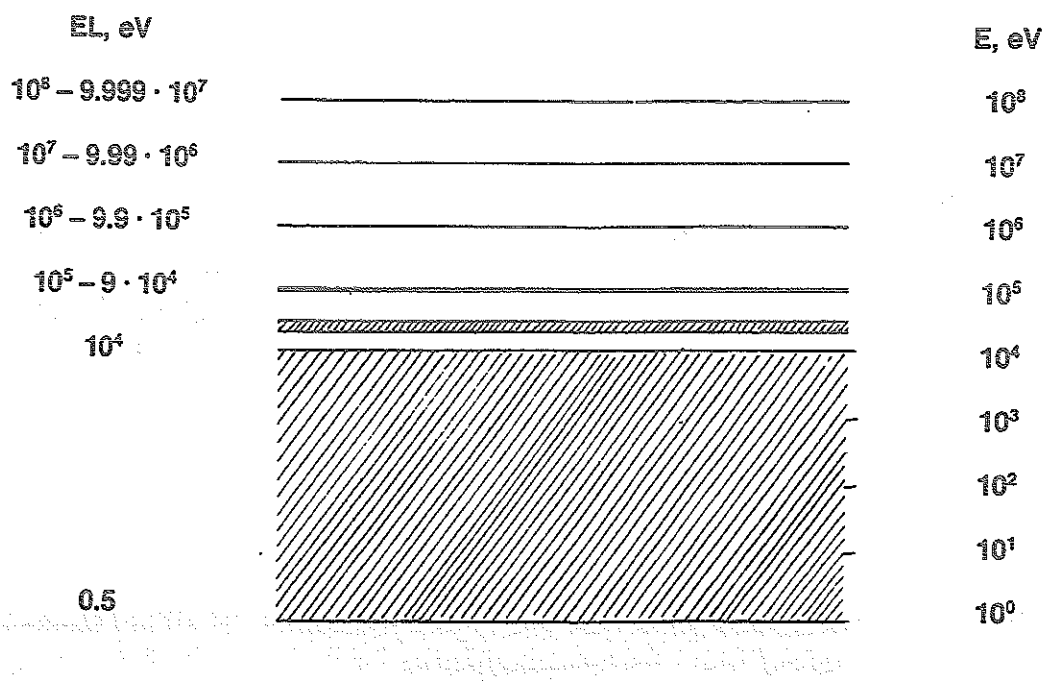

Fig 2.6 : Calculation of 10^4 eV energy stripes for full cascade evaluation

time consuming and expensive in view of computer time allotted to the user, in particular if good statistics ($\geq 10^4$ cascades) are demanded.
For energies beyond 10^4, eV the so called stripe procedure is applied. It consists generally speaking in calculating *MARLOWE* data for stripes of 10 keV for each energy decade (10^4,10^5,10^6,10^7,and 10^8 eV) cf. Fig 2.6 and extrapolating to full collision cascades. For this calculation the parameter PRIM = T,F is used. Output data are the number of secondary particles created by energy transfers exceeding E_d, which in the above mode are stopped immediately after their formation and do not generate tertiaries, etc. Their energy distribution is represented in a grid (0.5-5, 5-10, 10-50, 50-100, 100-500, 500-10^3, 10^3-5·10^3, 5·10^3→ higher). Another output are data on their range (penetration),.The procedure to obtain from the seconderies and their energy distribution the number of all hot atoms generated in a full cascade in this stripe is reported schematically in Fig 2.7.

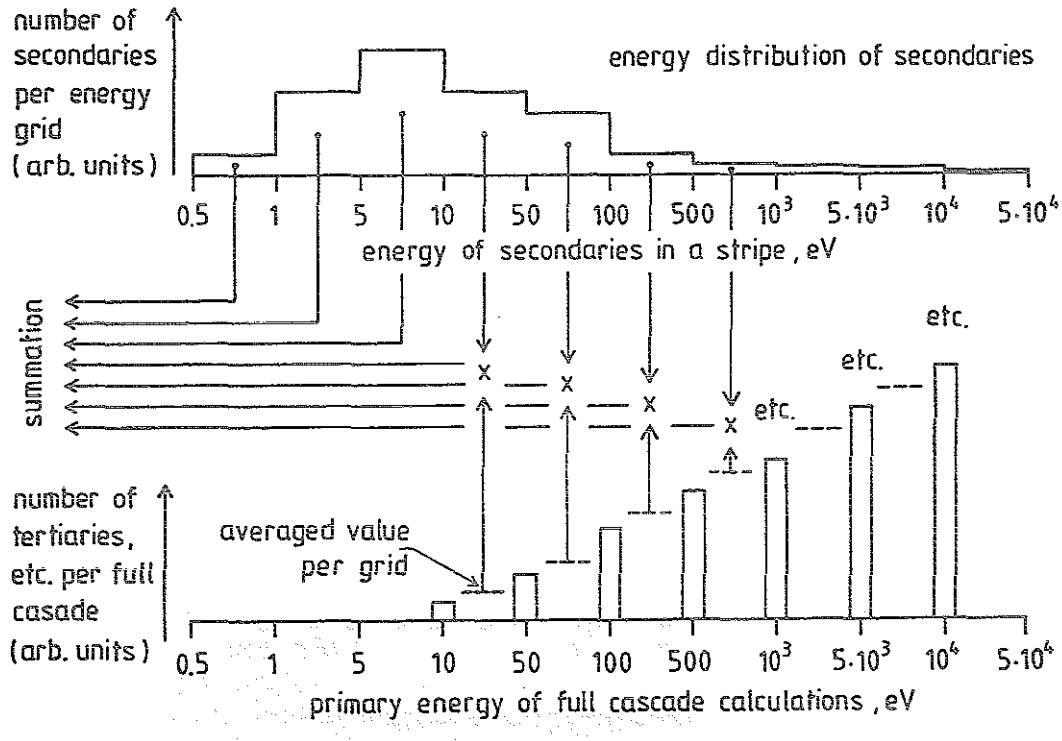

Fig. 2.7 : Schematic procedure to evaluate the number of all hot atoms from secondaries of stripe calculations using the results from full cascades up to 10^4 eV kinetic energy.

The number of all tertiaries, which would be created by these secondaries if the collision cascade would have continued is evaluated from the results of full cascade calculations with 10^4, $5 \cdot 10^3$, 10^3, 500, 100, 50, and 10 eV primary energies. The full number of all displaced atoms is then averaged for the energy intervals , i.e., e.g., 10^4 to $5 \cdot 10^3$, $5 \cdot 10^3$ to 10^3, etc. as a mathematical mean of the extremes. These intervals correspond to those of the grid of the secondaries' energy distribution. By multiplying the number in each energy interval with the corresponding result from the low energy full cascades, the number of all hot atoms under full cascade conditions can be obtained, cf. Fig 2.7. This procedure is followed for all four projectiles and all secondary atoms (N, Ar, C, H) in the three targets.

Finally all hot atoms of one type (N, Ar, C, H) are summed up to give the total number produced in one stripe. To the teritaries, etc. also those secondaries are added with did not induce a further cascade. To obtain the number of hot particles in the full energy decades, the mean value between two neighboring stripes is calculated as a mathematical average and then multiplied with the number of 10 keV stripes between the decades: i.e. 9 from 10^4 to 10^5 eV, 90 from 10^5 to 10^6 eV, 900 from 10^6 to 10^7 eV, and $9 \cdot 10^3$ from 10^7 to 10^8 eV. Total number of hot atoms for a specific energy can be evaluated by adding the results of the corresponding energy decades.

The energy distribution for the secondaries is important for the above mentioned evaluation of all hot atoms, but not for the final chemical reactions. As has been demonstrated in chapter 1.4, hot atom chemistry in the gas phase does proceed only for kinetic energies from some 10 eV down to about 0.5 eV. Thus, it is more important to know the final energy distribution of the hot atoms after the last displacive collision, i.e. when the hot atoms do not any more induce displacements of other atoms. This is in general the case for energies below 50 eV. The energy distribution of all hot atoms in the lower energy full cascades at the moment of their (tertiary) generation shows that only approx., 10 to 15% of the hot atoms obtain energies beyond 50 eV, cf. chapter 3.5. That the energies are greater than the cutoff energy at all is due to the fact that the search for "new cascade atoms" (cf. chapter 2.1.6) includes the high energetic tertiaries and the quaternaries, etc. formed over the whole duration of the cascade, i.e. it lists also all those particles which will give away these energies by collision soon. For hot atom chemistry the individual energy distribution at one moment is also not too important, since the hot species will reach a lower energy just some time thereafter, finally ending up at the cutoff energy. Thus, a treatment of energy distribution of all hot atoms depends very much on the time of cascade development and is of limited value only.

The range estimations are of highest importance for this work.. Ranges calculated for neighboring stripes were averaged and multiplied in the same procedure as done for the total number of hot atoms.

2.3 Input data to *MARLOWE*

This section is concerned with the input parameters. Table 2.8 shows only those which were chosen other than the default option, given by the program. The choice of energy parameters E_d, E_b, and E_c has already been discussed in chapter 2.2.2 (Table 2.2).

Some important input parameters were varied in order to check their influence on the results. First, the variation of TIM (7) between false and true, i.e. whether cascade atoms may be taken as targets for collisions or not, resp., did not yield big differences, cf. Fig. 2.8.

Table 2.8 : Input for *MARLOWE* other than default values.

MARLOWE expression	signification	target I	target II and III
NTYPE	number of typical atoms (target and projectile)	4	5
TYPE	array of alphanumeric atom type labels	N, C, H	N,Ar,C,H (projectile: H, He, C, Fe)
NEIGH	number of neighbors of each type of lattice site.	all target atoms: 26 all projectiles: 0	
Z	the atomic number of each type of atom	N(7), C(6) H(1)	N(7), Ar(18) C(6), H(1) projectile: H(1), He(2), C(6) Fe(26)
ALAT	lattice constant a_o	2.5 Å	
RB	search radius for interaction in units of a_o	0.7; 0.7	
POLY	amorphous crystal	POLY (T,T)	
MIXT	chemical disordering of lattice	MIXT=T	
LAIP	the type number of the primary recoil	4	5
LRIP	the type number of a lattice site at (or near) which the primary recoil starts	1	1
ICHAN	number of successive non-displacive collisions before a stenon trajectory is truncated	5000	

TIM	model parameters search ahead by atom position, radial search by atom position, cascade atom may be targets, lost projectiles allowed, collision ordered by speed, close or near pairs not sought, and distant pairs not identified.	 TIM(3) =T TIM(4) =T TIM(7) =F TIM(8) =F TIM(10) TIM(11) =T TIM(12) =T
MAXRUN	number of cascades calculated for average	10^4 (in general)

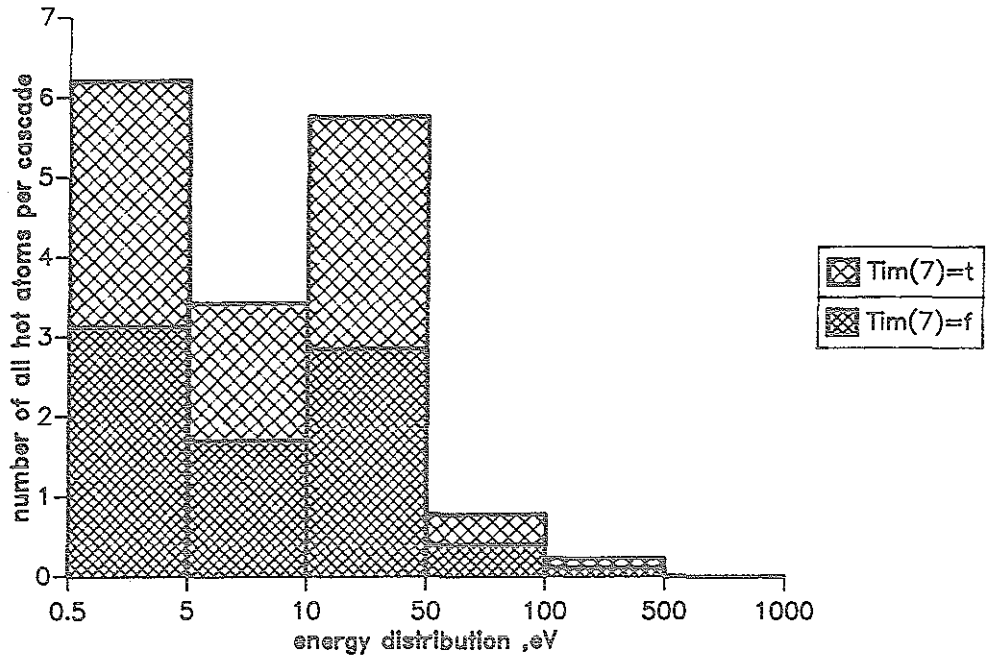

Fig 2.8 : Effect of variation of parameter TIM (7) in the calculation of energy distribution of secondary projectiles in cascades by 10^3 eV H primary in target II.

The variation of the binding loss energy E_b by a factor 0.5 of the value in Table 2.2 induced only a shift of energy distribution of the hot atoms formed from the first bin (0.5 to 5 eV) into the second one (5 to 10 eV) which is without importance for the problems of this work, as is discussed in chapter 3.5 .

2.4 Controls with TRIM

TRIM [2.33-35] is a very wide spread program which allows fast calculation of collision cascades in the Monte Carlo mode. TRIM is a more

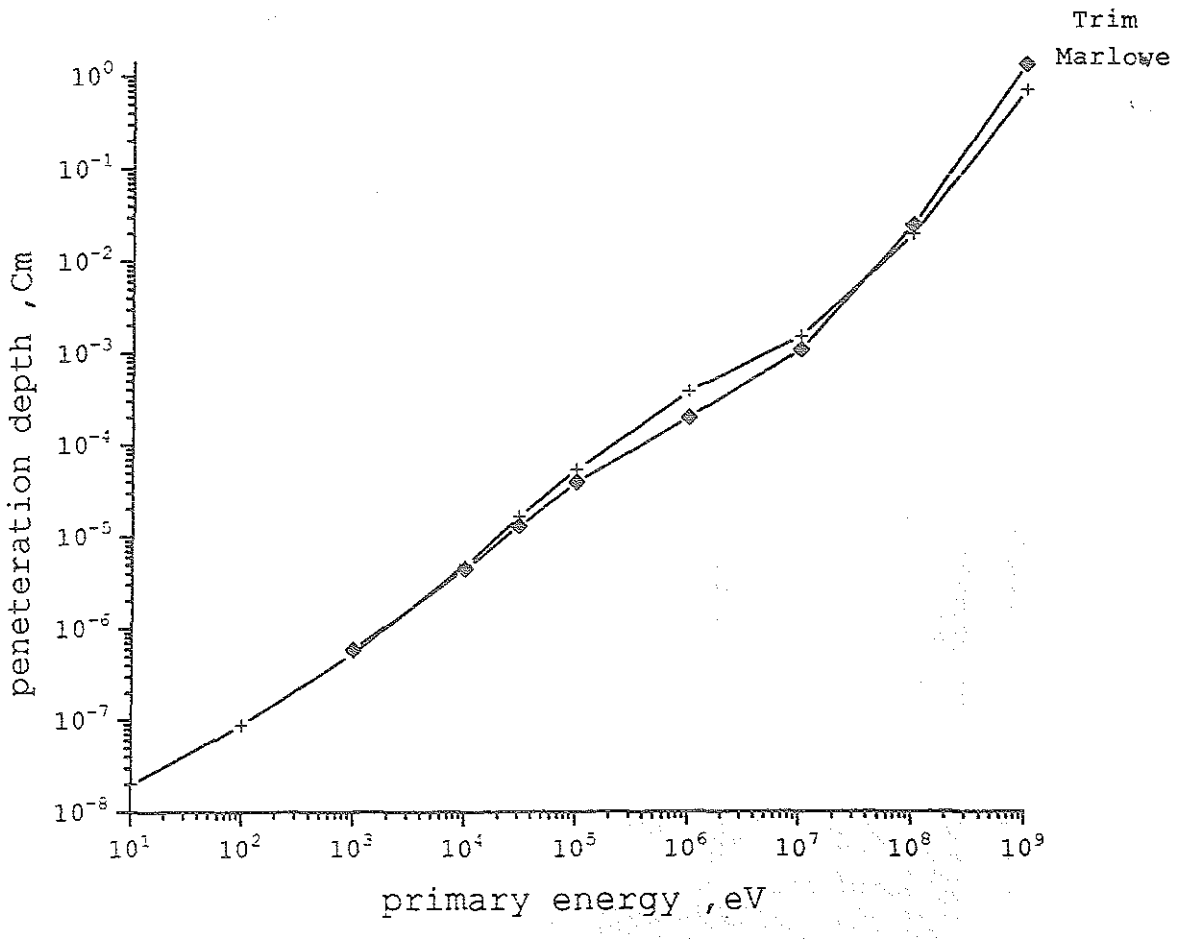

Fig 2.9 : Penetration depths of carbon projectiles in target I as calculated by TRIM and *MARLOWE*.

analytical program than *MARLOWE* which concentrates on the single binary collision. Even if some issues of TRIM have limitations, especially in the calculation of number and energy distribution of different types of atoms, it was helpful to make some comparison of data calculated by both programs. In TRIM, collision partners are determined by a stochastic choice of an impact parameter p defined, as : $0 < p < p_{max}$ and an azimuthal angle ϕ defined as : $0 < \phi < 2\pi$. From the scattering angle in center of mass system and the recoil angle in the laboratory system, the directions of scattered projectile and newly created primary knock on atom (PKA) are thus fixed. The energies of projectiles are reduced by the energy transferred to the PKA. The PKA is followed only if its energy is larger than the surface binding energy and if its distance from the surface is smaller than its determined range. The PKA can set other target atoms in motion, which will be called secondary knock on atoms (SKAs). This

subcascade is treated by the following storage logic. The PKA is given the label i, in the next collision the PKA is given the label i+1, while information on the newly created SKA is stored under label i,. If after several collisions, the PKA is sputtered, transmitted or stopped, the program returns to the last SKA with label i. After following this SKA in the same way as the PKA, the program finally comes back after treating all SKAs created by the PKA to the projectile (i = 0). Then the projectile proceeds to the next collision and so forth. The projectile and the recoils also loose energy inelastically between subsequent collisions by a continuous loss, taking the time integral into account, or by a local loss. If the projectile has reached an energy below the cutoff energy E_c or if the projectile is backscattered or transmitted, then the next projectile is started and the whole procedure begins again. It can be seen e.g. that the way to follow the development of a cascade in time is less sophisticated as in *MARLOWE*.
By TRIM program the penetration depth data from *MARLOWE* have been checked. Fig 2.9 shows that there is no big difference between the results of both programs for e.g. carbon projectiles in target I.

CHAPTER 3

NUMERICAL RESULTS OF THE CALCULATION IN MODEL LATTICE

3.1 Full cascade calculations with primary energies ≤ 10^4 eV

The impact of energetic primary species does not only induce excitation, ionization and displacements, but also leads to some specific interactions of the target atoms with each other. Many of the first knock-on atoms in the collision cascade, the so called secondaries, may obtain energies which enable them to create tertiary projectiles or displacements and/or to undergo hot chemical reactions. The problem of number and energy distributions of secondaries is very difficult to tackle experimentally. The total number of hot atoms has been calculated for the three targets (I, II, and III) and four projectiles (H, He, C, and Fe) at energies up to 10^4 eV where the cascades could be followed to the full length with all side branches down to the cutoff energy. A typical result of this calculation is shown in Fig. 3.1 for target II.

Fig 3.2 reports a comparison of the energy distribution of secondary projectiles in target I by 10 to 10^4 H and Fe primaries as examples for light and heavy particles. It can be seen that the distribution is in principle similar, only the absolute number is much greater for the Fe projectiles. Interesting to note that few, but very high energy transfers between 50 to almost 100% of the primary energy may happen in the latter case. The energies of secondaries are sufficient to create many new branches of the cascade. The already high number of secondaries is increased by a factor 2 to 3 for the full cascades, if all tertiaries, etc. are considered. Fig. 3.3 reports a comparison of energy distribution of secondary (PRIM = T,F) and all hot atoms (PRIM = F,F) formed by 10 keV H, He and C primaries in target II. It can be seen here too, that the cascades of light primaries produce a factor of approx. 2 more hot atoms from the secondaries, whereas the secondaries formed by primary carbons lead to formation of 8 to 9 times more hot atoms in the full cascade.

Besides the preferential formation of secondaries by S_n (nuclear stopping), there is one operating in solids via S_e (electronic stopping): the Coulomb repulsion in tracks of very high energetic heavy ions. Electrons are liberated and emitted into remote parts of the target, the positively charged ions repell each other and obtain kinetic energy. This applies only for the solid and is not considered in this case for calculations which finally are applied to the gaseous state.
This calculation of the number of all displaced hot atoms for all targets (I, II, III) is the base of extrapolation for the high energy calculations (10^5 - 10^8 eV) in the stripe mode. Primary energies are considered in half decades: 10, 50, 10^2, 500, 10^3, $5 \cdot 10^3$, and 10^4 eV.

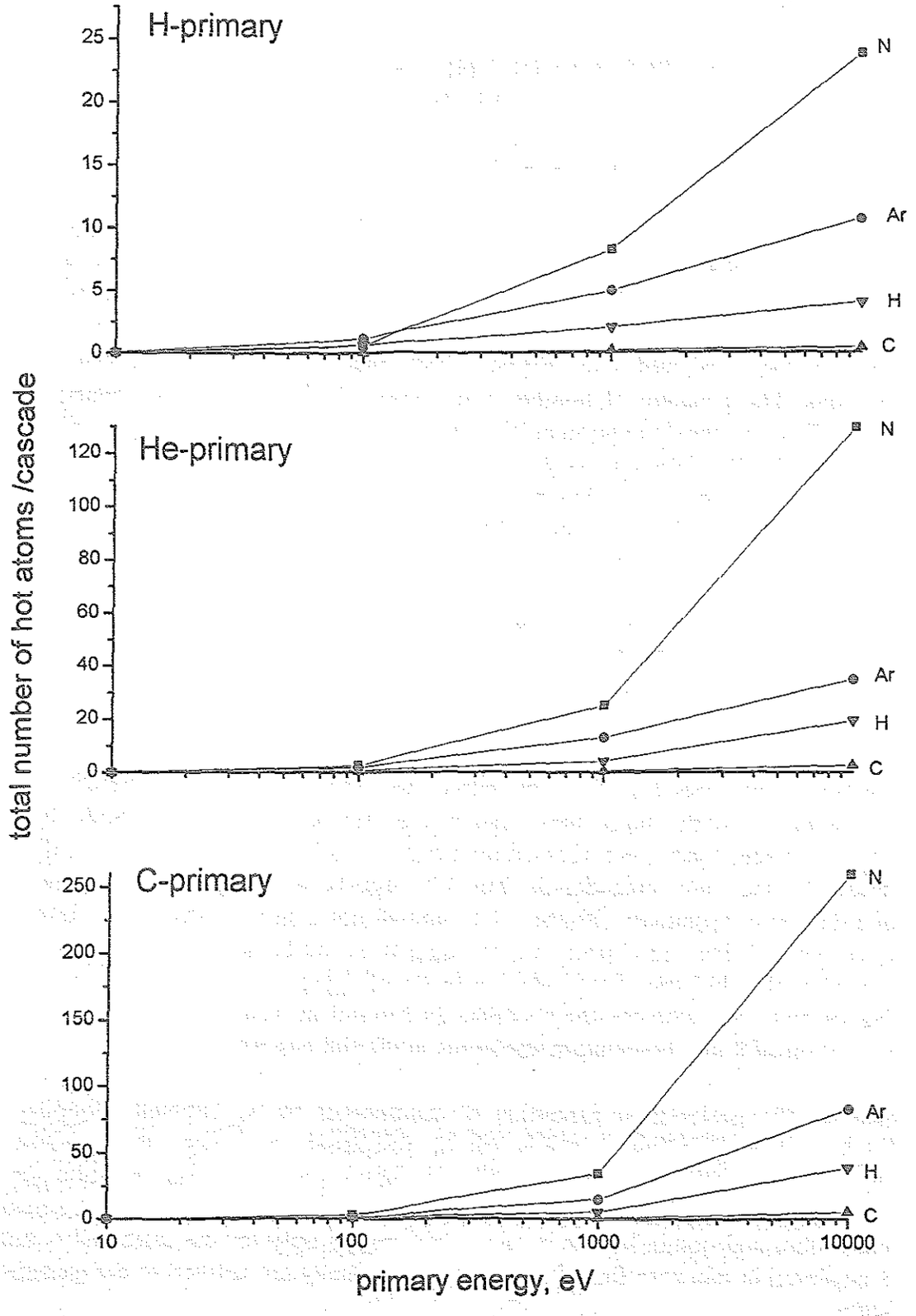

Fig. 3.1: Number of all hot N, Ar, C, and H atoms generated by H, He, and primaries in target II

The values in Table 3.1 are averages of 10^4 cascades each. Fe projectiles have only been followed in target I, which in the present discussion of Titan's atmospheric composition represents a N_2 atmosphere with a relatively low amount of other components, a very probable case. The energies of the hot atoms after their last displacive collision are listed in half decade bins in eV, such as in Fig. 3.2. The results are given for each of the target components. Table 8.1 in the Appendix shows the average number of hot atoms formed in the intervals between the primary energies, i.e. the half decade energy bins in eV.

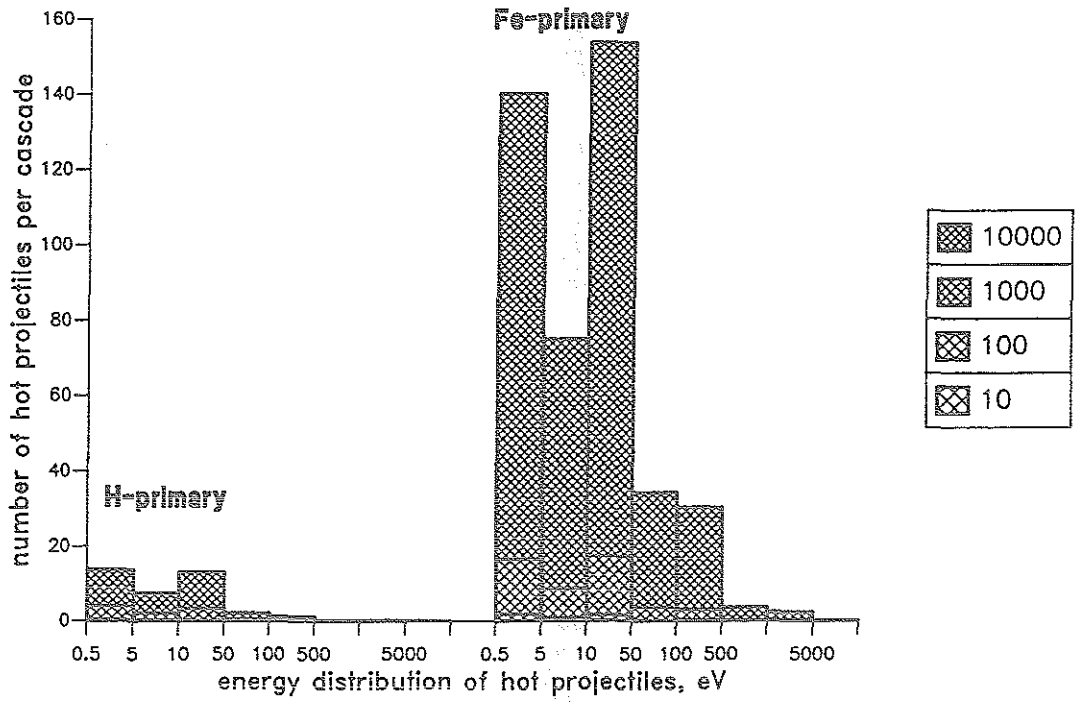

Fig. 3.2: Comparison of hot secondary atoms formed in full cascades by 10 to 10^4 eV H and Fe primaries in target I.

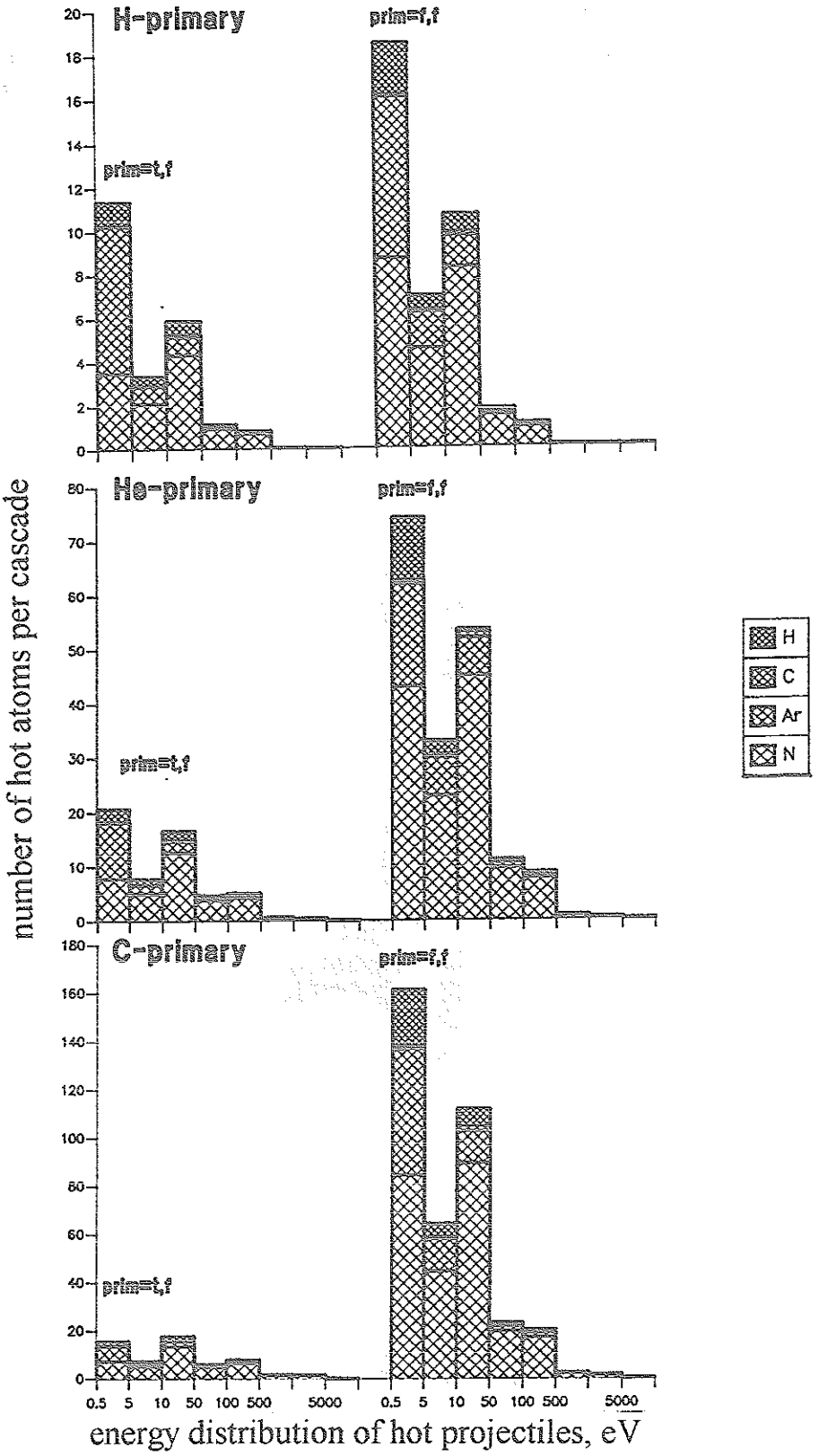

Fig. 3.3: Energy distributions of hot atoms in calculations of complete (PRIM = T, F) and primary only cascades (PRIM = T, F) for 10 keV primaries in target II

Table 3.1 : Energy distribution of all hot atoms generated in full cascades by H, He,C,and Fe primaries in the three targets (*MARLOWE* in LSS mode).

1E+01 eV

target number		I			II				III			
projectiles	energy bins	N	C	H	N	Ar	C	H	N	Ar	C	H
H	0.5-5	0.000	0.000	0.020	0.000	0.060	0.000	0.050	0.000	0.100	0.000	0.090
He	0.5-5	0.000	0.000	0.010	0.000	0.210	0.000	0.003	0.000	0.460	0.000	0.060
C	0.5-5	0.020	0.000	0.000	0.020	0.210	0.000	0.000	0.010	0.510	0.000	0.000
	5-10	0.000	0.000	0.000	0.000	0.010	0.000	0.000	0.000	0.020	0.000	0.000
Fe	0.5-5	0.000	0.000	0.000								

5E+01 eV

H	0.5-5	0.075	0.000	0.070	0.064	0.640	0.000	0.220	0.040	1.500	0.000	0.000
	5-10	0.000	0.000	0.030	0.000	0.000	0.000	0.080	0.000	0.000	0.000	0.150
	10-50	0.000	0.000	0.020	0.000	0.000	0.000	0.070	0.000	0.000	0.000	0.100
He	0.5-5	0.500	0.000	0.070	0.450	0.840	0.006	0.210	0.370	1.900	0.010	0.370
	5-10	0.310	0.000	0.014	0.220	0.068	0.001	0.067	0.170	0.150	0.006	0.100
	10-50	0.230	0.000	0.014	0.200	0.020	0.001	0.050	0.180	0.040	0.006	0.070
C	0.5-5	0.750	0.001	0.070	0.700	0.700	0.006	0.200	0.570	2.500	0.015	0.360
	5-10	0.390	0.001	0.009	0.300	0.100	0.006	0.030	0.270	0.250	0.008	0.060
	10-50	0.600	0.003	0.000	0.540	0.080	0.010	0.000	0.450	0.160	0.019	0.000
Fe	0.5-5	0.960	0.003	0.003								
	5-10	0.450	0.001	0.000								
	10-50	0.440	0.000	0.000								

1E+02 eV

H	0.5-5	0.440	0.000	0.110	0.380	0.100	0.000	0.340	0.320	2.800	0.010	0.620
	5-10	0.170	0.000	0.040	0.140	0.040	0.000	0.130	0.120	0.100	0.000	0.210
	10-50	0.050	0.000	0.050	0.040	0.000	0.000	0.150	0.040	0.000	0.000	0.210
	50-100	0.000	0.000	0.000	0.000	0.000	0.000	0.010	0.000	0.000	0.000	0.020
He	0.5- 5	1.160	0.000	0.110	0.990	1.440	0.010	0.320	0.780	3.480	0.010	0.630
	5-10	0.610	0.000	0.030	0.540	0.140	0.000	0.100	0.400	0.350	0.020	0.200
	10-50	0.930	0.000	0.050	0.790	0.080	0.020	0.130	0.700	0.200	0.030	0.210
	50-100	0.020	0.000	0.000	0.020	0.000	0.000	0.000	0.020	0.000	0.000	0.000
C	0.5-5	1.460	0.000	0.100	0.680	0.460	0.010	0.190	1.060	3.070	0.040	0.710
	5-10	0.750	0.000	0.030	0.460	0.090	0.010	0.070	0.610	0.430	0.020	0.140
	10-50	1.500	0.010	0.020	1.060	0.140	0.020	0.070	1.130	0.420	0.050	0.110
	50-100	0.200	0.000	0.000	0.170	0.010	0.000	0.000	0.140	0.020	0.000	0.000
Fe	0.5-5	1.830	0.007	0.060								
	5-10	0.930	0.003	0.001								
	10-50	1.600	0.008	0.000								
	50-100	0.030	0.000	0.000								

5E+02 eV

H	0.5-5	2.300	0.009	0.250	1.950	4.000	0.020	0.750	1.540	9.000	0.051	1.320
	5-10	1.190	0.003	0.840	1.022	0.362	0.019	0.260	0.800	0.710	0.020	0.450
	10-50	1.870	0.009	0.090	1.577	0.200	0.027	0.350	1.300	0.420	0.056	0.580
	50-100	0.190	0.001	0.015	0.150	0.001	0.002	0.050	0.130	0.000	0.007	0.084
	100-500	0.006	0.000	0.009	0.003	0.000	0.000	0.040	0.005	0.000	0.000	0.039

e	0.5-5	5.500	0.009	0.360	4.600	5.680	0.060	1.390	3.960	14.01	0.121	2.400
	5-10	2.900	0.010	0.120	2.500	0.790	0.047	0.370	2.000	1.700	0.064	.6800
	10-50	5.700	0.040	0.170	4.800	0.670	0.110	0.460	3.900	1.490	0.194	0.890
	50-100	1.060	0.009	0.023	0.897	0.070	0.020	0.079	0.750	0.150	0.035	0.060
	100-500	0.570	0.003	0.017	0.490	0.013	0.016	0.041	0.390	0.032	0.030	0.059
C	0.5-5	6.500	0.020	0.410	6.100	5.610	0.100	1.540	5.050	28.00	0.160	3.400
	5-10	3.600	0.012	0.140	3.130	0.910	0.038	0.410	2.630	2.050	0.930	0.760
	10-50	7.400	0.050	0.160	6.400	0.899	0.136	0.530	5.200	1.200	0.250	0.850
	50-100	1.700	0.020	0.020	1.310	0.112	0.041	0.049	1.030	0.310	0.067	0.100
	100-500	1.100	0.008	0.004	0.990	0.065	0.045	0.008	0.830	0.160	0.050	0.014
Fe	0.5-5	7.800	0.032	0.520								
	5-10	4.035	0.019	0.110								
	10-50	8.260	0.054	0.100								
	50-100	1.830	0.014	0.002								
	100-500	1.120	0.009	0.000								

1E+03 eV

H	0.5-5	3.720	0.010	0.310	3.210	3.830	0.040	1.060	2.600	8.330	0.010	1.890
	5-10	2.020	0.010	0.100	1.690	0.600	0.030	0.350	1.360	1.270	0.050	0.610
	10-50	3.380	0.020	0.140	2.820	0.440	0.060	0.440	2.290	0.910	0.100	0.770
	50-100	0.460	0.000	0.020	0.390	0.020	0.010	0.070	0.330	0.040	0.020	0.110
	100-500	0.140	0.000	0.010	0.110	0.000	0.000	0.040	0.090	0.000	0.010	0.070
	500-1000	0.000	0.000	0.000	0.000	0.000	0.000	0.000	0.000	0.000	0.000	0.000
He	0.5-5	9.940	0.040	0.690	8.710	10.08	0.110	2.420	7.230	17.66	0.210	4.540
	5-10	5.420	0.030	0.220	4.530	1.400	0.080	0.610	3.740	3.240	0.130	1.170
	10-50	10.62	0.070	0.270	8.880	1.310	0.190	0.830	7.160	2.890	0.330	1.480
	50-100	2.140	0.020	0.040	1.770	0.170	0.100	0.750	1.440	0.340	0.090	0.240
	100-500	1.480	0.010	0.030	1.270	0.070	0.045	0.090	1.010	0.160	0.070	0.160
	500-1000	0.030	0.000	0.000	0.010	0.000	0.000	0.000	0.020	0.160	0.000	0.000
C	0.5-5	12.72	0.050	0.870	11.27	10.67	0.150	3.010	9.720	37.61	0.290	6.260
	5-10	6.900	0.040	0.250	6.050	1.700	0.100	0.750	4.970	3.980	0.180	1.340
	10-50	14.06	0.090	0.310	12.06	1.800	0.270	0.960	9.910	3.830	0.480	1.690
	50-100	3.060	0.030	0.040	2.650	0.260	0.050	0.140	2.130	0.540	0.140	0.240
	100-500	2.490	0.020	0.020	2.190	0.180	0.070	0.060	1.770	0.380	0.120	0.110
	500-1000	0.170	0.000	0.000	0.140	0.010	0.01	0.000	0.120	0.010	0.010	0.000
Fe	0.5-5	14.80	0.060	1.040								
	5-10	7.700	0.030	0.260								
	10-50	15.88	0.110	0.280								
	50-100	3.600	0.030	0.100								
	100-500	3.000	0.029	0.000								
	500-1000	0.070	0.000	0.000								

1E+04 eV

H	0.5-5	9.87	0.04	0.68	8.71	7.93	0.11	2.34	7.27	15.58	0.020	4.21
	5-10	5.33	0.03	0.22	4.55	1.65	0.07	0.68	3.72	3.62	0.11	1.17
	10-50	9.76	0.06	0.26	8.28	1.45	0.18	0.83	6.70	3.04	0.29	1.40
	50-100	1.71	0.01	0.14	1.46	0.15	0.04	0.11	1.21	0.39	0.66	0.19
	100-500	1.06	0.01	0.04	0.90	0.08	0.03	0.07	0.71	0.16	0.05	0.13
	500-1000	0.06	0.00	0.00	0.05	0.00	0.00	0.01	0.04	0.00	0.00	0.01
	1000-5000	0.01	0.00	0.00	0.01	0.00	0.00	0.00	0.01	0.00	0.00	0.01
	5000-10000	0.00	0.00	0.00	0.00	0.00	0.00	0.00	0.00	0.00	0.00	0.00

□	0.5-5	48.91	0.20	3 23	43.14	18.99	0.61	11.60	37.20	45.29	1.06	22.22
He	5-10	26.64	0.130	0.790	22.89	7.070	0.380	2.99	19.03	16.23	0.660	5.240
	10-50	53.25	0.340	1.180	45.07	7.060	1.040	3.690	36.99	15.24	1.780	6.290
	50-100	11.33	0.090	0.170	9.500	0.940	0.270	0.510	7.680	2.020	0.480	0.930
	100-500	9.050	0.080	0.120	7.670	0.690	0.260	0.360	6.320	1.530	0.420	0.670
	500-1000	0.870	0.010	0.010	0.760	0.070	0.020	0.040	0.570	0.130	0.030	0.060
	1000-5000	0.430	0.000	0.000	0.360	0.020	0.010	0.020	0.320	0.050	0.030	0.030
	5000-10000	0.000	0.000	0.000	0.000	0.000	0.000	0.000	0.000	0.000	0.000	0.000
C	0.5-5	95.63	0.400	6.500	84.65	52.24	1.270	23.56	72.94	84.28	2.190	45.83
	5-10	51.94	0.250	1.880	44.48	13.37	0.780	5.810	36.73	30.04	1.300	10.01
	10-50	105.79	0.680	2.330	89.64	13.29	2.070	7.250	73.03	28.89	3.470	12.30
	50-100	23.16	0.190	0.340	19.58	1.910	0.570	1.060	15.85	4.050	0.970	1.800
	100-500	20.15	0.190	0.270	17.00	1.520	0.560	0.810	13.90	3.290	0.980	1.400
	500-1000	2.410	0.030	0.270	2.070	0.190	0.070	0.090	1.660	0.340	0.120	0.140
	1000-5000	1.640	0.010	0.010	1.380	0.120	0.050	0.030	1.140	0.260	0.090	0.450
	5000-10000	0.080	0.000	0.000	0.070	0.000	0.000	0.000	0.050	0.010	0.000	0.000
Fe	0.5-5	123.0	0.500	8.600								
	5-10	66.00	0.300	2.40								
	10-50	136.0	0.980	3.000								
	50-100	30.00	0.260	0.400								
	100-500	27.00	0.240	0.300								
	500-1000	3.500	0.040	0.008								
	1000-5000	2.400	0.020	0.000								
	5000-10000	0.042	0.000	0.000								

3.2 Stripe calculations with primary energies > 10^4 eV

The aim of the 10 keV stripe calculations of high energetic projectiles is to obtain information on the generation of secondaries (by the primary species) from which the number of hot atoms formed in the complete (full) cascade can be extrapolated using the values in Table 3.1 and Tables 8.1 - 8.3 in Appendix. Table 3.2 shows all the stripe results for 10^5 to 10^8 primaries: H, He, C, and Fe in the LSS mode. The values are averages from 10^4 cascades. Taking into account, that the classical Lindhard-Scharff-Schiott equation for inelastic energy transfer is not longer valuable for light ions and energies exceeding 10^5 or 10^6 eV, the LSS approach had to be replaced by the Bethe Bloch (BB) treatment which for higher energies yields more reliable values. Table 3.3 lists the results of the BB calculation for stripe cases.

It can be seen that the high energetic projectiles do not produce too many secondaries at the beginning. It is however important to note that there are displacements, i.e. elastic energy transfers even at relatively high energies, for heavier much more than for light projectiles and that their number is somewhat higher in the BB mode. This is due to the fact, that the inelastic transfer decreases with increasing energy. The resulting higher number of collisions for inelastic transfer enables here and there an elastic transfer sufficient to displace an atom. This will be treated in somewhat more detail in chapter 3.6.

Fe with up to 10^8 eV energy yields same results in LSS and BB modes. This is due to the fact that the BB criteria do not apply to relatively heavy projectiles of this energy.

Table 3.2 : Energy distribution of secondaries in 10 keV stripe cascades by H, He, C, and Fe primaries in three targets *(MARLOWE* in LSS mode)

1E+05 eV

target number		I			II				III			
projectiles	energy bins	N	C	H	N	Ar	C	H	N	Ar	C	H
H	0.5-5	0.040	0.000	0.000	0.029	0.140	0.000	0.005	0.025	0.273	0.000	0.006
	5-10	0.016	0.000	0.000	0.014	0.016	0.000	0.003	0.015	0.025	0.001	0.003
	10-50	0.033	0.000	0.001	0.037	0.012	0.000	0.001	0.036	0.017	0.000	0.003
	50-100	0.014	0.000	0.000	0.011	0.002	0.002	0.000	0.007	0.002	0.002	0.000
	100-500	0.007	0.000	0.001	0.010	0.002	0.000	0.000	0.009	0.002	0.000	0.000
	500-1000	0.002	0.000	0.000	0.000	0.000	0.000	0.001	0.001	0.000	0.000	0.000
	1000-5000	0.001	0.000	0.000	0.000	0.001	0.000	0.000	0.001	0.000	0.000	0.000
He	0.5 5	0.350	0.003	0.023	0.307	0.635	0.006	0.054	0.248	1.402	0.010	0.100
	5-10	0.203	0.000	0.007	0.184	0.085	0.001	0.015	0.160	0.180	0.007	0.039
	10-50	0.455	0.003	0.023	0.338	0.082	0.014	0.034	0.303	0.197	0.018	0.055
	50-100	0.098	0.000	0.007	0.105	0.013	0.002	0.004	0.075	0.034	0.004	0.016
	100-500	0.118	0.003	0.008	0.101	0.022	0.003	0.008	0.092	0.027	0.008	0.007
	500-1000	0.012	0.000	0.000	0.014	0.000	0.000	0.000	0.011	0.004	0.001	0.001
	1000-5000	0.018	0.000	0.001	0.008	0.004	0.000	0.001	0.008	0.004	0.000	0.000
	5000-10000	0.001	0.000	0.000	0.000	0.000	0.000	0.000	0.001	0.003	0.001	0.000
	1E+4-5E+4	0.000	0.000	0.000	0.001	0.000	0.000	0.000	0.001	0.000	0.000	0.000
C	0.5-5	1.358	0.009	0.094	1.106	1.709	0.021	0.284	0.922	3.576	0.028	0.511
	5-10	0.908	0.004	0.043	0.816	0.249	0.018	0.120	0.582	0.525	0.030	0.220
	10-50	2.237	0.017	0.093	1.935	0.349	0.051	0.268	1.568	0.699	0.088	0.400
	50-100	0.793	0.008	0.021	0.629	0.078	0.022	0.029	0.532	0.147	0.038	0.089
	100-500	0.943	0.007	0.013	0.830	0.099	0.024	0.061	0.586	0.198	0.042	0.083
	500-1000	0.196	0.001	0.001	0.143	0.014	0.004	0.012	0.125	0.040	0.009	0.024
	1000-5000	0.171	0.003	0.000	0.147	0.025	0.002	0.013	0.115	0.038	0.005	0.015
	5000-10000	0.023	0.000	0.001	0.016	0.002	0.002	0.000	0.018	0.015	0.000	0.001
	1E+4-5E+4	0.027	0.000	0.000	0.015	0.002	0.001	0.001	0.016	0.008	0.003	0.002
	5E+4-1E+5	0.003	0.000	0.000	0.000	0.001	0.000	0.000	0.001	0.000	0.000	0.000
	1E+5-5E+5	0.000	0.000	0.000	0.000	0.000	0.000	0.000	0.000	0.000	0.000	0.000
Fe	0.5-5	2.470	0.012	0.180								
	5-10	1.760	0.009	0.096								
	10-50	5.010	0.040	0.210								
	50-100	1.900	0.017	0.057								
	100-500	2.290	0.028	0.080								
	500-1000	0.760	0.007	0.019								
	1000-5000	1.000	0.009	0.022								
	5000-10000	0.230	0.001	0.001								
	1E+4-5E+4	0.240	0.002	0.000								
	5E+4-1E+5	0.013	0.000	0.000								
	1E+5-5E+5	0.000	0.000	0.000								

1E+06 eV

H	0.5-5	0.002	0.000	0.000	0.001	0.005	0.000	0.000	0.002	0.014	0.000	0.001
	5-10	0.003	0.000	0.000	0.001	0.000	0.000	0.000	0.000	0.000	0.000	0.000
	10-50	0.000	0.000	0.000	0.002	0.000	0.000	0.000	0.000	0.001	0.000	0.000
	50-100	0.000	0.000	0.000	0.000	0.000	0.000	0.000	0.000	0.000	0.000	0.000
	100-500	0.001	0.000	0.000	0.001	0.000	0.000	0.000	0.001	0.000	0.000	0.000

□ He	0.5-5	0.018	0.001	0.000	0.014	0.048	0.002	0.014	0.013	0.129	0.001	0.002
	5-10	0.005	0.000	0.000	0.005	0.002	0.001	0.005	0.010	0.009	0.000	0.002
	10-50	0.017	0.000	0.001	0.016	0.005	0.002	0.016	0.012	0.008	0.000	0.000
	50-100	0.006	0.000	0.000	0.004	0.000	0.000	0.004	0.003	0.000	0.000	0.000
	100-500	0.004	0.000	0.000	0.001	0.000	0.000	0.001	0.001	0.000	0.000	0.000
	500-1000	0.001	0.000	0.000	0.000	0.000	0.000	0.000	0.000	0.001	0.000	0.000
	1000-5000	0.000	0.000	0.000	0.001	0.000	0.000	0.001	0.000	0.000	0.000	0.000
	5000-10000	0.000	0.000	0.000	0.000	0.000	0.000	0.000	0.000	0.000	0.000	0.000
	1E+4-5E+5	0.000	0.000	0.000	0.000	0.000	0.000	0.001	0.000	0.000	0.000	0.000
C	0.5-5	0.119	0.000	0.008	0.108	0.185	0.003	0.019	0.090	0.446	0.002	0.036
	5-10	0.088	0.001	0.003	0.077	0.032	0.002	0.014	0.066	0.060	0.001	0.018
	10-50	0.179	0.000	0.004	0.155	0.041	0.003	0.019	0.120	0.065	0.005	0.023
	50-100	0.054	0.001	0.000	0.044	0.006	0.002	0.002	0.032	0.013	0.001	0.003
	100-500	0.049	0.001	0.003	0.040	0.012	0.001	0.005	0.043	0.010	0.004	0.007
	500-1000	0.009	0.000	0.000	0.003	0.000	0.000	0.000	0.007	0.001	0.000	0.000
	1000-5000	0.007	0.000	0.000	0.010	0.001	0.000	0.000	0.007	0.004	0.000	0.001
	5000-10000	0.001	0.000	0.000	0.004	0.000	0.000	0.000	0.001	0.000	0.000	0.000
	1E+4-5E+4	0.000	0.000	0.000	0.001	0.001	0.000	0.000	0.001	0.000	0.000	0.000
	5E+4-1E+5	0.000	0.000	0.000	0.000	0.000	0.000	0.000	0.000	0.000	0.000	0.000
	1E+5-5E+5	0.000	0.000	0.000	0.001	0.000	0.000	0.000	0.000	0.000	0.000	0.000
Fe	0.5-5	0.740	0.002	0.050								
	5-10	0.500	0.003	0.021								
	10-50	1.350	0.009	0.050								
	50-100	0.460	0.003	0.015								
	100-500	0.690	0.006	0.017								
	500-1000	0.169	0.001	0.003								
	1000-5000	0.190	0.001	0.004								
	5000-10000	0.040	0.000	0.000								
	1E+4-5E+4	0.030	0.000	0.000								
	5E+4-1E+5	0.004	0.000	0.000								
	1E+5 5E+5	0.000	0.000	0.000								

1E+07 eV

H	0.5-5	0.000	0.000	0.000	0.000	0.000	0.000	0.000	0.001	0.001	0.000	0.000
He	0.5-5	0.000	0.000	0.000	0.001	0.003	0.000	0.000	0.004	0.000	0.000	0.001
	5-10	0.001	0.000	0.000	0.000	0.001	0.000	0.000	0.000	0.000	0.000	0.000
	10-50	0.001	0.000	0.000	0.000	0.002	0.000	0.000	0.001	0.000	0.000	0.000
	50-100	0.000	0.000	0.000	0.000	0.000	0.000	0.000	0.000	0.000	0.000	0.000
	100-500	0.000	0.000	0.000	0.000	0.000	0.000	0.000	0.000	0.000	0.000	0.000
C	0.5-5	0.008	0.000	0.000	0.010	0.015	0.000	0.002	0.005	0.043	0.000	0.002
	5-10	0.003	0.000	0.000	0.007	0.005	0.000	0.000	0.002	0.007	0.000	0.001
	10-50	0.005	0.000	0.000	0.004	0.001	0.001	0.000	0.005	0.001	0.001	0.002
	50-100	0.002	0.000	0.000	0.001	0.000	0.000	0.000	0.000	0.000	0.000	0.000
	100-500	0.004	0.000	0.000	0.002	0.001	0.000	0.000	0.001	0.001	0.000	0.000
	500-1000	0.001	0.000	0.000	0.000	0.000	0.000	0.000	0.000	0.000	0.000	0.000
	1000-5000	0.000	0.000	0.000	0.000	0.000	0.000	0.000	0.000	0.002	0.000	0.000
Fe	0.5-5	0.099	0.001	0.005								
	5-10	0.060	0.000	0.003								
	10-50	0.160	0.001	0.005								
	50-100	0.050	0.000	0.001								
	100-500	0.070	0.000	0.001								
	500-1000	0.010	0.000	0.000								
	1000-5000	0.010	0.000	0.000								
	5000-10000	0.002	0.000	0.000								
	1E+4-5E+4	0.000	0.000	0.000								

1E+08 eV

Fe	0.5-5	0.011	0.000	0.000
	5-10	0.012	0.000	0.000
	10-50	0.004	0.000	0.000
	50-100	0.006	0.000	0.000
	100-500	0.001	0.000	0.000

Table 3.3 : Energy distribution of secondaries in 10 keV stripe cascades by H, He, C, and Fe primaries in three targets (*MARLOWE* in Bethe Bloch mode)

1E+06 eV

target number		I			II				III			
projectile	energy bins	N	C	H	N	Ar	C	H	N	Ar	C	H
H	0.5-5	0.013	0.000	0.000	0.007	0.115	0.000	0.001	0.017	0.293	0.001	0.002
	5-10	0.005	0.000	0.000	0.013	0.004	0.000	0.001	0.011	0.015	0.001	0.001
	10-50	0.012	0.000	0.001	0.011	0.005	0.001	0.002	0.021	0.013	0.000	0.001
	50-100	0.004	0.000	0.000	0.002	0.000	0.001	0.001	0.001	0.000	0.000	0.000
	100-500	0.005	0.000	0.000	0.002	0.001	0.000	0.000	0.000	0.001	0.000	0.000
	500-1000	0.000	0.000	0.000	0.000	0.000	0.000	0.000	0.000	0.001	0.000	0.000
He	0.5 5	0.016	0.000	0.001	0.016	0.095	0.000	0.003	0.013	0.189	0.000	0.006
	5-10	0.017	0.000	0.001	0.011	0.009	0.000	0.001	0.008	0.025	0.001	0.005
	10-50	0.031	0.000	0.001	0.019	0.006	0.000	0.000	0.022	0.030	0.002	0.004
	50-100	0.004	0.000	0.000	0.006	0.001	0.000	0.000	0.005	0.001	0.000	0.001
	100-500	0.003	0.000	0.000	0.004	0.001	0.001	0.000	0.004	0.004	0.000	0.000
	500-1000	0.003	0.000	0.000	0.000	0.000	0.000	0.000	0.000	0.000	0.000	0.000
	1000-5000	0.000	0.000	0.000	0.002	0.000	0.000	0.000	0.000	0.000	0.000	0.000
C	0.5-5	0.000	0.000	0.000	0.000	0.000	0.000	0.000	0.000	0.000	0.000	0.000

1E+07 eV

H	0.5-5	0.000	0.000	0.000	0.000	0.000	0.000	0.000	0.000	0.000	0.000	0.000
He	0.5-5	0.012	0.000	0.000	0.004	0.046	0.000	0.002	0.002	0.082	0.000	0.000
	5-10	0.008	0.000	0.000	0.004	0.007	0.001	0.001	0.004	0.006	0.001	0.001
	10-50	0.006	0.000	0.000	0.003	0.005	0.000	0.000	0.007	0.008	0.001	0.002
	50-100	0.004	0.000	0.000	0.003	0.000	0.000	0.000	0.001	0.000	0.000	0.000
	100-500	0.002	0.000	0.000	0.000	0.001	0.000	0.001	0.001	0.000	0.000	0.000
C	0.5-5	0.010	0.000	0.000	0.005	0.031	0.000	0.001	0.008	0.078	0.000	0.002
	5-10	0.007	0.000	0.000	0.005	0.004	0.000	0.000	0.004	0.009	0.001	0.001
	10-50	0.012	0.000	0.000	0.005	0.000	0.000	0.000	0.010	0.003	0.000	0.003
	50-100	0.001	0.000	0.000	0.004	0.000	0.000	0.000	0.004	0.001	0.000	0.001
	100-500	0.001	0.000	0.000	0.002	0.000	0.000	0.000	0.000	0.001	0.001	0.000
	500-1000	0.000	0.000	0.000	0.000	0.000	0.000	0.000	0.000	0.001	0.001	0.000

1E+08 eV

H	0.5-5	0.000	0.000	0.000	0.000	0.000	0.000	0.000	0.000	0.000	0.000	0.000
He	0.5-5	0.000	0.000	0.000	0.000	0.001	0.000	0.000	0.000	0.003	0.000	0.000
	5-10	0.001	0.000	0.000	0.000	0.000	0.000	0.000	0.000	0.002	0.000	0.000
	10-50	0.001	0.000	0.000	0.001	0.001	0.000	0.000	0.000	0.000	0.000	0.000
	50-100	0.000	0.000	0.000	0.000	0.000	0.000	0.000	0.001	0.000	0.000	0.000
C	0.5-5	0.015	0.000	0.000	0.014	0.000	0.000	0.000	0.010	0.000	0.000	0.001
	5-10	0.000	0.000	0.000	0.000	0.001	0.000	0.000	0.000	0.008	0.001	0.000
	10-50	0.006	0.000	0.000	0.003	0.001	0.000	0.000	0.004	0.002	0.000	0.000
	50-100	0.000	0.000	0.000	0.000	0.001	0.000	0.000	0.000	0.000	0.000	0.000
	100-500	0.000	0.000	0.000	0.003	0.000	0.001	0.000	0.000	0.000	0.000	0.000
	500-1000	0.000	0.000	0.000	0.001	0.000	0.000	0.000	0.001	0.000	0.000	0.000
	1000-5000	0.001	0.000	0.000	0.001	0.000	0.000	0.000	0.000	0.000	0.000	0.000

3.3 Ranges of primaries

The projectile looses its kinetic energy E_{kin} along its path through the solid by successsive collisions with the target particles of the material and will suffer deflections (multiple scattering) from its initial direction by elastic but not by inelastic collisions. It forms a trajectory which ends at the stopping point p, where the kinetic energy has dropped to the cutoff value. In order to describe the fate of the projectile geometrically different ranges are defined, cf. also Fig. 3.4:

a) linear (total, effective) range R_L, which is the total path length traversed by the particle,
b) the vector range R_V, which is the vector between starting and stopping point,
c) the projected range, R_P, which is the normal projection of the vector range on the starting direction (penetration depth),
d) the lateral range $R_\perp$, which is the distance of the stopping point from a straight line through the starting point along the starting direction. This is also called transverse straggling.

Calculations of energetic ions profile in Titan's atmosphere necessitate the calculation of the penetration of the primaries.

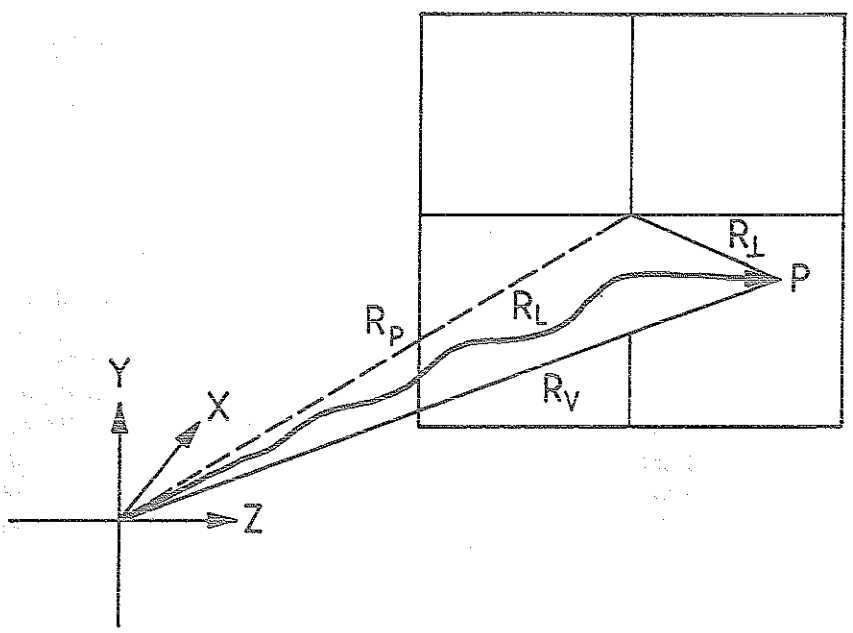

Fig. 3.4: Illustration of linear range (R_L), vector range (R_V), projected range (R_P), and lateral range ($R_\perp$) for the given trajectory of a projectile.

Table 3.4 illustrates the different values obtained for penetration depth of various projectiles with energies ranging from 10 to 10^8 eV in the three targets via LSS and BB theories. The later gives more reliable values for higher energies.

Table 3.4 : Mean penetration depths (a_o) of H, He, C, and Fe primaries in the three targets. Values for energies $E \leq 10^4$ eV are from full cascades, those for $E > 10^4$ eV are extrapolated from stripe calculations (*MARLOWE* in LSS and BB modes)

H - projectile

target number	I		II		III	
primary energy, eV	LSS	BB	LSS	BB	LSS	BB
1E+08		2.30E+08		2.75E+08		1.21E+08
1E+07	8.85E+04	2.69E+06	9.16E+04	2.71E+06	9.44E+04	2.73E+06
1E+06	2.62E+04	7.64E+04	2.70E+04	8.52E+04	2.78E+04	9.67E+04
1E+05	6.24E+03		6.39E+03		6.51E+03	
3E+04	2.77E+03		2.79E+03		2.81E+03	
1E+04	1.06E+03		1.05E+03		1.06E+03	
1E+03	1.18E+02		1.18E+02		1.19E+02	
1E+02	1.23E+01		1.24E+01		1.33E+01	
1E+01	1.70E+00		1.77E+00		1.76E+00	

He - projectile

1E+08		4.98E+06		5.14E+06		5.31E+06
1E+07	8.88E+04	3.39E+05	9.17E+04	3.43E+05	9.47E+04	3.46E+05
1E+06	2.53E+04	2.75E+04	2.61E+04	2.86E+04	2.68E+04	3.98E+04
1E+05	5.27E+03		5.35E+03		5.46E+03	
3E+04	1.92E+03		1.94E+03		1.93E+03	
1E+04	6.53E+02		6.55E+02		6.40E+02	
1E+03	5.97E+01		6.17E+01		6.09E+01	
1E+02	6.57E+00		7.17E+00		7.36E+00	
1E+01	1.15E+00		1.20E+00		1.26E+00	

C - projectile

1E+08		2.91E+07		2.37E+07		1.94E+07
1E+07	5.79E+04	7.72E+05	5.99E+04	7.61E+05	6.16E+04	7.45E+05
1E+06	1.47E+04	5.94E+04	1.54E+04	6.16E+04	1.57E+04	6.24E+04
1E+05	2.34E+03		2.41E+03		2.45E+03	
3E+04	6.61E+02		6.79E+02		6.85E+02	
1E+04	1.94E+02		1.98E+02		1.99E+02	
1E+03	2.15E+01		2.16E+01		2.24E+01	
1E+02	3.51E+00		3.60E+00		3.80E+00	
1E+01	0.80E+00		0.90E+00		1.02E+00	

Fe - projectile

1E+08	2.84E+05
1E+07	4.02E+04
1E+06	6.44E+03
1E+05	6.46E+02
3E+04	1.81E+02
1E+04	6.14E+01
1E+03	1.45E+01
1E+02	5.53E+00
1E+01	2.43E+00

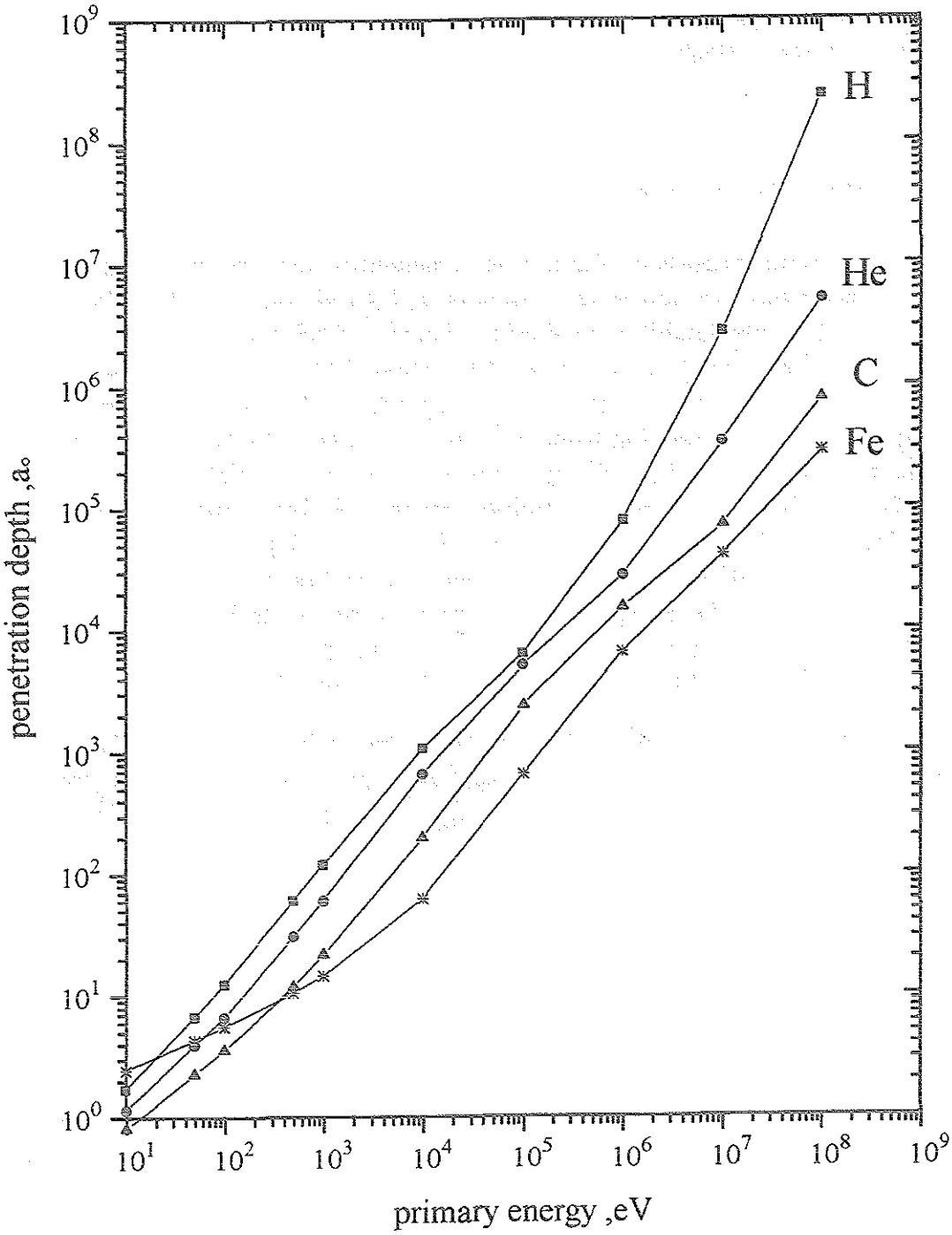

Fig. 3.5: Penetration dephts (a_o) of H, He, C, and Fe primaries in target I
(MARLOWE in LSS mode for lower and BB mode for higher energies)

For better comparison, the results are plotted in Fig. 3.5. As expected, H shows the highest penetration. Since at high energies the preferential inelastic loss does not lead to deviations from the primary direction, all trajectories are very straight, i.e. the lateral range or straggling is negligible. This is of importance since the above reported values are attributed to perpendicular infall of energetic ions into Titan's atmosphere in chapter 4.1. The variation by a 45° infall is evaluated in chapter 4.3.

3.4 Total number of hot atoms

This section reports on the results of numerical evaluations of the total number of hot atoms created in full cascades at high energies, as described in chapter 2. The results enable a comparison between LSS and BB approach at high energies. The later gives more reliable values. Tables 3.5 - 3.7 show the number of all hot N, Ar, H, and C atoms produced by H, He, C, and Fe primaries with energies ranging from 10 to 10^8 eV in all three targets. It can be seen that the production of hot nitrogen and argon atoms is much stronger than that of H or C due to collision dynamical reasons, i.e. better mass match and higher abundance. Heavier primaries such as C and Fe at high energies produce even up to several 10^4 hot atoms per cascade. The averaging evaluation of the hot atoms formed in the energy intervals between the 10 keV stripes from a concrete number of hot atoms formed at 10^7 eV primary energy to a zero value for 10^8 eV, such as e.g. for H and He projectiles, is somewhat critical.

Fig. 3.6 shows a plot of number of hot nitrogen atoms formed by H-projectile in target I, in a 10 keV stripe. The lower curve shows the values from MARLOWE. The upper curve reports the energy values of a 10 keV stripe in between the energy decades. It can be seen that even if the MARLOWE value for 10^8 eV becomes close to zero, the averaged values seem to be quite meaningful.

Table 3.5 : Number of all N, C, and H hot atoms generated by H, He, C, and Fe primaries in target I (*MARLOWE* in LSS and BB modes)

H - projectile

primary energy (eV)	N(LSS)	N(BB)	C(LSS)	C(BB)	H(LSS)	H(BB)
1E+08	———	298	———	1.7	———	7.3
1E+07	91.3	165	0.45	1.5	3.3	5.7
1E+06	89.0	94.1	0.45	1.3	3.3	3.6
1E+05	69.1		0.38		2.8	
3E+04	58.2		0.31		2.5	
1E+04	27.8		0.14		1.2	
1E+03	9.7		0.05		0.6	
5E+02	5.6		0.02		0.5	
1E+02	0.7		0		0.2	
5E+01	0.1		0		0.1	
1E+01	0		0		0	

He - projectile

1E+08	———	1171	———	6.7	———	33.6
1E+07	748	817	5.6	5.6	31.1	31.2
1E+06	668	671	4.7	4.6	28.4	28.4
1E+05	445		3.0		18.2	
3E+04	329		2.0		12.7	
1E+04	150		0.9		5.7	
1E+03	29.6		0.2		1.3	
5E+02	15.7		0.1		0.7	
1E+02	2.7		0.0		0.2	
5E+01	1.1		0		0.1	
1E+01	0		0		0	

C - projectile

1E+08	———	5471	———	40.7	———	255
1E+07	4950	4922	36.9	36.8	231	231
1E+06	3870		29.1		184	
1E+05	1513		10.7		72.4	
3E+04	765		4.8		31.9	
1E+04	300		1.8		11.4	
1E+03	39.4		0.2		1.5	
5E+02	20.3		0.1		0.7	
1E+02	3.9		0		0.1	
5E+01	1.8		0		0.1	
1E+01	0		0		0	

Fe - projectile

1E+08	65636	———	814	———	3324	———
1E+07	44456		411		2097	
1E+06	18024		141		809	
1E+05	3652		23.3		144	
3E+04	1212		7.1		46	
1E+04	390		2.3		14.8	
1E+03	44.9		0.3		1.6	
5E+02	23.0		0.1		0.7	
1E+02	4.4		0		0.1	
5E+01	1.9		0		0	
1E+01	0		0		0	

Table 3.6 : Number of all N, Ar, C, and H hot atoms generated by H, He, and C primaries in target II (*MARLOWE* in LSS and BB modes)

H - projectile

primary energy (eV)	N(LSS)	N(BB)	Ar(LSS)	Ar(BB)	C(LSS)	C(BB)	H(LSS)	H(BB)
1E+08	-------	131	-------	128	-------	2.9	-------	20
1E+07	94.7	127	50.6	124	1.5	2.9	14.2	20
1E+06	82.4	85.7	47.4		1.4	1.6	13.2	13.7
1E+05	62.4		32.1		1.1		10	
3E+04	50.7		23.6		0.9		8.5	
1E+04	23.9		10.7		0.4		4	
1E+03	8.2		4.9		0.1		1.9	
5E+02	4.7		4.7		0.07		1.4	
1E+02	0.65		1.1		0.00		0.6	
5E+01	0.06		0.6		0.00		0.4	
1E+01	0.00		0.06		0.00		0.05	

He - projectile

1E+08	-------	1022	-------	807	-------	16.7	-------	156
1E+07	840	812	395	451	21.5	15.9	118	113
1E+06	638	634	268	270	13.3	12.7	90.4	90.4
1E+05	428		164		8.6		62.4	
3E+04	293		89.2		5.9		43.3	
1E+04	129		34		2.8		19.1	
1E+03	25.1		13		0.4		4.	
5E+02	13.3		7		0.2		2.3	
1E+02	2.3		1.6		0.04		0.55	
5E+01	0.87		0.93		0.01		0.33	
1E+01	0.00		0.21		0.00		0.03	

C - projectile

1E+08	-------	7029	-------	3939.40	-------	143.20	-------	1008
1E+07	5906	5902	3165	3170.80	120	119.80	871	868
1E+06	3977		2088		79.9		604	
1E+05	1482		703		30.1		220	
3E+04	692		262		14		102	
1E+04	258		82.6		5.2		38.6	
1E+03	34.4		14.6		0.6		4.9	
5E+02	17.9		7.6		0.36		2.5	
1E+02	2.3		0.7		0.04		0.33	
5E+01	1.6		0.9		0.02		0.04	
1E+01	0.02		0.22		0.00		0.00	

Table 3.7 : Number of all N, Ar, C, and H hot atoms generated by H, He, and C primaries in target III (*MARLOWE* in LSS and BB modes)

H - projectile

primary energy (eV)	N(LSS)	N(BB)	Ar(LSS)	Ar(BB)	C(LSS)	C(BB)	H(LSS)	H(BB)
1E+08	-------	133	-------	311	-------	6.2	-------	31.9
1E+07	93.4	133	110	311	4.5	6.2	34.	31.9
1E+06	72.7	77.3	97.8	116	3.9	4	21.7	21.3
1E+05	52.2		65.3		3		16.8	
3E+04	41.8		49.5		2.7		14.7	
1E+04	19.7		22.8		1.3		7.1	
1E+03	6.6		10.6		0.24		3.5	
5E+02	3.8		10.2		0.13		2.5	
1E+02	0.48		2.9		0.01		1.1	
5E+01	0.04		1.5		0		0.66	
1E+01	0		0.1		0		0.09	

He - projectile

1E+08	-------	1049	-------	1601	-------	41.8	-------	223
1E+07	748	819	767	967	25.5	28.8	179	191
1E+06	696	699	661	671	23.8	24.1	169	170
1E+05	392		347		14.5		109	
3E+04	250		197		9.9		78.2	
1E+04	108		80		4.4		35.4	
1E+03	20.6		24.4		0.83		7.6	
5E+02	11		17.4		0.44		4.1	
1E+02	1.9		4		0.05		1.1	
5E+01	0.7		2.1		0.02		0.54	
1E+01	0		0.46		0		0.06	

C - projectile

1E+08	-------	6206	-------	7024	-------	228	-------	1648
1E+07	5541	5499	5728	5702	159	189	1469	1449
1E+06	4068		4093		146		1139	
1E+05	1445		1332		53.8		392	
3E+04	615		486		24.6		320	
1E+04	215		151		9.1		71.5	
1E+03	28.6		46.3		1.2		9.6	
5E+02	14.8		18.4		0.7		4.8	
1E+02	2.9		3.9		0.11		0.95	
5E+01	1.3		2.1		0.04		0.45	
1E+01	0		0.5		0		0	

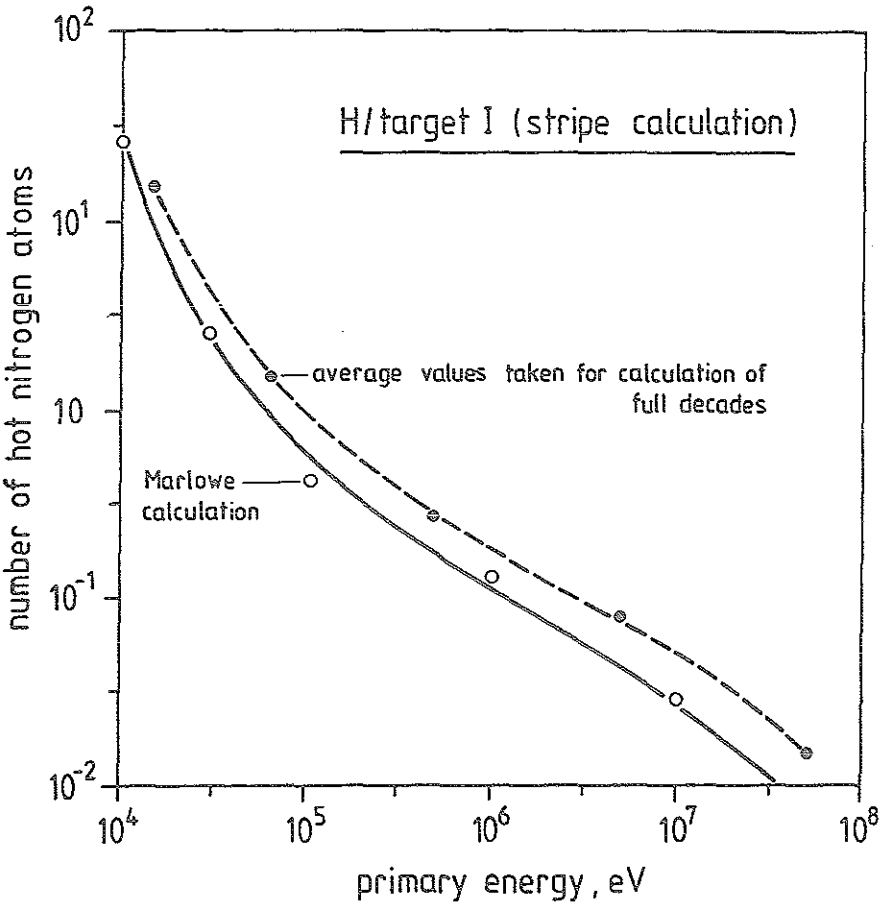

Fig. 3.6: Numbers of nitrogen primaries in 10 keV stripe calculations of H primary in target I, MARLOWE results and average values for calculation of the contents between two energy intervalls

Even if the elastic energy transfer decreases with energy there are still some few elastic collisions possible which generate secondaries and cascades at lower primary energies. Thus the absolute number of hot atoms increases steadily up to a certain energy limit of 10^8 eV for H primaries and much higher for Fe projectiles (10^9 - 10^{10} eV). In target I which is relatively poor in CH_4 only few C and H atoms are liberated; the majority of hot species are N atoms. However, the number of C and H atoms increases dramatically with the mass (and Z) of the projectile. It can be seen that the BB modes lead to an increase of the number of hot atoms at high energies, as compared to the LSS approach, cf. chapter 3.6.

Fig. 3.7 reports for better comparison the total number of all hot atoms for the three targets and three primaries. In the logarithmic scale a certain saturation becomes visible for very high energies. Target III results in somewhat more secondaries than targets II and I. This may be due to the fact, that Ar has no binding or threshold energy and, thus, can serve as an energy transfer unit to N_2 and CH_4.

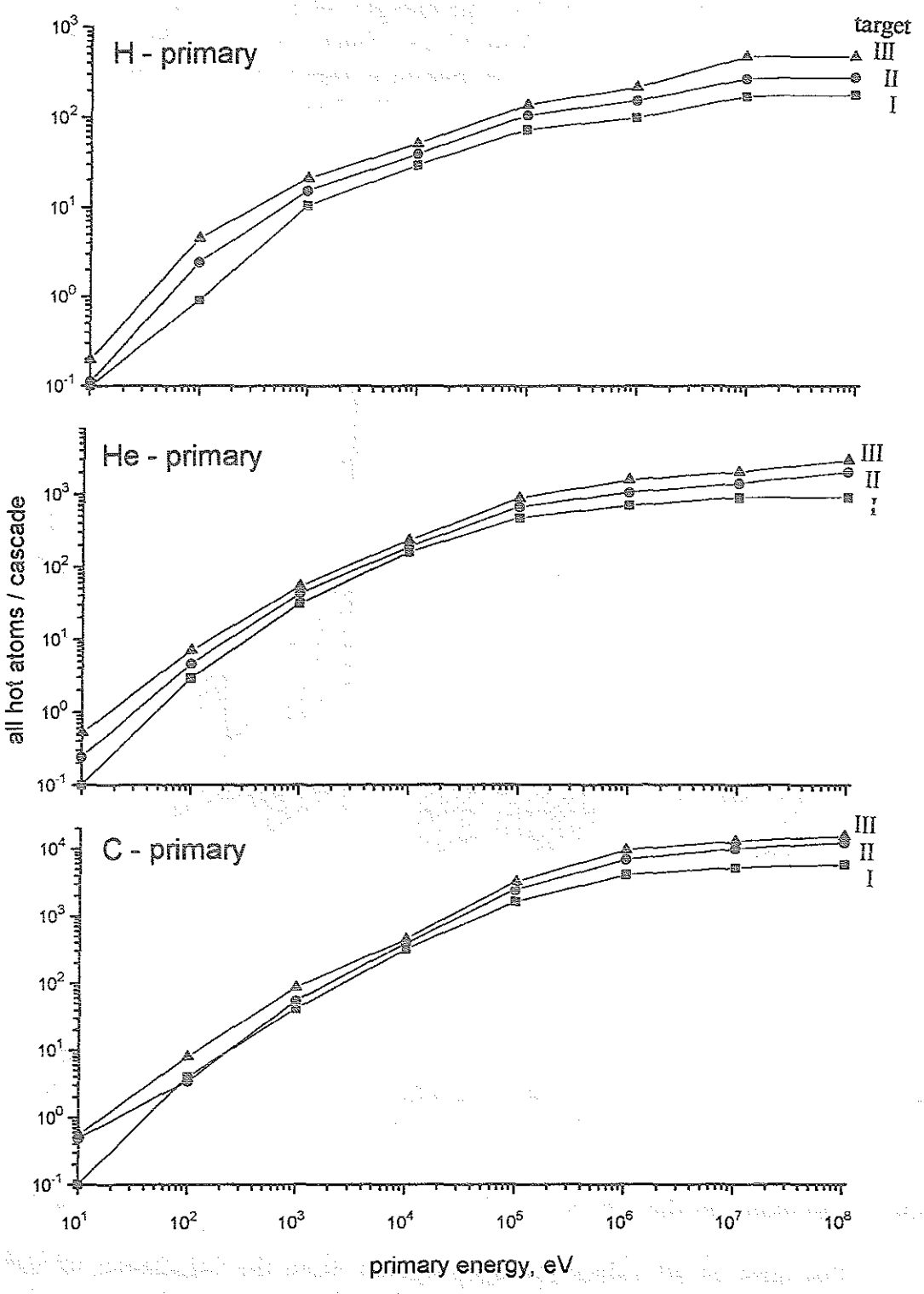

Fig. 3.7: Cumulative number of all hot atoms (N + Ar + C + H) generated by H, He and C primaries in three targets

3.5 Final energy distribution

The energy distributions of hot N, Ar, C and H for 10^5 H after the last displacive event are shown in Fig. 3.8. The energies of the species which now can react chemically range from 0.5 to 50 eV. Since the energy bins in this system are somewhat arbitrary, the distribution is shown again in Fig. 3.9 in units of number per eV energy bin. A normal distribution of energies results. There are quite a number of particles with 10 and more eV energy, which upon their gradual thermalization can undergo hot chemical reactions.

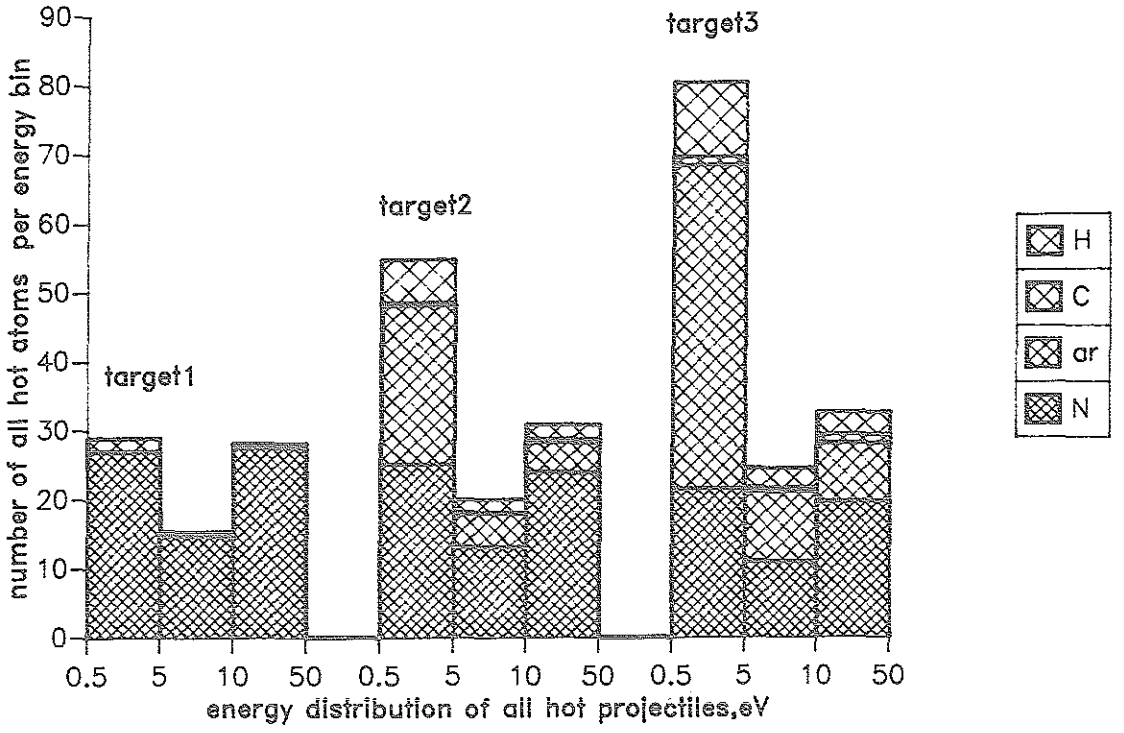

Fig. 3.8: Energy distribution of all hot atoms generated by 10^5 eV H in three targets after the last displacive collision.

3.6 Discussion of the numerical data

The error of all values averaged directly from the calculation of 10^4 cascades is in the order of $\pm \delta = 5$ to 10 %. For all data evaluated by averaging procedures from stripe calculations this value may increase to $\pm \delta = 10$ to 20 %.

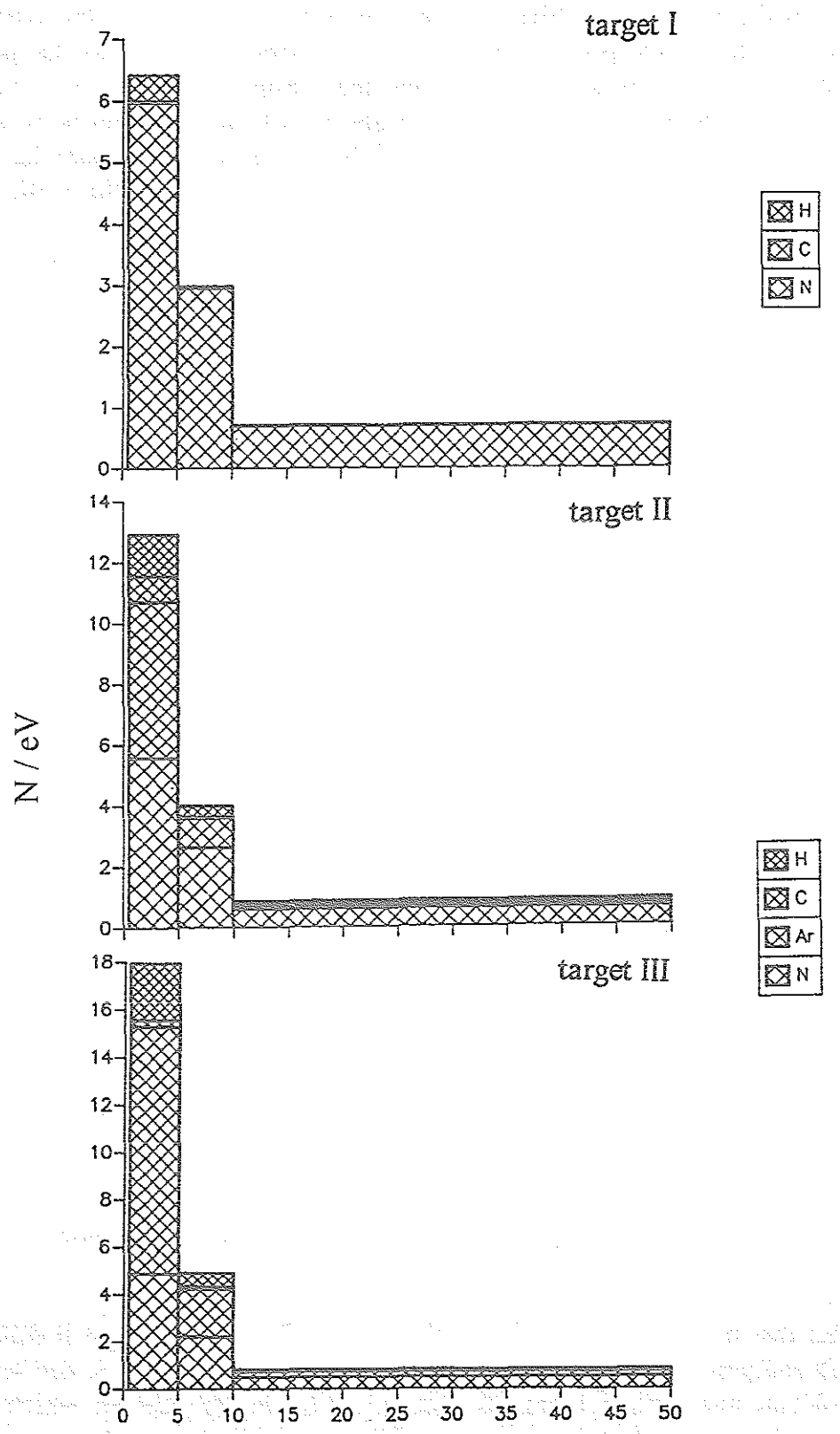

Fig. 3.9 : Energy distributions of hot atoms after the last displacive collision.

The most astonishing fact is the relatively high number of hot atoms by collisions at high energies. When looking somewhat more in detail into the structure of the collision cascades it can be seen from Table 3.8 that the average inelastic transfer in eV per collision rises with primary energy to the point where the BB mode has to be applied and than drops, cf. Fig. 3.10. Totally unexpected was the fact that the number of elastic collisions did not go to zero at higher energies, only to vanish for very high energies and light particles (H: 10^8 eV), i.e. the domain where relativistic effects begin. Due to the maller S_e per collision the projectile undergoes more collisions before thermalization. This increases the chance for some of the few elastic collisions which can transfer enough energy to exceed the threshold energy. Thus, S_n is relatively seldom, but it happens and due to the discipation of high energies it plays an important role also with respect to the classical low energy elastic transfer.

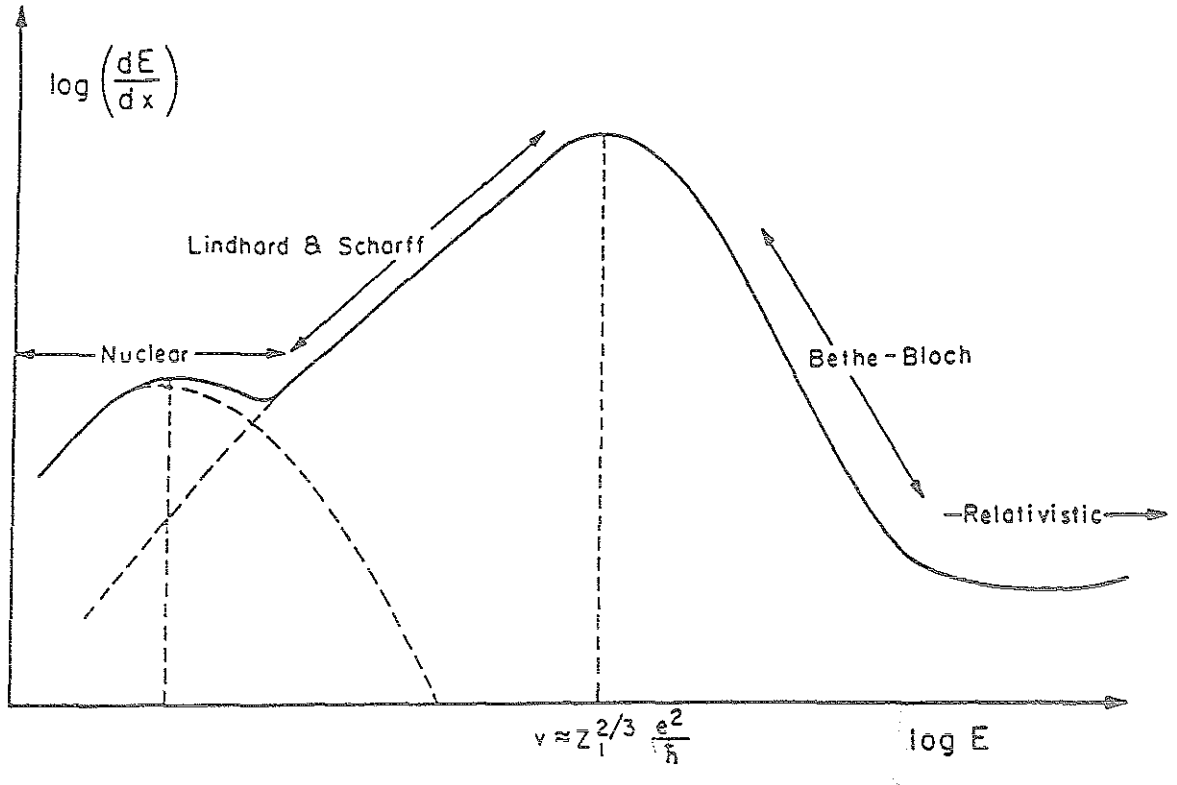

Fig. 3.10: Collisional energy transfer modes as depending on energy

The fact that the inelastic transfer finally drops with energy makes it difficult for high energetic H and He to induce classical ionization processes, and with it ion-molecule interactions. It sounds strange, but the heavy particles which lead to more elastic transfer also induce a sufficient inelastic transfer to yield electronic damage and not excitation only, cf. Table 3.9. Carbon projectiles at 10^8 eV exhibit already a decrease of S_e, whereas the Fe projectiles still show a steady increase.For further work in this domain the values for 10^9 eV C and Fe and for 10^{10} eV Fe should be calculated.

Very interesting is the mutual role of nitrogen (the majority component) and Ar (with a very low displacement threshold). These particles serve as energy carriers to the chemically interesting CH_4. Fig. 3.11 shows a comparison of the number of hot nitrogen atoms formed in the three targets as depending on the Ar content. In order to eliminate the trivial dilution effect, the number of hot nitrogens is normalized to 100 % nitrogen content. It can be seen that H, He and C primaries at lower energies (10^4 eV) do not yield different values for nitrogen recoils with the composition. However, at higher primary energies in particular the heavier projectile gives rise to more nitrogen atoms (even if normalized) in the targets rich in argon. This is an effect of the mutual interplay of N and Ar hot atoms from a certain concentration and energy level on, an interesting insight into the collision dynamics of chemically mixed systems.

Table 3.8 : Average inelastic energy loss, eV per collision for different projectiles in target I from MARLOWE.

primary energy eV	H	He	C	Fe
1E+08	1.0*	2.0*	42.4*	1097
1E+07	1.0*	11.8*	245*	343
1E+06	5.4*	42.5*	91.4	108
1E+05	19.5	19.2	28.2	32.8
3E+04	10.0	9.8	14.4	15.9
1E+04	3.3	2.3	0.69	0.59
1E+03	1.1	0.73	2.3	0.20
5E+02	0.73	0.51	0.31	0.13
1E+02	0.28	0.20	0.11	0.05
5E+01	0.18	0.13	0.09	0.02
1E+01	0.05	0.03	0.02	0.00

* BB mode, otherwise LSS.

Table 3.9 : Ionization potentials of elements (Handbook of Chemistry and Physics).

elements	ionization potentials in Volts								
	atom no.	I	II	III	IV	V	VI	VII	VIII
H	1	13.6							
He	2	24.5	54.4						
C	6	11.3	24.4	47.9	64.5	391	490		
N	7	14.5	29.5	47.4	77.4	97.9	552	667	
Ar	18	15.8	27.6	40.9	59.8	75	91.3	124	143
Fe	26	7.9	16.2	30.6	56.8				151

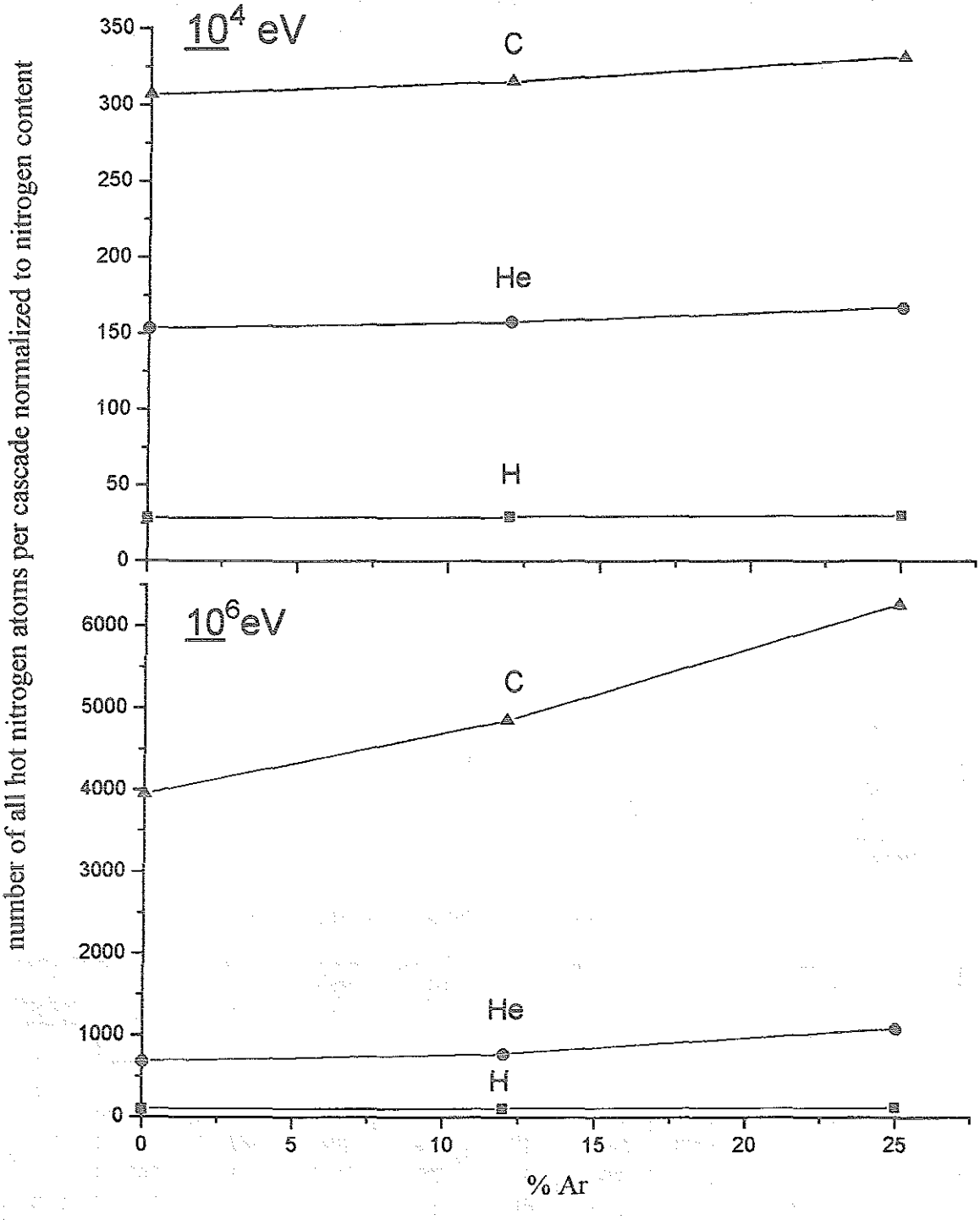

Fig. 3.11: Comparison of number of hot nitrogen atoms formed in the three targets as depending on dilution (by Ar), the kind of primary (H, He, C) and its energy

CHAPTER 4

APPLICATION TO TITAN'S ATMOSPHERE

4.1 Penetration into the atmosphere

The results of numerical calculation of collision cascades in the condensed model lattice have now to be transformed to fit the dynamics of Titan's atmosphere . The first approach is to evaluate the penetration of the energetic primaries from solar wind and cosmic rays. Here the expression "column density $\bar{n}$" is introduced, which signifies the number of molecules or atoms in a whole object seen along a rectangular column with 1 cm^2 area. This expression often used in astronomy and astrophysics to describe the density of interstellar clouds. In the present case it is applied to the penetration data in the model lattice.

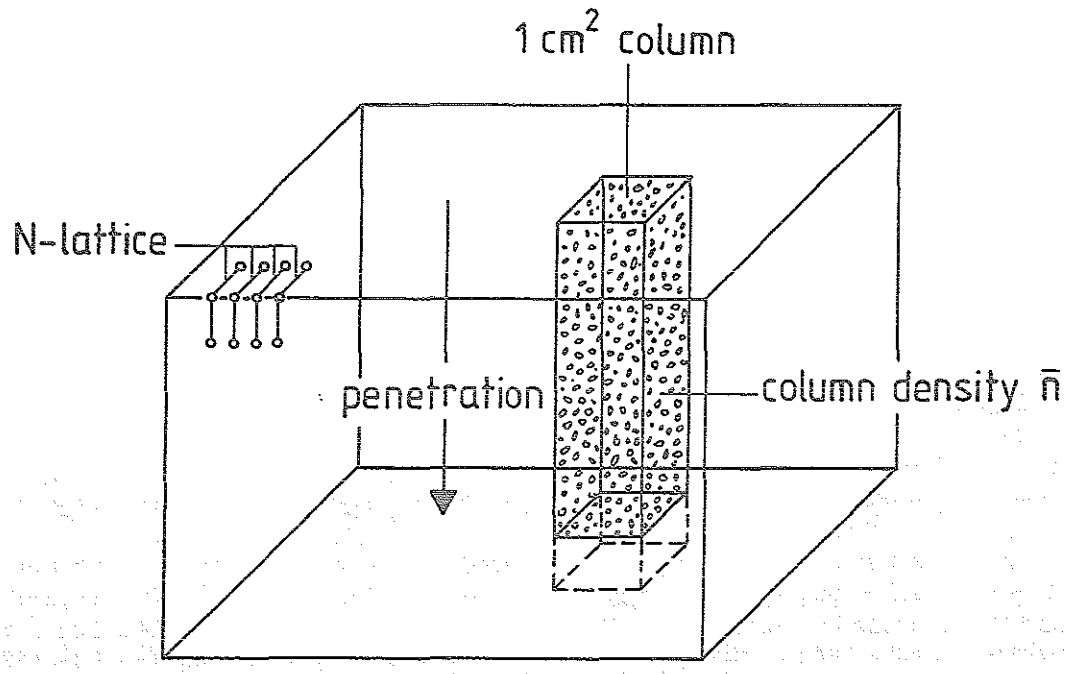

Fig. 4.1: Column density $\bar{n}$ in model lattice.

Fig. 4.1 shows the column with 1 cm^2 area and the height of the penetration depth in the basically cubic lattice. Here one atom (mostly N) is sitting in a 15.6 $Å^3$ cell volume, which corresponds to a number density $n = 6.4 \times 10^{22}$ atoms cm^{-3}.

This chapter treats only the most probable compositions of Titan's atmosphere as given in target I and II of the numerical calculations, for the sake of a more condensed representation. In order to compare with the number density n for the atmospheric composition of Titan such as derived from the curve in Fig. 1.6 the column density $\bar{n}$ values given in Table 4.1 for the single atoms (cf. chapter 2.2.1). They have to be converted to those for molecules or independent atoms : N_2, Ar, and CH_4.

Table 4.1 : Penetration of primaries in terms of column density $\bar{n}$, atoms cm^{-2} (such as derived from the model lattice).

target	I				II		
primary energy, eV	H	He	C	Fe	H	He	C
1E+01	2.72E+15	1.84E+15	6.40E+14	3.89E+15	2.83E+15	1.92E+15	1.44E+15
1E+02	1.98E+16	1.05E+16	5.62E+15	8.85E+15	1.98E+16	1.15E+16	5.76E+15
1E+03	1.89E+17	9.54E+16	3.44E+16	2.30E+16	1.90E+17	9.87E+16	3.45E+16
1E+04	1.69E+18	1.05E+18	3.11E+17	9.79E+16	1.69E+18	1.05E+18	3.18E+17
3E+04	4.43E+18	3.08E+18	1.05E+18	2.91E+17	4.47E+18	3.10E+18	1.09E+18
1E+05	9.98E+18	8.42E+18	3.43E+18	1.02E+18	1.02E+19	8.56E+18	3.86E+18
1E+06	1.22E+20	4.40E+19	2.38E+19	1.02E+19	1.36E+20	4.58E+19	2.46E+19
1E+07	4.31E+21	5.44E+20	9.50E+19	6.43E+19	4.33E+21	5.49E+20	9.78E+19
1E+08	3.69E+23	7.97E+21	1.24E+21	4.54E+20	3.91E+23	8.28E+21	2.34E+21

Table 4.2 : Penetration of primaries in terms of column density $\bar{n}$, molecules cm^{-2}

target	I				II		
primary energy, eV	H	He	C	Fe	H	He	C
1E+01	1.34E+15	9.09E+14	3.16E+14	1.92E+15	1.53E+15	1.04E+15	7.81E+14
1E+02	9.78E+15	5.19E+15	2.78E+15	4.37E+15	1.07E+16	6.23E+15	3.12E+15
1E+03	9.34E+16	4.71E+16	1.70E+16	1.14E+16	1.03E+17	5.35E+16	1.87E+16
1E+04	8.35E+17	5.19E+17	1.54E+17	4.84E+16	9.16E+17	5.69E+17	1.72E+17
3E+04	2.19E+18	1.52E+18	5.19E+17	1.44E+17	2.42E+18	1.68E+18	5.91E+17
1E+05	4.93E+18	4.16E+18	1.69E+18	5.04E+17	6.61E+18	4.64E+18	2.09E+18
1E+06	6.03E+19	2.17E+19	1.18E+19	5.04E+18	7.37E+19	2.48E+19	1.33E+19
1E+07	9.16E+21	2.67E+20	4.69E+19	3.18E+19	2.35E+21	2.98E+20	5.30E+19
1E+08	1.82E+23	3.94E+21	6.13E+20	2.24E+20	2.12E+23	4.49E+21	1.27E+21

To calculate the penetration depth for perpendicular infall into Titan's atmosphere the scheme given in Fig. 4.2 was used. It describes the atmosphere in terms of number density n (cm^{-3}) ordered in decades and derived from the 1.6 bar pressure at the surface using the Eq. 1.5 and Fig 1.6 - column on outer right side - and corresponding altitudes (km) - column on the outer left side -. A finer division of the altitude is made in 10 km bins. The row on the inner right side shows the column densities $\bar{n}$ of molecules for the 10 km bin and a sum over the number

density decade divisions. It has to be mentioned that this scheme does not contain density inhomogeneities due to atmospheric layering or the presence of hazes.

The column densities for the different projectiles at different energies from Table 4.2 are given here as values in the middle. It is assumed that any significant collisional interaction starts only at a minimum number density $n \geq 10^8$ cm^{-2} which corresponds to an altitude of 1360 km.
For the sake of easy conception of the scheme, lines guide the eye from the beginning of trajectory at the 1360 km level down to the site of stopping. This stopping altitude was calculated from the column density $\bar{n}$ by subtracting the contents of the bins in the inner right column, till the number density reached zero value. The values in Fig. 4.2 are for H primaries in an atmosphere of 82% N_2 + 12 % Ar + 6 % CH_4, (target II). It can be seen that 10^8 eV H are stopped in the atmosphere and do not reach the surface of Titan, even in perpendicular infall. It could be estimated that first 10^9 eV H pass through the atmosphere to the surface, however, with a substantial loss of their energy.

4.2 Hot atom profiles for single cascades

In order to evaluate the profile of energetic atoms per averaged single cascade the numerical values of Table 3.5 had to be distributed along the trajectory as calculated in chapter 4.1. For the sake of data reduction the penetration depths for the different systems are not shown in detail there.
They are incorporated in the following figures. The method is schematically shown in Fig. 4.3 for a 10^4 eV primary.
This scheme is derived from that in Fig. 4.2. It contains on the right side the number density profile of Titan's atmosphere (or, inversely, the altitude) in an abbreviated way. The left column reports the remaining energy of the primary in decades and half decades. The positions in the diagram are evaluated in terms of penetration depths from Table 4.2 starting from the value for 10^4 eV. The corresponding distribution of total number of hot atoms is calculated as N for each energy interval from Tables 3.5 and 3.6 (for targets I and II) with the help of a FORTRAN program. The range intervals between the lower decades of remaining energy are relatively small and fit into one 10 km bin, thus, the numbers N of hot atoms are added to it. For the higher energy intervals which cover more than one 10 km bin, the corresponding N has to be distributed according to the column density of the bins, i.e. it the profile is weighted to the density of the atmosphere. By this procedure the hot atom profiles in Figs. 4.4 to 4.27 were obtained. It should be noticed that in this model the secondary and all hot atoms stay in the 10 km bin of their generation. As it was shown above in Figs. 3.2 and 3.3 as well as in Tables 3.1-3.3, only very few secondaries carry energies which would enable them to reach the next 10 km bin.
Thus, a calculation of the additional pathways in particular of the secondaries was omitted in the present approach. This is even more justified by the fact, that only few knock on atoms proceed in the same direction than that of the primary.

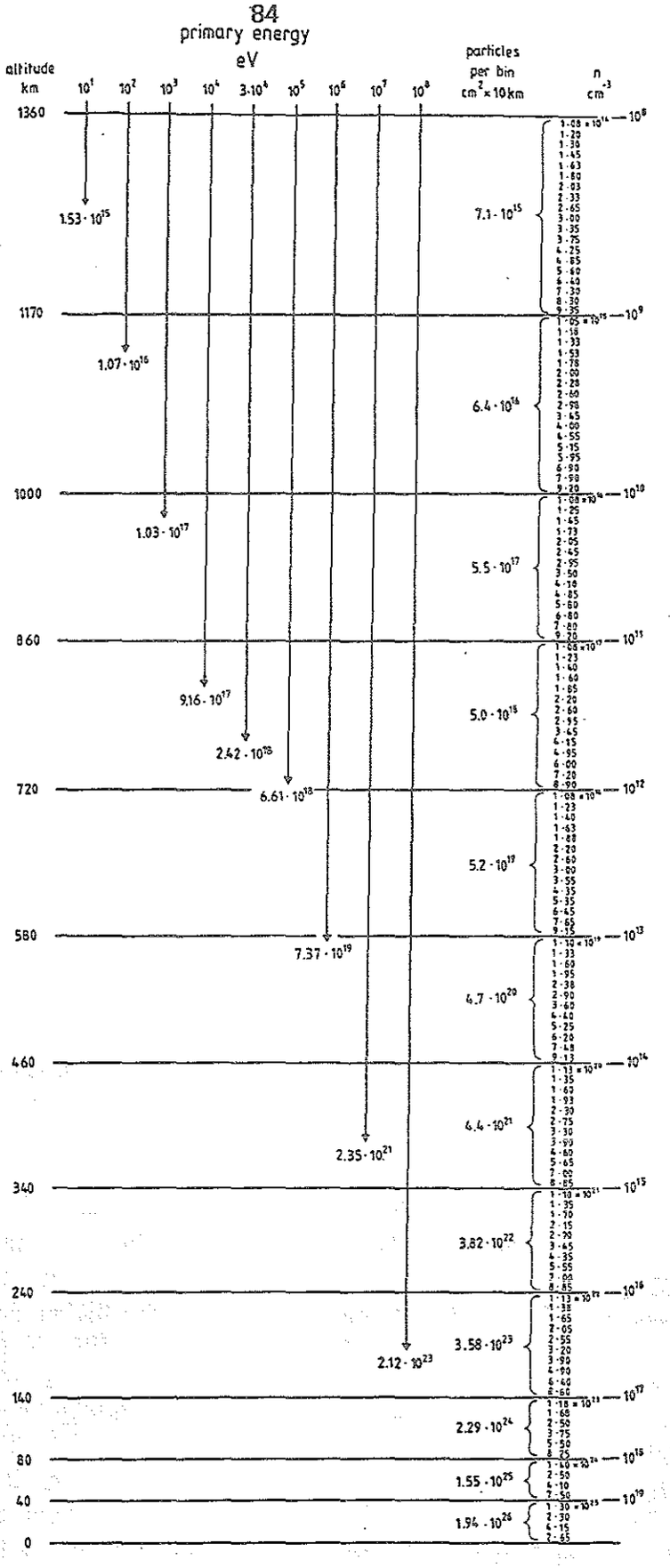

Fig. 4.2 : Scheme of Titan's atmosphere with penetration of H primaries in 82% N_2 + 12% Ar + 6% CH_4 mixture.

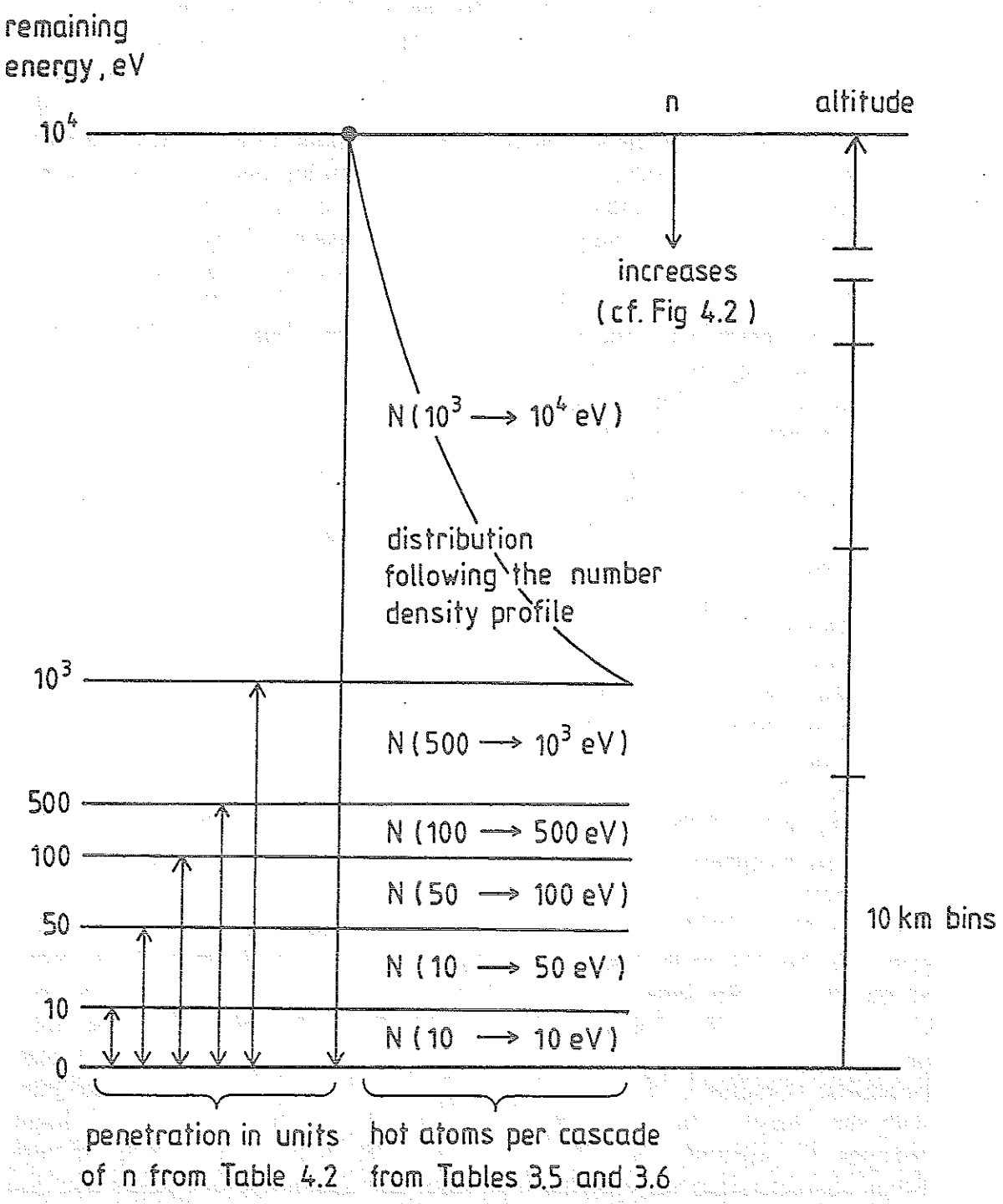

Fig. 4.3 : Schematic flow diagram for the evaluation of hot atom profiles in Titan's atmosphere induced by a 10^4 eV primary.

Most of them will straggle at least to a certain degree perpendicularly to the axis of infall.

The profiles are given for hot nitrogen, carbon and hydrogen atoms in a 98% N_2 + 2% CH_4 atmosphere (target I) for H, He, C, and Fe primaries in Figs. 4.4 to 4.15. There the contents of hot atoms of each type in 10 km bins is plotted against altitude (km). It should be noted that the altitude axis for the higher energies (10^6-10^8 eV) is composed of 20 km bin units, however with two data points, whereas the two other curves show regular 10 km bins. A general feature of the curves is that the majority of hot atoms is generated at the end of the cascades at lower altitude due to the steadily increasing density. However, there is a distinct difference between hot H and the heavier N and C : for light projectiles the curves for hot H are steeper than for the latter ones, and the steepness increases with the energy. N even more than C profiles show a maximum of steepness at medium energies. At very high primary energies they rise more smoothly. For carbon and iron primaries the steepness of hot atom profiles increases steadily with the energy.

The corresponding profiles for hot N, Ar, C, and H atoms in a 82% N_2 + 12% Ar + 6% CH_4 atmosphere (target II) in Figs. 4.16 to 4.27 show some fine differences. Here even for light particles the steepness of the profiles increases steadily with the energy. The largest difference is found for the profiles of hot Ar generated by light projectiles which are definitely broader than those for the others. This may be due to the fact, that Ar has almost no threshold energy. This differences, however, disappear for heavy carbon projectiles.

One characteristic feature applies for all profiles : all primaries, even the light H projectiles with 10^8 eV, are stopped in the two model atmospheres, i.e. they do not touch the surface of the satellite. This might be, however, the case for 10^9 eV particles.

The other feature is the broadening of the right foot of the peaks (decreasing steepness) when going to light, high energetic primaries in target I. The general tendency of most of the other cascades is an increase of the steepness. Fig. 4.28 shows for hot nitrogen atoms induced in target I by H and Fe primaries the ratio of the content of hot atoms in the peak value to the sum over all the other 10 km bins versus the primary energy. This value N_p / sum N is characteristic for the steepness of the curve. It can be seen shows that for H primaries the distributions are steepest for medium energies and get broader (foothills) at higher ones. Fe projectiles lead to a steady increase of steepness with the energy. This represents an effect of collision dynamics at higher energies. Fe projectiles up to 10^8 eV do not yet fall into the domain of Bethe Bloch characteristics for inelastic loss. Thus the number of hot atoms increases steadily but is concentrated in a narrow interval at the end of trajectory. H projectiles which obey the Bethe Bloch formalism already from 10^6 eV on show a relative increase in range, thus the knock-on atoms are distributed over a wider altitude profile. This is of some practical interest for chemical reactions in Titan's atmosphere : Heavy projectiles concentrate their hot atoms in a narrow atmospheric layer which may enable mutual interactions, light ones distribute

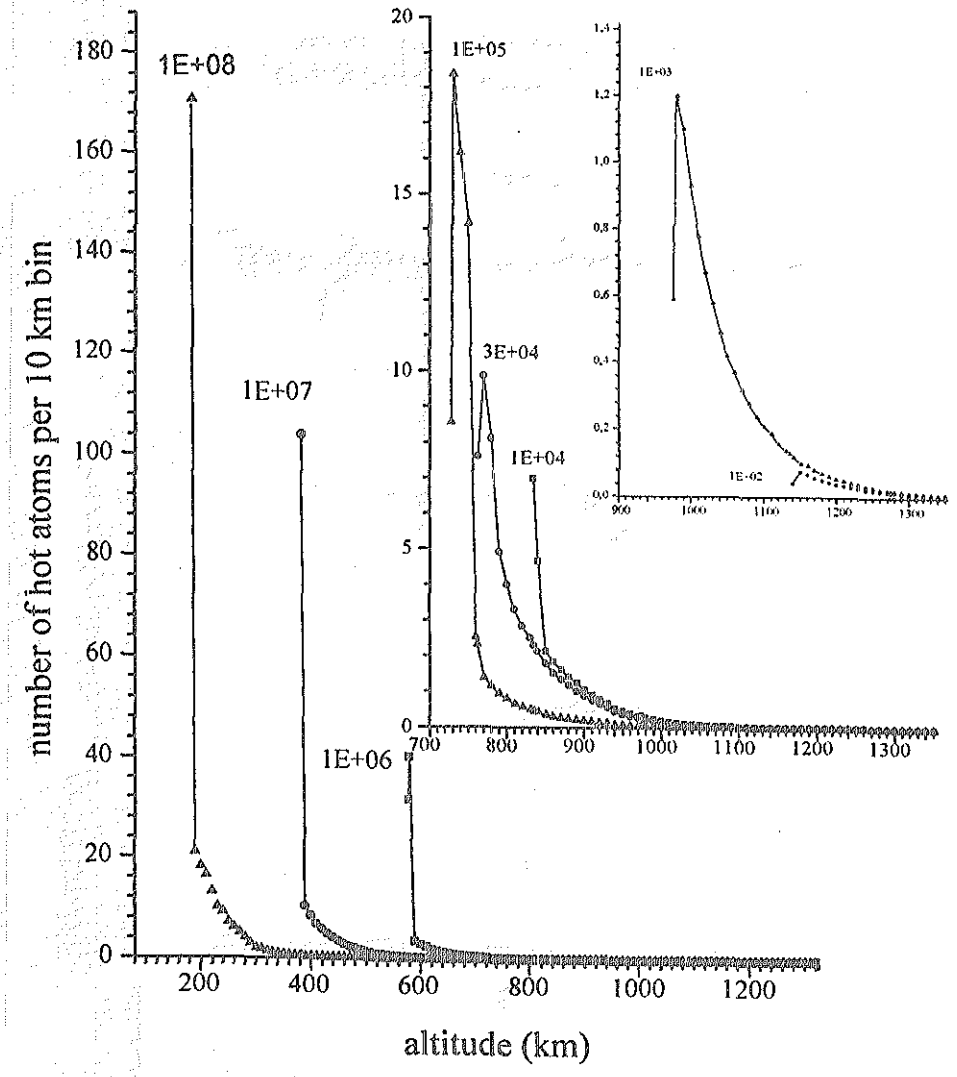

Fig 4.4 : Hot nitrogen profile by 1E+01 to 1E+08 eV H in 98% N_2 + 2% CH_4 atmosphere of Titan

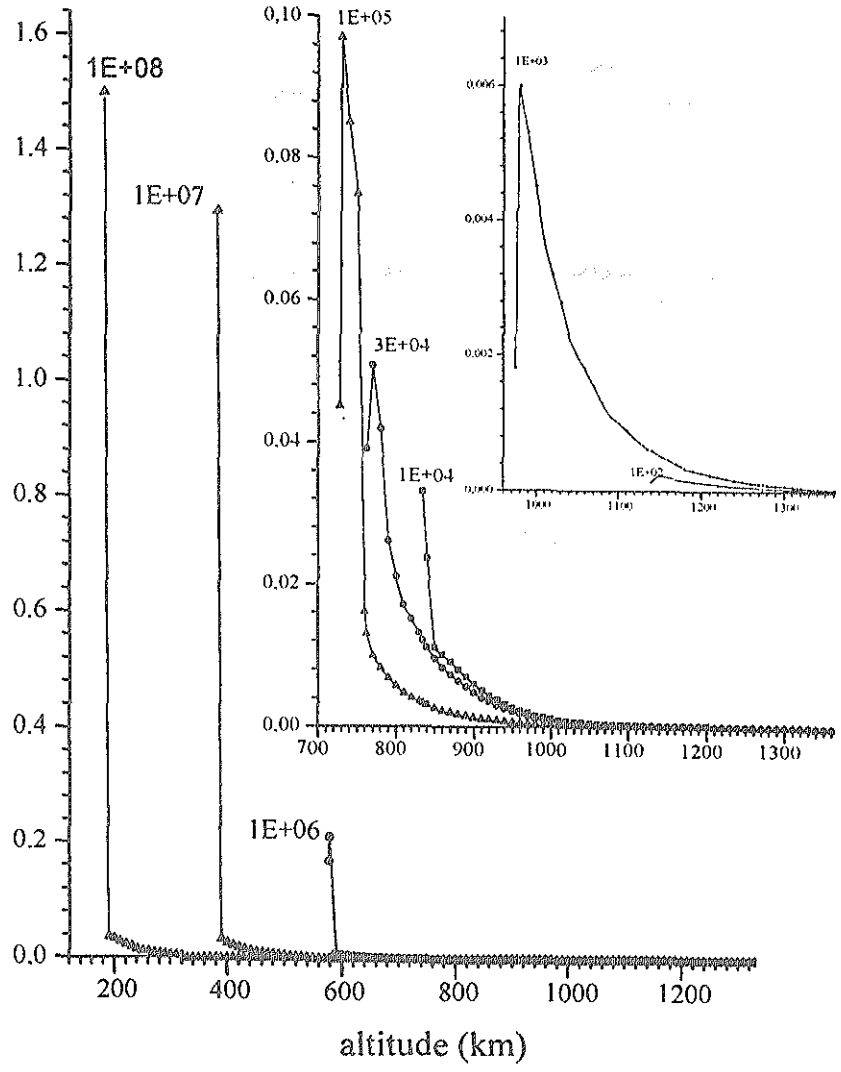

Fig 4.5 : Hot carbon profile by 1E+01 to 10E+08 eV H in 98% N_2 + 2% CH_4 atmosphere of Titan

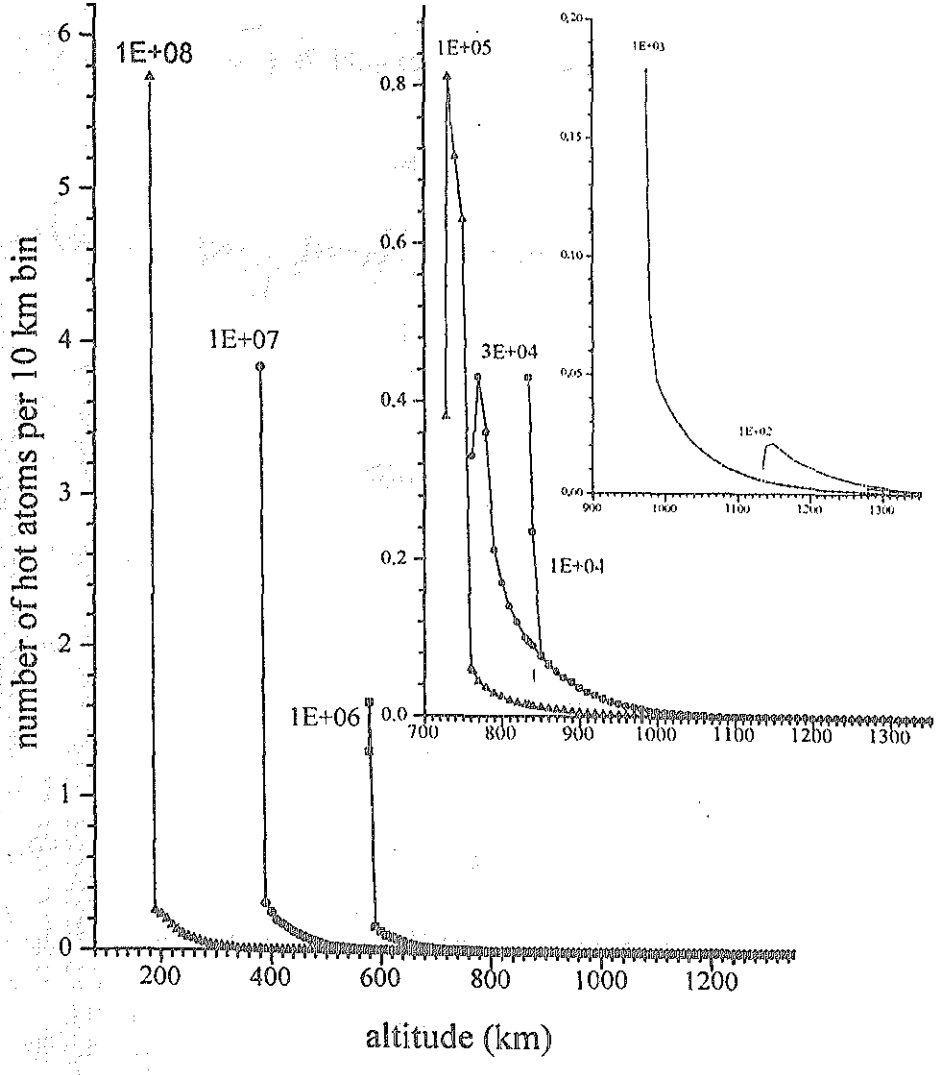

Fig 4.6 : Hot hydrogen profile by 1E+01 to 1E+08 eV H in 98% N_2 +2% CH_4 atmosphere of Titan

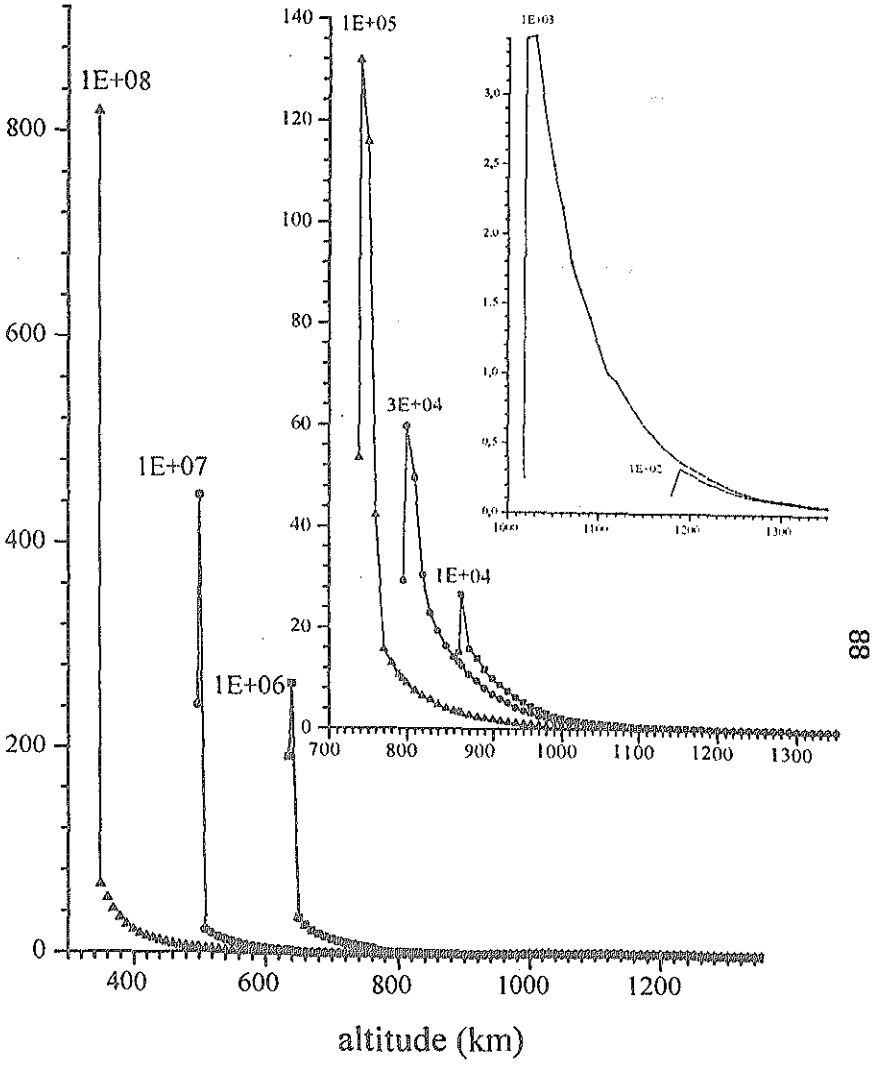

Fig. 4.7: Hot nitrogen profile by 1E+01 to 1E+08 eV He in 98% N_2 + 2% CH_4 atmosphere of Titan

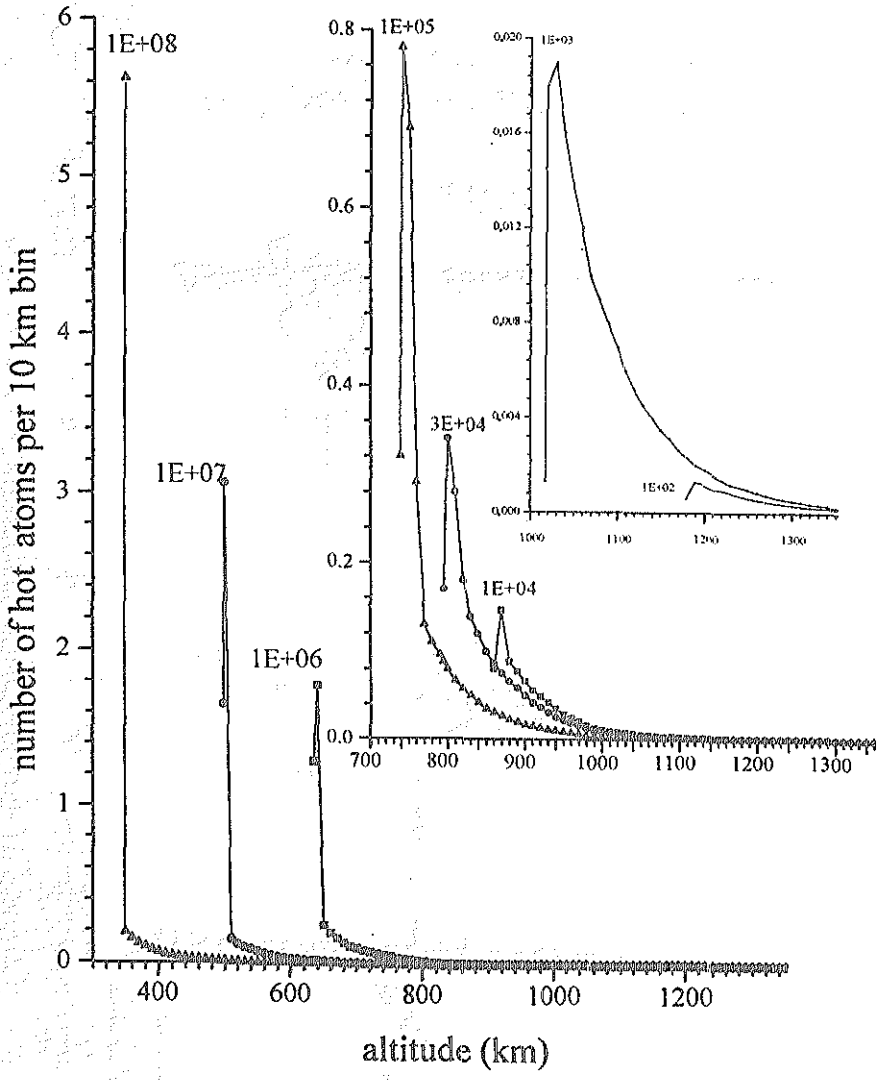

Fig 4.8 : Hot carbon profile by 1E+01 to1E+08 eV He in 98% N_2 + 2% CH_4 atmosphere of Titan

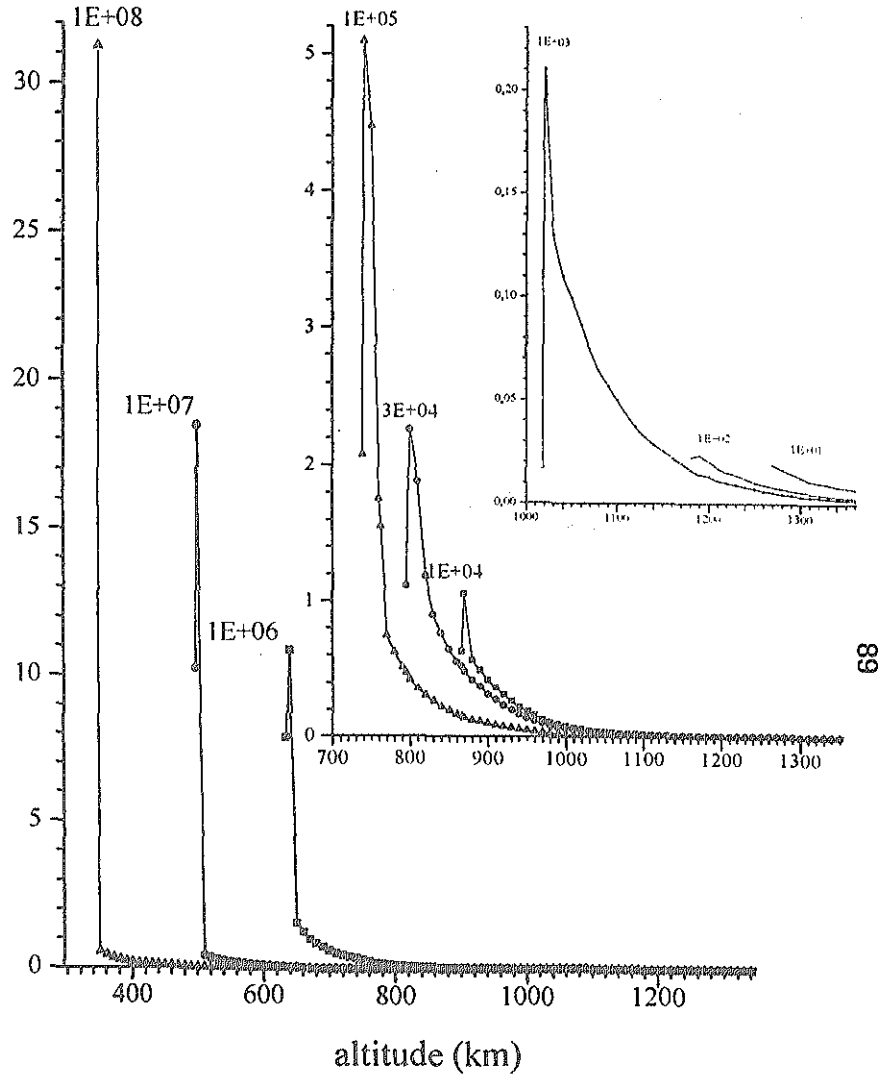

Fig 4.9 : Hot hydrogen profile by 1E+01 to 1E+08 eV He in 98% N_2 + 2% CH_4 atmosphere of Titan

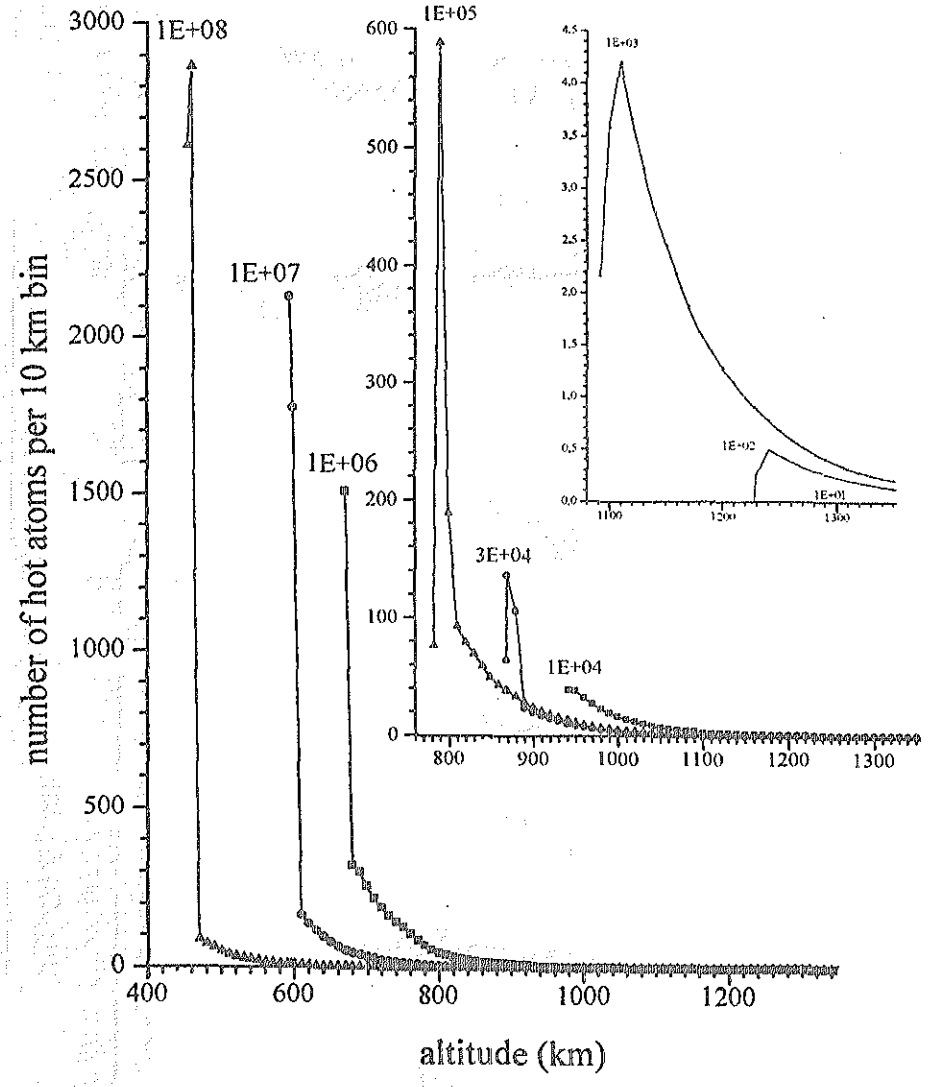

Fig 4.10 : Hot nitrogen profile by 1E+01 to 1E+08 eV C in 98% N_2 + 2% CH_4 atmosphere of Titan

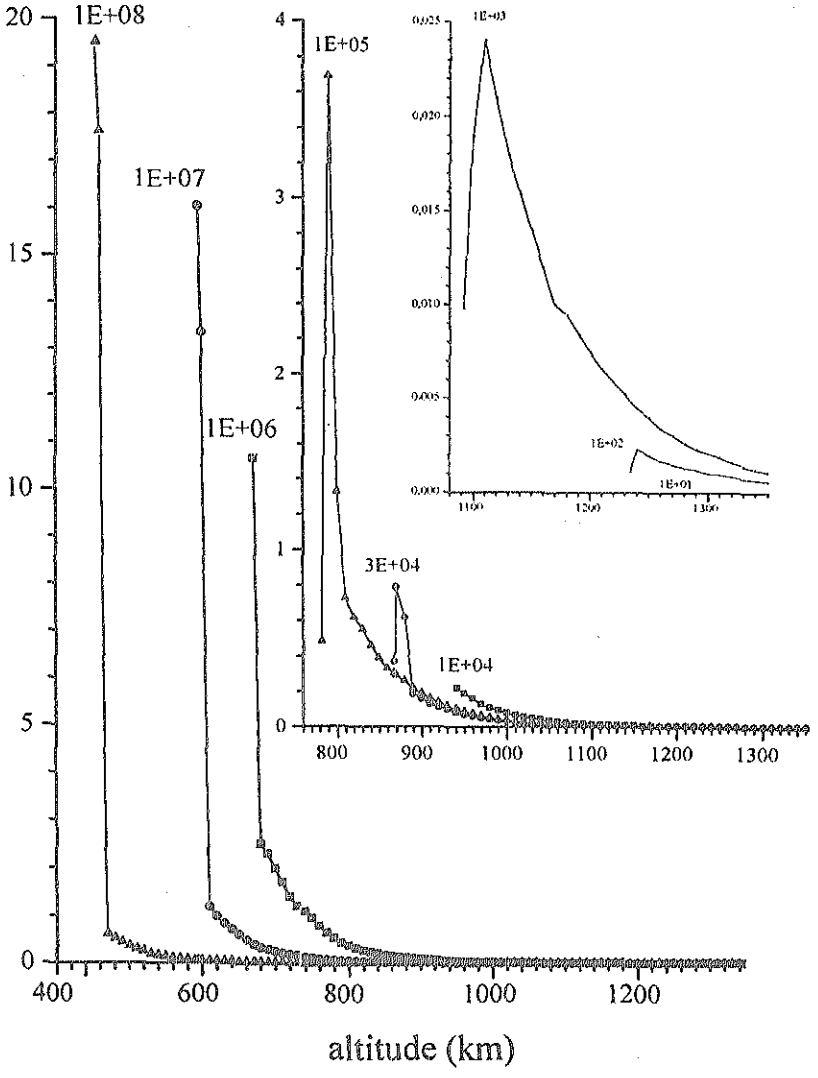

Fig 4.11 : Hot carbon profile by 1E+01 to1E+08 eV C in 98% N_2 + 2% CH_4 atmosphere of Titan

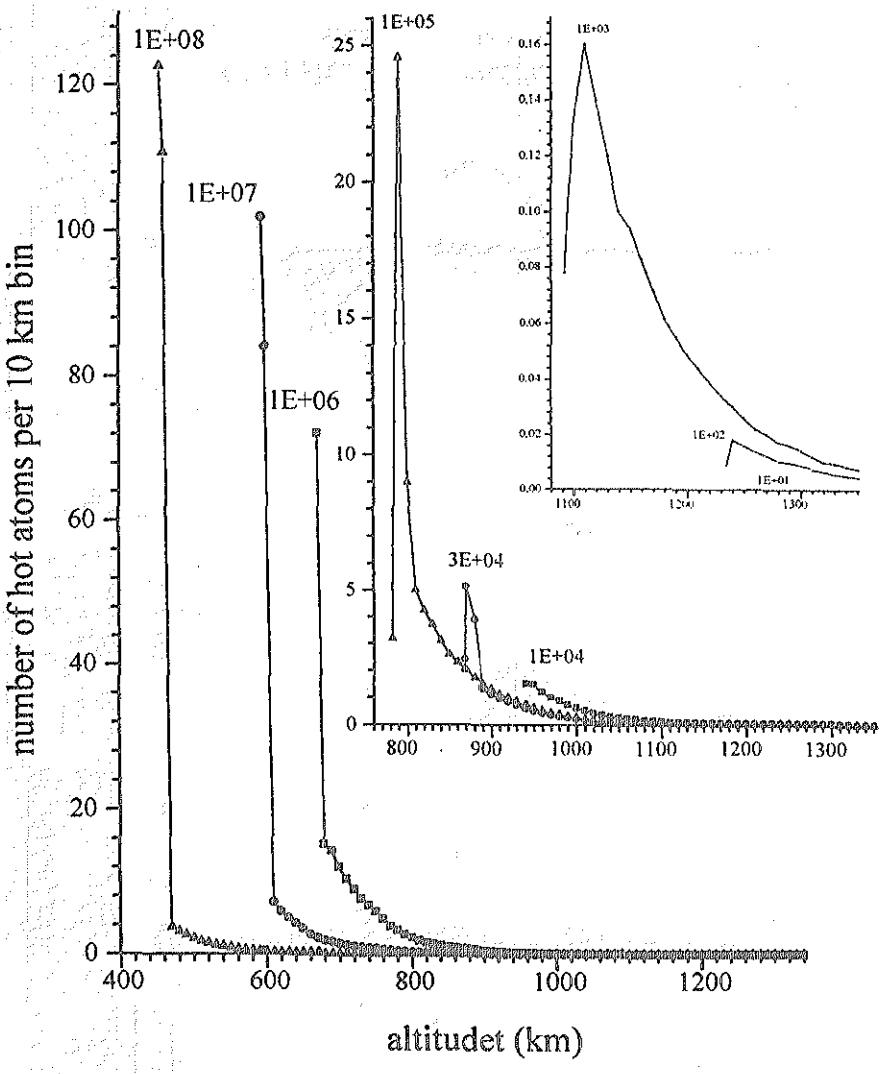

Fig 4.12 : Hot hydrogen profile by 1E+01 to 1E+08 eV C in 98% N_2 + 2% CH_4 atmosphere of Titan

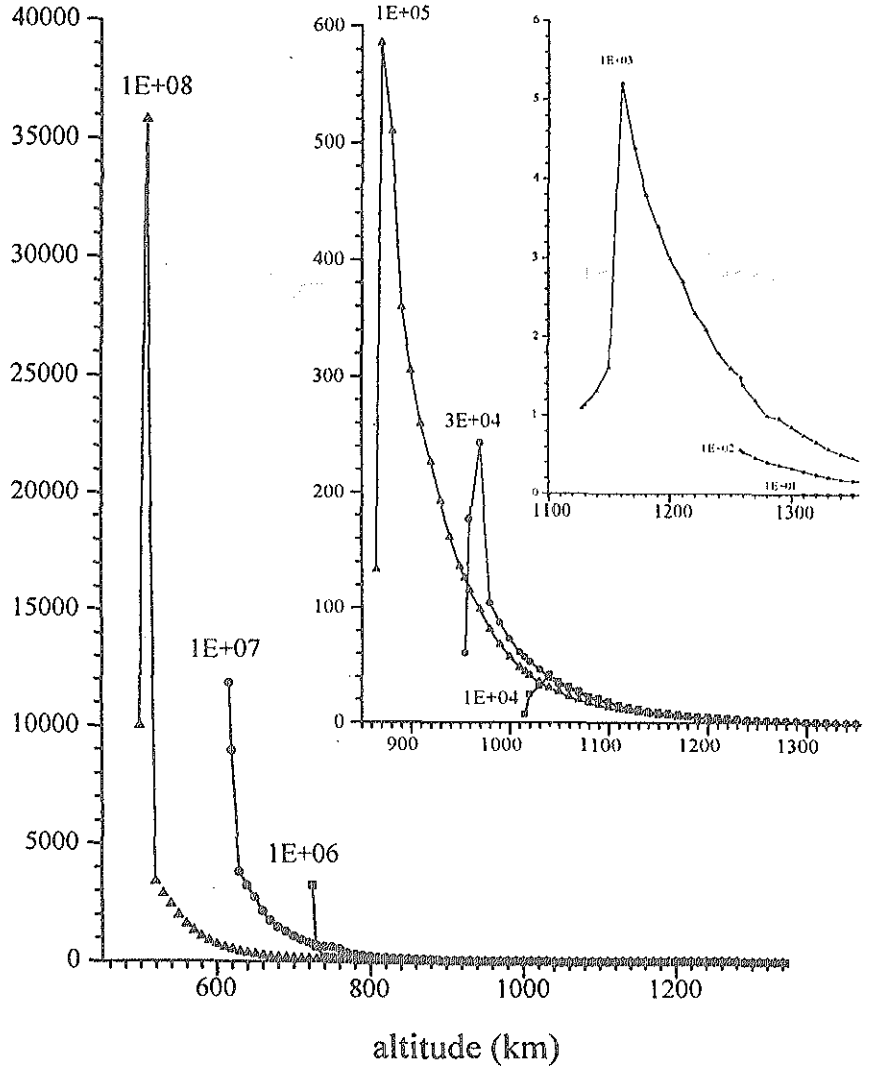

Fig 4.13 : Hot nitrogen profile by 1E+01 to 1E+08 eV Fe in 98% N_2 + 2% CH_4 atmosphere of Titan

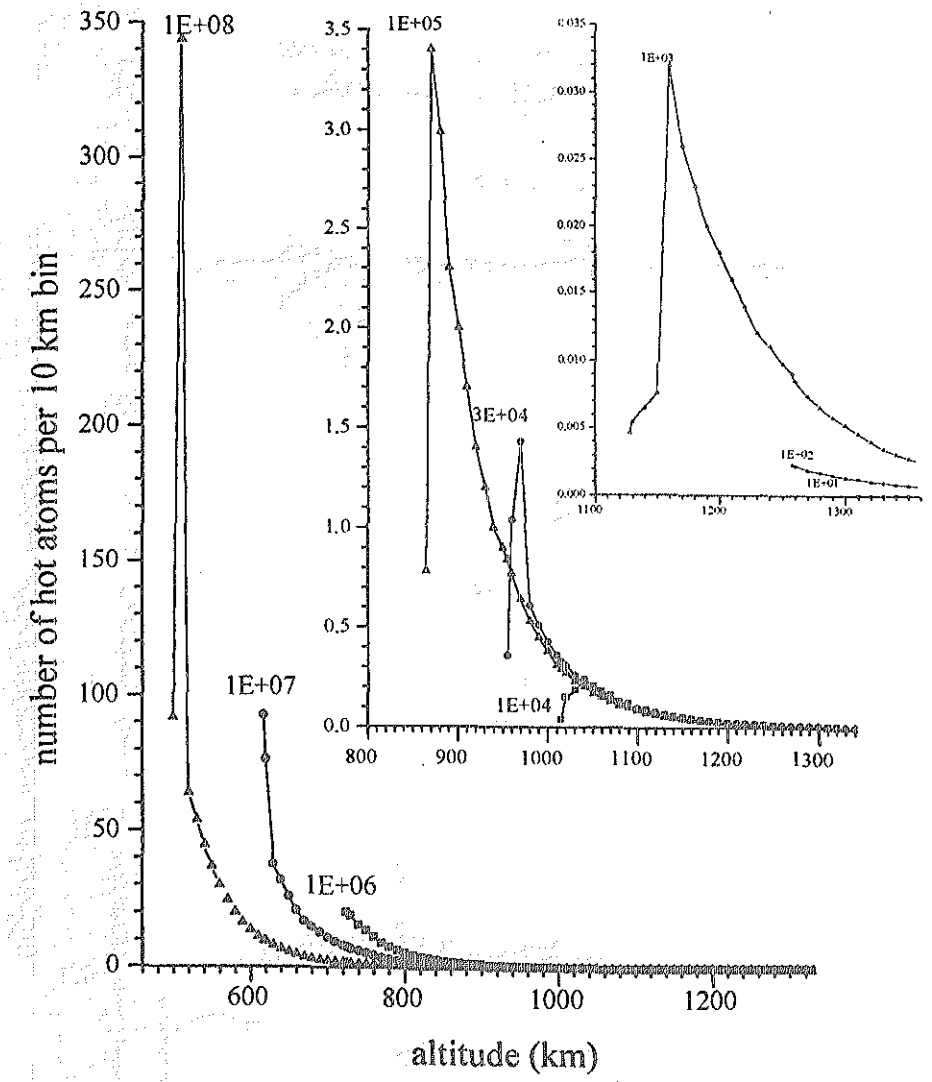

Fig 4.14 : Hot carbon profile by 1E+01 to1E+08 eV Fe in 98% N_2 + 2% CH_4 atmosphere of Titan

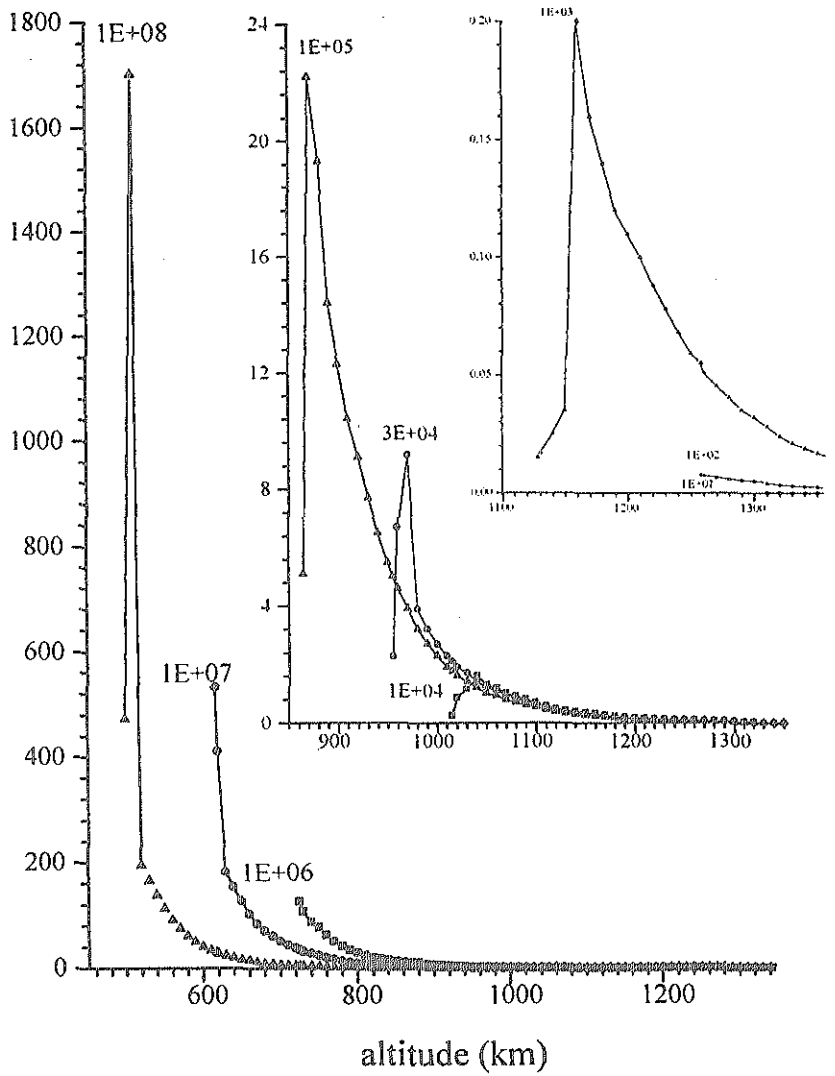

Fig 4.15 : Hot hydrogen profile by 1E+01 to 1E+08 eV Fe in 98% N_2 + 2% CH_4 atmosphere of Titan

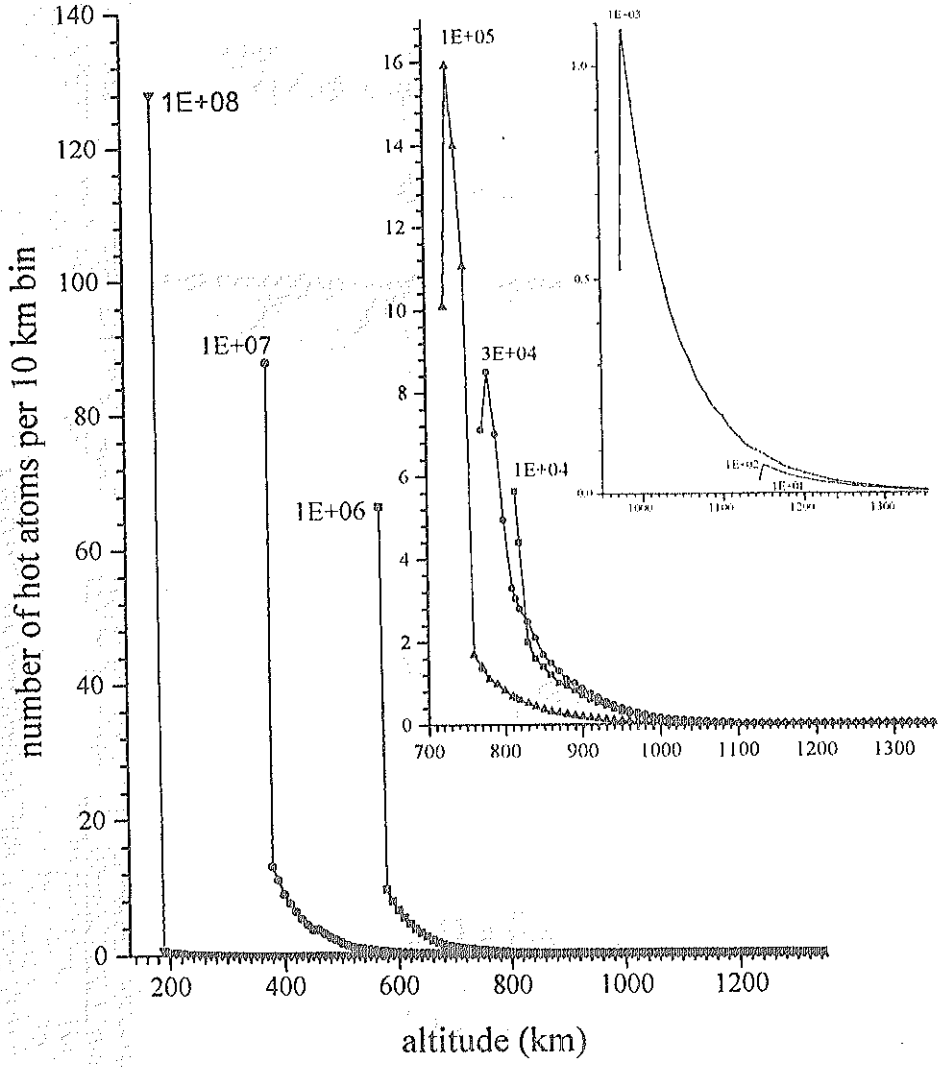

Fig 4.16 : Hot nitrogen profile by 1E+01 to 1E+08 eV H in 82% N_2 + 12% Ar + 6% CH_4 atmosphere of Titan

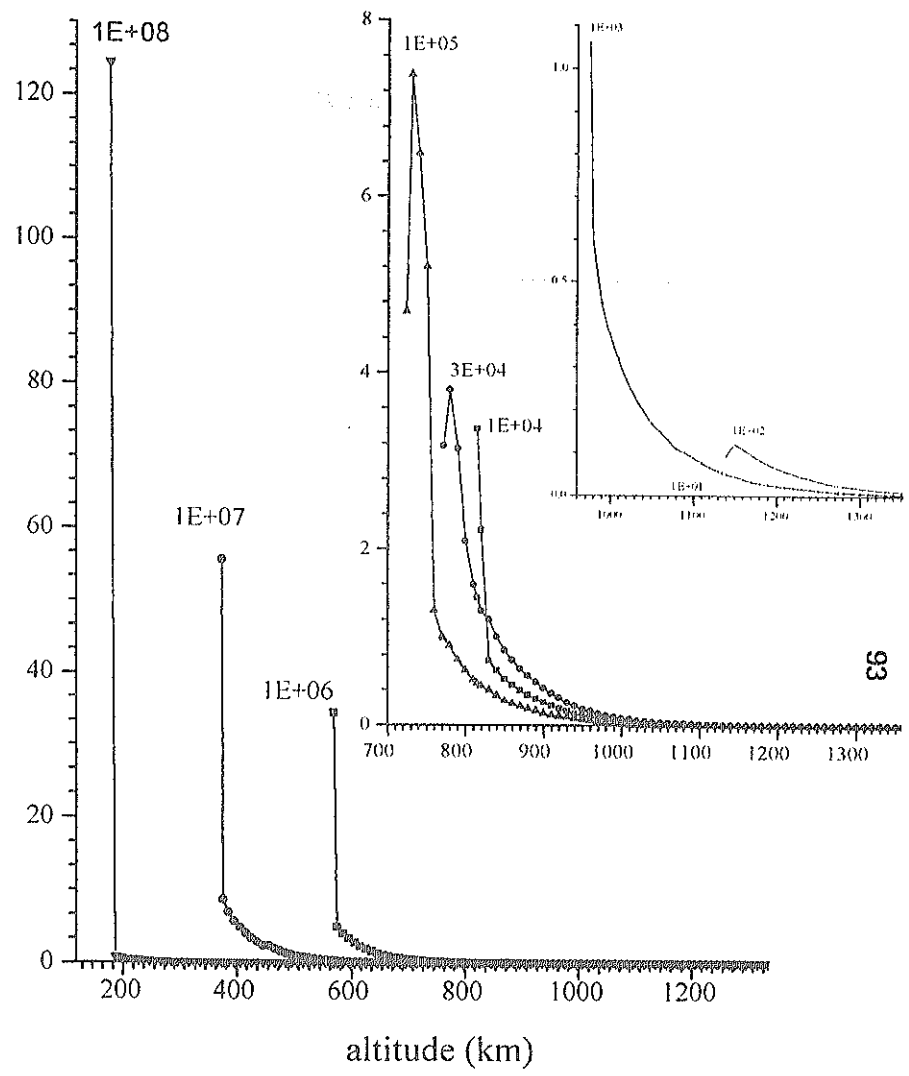

Fig 4.17 : Hot argon profile by 1E+01 to 1E+08 eV H in 82% N_2 + 12% Ar + 6% CH_4 atmosphere of Titan

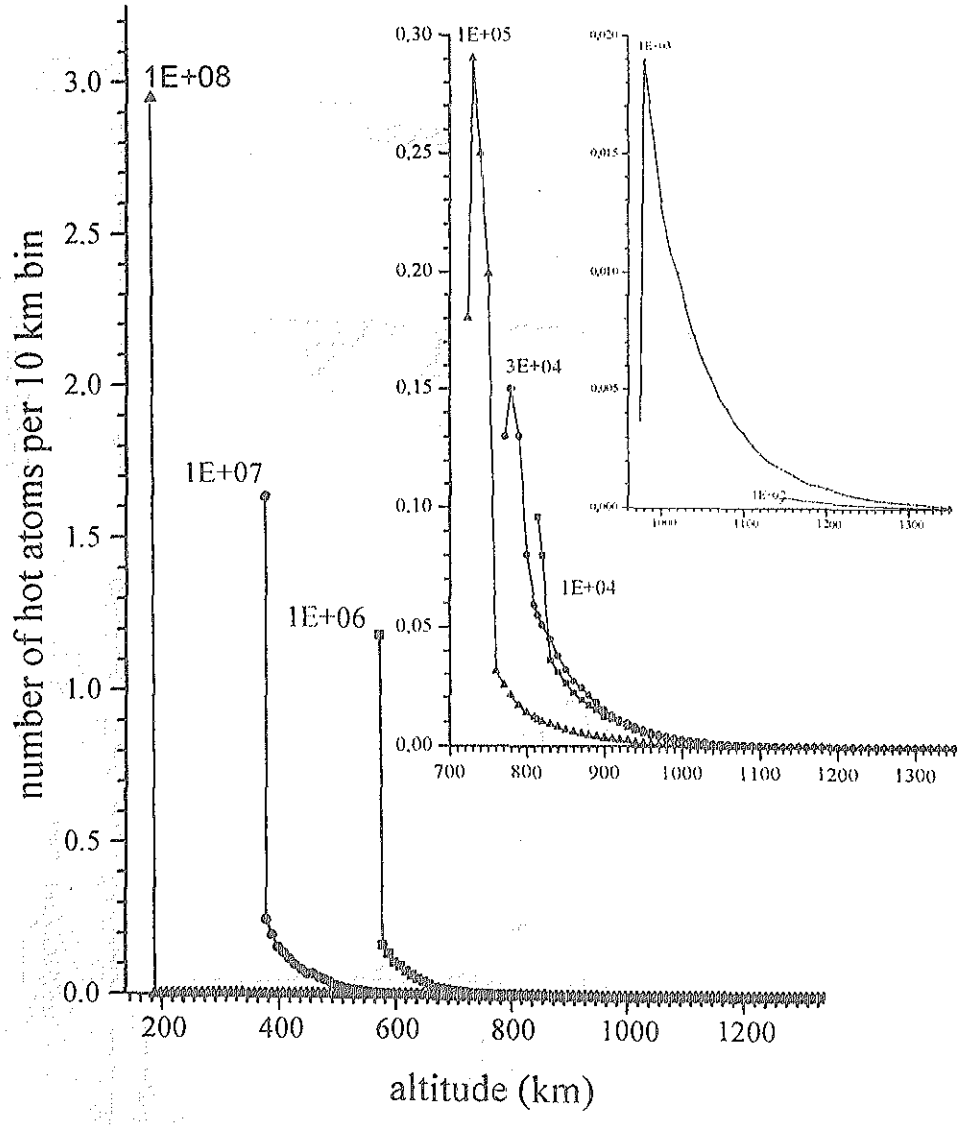

Fig 4.18 : Hot carbon profile by 1E+01 to 1E+08 eV H in 82% N_2 + 12% Ar + 6% CH_4 atmosphere of Titan

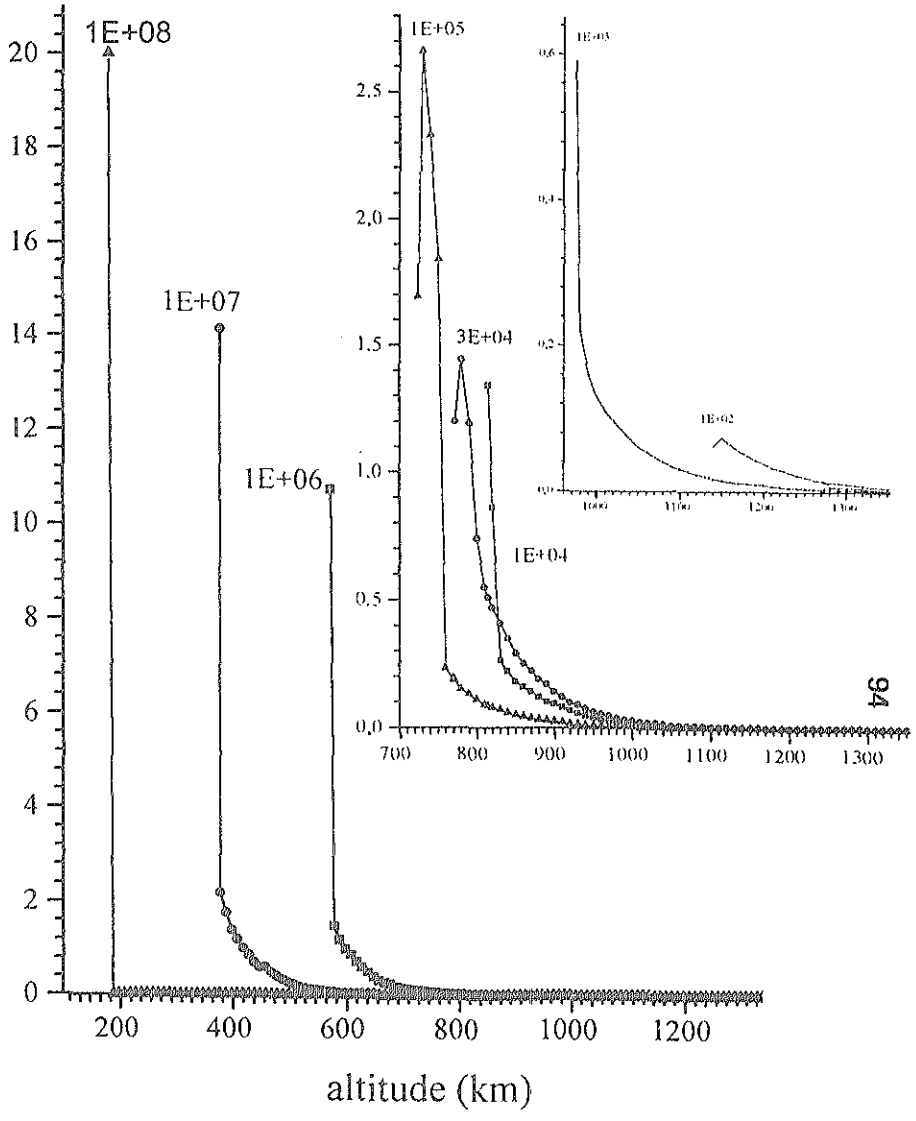

Fig. 4.19: Hot hydrogen profile by 1E+01 to 1E+07 eV H in 82% N_2 + 12% Ar + 6% CH_4 atmosphere of Titan

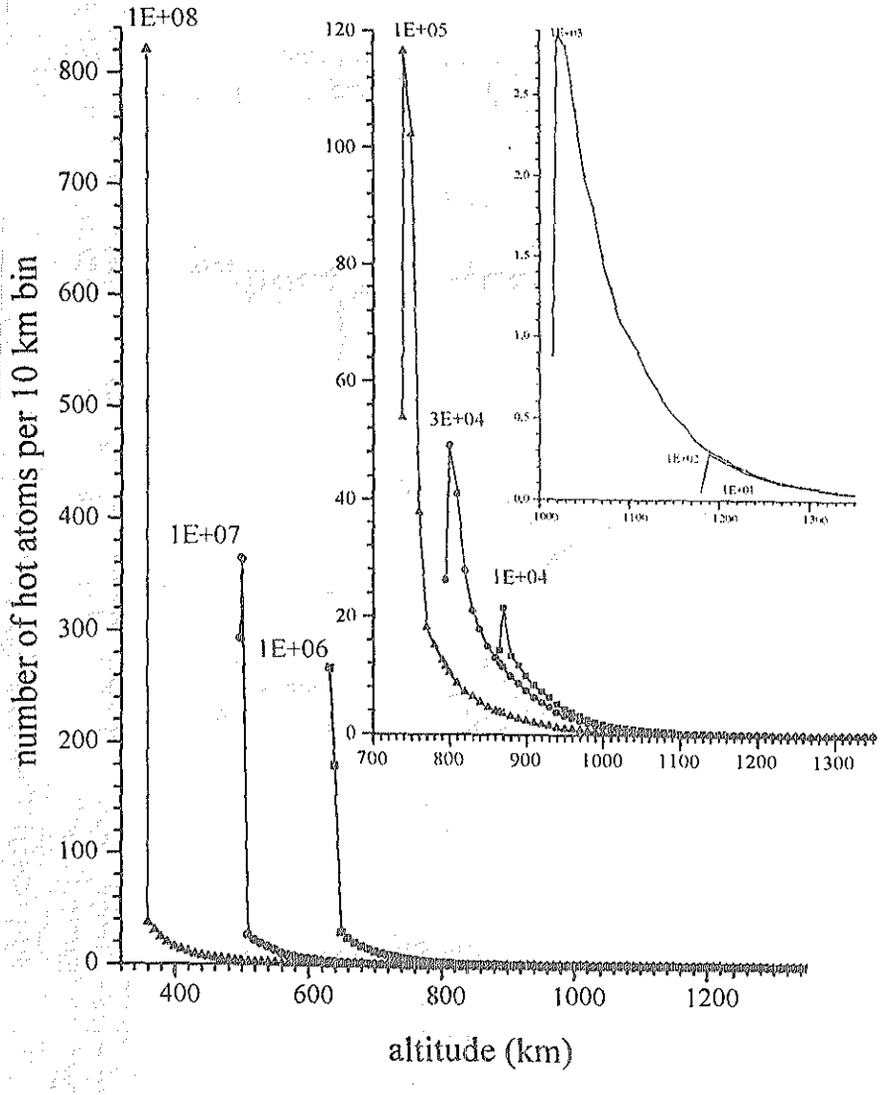

Fig 4.20 : Hot nitrogen profile by 1E+01 to 1E+08 eV He in 82%N_2 + 12% Ar + 6% CH_4 atmosphere of Titan

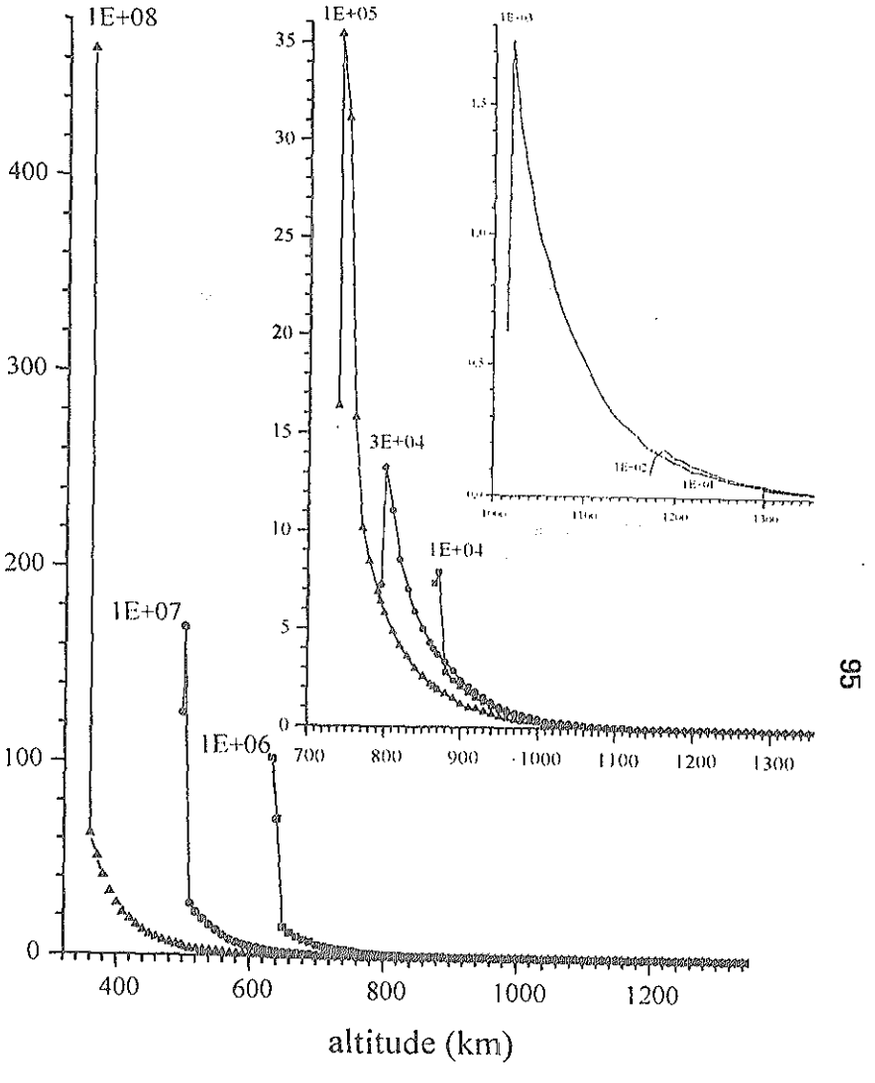

Fig 4.21 : Hot argon profile by 1E+01 to1E+08 eV He in 82%N_2 + 12%Ar + 6% CH_4 atmosphere of Titan

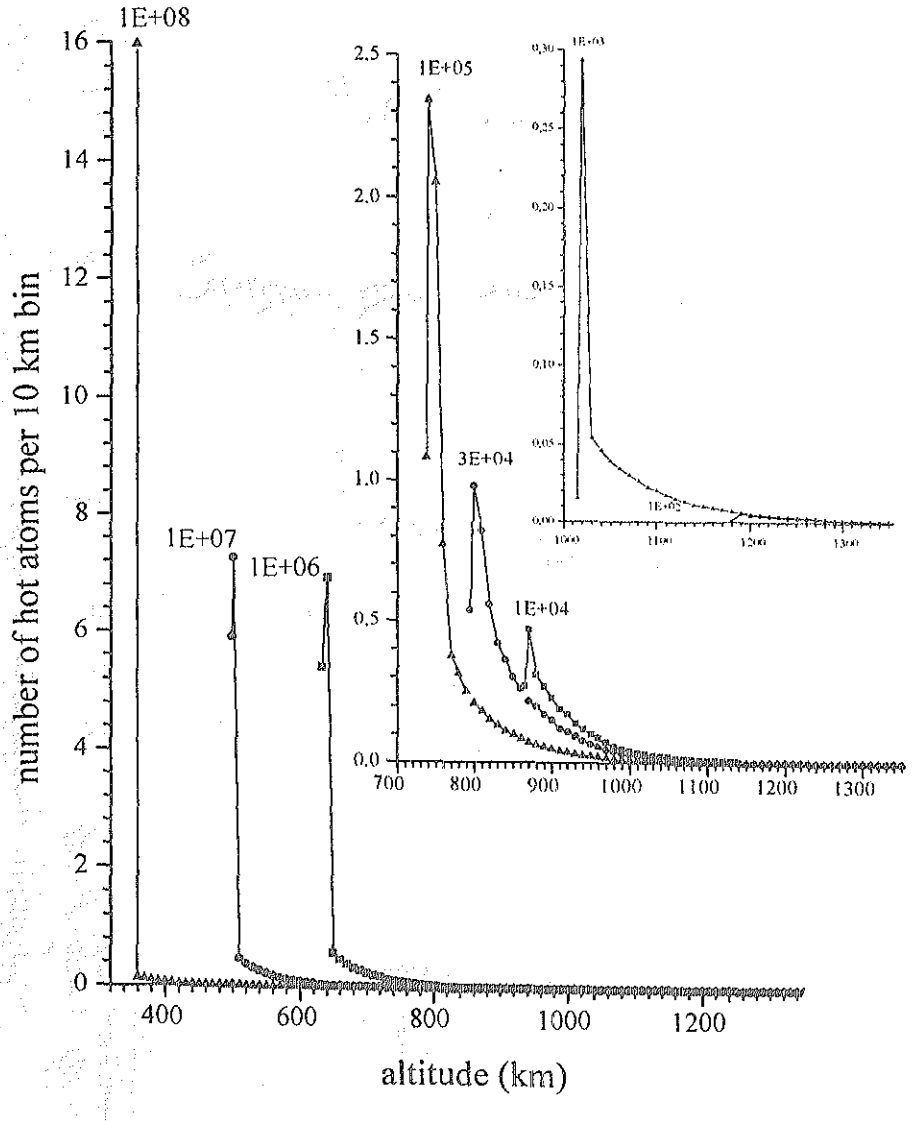

Fig 4.22 : Hot carbon profile by 1E+01 to1E+08 eV He in 82% N_2 + 12% Ar + 6% CH_4 atmosphere of Titan

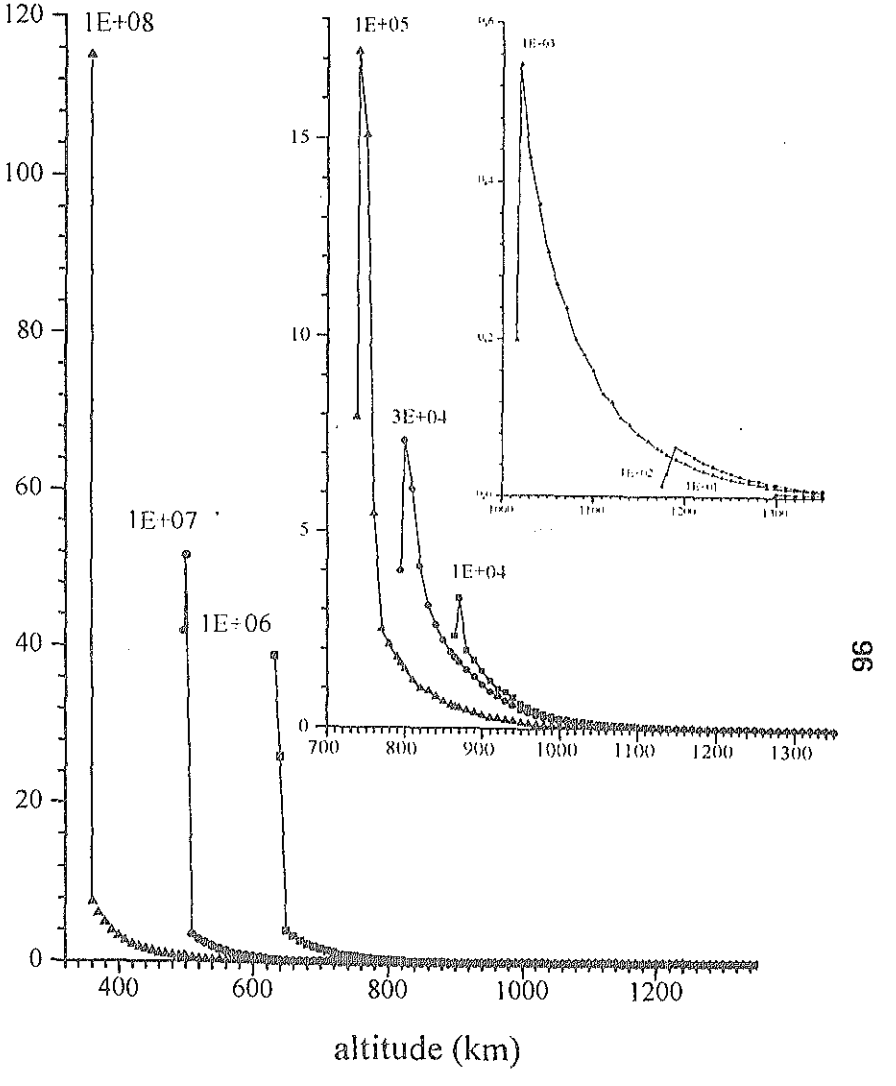

Fig 4.23 : Hot hydrogen profile by 1E+01 to 1E+08 eV He in 82% N_2 + 12% Ar + 6% CH_4 atmosphere of Titan

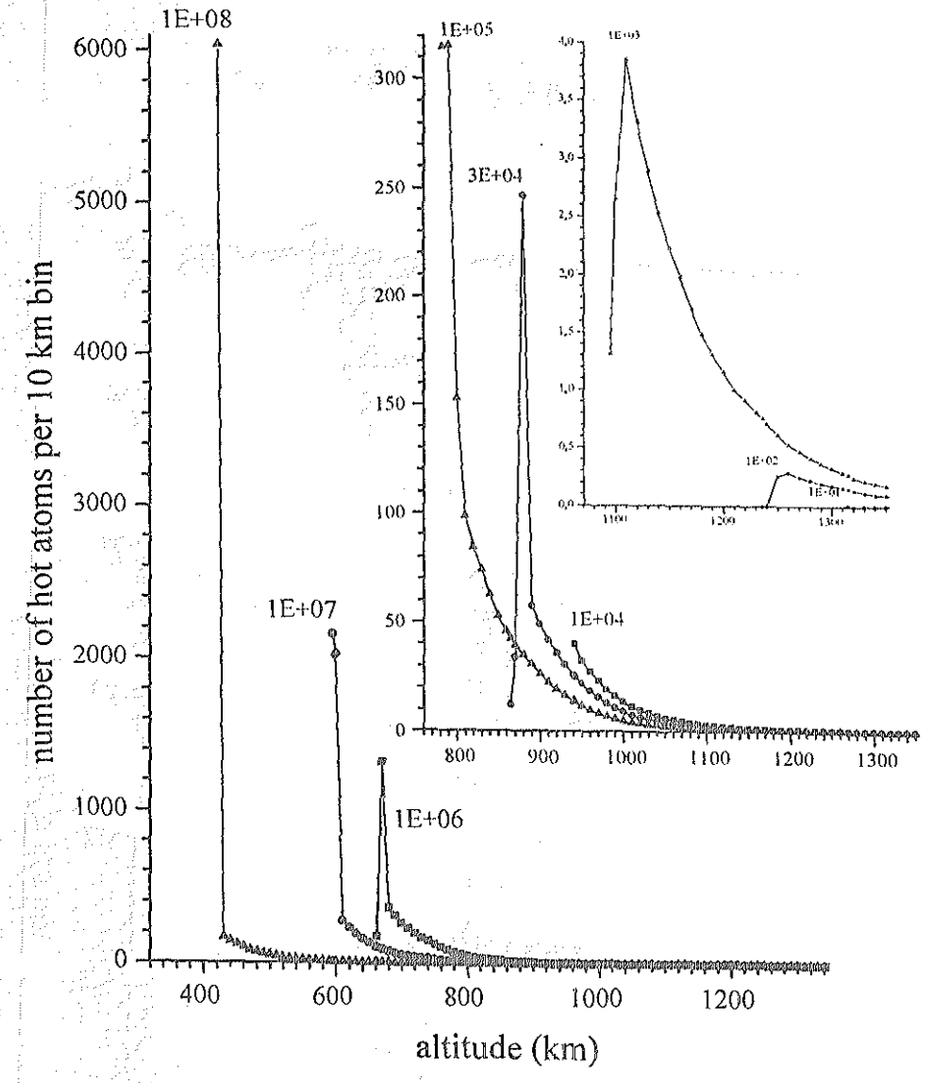

Fig 2.24 : Hot nitrogen profile by 1E+01 to 1E+08 eV C in 82% N_2 + 12% Ar+ 6% CH_4 atmosphere of Titan

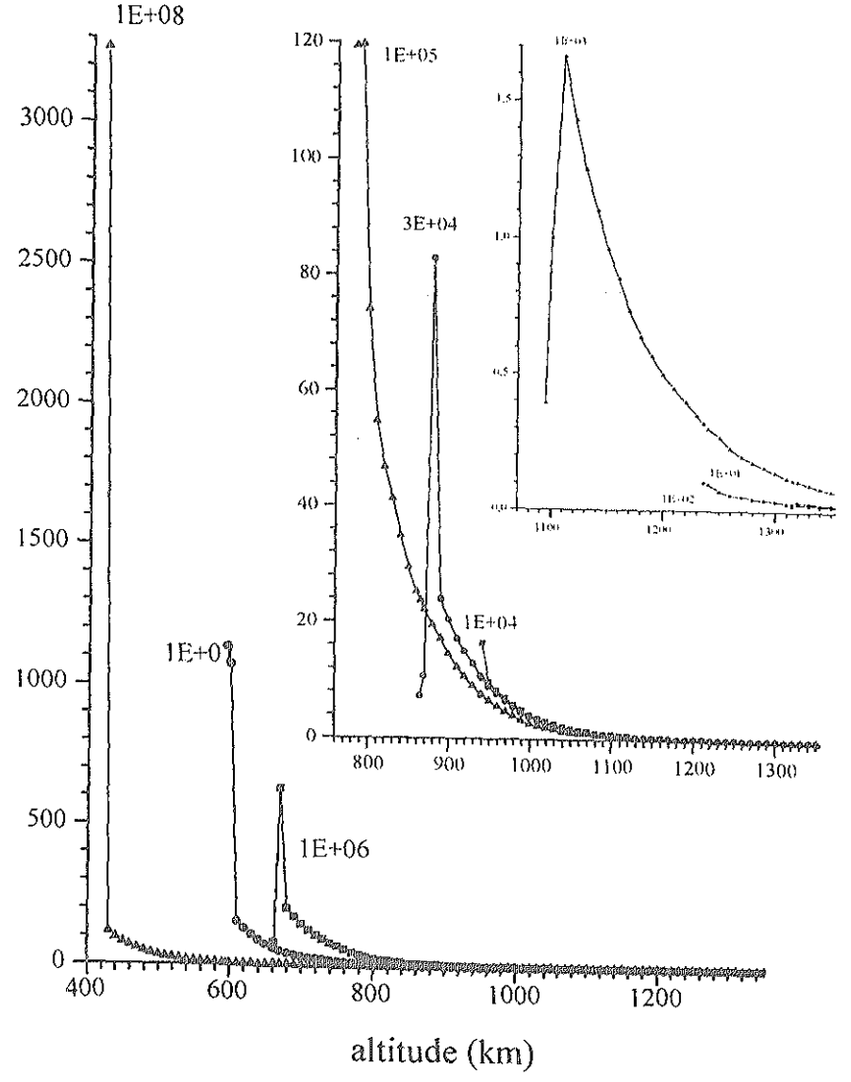

Fig 4.25 : Hot argon profile by 1E+01 to 1E+08 eV C in 82% N_2 + 12% Ar + 6% CH_4 atmosphere of Titan

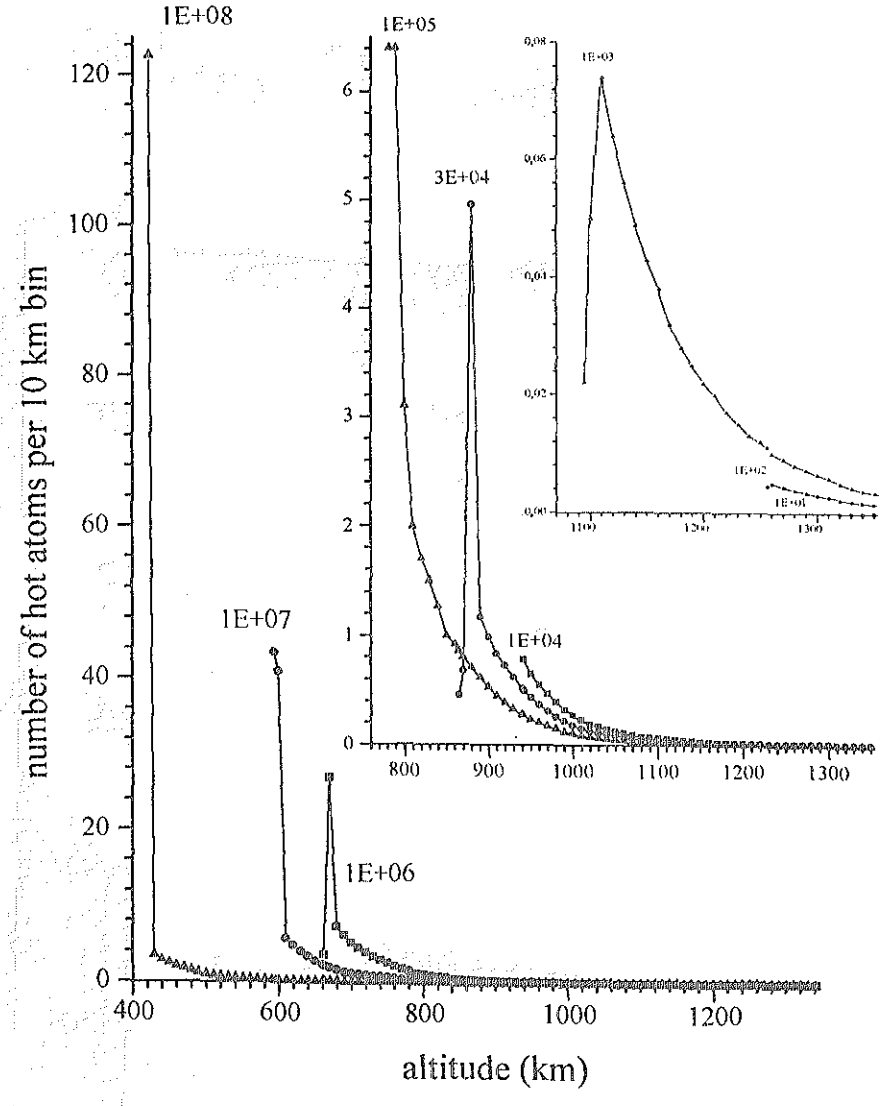

Fig 4.26 : Hot carbon profile by 1E+01 to 1E+08 eV C in 98% N_2 + 12% Ar + 6% CH_4 atmosphere of Titan

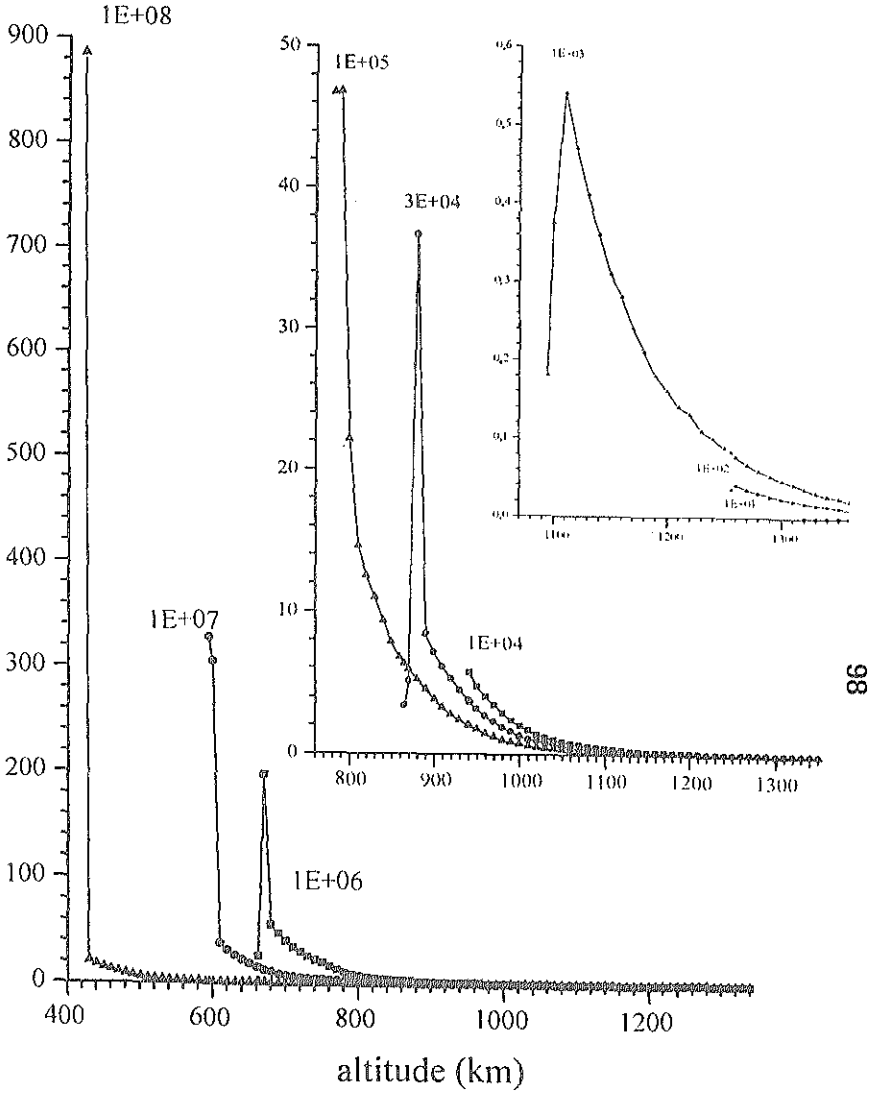

Fig 4.27 : Hot hydrogen profile by 1E+01 to 1E+08 eV C in 82% N_2 + 12% Ar + 6% CH_4 atmosphere of Titan

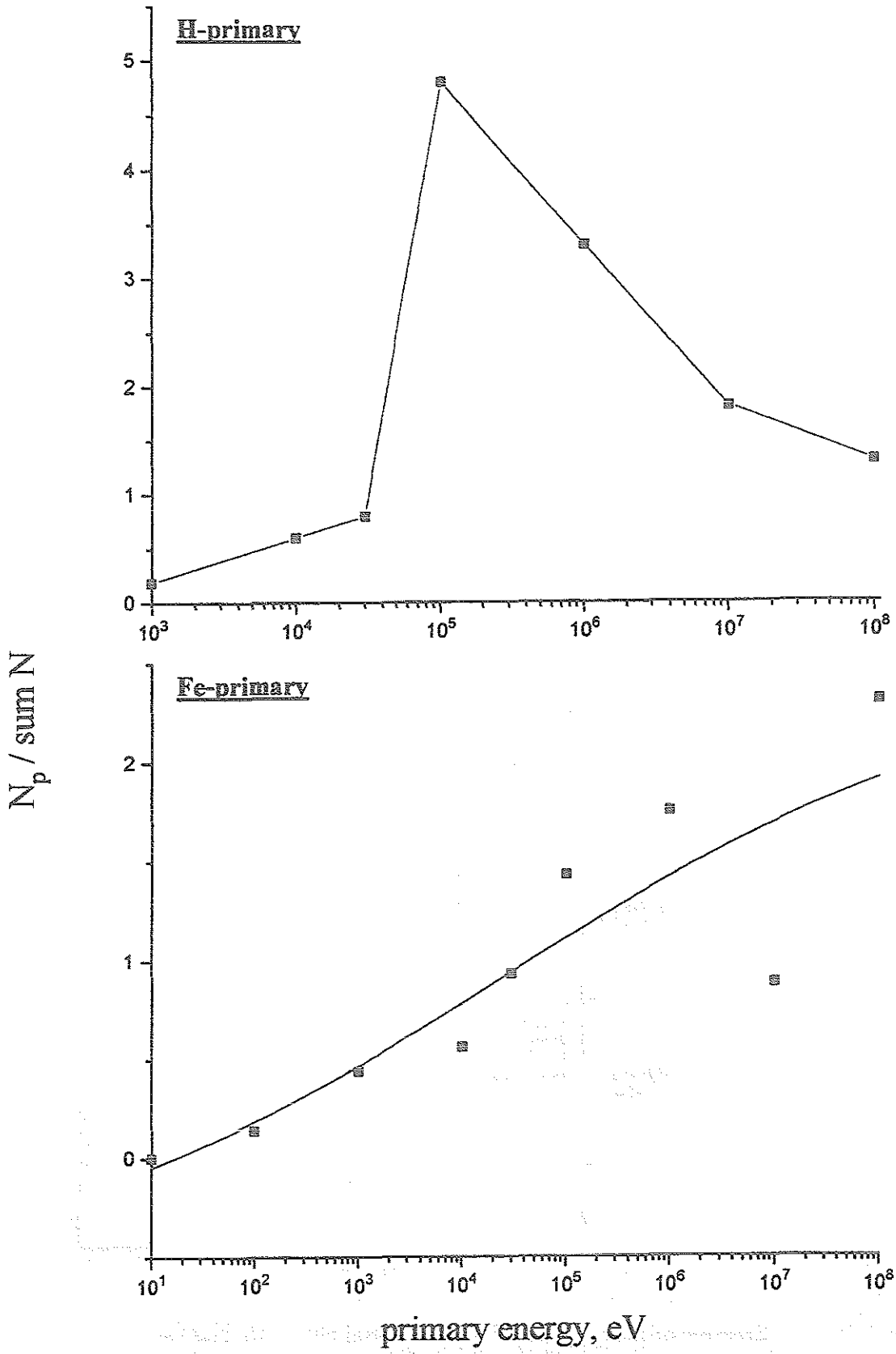

Fig. 4.28: Comparison of steepness of hot atom profiles for H and Fe primaries in 98% N_2 + 2% CH_4 atmosphere in terms of number of hot atom in peak value up to total number sum N.

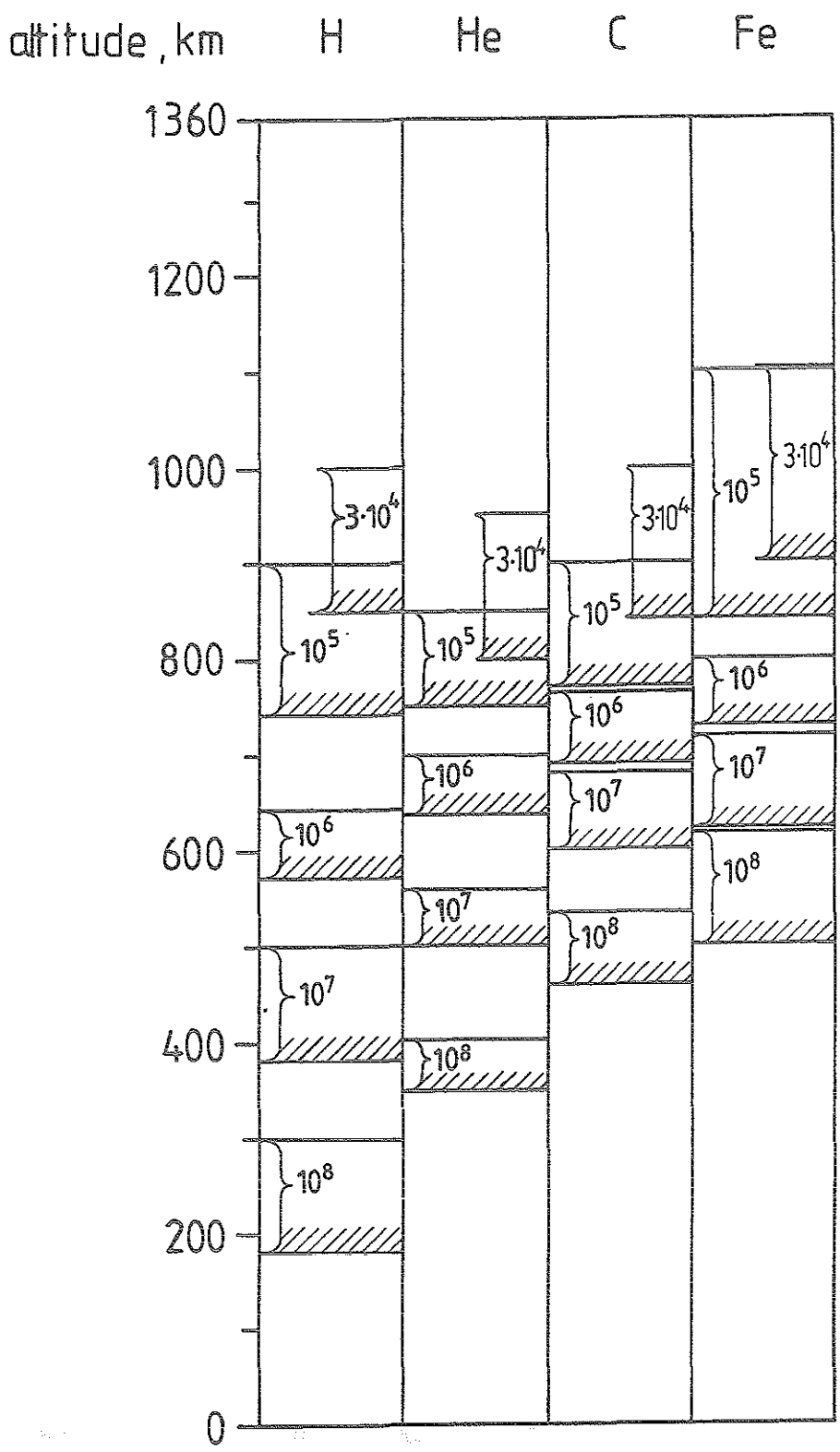

Fig 4.29 : Profiles of production of suprathermal atoms in Titan's atmosphere as depending on primary energy of H, He, C, and Fe particles.

more broadly and the chance of interactions of hot projectiles with hot products decreases. To close this chapter, Fig. 4.29 exhibits an overview on the distribution of suprathermal atoms within Titan's atmosphere as produced by H, He, C, and Fe primaries of different energies.

4.3 Effect of nonperpendicular infall

Since only a part of the rays show perpendicular infall characteristics, the hot atom profiles where checked for non perpendicular infall. Fig. 4.29 shows the nitrogen profile for H primaries in target II atmosphere for perpendicular and 45° infall. It can be seen that the profiles are quite similar and that the 45° infall penetrates approx. 30 to 40 km less.

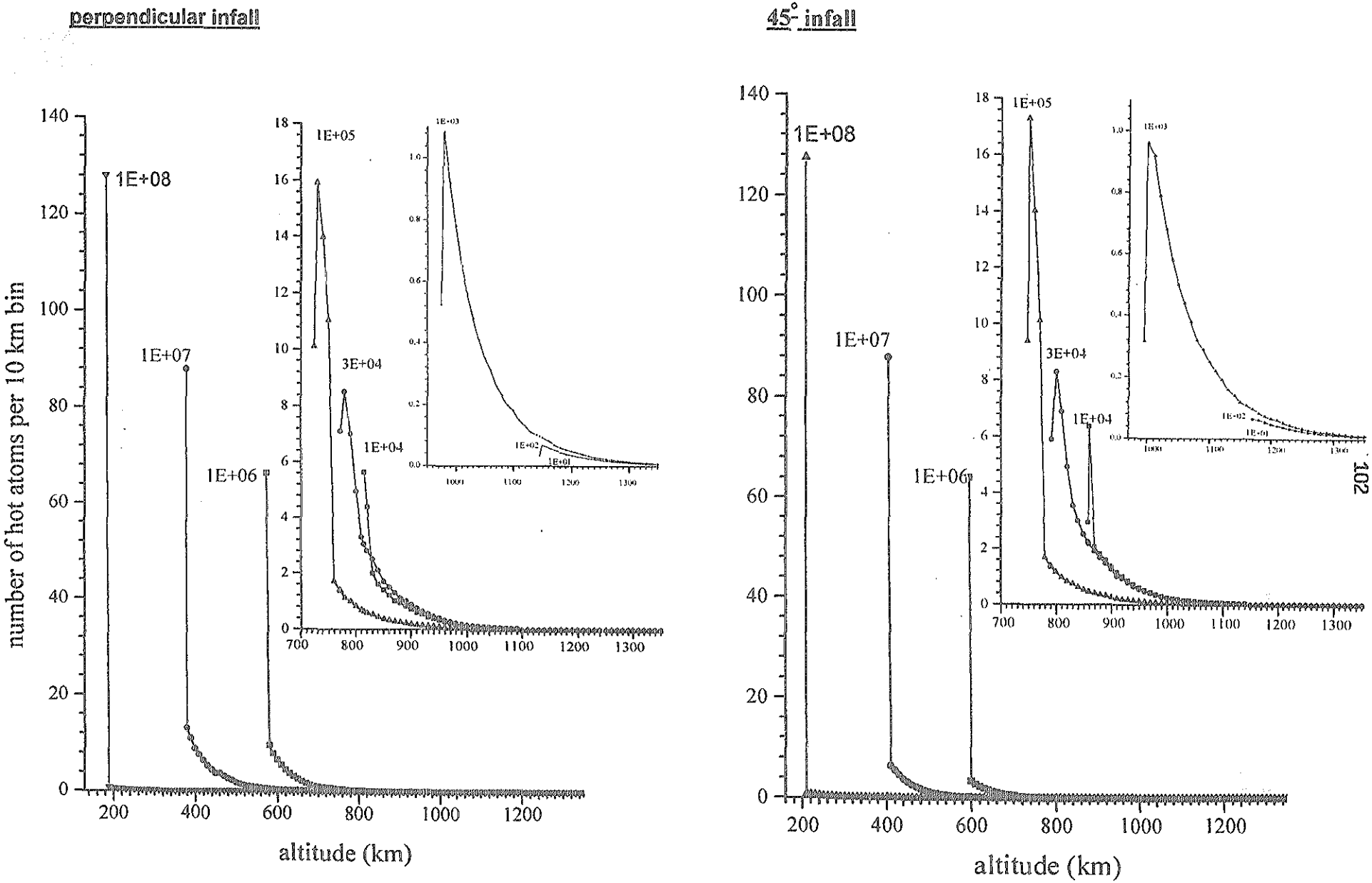

Fig. 4.30 : Comparison of hot nitrogen profiles for perpendicular (left part) and 45° infall (right part) of H into 82% N_2 + 12% Ar + 6% CH_4 atmosphere (target II).

4.4 Column densities of suprathermal atoms by particle component of space radiation

For one gas mixture : 98% N_2 + 2% CH_4 the effect of infall of space particle radiation is calculated. The flux data for particles between H and Fe are for the solar system position of Titan in Table 4.3. Li to B are treated as a group, likewise the elements from N to Mn. The data for the fluxes were evaluated in a very general way, since only few exact data exist for the high energy components and for the low energy part it is not clear at the moment which energy passes the magnetosphere and the inner boundary layers. Also the production rate of neutrals formed, e.g. by neutralization processes, and which would penetrate without rejection, is not known. In this situation it seemed better to make a first approach (and only for target I) with the set of data given here which includes energies down to 10^3 eV.
It was derived from the proton flux in space as a function of energy given by the dashed curve in Fig. 1.9 and from the famous curve of dependence of cosmic ray fluxes for H, He, C+O, and Fe nuclei on energy in Fig. 1.7 . It has to be noted, that most of the data in Fig 1.9 are minimum values and in Fig. 1.7 the values for solar minimum were taken. Since the flux of space particles in Table 4.3 is given in cm^{-2} s^{-1}, one can follow the column density formalism already applied in the previous chapters 4.1-3. These data were now multiplied with the total number of hot atoms from Table 3.5 (obtained by summation of N+C+H, but mostly N atoms). For Li-B and N-Mn average values between He and C, as well as between C and Fe were taken. From this results Table 4.4 which lists the column densities of all suprathermal (hot) atoms formed per cm^{-2}. The lowest row gives the sum for one energy over all elements, the column on the outer right side reports the sum for one kind of particle. Altogether about 10^9 hot atoms are formed within one cm^2 column in a 1 sec irradiation. These numbers can easily be modified by omitting energies which do not lead to penetration or by adding other (higher) flux values including ions from Titan's plasma, interaction with ISM, etc. Also the effects of particles from C to Fe and heavier ones at energies > 10^8 eV (for C up to 10^9 eV, for Fe even up to 10^{10} eV and beyond) have to be included. However, the increase of the sum of all contribution will only be by approx. 10% higher than the value of 10^9 cm^{-2} given above. Taking this into account, a column density $\bar{n} \approx 1\text{-}1.5 \cdot 10^9$ cm^{-2} may be reasonable even under relatively conservative assumptions. Fig. 4.31 displays the geometrical conditions of Titan's atmosphere relative to the nucleus. It can be seen that the columns at lower altitudes will overlap to a certain degree. Thus, column densities in the lower part (which is that for the 10^6 - 10^8 eV primary energies) may rise up to $2 \cdot 10^9$ cm^{-2} in 1 s irradiation. Even this number seems small compared to the total column density of the gas phase of about $2.1 \cdot 10^{26}$ cm^{-2}. However, most of the particles are stopped at altitudes with lower local column densities, cf. Fig. 4.2. When looking for local effects at defined altitudes the ratio can be more in favor of the hot atom component.

Table 4.3 : Space flux at Titan, particles cm^{-2} s^{-1} (minimum values).

primary energy, eV	10^8	10^7	10^6	10^5	10^4	10^3
H	1	5×10^{-1}	1.7×10	3.3×10^3	3.3×10^6	6.6×10^7
He	5×10^{-2}	2.5×10^{-2}	8.5×10^{-1}	1.7×10^2	2.5×10^3	3.3×10^6
Li-B	7×10^{-5}	3.5×10^{-5}	1.2×10^{-3}	2.3×10^{-1}	2.3×10^2	4.6×10^3
C	3×10^{-4}	1.5×10^{-4}	5.1×10^{-3}	9.9×10^{-1}	9.9×10^2	2×10^4
N-Mn	7×10^{-4}	3.5×10^{-4}	1.2×10^{-2}	2.3	2.3×10^3	4.6×10^4
Fe	2.3×10^{-5}	1.1×10^{-5}	3.8×10^{-4}	7.4×10^{-2}	7.4×10^2	1.5×10^3

Table 4.4 : Column densities $\bar{n}$ cm^{-2} of hot atoms in 98% N_2 + 2% CH_4 Titan's atmosphere per 1s irradiation.

primary energy, eV	10^8	10^7	10^6	10^5	10^4	10^3	$\sum_{E=10^3}^{E=10^8}$
H	3.1×10^2	8.6×10	1.7×10^3	2.4×10^5	9.6×10^7	6.8×10^8	7.8×10^8
He	6.1×10	2.2×10	6×10^2	7.9×10^4	3.9×10^5	1×10^8	1×10^8
Li-B	2.4×10^{-1}	1.1×10^{-1}	2.9	2.4×10^2	2×10^5	1.7×10^5	3.7×10^5
C	1.7	7.8×10^{-1}	2.1×10	4×10^3	3.1×10^5	8.1×10^5	1.1×10^6
N-Mn	2.6×10	9.1	1.4×10^2	6.2×10^3	8.2×10^5	2.0×10^6	2.8×10^6
Fe	1.6	5.2×10^{-1}	7.2	2.8×10^2	3×10^5	7×10^4	3.7×10^5
$\sum_{z=1}^{z=26}$	3.9×10^2	1.2×10^2	2.5×10^3	3.3×10^5	9.8×10^7	7.8×10^8	8.9×10^8

The values above are given for 1 s. When calculating for the duration of the solar system, e.g. to evaluate the problem of changing of a primordially NH_3 + CO atmosphere to the present N_2 + CH_4 atmosphere, the factor of $1.45 \cdot 10^{17}$ s ($4.6 \cdot 10^9$ a) comes into play. The total number of hot atoms formed in the lifetime of the solar system would then be about $2 \cdot 10^{26}$ cm^{-2}, i.e. sufficient to change everything by hot atom reaction. Including the hot atoms formed by photo-dissociation and dissociation induced by electronical excitation by some effective inelastic collisions (cf. chapter 3.6), it can be stated that suprathermal chemistry is a very important factor in Titan's atmosphere for local and global processes.

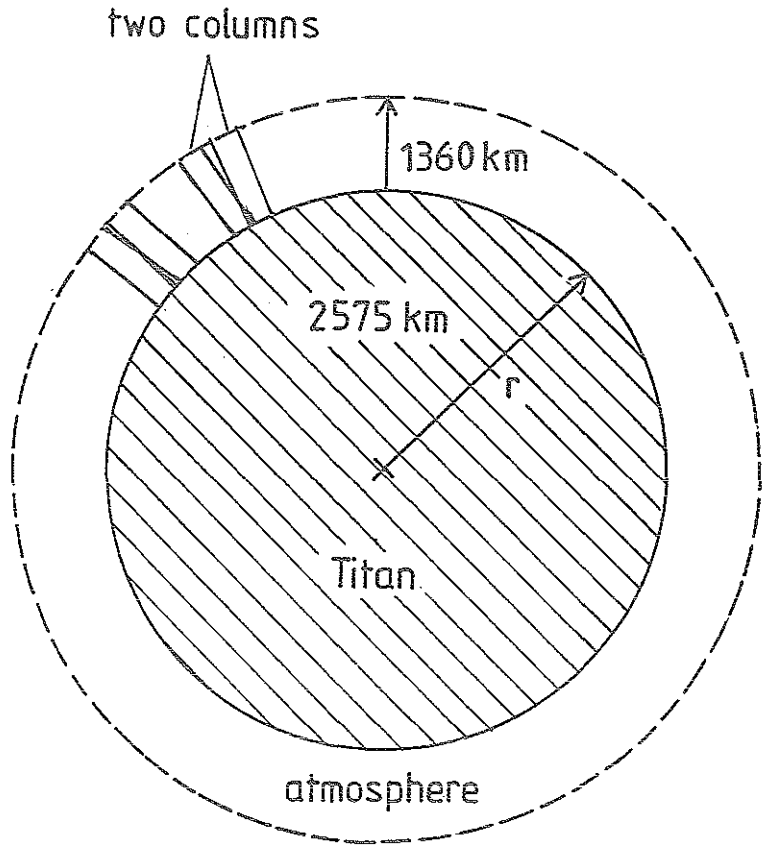

Fig. 4.31 Schematical representation of Titan's atmosphere with overlap of columns.

CHAPTER 5

EXPERIMENT WITH 32 MeV $^3He^{2+}$ IONS IN GAS TARGET

In this work the chemical effects of 32 MeV $^3He^{2+}$ ions as a representative for cosmic rays, have been studied in pure CH_4 and two CH_4+N_2 mixtures at a pressure of 1.6 bar in a gas target to simulate the conditions in Titan's atmosphere at different doses $2 \cdot 10^{-3} \leq D^* \leq 1.7 \cdot 10^{-1}$ eV per target molecule. Irradiation was carried out in the CV 28 compact cyclotron of the Institute of Solid State Research (IFF) of Forschungszentrum Jülich.

5.1 Experimental set-up

5.1.1 Target

For the construction of the gas target it was an important demand that quick mounting and demounting was possible at the cyclotron. A second demand was to minimize the activation of the walls by the particle flux. Also there should be an easy connection to gas mixing chamber for the filling and to the gaschromatograph for analysis. In order to meat these conditions, a 2 mm thick steel tube with 25 mm inner radius and 100 mm length was selected. It was closed with a 25 µm Ti-foil in front of the beam and a 50 µm Ti-foil at the other side tightened by flanges and rubber O-rings, cf. Fig. 5.1. The principles can be found in [1.67, 5.1, 2].

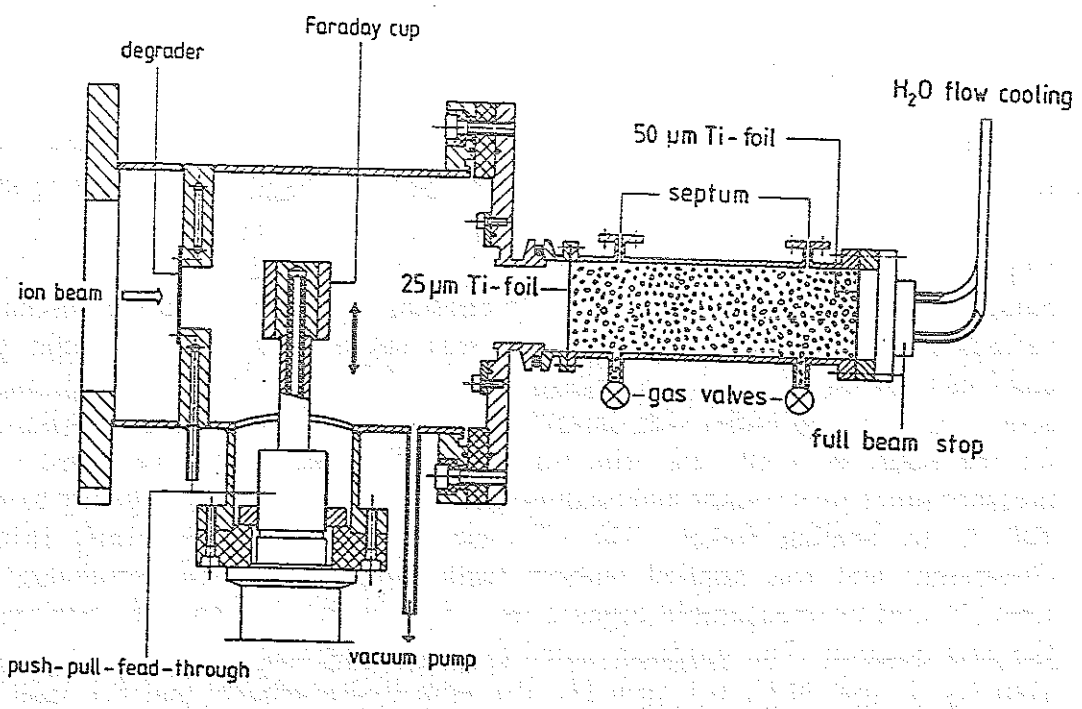

Fig. 5.1 : Scheme of gas target

Two septums allowed the takeout of gas samples by a syringe to feed it into the gaschromatograph. Two valves (Nupro) were used for connection to the gas mixing chamber for flushing and filling. At the end the target carried a full beam stop out of a 1 cm Al layers mounted by a flange and O-ring. It was cooled by a water loop. The target was mounted on to a vacuum chamber with an electrically isolated Faraday cup on a push-pull fead through for current measurement. This chamber was closed against the vacuum of the cyclotron with a 100 μm Al degrader.

The ion beam from the cyclotron was shaped circulary by four water cooled segments with a diameter of 10 mm before reaching the degrader. By passing the degrader and the front Ti-foil its diameter widened to 14 mm diameter. This could be checked by the coloration of filter paper brought into the beam at the exact geometry in front and behind the target. The inner diameter of 25 mm ensured that the walls of the target cylinder were not hit directly. The beam passed only through the Ti-foils. This is a condition necessary to calculate the dose delivered to the gas phase.

The target diameter prevents also that the 4.6 MeV ^{11}C recoils generated by the ^{12}C (^{3}He,^{4}He) ^{11}C nuclear reaction with CH_4 could reach the walls by direct flight. TRIM calculations for the C recoils in 1.6 bar CH_4 yielded a penetration of 4 to 5 mm. The distance between the 14 mm diameter of the zone of production and the walls is with 5.5 mm larger than the range. Similar holds for the CH_4-N_2 mixtures at 1.6 bar.

The target was mounted on to the vacuum chamber with the Faraday cup by metal flanges. This last part of the chamber was mounted via an Teflon insulator. Thus, a measurement of the whole current hitting the foils, the gas and the beam stop was possible.

5.1.2 Gas mixing chamber

Gases are often difficult to mix in larger volumes. In order to obtain a fast and complete mixing of CH_4 and N_2 a gas mixing chamber was used [1.67]. It consists of a cylindrical stainless steel chamber with 29 cm diameter and 30.5 cm height and 15 liters volume. It contains many vacuum connections for gas in- and outlet cf. Fig. 5.2. The big volume was chosen, to use an actual gas mixture for various fillings of target. The vacuum was made by a turbomolecular pump connected to an oil-rotator prepump and reached 10^{-4} Pa. The exact pressure setting of inlet and outlet was controlled by a mbar-meter instrument (Baratron) for the range of $1\text{-}10^{-4}$ Pa. The mixing of the gases was accelerated at this pressure range by a rotator and heating the outside of the chamber gently to above 100 °C by heating jackets. The CH_4 gas was of 99.9995% purity (Messer-Griesheim) and was applied without further purification. Gaschromatographic tests showed no measurable organic impurities within the applied sensitivity of the FID detector. The producer listed the following impurities : 0.5 vpm O_2, 2 vpm N_2, 2 vpm H_2O, 0.1 vpm H_2, 0.1 vpm hydrocarbons, and 0.1 vpm CO_2. Nitrogen gas was of 99.9996% purity (Messer-Griesheim) containing 0.5 vpm O_2,

1 vpm H_2O, 0.1 vpm CO, 0.1 vpm C_nH_m, and 3 vpm Ar. The mixing ratio between two gases represented those of the model targets I to III, however, without Ar. Thus the mixtures are 98% N_2 + 2% CH_4 and 90% N_2 + 10% CH_4.

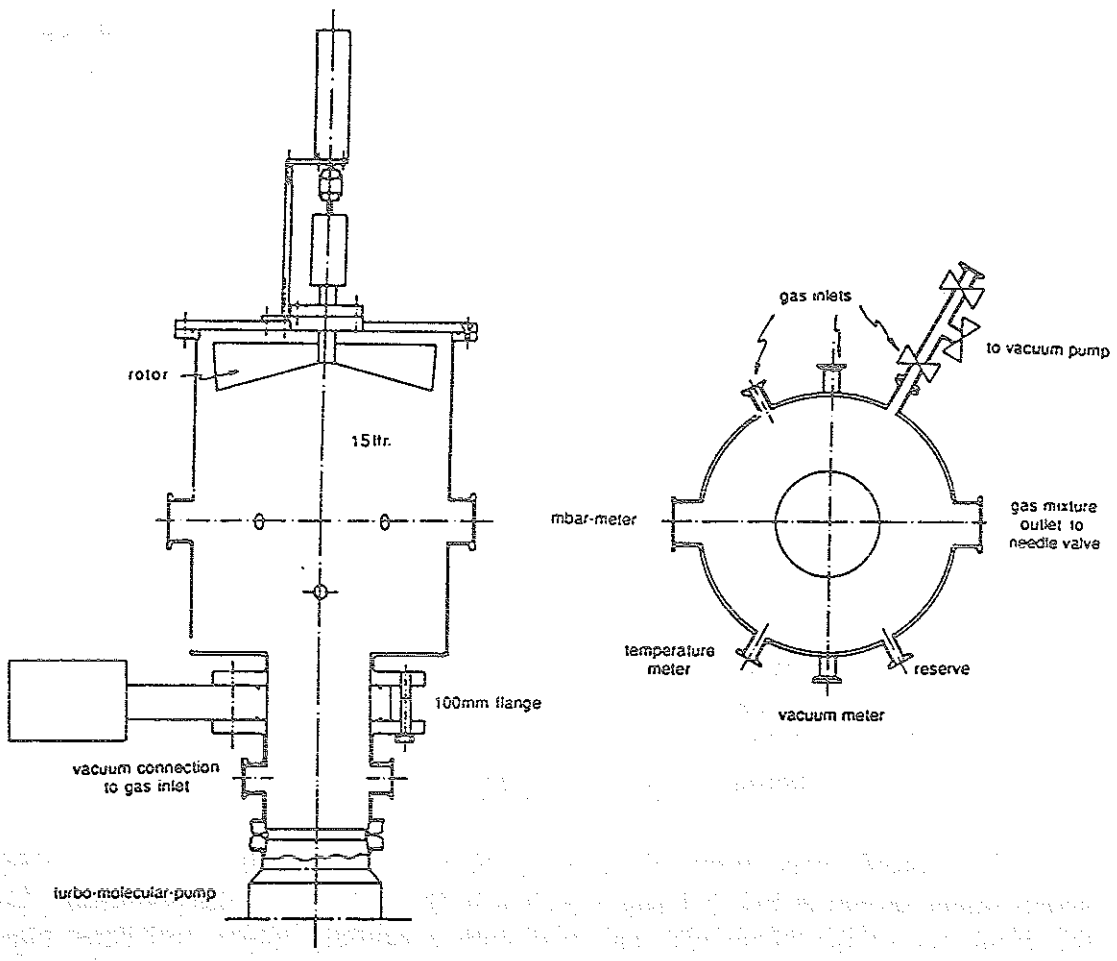

Fig 5.2 : Scheme of the gas mixing chamber, from [1.67] .

The mixing was achieved by evacuating the cylinder and the targets attached to it, then by filling the cylinder with the appropriate gases. The partial pressures were controlled by the Baratron. The mixing lasted for about one hour with stirring by the rotor and heating. After one hour cooling 2 to 3 targets were opened to the cylinder. Filling some targets with 49.5 ml content changed the pressure of the 15 ltr. cylinder by less than 1%. Thus, the targets were filled all from the same stock, without correcting the pressure.

5.1.3 Cyclotron irradiation

The cyclotron principle was conceived by E.O.Lawrence in 1929 and the successful operation of the first machine was achieved in 1931 by Lawrence and M.S.Livingston in Berkeley. It accelerates light positive ions to high energy without the use of high voltage, thereby avoiding the limitations of insulation breakdown. Ions move in widening semicircular paths in a uniform magnetic field, crossing back and forth between two electrodes in resonance with an oscillatory electric field. The ions are accelerated at each traversal of the electric field, attaining a final energy hundreds of times greater than that available from the voltage imposed on the electrodes.

The compact cyclotron CV 28 in IFF of KFA from The Cyclotron Corporation, Berkeley, California. is restricted to ions of maximum mass 4, i.e. $^{4}He^{2+}$. The energies which can be reached for the light ions are listed in Table 5.1.

Table 5.1 : Particles from CV 28, their energies and currents

particle	energy MeV	max. external current μA
protons	6-24	70
deuterons	3-14	100
3-helium	5-36	70
4-helium	6-28	50

The target was mounted to the vacuum antechamber, and the whole arrangement shown in Fig. 5.1 was attached to the end part of the beam line. First the geometry of the beam was checked with a dummy target and filter paper, which by a shot of ions (10 min. 100 nA cm^{-2} 36 MeV $^{3}He^{2+}$) was colored brown to indicate the beam geometry. Then, the Faraday cup in the antechamber was moved into the beam, and the real target was mounted. The beam was then adjusted to 200 nA for the whole area (i.e. approx. 100 nA cm^{-2}). The Faraday cup removed, the irradiation was started and controlled for flux and time. The beam was wobbled (swept) over the whole target area to guarantee a homogeneous flux. The beam profile could also be controlled by a beam scanner. In general it proved to be rather homogenous. The irradiation were carried out for 5, 10 and 30 sec, 1, 2, 5, and 20 min., resp. At the low beam intensity of

100 nA cm^{-2}, no cooling of the target was necessary. The power delivered to the gas amounted to 0.4 to 0.6 Watts which by diffusional processes was easily spread over the whole 45 ml volume and then to the walls. Thus the whole heating was not too serious and yielded a maximum temperature rise of the gas and in equilibrium also of the target walls of about 1-2 K only. The power delivered to the Ti-foils amounted to about 0.7 Watt, but was partially transported away by heat conductivity. cf. [5.1,2]. Most of the power was delivered to the beam stop which was cooled by water and thus did not contribute to the temperature of the proper target. At the end of the irradiation the target was demounted immediately. The radioactivity hazards at the low current applied were minimal. Nevertheless, the target was transported from the cyclotron room to the laboratory (ca. 5 min.) in a lead box.

5.1.4 Dose calculations

Fig. 5.3 shows schematically the energy losses of the $^3He^{2+}$ ions with a primary energy of 36 MeV in the target arrangement for 1.6 bar pure CH_4 and 98% N_2 + 2% CH_4 fillings.

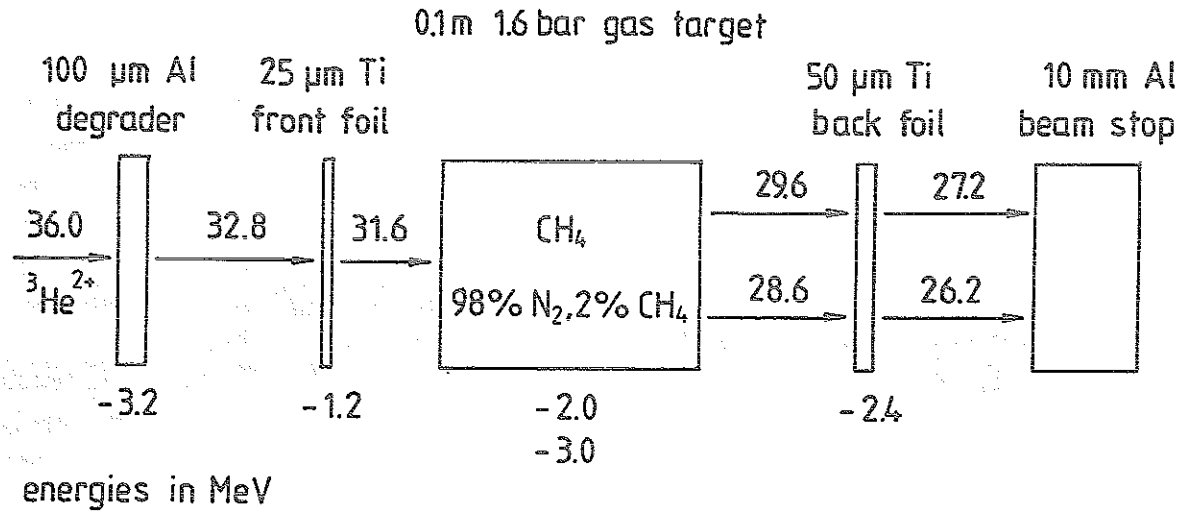

Fig 5.3 : Energy loss of 36 MeV $^3He^{2+}$ beam in Al-degrader, Ti-foils, CH_4 or 98% N_2 + 2% CH_4 targets and beam stop.

The energy dependent stopping powers of Al-degrader, Ti-foils, and N_2 a were taken from standard tables [1.21]. The energy loss of the projectile ΔE_p in the compound CH_4 calculated from data for the pure elements in [2.32] according to the formula :

$$\Delta E_p = \sum_E B_{Ei} x_{Ei} d_{Ei} \qquad (5.1)$$

where d_{Ei} signifies the area density of the target elements i, and x_{Ei} their molar fraction. From the number N_T of CH_4 and N_2 molecules in the gas phase under 1.6 bar within the cavity and the absorbed energy ΔE_p, the integral dose D* is :

$$D^* = \frac{E_p I_p t}{N_T} \quad \text{(eV per target molecule)}, \qquad (5.2)$$

with :

E_p energy loss of projectile in target (eV),
I_p intensity of projectile beam (cm^{-2} s^{-1}),
t duration of irradiation (s), and
N_T number of target molecules (CH_4,N_2).

N_T is defined as :

$$N_T = \frac{V \cdot p}{22400} N_A \qquad (5.3)$$

where N_A is Avogadro's number, V the volume in cm^3, and p the pressure in bar. Because of convection of gas from the proper area covered by the ion beam. (15 mm diameter) to the target volume (25 mm diameter) the latter has been taken a base for the dose calculations. It is however somewhat questionable, whether in the short irradiation times (5 and 10 s) a complete convection can be achieved within the target. Thus, the effective dose for short irradiations may be somewhat higher than given by the straight foreword calculation applied here.

The dose effects are mainly due to $^3He^{2+}$ ions. The effects of ^{11}C recoils, accompanying γ and β^+ emissions, and α particles from the nuclear reaction can be neglected with respect to bulk radiation damage. Table 5.2 lists the irradiation doses applied.

Table 5.2 : Doses D*, eV per target molecule, for the three gas targets (1.6 bar)

duration of irradiation, s	pure CH_4	10% CH_4+90% N_2	2% CH_4+98% N_2
5	0.0028	0.0035	0.0031
10	0.0056	0.007	0.006
30	0.016	0.021	0.019
60	0.034	0.045	0.04
120	0.068	0.09	0.08
300	0.17	0.22	0.21
600	0.34	0.44	0.42
1200	0.67	0.88	0.84

5.1.5 Nuclear reactions

The nuclear reaction $^{12}C(^3He,^4He)^{11}C$ which accompanied the $^3He^{2+}$ irradiation in containing CH_4 targets has an activation cross section σ = 60 mbarn (for 32 MeV), cf. Fig 5.4 from [5.3]. The recoil energy is calculated to 4.6 MeV [1.67]. The half-life of ^{11}C is T = 20.3 min. It disintegrates mainly via β^+-decay, which by positron annihilation leads to the final emission of two 0.511 MeV γ-quanta. The nuclear reaction $^{12}C(^3He,pn)^{13}N$ has a lower cross section of about 25-30 mbarn [5.4].

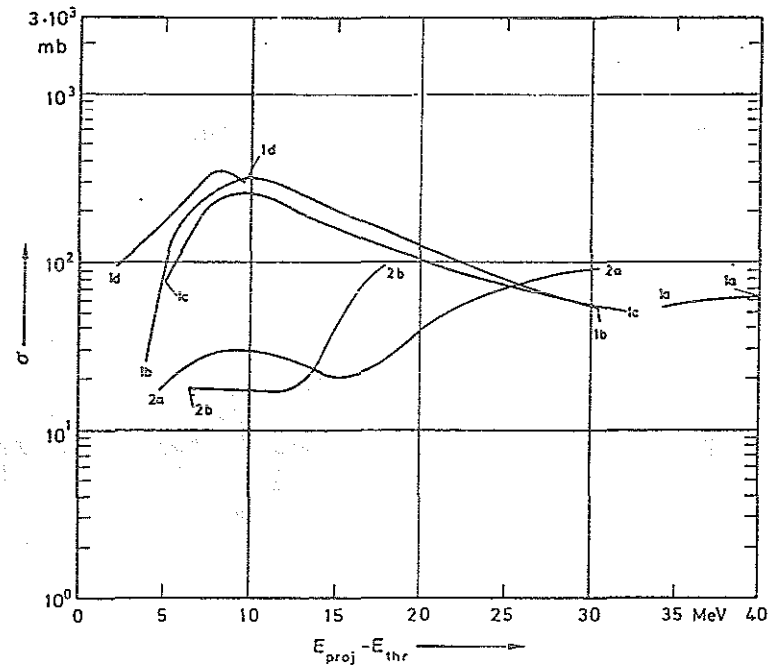

Fig 5.4: Activation cross section for $^{12}C(^3He,^4He)^{11}C$ nuclear reaction from several autors (1a-1d) and for $^{14}N(^3He,^4He)^{13}N$ from two authors (2a, b) from [5.3].

Since ^{13}N decays with a half-life of T=10 m, and its cross section is lower, it does not disturb the radioactivity measurements of ^{11}C which take place approx. 30 m after EOB (end of beam). The decay curve at this time after EOB showed the 20 m decay curve of ^{11}C only. In the nitrogen containing targets the nuclear reaction $^{14}N(^{3}He,^{4}He)^{13}N$ leading to a β^{+}-emitting nuclide with T=10 m with cross section of up to 100 mbarn for 32 MeV $^{3}He^{2+}$ cf. Fig 5.4, should become important. However, the decay curves of a freshly irradiated mixture of 10% CH_4 + 90% N_2 20 m after EOB showed only a T=20 m component. One only can suppose that the cross section activation are wrong by a least one order of magnitude. The radiochromatograms reported in chapter 5.2 show practically very similar peaks for all three targets compositions, i.e. the ^{11}C activity at the moment of measurements is much stronger than that of ^{13}N.

5.1.6 Analysis by GC

A gaschromatograph GC-9A from Shimadzu Corporation Kyoto with two separate ovens was used for the analysis, cf. Fig. 5.5. The gas samples were injected into a heated port, and taken by the carrier gas He 6.0 with a flow of 50 ml m^{-1} through 316 stainless steel capillaries to oven 2 with a six way valve Valco V6U^{R}. Then the gas passed a 10 cm long glass column of 3.5 mm inner diameter filled with Tenax GC as a trapping material. This Tenax column could be cooled by means of a dry ice-methanol bath to approx. 200 K. The gas then was led through capillaries in to oven 1 with two interconnected (in series) Pyrex glass columns of 3m length each and 3 mm inner diameter, filled with Poropak Q and S (50-80 mesh), resp.

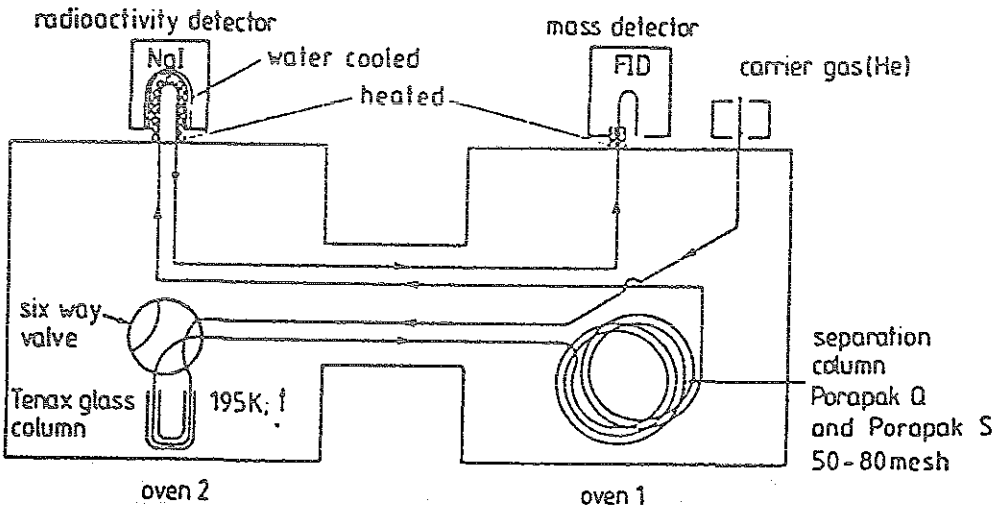

Fig 5.5 : Double oven radiogaschromatography set-up from [5.2].

The gas flow then continued outside the oven to a NaI (Tl) scintillation radioactivity detector with a borehole, into which the capillary is wound in form of a spiral. The detection volume within the 3×3 inch detector amounted to 3 ml. All capillaries leaving the gaschromatograph to the detector were kept at a constant temperature of 150 °C via electrical resistance heating in order to prevent condensation of less volatile products. The inner walls of the detector were cooled by a water flow mantle in order to prevent thermal damage by the hot capillaries. The gas continued to a flame ionization detector (FID) operated with O_2 and H_2 gas. It allowed the analysis of nanogram amounts of hydrocarbons. The gas flow was then led into a general gas line operated with filters to retain at least for a while the short lived activities till their decay.

The chromatography was started by switching the six way valve so that the carrier gas could pass the Tenax column. Samples of 10 ml were taken out of the target via the rubber septums with a gas syringe and were injected carefully within 2 s into the port. Oven 1 and the port were already at 50°C before injection.

Table 5.3 : Retention times of standard gases for Poropak Q+S columns.

standard gas	chemical formula	retention time, min.
methane	CH_4	5.4±0.1
ethylene	C_2H_4	10.5±0.2
acetylene	C_2H_2	11.3±0.1
ethane	C_2H_6	11.7±0.05
ammonia	NH_3	14.1±0.2
propene	C_3H_6	17.1±0.3
propane	C_3H_8	17.8±0.6
methaylamine	CH_3NH_2	19.1±0.5
hydrocyanic-acid	HCN	22.1±0.5
1-butylene	C_4H_8	22.5±0.4
n-butane	C_4H_{10}	23.1±0.4
iso-butane	C_4H_{10}	23.1±0.4
acetonitrile	CH_3CN	28.7±0.3
cyclopentane	C_5H_{10}	36.5±0.7
n-hexane	C_6H_{12}	50.2±0.8

The Tenax column in oven 2 cooled to dry ice temperature, retained all hydrocarbons starting from C_2 and most of nitrogen compounds. CO, CH_4, and N_2 passed the column. Both, radioactivity detector and FID measured the passage of CO, N_2 and CH_4 for about 12 min. Then the dry ice methanol bath was removed and the Tenax column was flash heated with fan above room temperature to evaporate the trapped gases. Subsequently, the temperature programs of both ovens were started. Oven 2 was heated with a rate of 10° m^{-1} from the initial temperature of 50°C (1 m initial time) till 200 °C and was kept at that temperature till the end of analysis, i.e. approx. 50 to 60 min. The flow was controlled regularly for its constancy. The peak signals from both detectors were processed

in a computer. Background subtraction and correction for radioactive decay of ^{11}C (T= 20.3 m) were performed automatically by the Ramona program. The position of the individual products in the chromatogram was checked with nonradioactive authentical standards. The ^{11}C fraction was checked by γ-spectroscopy and half-life determination that the fractions did not contain other radioactivity than ^{11}C.

5.2 Product spectrum (first results)

Some of the first preliminary results are given here. Fig. 5.6 exhibits a typical gas chromatogram measured with FID (upper curve) and radioactivity detector (lower curve) for an irradiation of 1.6 bar CH_4 with 32 MeV $^3He^{2+}$ with a dose D* = 0.17 eV per molecule. The CO peak only shows up in the radioactivity detector but not in the FID. This implies that it stemms from the reaction of hot ^{11}C with trace amounts of O_2 impurities in the gas mixture. The first broad peak in FID is that of target CH_4.

It should be noted that the CO and CH_4 peaks come from the first part of the chromatography with a cold Tenax column. In Fig. 5.6 and following chromatograms this part is combined for the sake of comparison with the chromatogram after heating the Tenax column. Peaks for butane and related C_4 compounds are evaluated together, such as those for C_5. Even when continuing the chromatography up to 60 m no further peaks appeared. Thus, a proper 100% balance determination by measuring a gas aliquot reaching the detectors via a bypass, was not thought to be necessary. The radiochemical yields were evaluated as % of the sum of all peak activities. ^{11}CO yields were eliminated from the calculation of the final yields which necessitated a new 100% renormalization without ^{11}C.

Table 5.4 lists the product distribution for 1.6 bar CH_4 for different doses. It can be seen, that due to the low number of runs in this preliminary approach the errors are quite high. The values with errors are averages from three individual runs, those without from one run only.

CH_4 is the only product the yield of which increases with dose. The yields of unsaturated compounds (C_2H_2, C_2H_4) decrease drastically with the dose, whereas the larger compounds ($\geq C_3$) show no big change within the error limits. For better comparison, the radiochemical yields of compounds up to C_4 are shown in Fig. 5.7 as a function of the dose D*. The results for the lowest dose run are somewhat dubious, since the radioactivity was very low at the time of measurement.

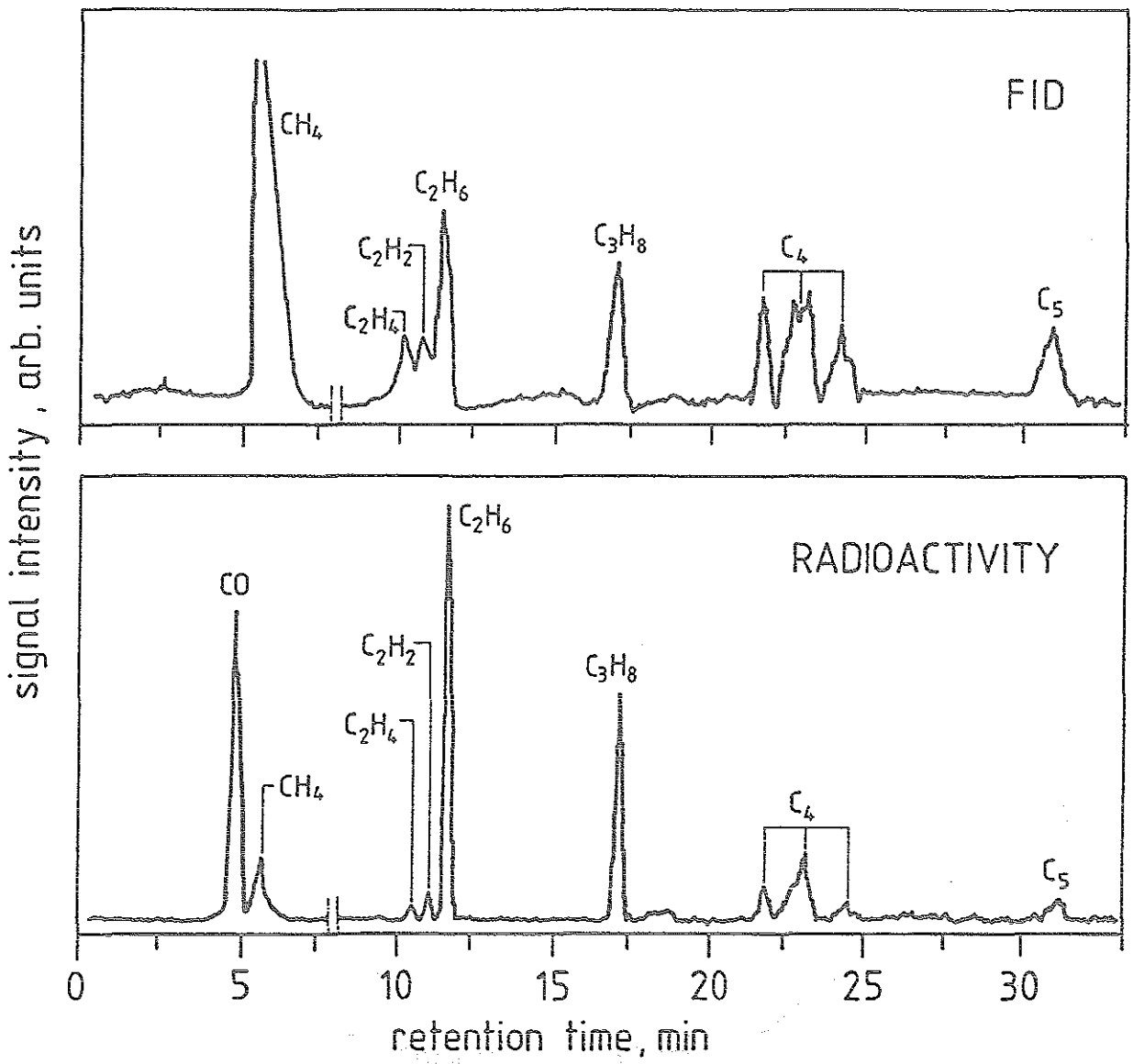

Fig. 5.6 : Gaschromatogram with FID and radioactivity detectors of 1.6 bar CH_4 irradiated with 32 MeV $^3He^{2+}$ ions at a dose D* = 0.17 eV per molecule at 295 K (correction for ^{11}C decay already included).

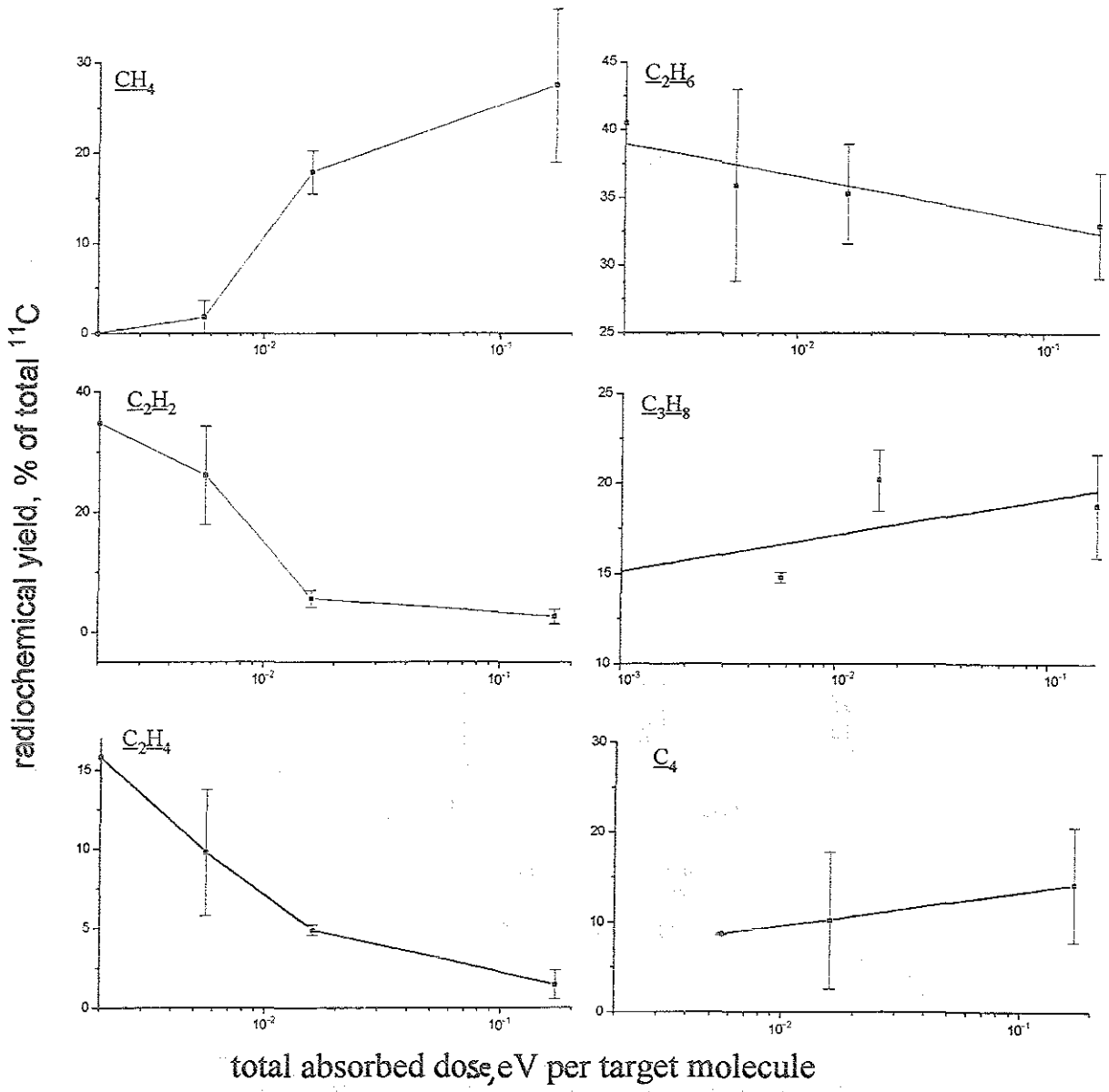

Fig 5.7 : Radiochemical yields in 1.6 bar CH_4 at 295 K after irradiation with 32 MeV $^3He^{2+}$ ions at different doses, % of total ^{11}C.

A similar calculation of the yields via the FID detectors was not carried, out first due to difficulties with a somewhat too broad representation of the peaks, second because this work concentrates on the ^{11}C hot chemical reactions.

Table 5.4 : Radiochemical yields of ^{11}C compounds in 1.6 bar CH_4, % of total ^{11}C.

D* eV per mol.	CH_4	C_2H_4	C_2H_2	C_2H_6	C_3H_8	ΣC_4	ΣC_5 and higher
0.002	0	15.8	34.8	40.5	-	-	-
0.0056	1.8±1.8	9.8±4.0	26.1±10.2	35.9±9.1	14.8±0.3	8.8±0.1	2.8±0.9
0.016	17.9±2.4	4.9±0.3	5.6±1.4	35.3±3.7	20.2±1.7	10.2±7.6	5.9±1.6
0.17	27.5±11.6	1.5±0.9	2.6±1.2	33.0±3.9	18.8±2.9	14.2±6.4	2.4±2.4

Fig 5.8 exhibits a chromatogram for a 1.6 bar 90% N_2 +10% CH_4 mixture for a dose D* = 0.042 eV per molecule from 32 MeV $^3He^{2+}$ ions at 295 K. Three new features show up : a small peak in front of the C_4 peaks which can be attributed to HCN, another peak at 28 ml retention time which is assigned to CH_3CN and a rather broad peak which shows a slight shift in the other chromatograms. It can be attributed to a nitrogen compound, eventually CH_3NH_2. Table 5.5 lists the radiochemical yields as function of dose. As in the case of the pure CH_4 the yield of the peak in front of the CH_4 was discarded in the calculation. It may not only contain ^{11}CO, but also $^{13}N_2$, the only radiochemical contamination of the products.

Table 5.5 : Radiochemical yields of some ^{11}C compounds in 1.6 bar 90% N_2 + 10% CH_4 mixture, % of total ^{11}C.

D* eV per mol.	CH_4	C_2H_4	C_2H_2	C_2H_6	C_3H_8	HCN	ΣC_4	CH_3CN	C_5	broad peak
0.045	10.7	2.0	4.3	22.2	15.7	1.2	6.6	12	0	46
0.22	8.9	1.8	4.3	20.4	16.6	< 0.2	9.9	8	6	24
0.88	13.5	1.1	2.4	25.3	15.5	0	12	3	5	20

Table 5.6 : Radiochemical yields of some ^{11}C compounds in 1.6 bar 98% N_2 + 2% CH_4 mixture, % of total ^{11}C.

D* eV per mol	CH_4	C_2H_2	C_2H_4	C_2H_6	C_3H_8	HCN	C_4	CH_3CN	C_5	broad peak
0.006	20.9	< 3	< 3	14.8	< 5	< 3	< 3	< 4	< 3	< 40
0.045	27.5	0.8	1.6	15.5	7.4	< 0.3	1.6	5	1.6	38.8
0.21	19± 6.7	0.7± 0.5	1.7± 0.9	18.2± 3.1	10.7± 2.7	?	5±3	3±2	1.2	37±8
0.84	24.7	0.8	1.3	23.6	12.5	?	6	3	3.5	27

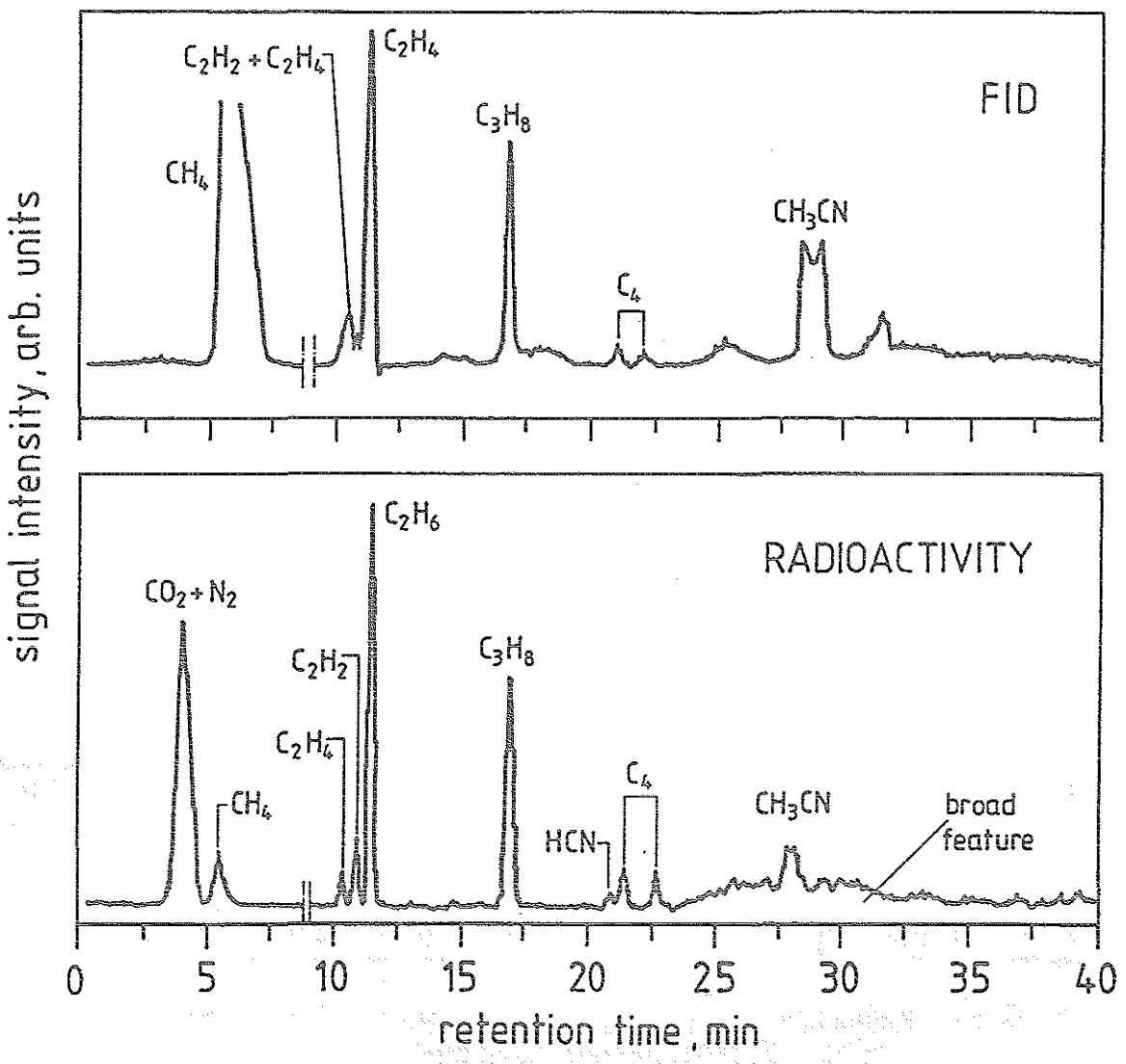

Fig. 5.8 : Gaschromatogram with FID and radioactivity detectors of 1.6 bar 90% N_2 + 10% CH_4 mixture irradiated with 32 MeV $^3He^{2+}$ ions at a dose D* = 0.042 eV per molecule at 295 K (correction for ^{11}C decay is already included).

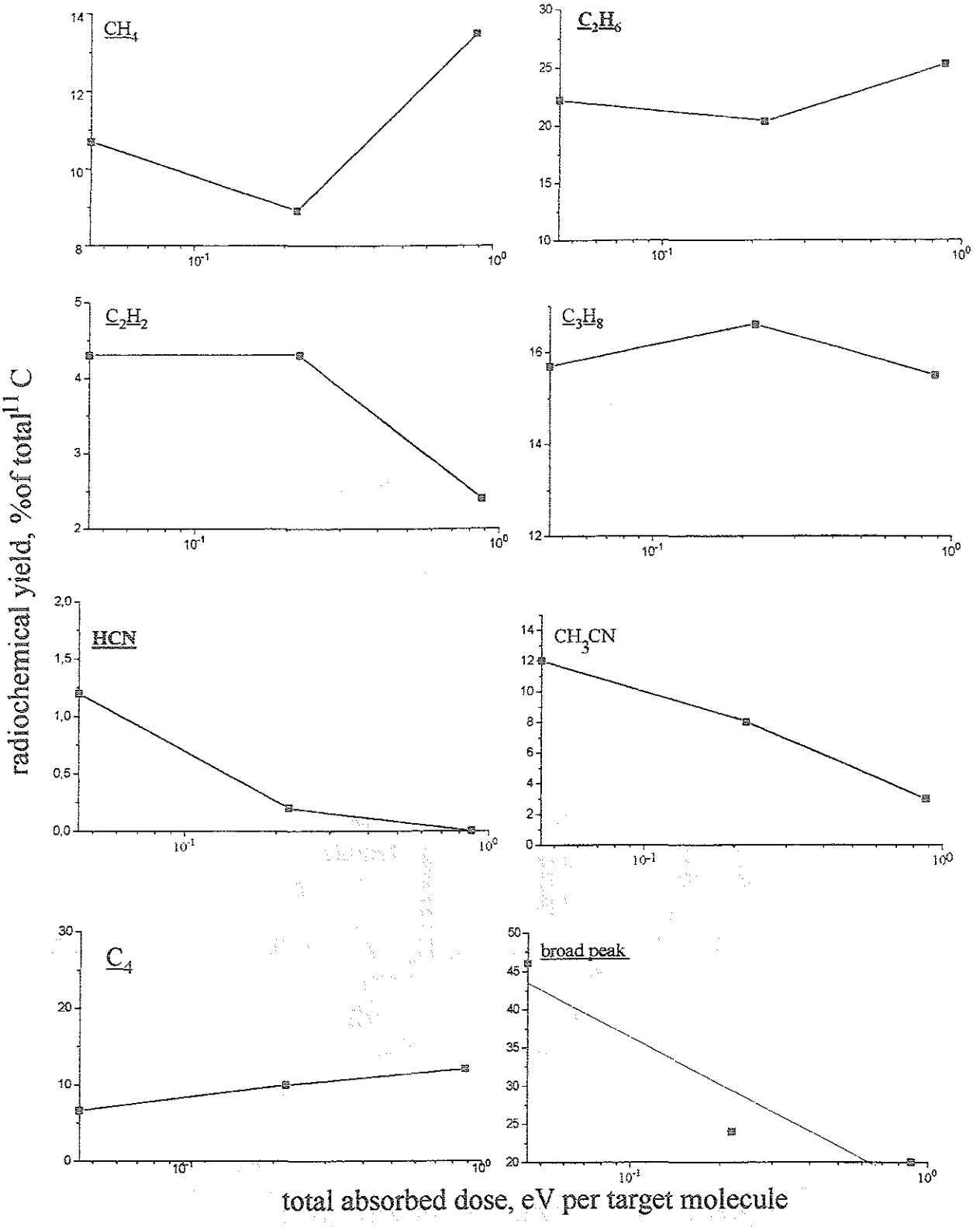

Fig. 5.9: Radiochemical yields in 1.6 bar 90% N_2 + 10% CH_4 mixture at 295 K after irradiation with 32 MeV $^3He^{2+}$ ions at different doses, % of total ^{11}C.

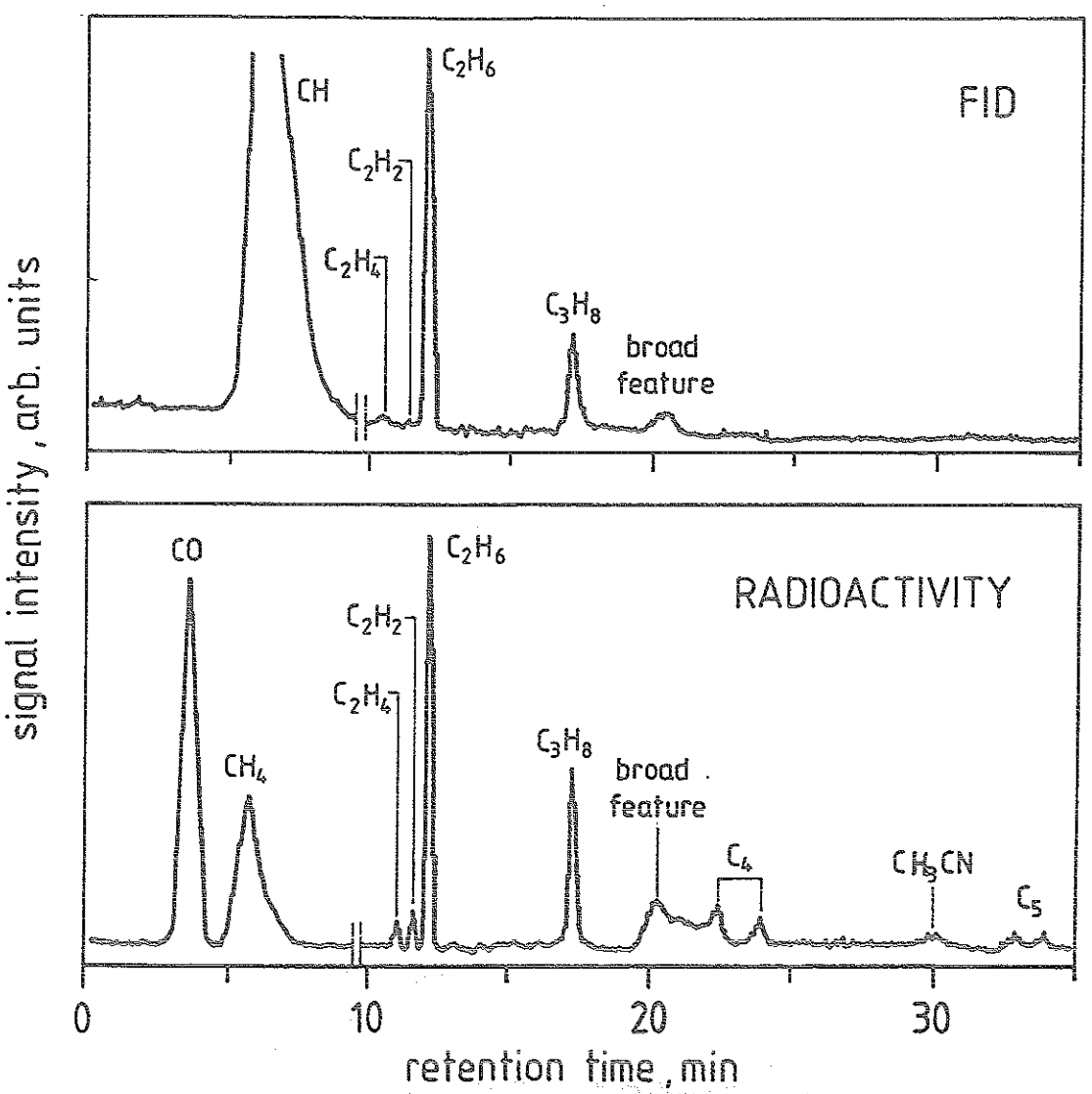

Fig. 5.10 : Gaschromatogram with FID and radioactivity detectors of 1.6 bar 98% N_2 + 2% CH_4 mixture irradiated with 32 MeV $^3He^{2+}$ ions at a dose D* = 0.21 eV per molecule at 295 K (correction for ^{11}C decay is already included).

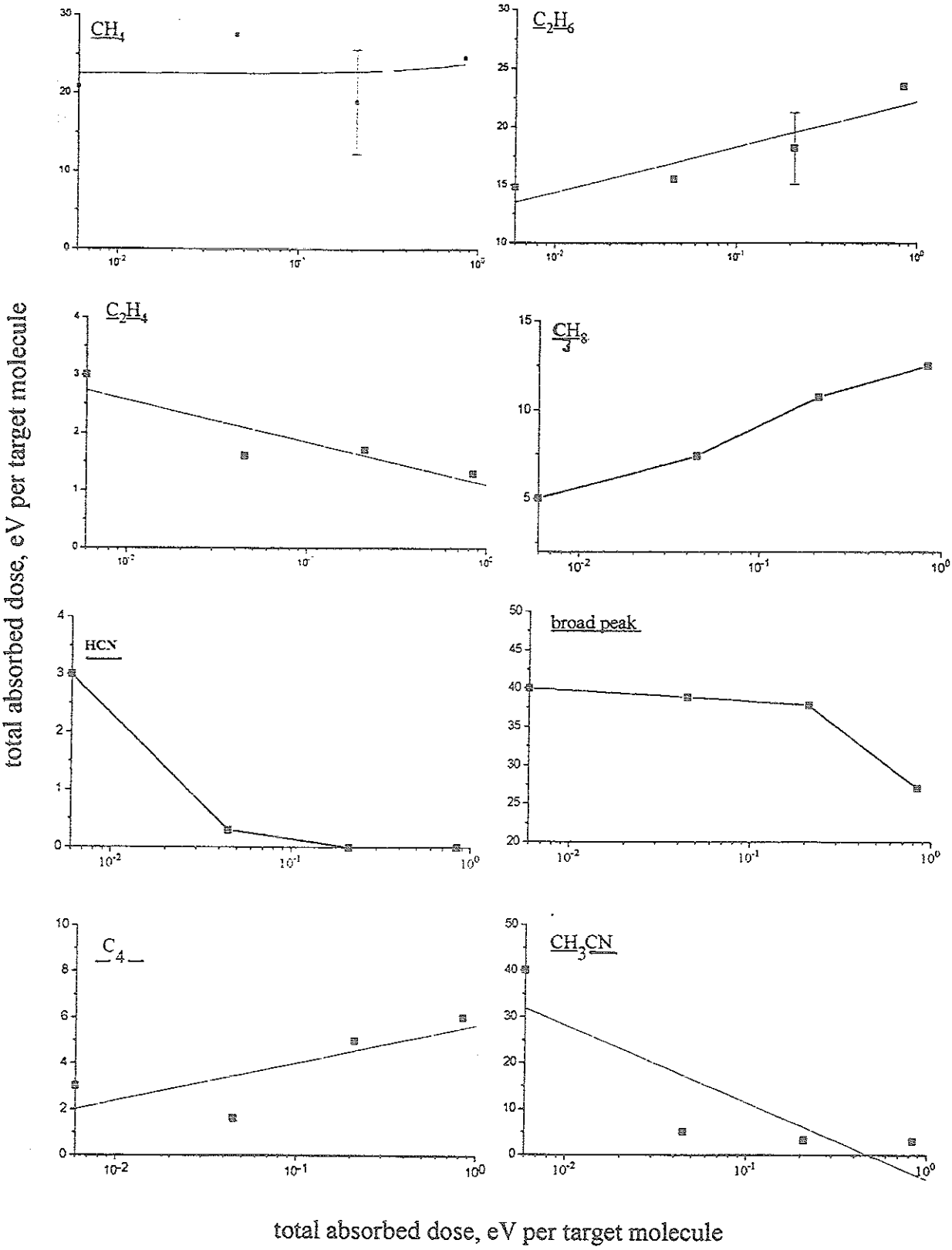

Fig. 5.11: Radiochemical yields in 1.6 bar 98% N_2 + 2% CH_4 mixture at 295 K after irradiation with 32 MeV $^3He^{2+}$ ions at different doses, % of total ^{11}C.

D* is slightly higher than for the case of pure CH_4. However the yields of the hydrocarbons fit quite well to those in Table 5.4. HCN is only generated and preserved at lower doses. Also the yields of the other nitrogen compounds decrease with dose.

Fig 5.10 shows a chromatogram for a 1.6 bar 98% N_2 + 2% CH_4 mixture for a dose D* = 0.21 eV per molecule of 32 MeV $^3He^{2+}$ ions at 295 K. It is in principle similar to that in Fig. 5.8, except that the broad feature is shifted to lower retention times and interferes with the C_4 peaks, where as CH_3CN and C_5 peaks are isolated. From the results in Table 5.3 one is tempted to assume that it might be due to HCN, which, however, should exhibit a sharper peak. Table 5.6 reports the corresponding radiochemical yields for four doses as already for the 98% N_2 + 2% CH_4 mixture, it can be seen that the formation of the hydrocarbons does not depend much on the dose. Fig. 5.11 shows a plot of these values.

5.3 Discussion

The results, even if preliminary, show clearly the formation of typical components of Titan's atmosphere by carbon atoms : C_2H_2, C_2H_4, C_2H_6, C_3H_8, C_4, and C_5 species, as well as HCN, CH_3CN, and ev. CH_3NH_2. The first astonishing information is that the hydrocarbon peaks are found with important yields in the mixtures with N_2, where the CH_4 is a minority compound, cf. compilation in Table 5.7. ^{11}C-hydrocarbon yields decrease somewhat with dilution.

Table 5.7: Comparison of hydrocarbon yields (by hot ^{11}C atoms) as depending on the composition of the gas mixture (rounded values)

composition	dose eV/molecule	CH_4	C_2H_4	C_2H_2	C_2H_6	C_3H_8	C_4	C_5
100% CH_4	0.17	2	2	3	33	19	14	2
10% CH_4 + 90% N_2	0.22		2	4	20	17	10	6
2% CH_4 + 98% N_2	0.21	1	1	2	18	11	2	2

Relative to the concentration of N_2 and the amount of hot nitrogen atoms (and thermal radicals, likewise) the yields of nitrogenous carbon compounds are too low. This, however, is due to the general tendency of hot carbon and nitrogen atoms to preferentially react with its own element or compound, cf. the reactivity sequence as follows [1.28]:

$$\begin{array}{c} \vec{C} : C \approx O > H \gg N \\ \vec{N} : N \geq H \approx O > C \end{array} \qquad (5.4)$$

This demonstrates that hot carbon does not like to react with nitrogen if a reasonable amount of other carbonaceous or oxygen containing partners are available. The appropriate holds for hot nitrogen. Its preferential product thus, will be substituted *NN molecule. Only in systems with a very low amount of hydrocarbons and oxygen, such as in the two targets studied, the formation of ^{11}CN-compounds takes place to a certain, however, still relatively low amount. If a secondary hot ^{14}N forms the ^{11}CN compounds it had to attack a preformed ^{11}C-compound and the yields of this process will be low. Thus, the ^{11}CN compounds are mainly formed by ^{11}C attack and consequent reactions. A particular effect of the dilution of a pure CH_4 atmosphere, which might be important for the discussion on the composition of Titan's atmosphere, was that the hydrocarbon yields do not change much in relation with the composition except those of the more complex molecules C_4 or C_5.

Altogether, the experiments can explain to a certain extent the low concentration of nitrogen-carbon compounds in Titan's atmosphere. The N_2 of the atmosphere, such as the Ar likewise, serve mainly as transfer agent of suprathermal energy and less as a direct reaction partner.

The effect of an increase of dose is that the yields of unsaturated hydrocarbons are decreased in pure CH_4 atmospheres where they are relatively high, but not in the mixed systems where, however, their yields are small anyhow. This effect has already been observed for gases at ambient pressure and solid hydrocarbons [1.67]. It is due to the fact that unsaturated compounds are preferentially formed by hot carbon atoms following the insection reaction into CH_4 to methylcarbene CH_3CH, and the subsequent processes shown in the mechanistic scheme in Fig. 5.12.

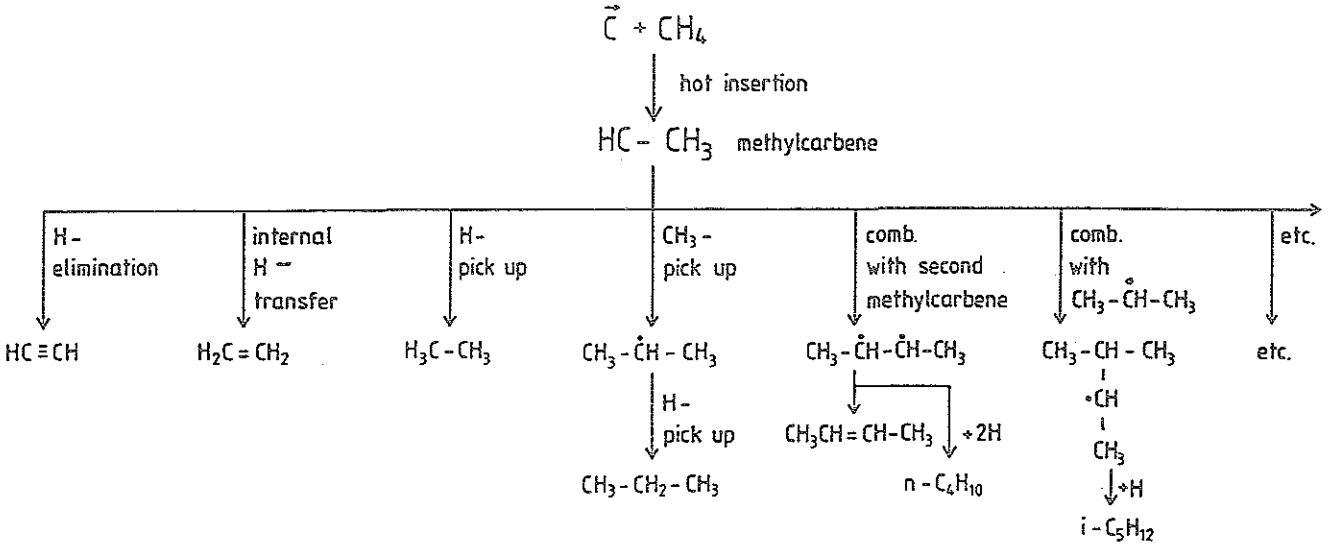

Fig 5.12 : Reaction scheme for hot carbon atoms in CH_4 [1.31]

With increasing radiolysis, free hydrogen radicals are formed by direct split off, but also or by elimination during non-equilibrium reactions, see chapter 1.4. The hydrogen can undergo a recombination with radical intermediates such as in Fig. 5.12 and hinder the elimination processes to the unsaturated compounds.

On the other hand also the yield of the carbon-nitrogen compounds is reduced with the dose, as seen from Tables 5.5 and 5.6. It seems that low dose conditions are favorable for both the production of unsaturated and nitrogenous carbon compounds [1.47, 1.53]. ^{11}CN-compounds formed are much more sensitive to radiolysis but also to hot ^{14}N attack, which abstracts the N from the compound to form N_2. The fact that the yield of unsaturated and nitrogeneous compounds is relatively low in Titan's atmosphere demonstrates the accompanying radiolytic effects. However, without hot atom chemistry, the present molecular composition would be not the same.

5.4 Planning of a new low temperature gas target

The present experiments were carried out with a target operated at room temperature. From the discussions of this work started the planning of a new low temperature gas target which is presented in Fig. 5.13. It consists of a gas chamber of same dimensions as the one used in the present experiments. It is, however, inserted into a LN_2-bath. In order to obtain the temperatures of different altitudes of Titan's atmosphere the target is surrounded by heating wires. Temperature is controlled by Pt-100 resistors which drive a computer assisted heating program. The critical issue of this arrangement is to avoid any part of the inner zone which is colder than the condensation temperature of CH_4 (90 K at 1 bar), i.e. in particular the foils, gas capillaries, etc. thus, the mounting of heating wires and the insertion of thermal insulation had to be optimized. Gas inlet and sample taking have to proceed in the cyclotron itself which necessitates the operation of a moveable gas mixing chamber. The whole arrangement is at present under construction and will be operated first in fall 1994.

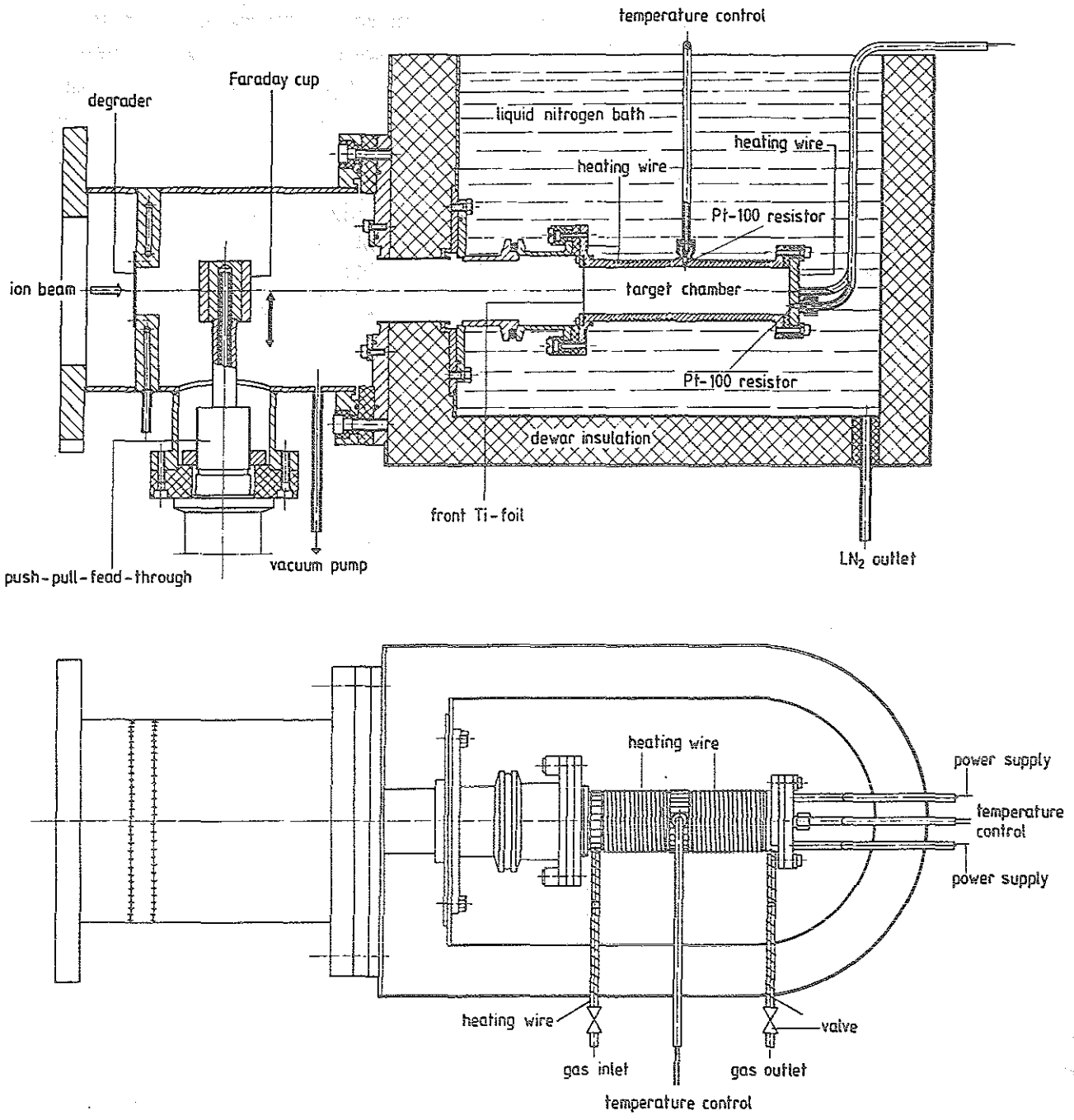

Fig. 5.13: Low temperature gas target for irradiation with cyclotron ions

REFERENCES

[1.1] D.M. Hunten, M.G. Tomasko, F.M. Flasar, R.E. Samuelson, D.F. Strobel, and D.J. Stevenson, Titan, in: Saturn, T. Gehrels, M.S. Matthews, eds., Univ. of Arizona Press, Tucson 1984, 671 - 759.

[1.2] S. K. Atreya, Atmospheres and Ionospheres of the Outer Planets and Their Satellites, Springer, Berlin 1986, 166 - 190.

[1.3] Proc. Symposium on Titan, Toulouse, France, 9 - 12 September 1991, ESA-SP-338 (1992).

[1.4] Proc. Int. Workshop on The Atmospheres of Saturn and Titan, Alpbach, Austria, 16 - 19 September 1985, ESA-SP-241 (1985).

[1.5] D.M. Hunten, The Atmosphere of Titan, NASA SP-340, Washington 1974.

[1.6] D.M. Hunten and D. Morrison, eds., The Saturn System, NASA-Conf. Publ. -2068, Washington 1978.

[1.7] D.M. Hunten, Titan's atmosphere and surface, in: Planetary Satellites, J.A. Burns, ed., Univ. of Arizona Press, Tucson 1977, 420 - 437.

[1.8] J. Caldwell, Thermal radiation from Titan's atmosphere, in: Planetary Satellites, J.A. Burns, ed., Univ. of Arizona Press, Tucson 1987, 438 - 450.

[1.9] T.C. Owen, The composition and origin of Titan's atmosphere, Plant. Space Sci. 30, 833 - 838 (1982).

[1.10] J. Comas Sola, Observations des satellites principeaux de Jupiter et de Titan, Astron. Nach. 171, 289 (1908).

[1.11] G.P. Kuiper, Infrared spectra of planets, Astrophys. J. 106, 251 - 254 (1947).

[1.12] G.P. Kuiper, D.P. Cruikshank, and U. Fink, The composition of Saturn's rings, Sky Teles. 39, 14 (1970).

[1.13] J.S. Lewis, Satellites of the outer planets: Their physical and chemical nature, Icarus 15, 174 - 189 (1971).

[1.14] D.M. Hunten, A Titan atmosphere with a surface temperature of 200 K, in ref. [1.6], 127 - 140.

[1.15] S.K. Atreya, T.M. Donahue, and W.R. Kuhn, Evolution of a nitrogen atmosphere on Titan, Science 201, 611 - 613 (1978).

[1.16] B.L. Lutz, T. Owen, and R.D. Cess, Laboratory band strengths of methane and their application to the atmosphere of Jupiter, Saturn, Uranus, Neptune, and Titan. Astrophys. J. 203, 541 - 551 (1976).

[1.17) M. Podolak and L.P. Giver, On inhomogeneous scattering models of atmosphere, Icarus 37, 361 - 376 (1979).

[1.18] W.R. Thompson and C. Sagan, Organic chemistry on Titan - Surface Irradiations, in ref. [1.3], 167 - 176.

[1.19] D.L. Matson, Cassini - A mission to Saturn and Titan, in ref. [1.3], 281 - 286.

[1.20] J.-P. Lebreton, The Huygens probe, in ref. [1.3], 287 - 292.

[1.21] R.C. Weast, ed., Handbook of Chemistry and Physics, The Chemical Rubber Company, Cleveland 1984.

[1.22] G.F. Lindal, G.E. Wood, H.B. Hotz, D.M. Sweetnam, V.R. Eshleman, and G.L. Tyler, The atmosphere of Titan: an analysis of the Voyager 1 ratio occultation measurements, Icarus 53, 348 - 363 (1983).

[1.23] R.E. Samuelson, R.H. Hand, V.G. Kunde, and W.C. Maquire, Mean molecular weight and hydrogen abundance of Titan's atmosphere, Nature 292, 688 - 693 (1981).

[1.24] A.L. Broadfoot, B.R. Sandel, D.E. Shemansky, et al., Extreme ultraviolet observations from Voyager 1 encounter with Saturn, Science 212, 206 - 211 (1981).

[1.25] G.R. Smith, D.F. Strobel, A.L. Broadfoot, B.R. Sandel, D.E. Shemansky, and G.B. Holberg, Titan's upper atmosphere: composition and temperature from the EUV solar occultation results, J. Geophys. Res. 87, 1351 - 1357 (1982).

[1.26] J.L. Bertaux and G. Kockarts, Distribution of molecular hydrogen in the atmosphere of Titan, J. Geophys. Res. 88, 8716 - 8720 (1983).

[1.27] K. Roessler, Institut für Nuklearchemie, Forschungszentrum KFA Jülich, Germany, personal communication.

[1.28] K. Roessler, Suprathermal chemistry in space, in: Solid-State Astrophysics, E. Bussoletti, G. Strazzulla, eds., North-Holland, Amsterdam, 197 - 266 (1991).

[1.29] K. Roessler, Non equilibrium chemistry in space, Nucl. Instr. Meth., 1365, 55 - 66 (1992).

[1.30] K. Roessler, Hot atoms in space - Simulation with nuclear methods, Radiochim. Acta 43, 123 - 125 (1988).

[1.31] J. Kissel, F.R. Krueger, and K. Roessler, Organic chemistry in comets from remote and in-situ observations, in press, 1994.

[1.32] K. Roessler, Hot atom chemistry and radiolysis of gaseous and solid components of planetary atmosphers, in ref. [1.4], 179 - 188.

[1.33] P. Meyer, R. Ramaty, W.R. Weber, Cosmic rays-astronomy with energetic particles, Physics Today, 27 (10) (1974).

[1.34] A.G.W. Cameron, Elementary and nuclide abundances in the solar system, in: Essays and Nuclear Astrophysics, C.A. Barnes et al., eds., Cambridge Univ. Press, Cambridge 1981.

[1.35] R.A. Mewalt, Rev. Geophys. Space Sci. 21, 295 - 309 (1983).

[1.36] G. Reitz, Institut für Luft- und Raumfahrtmedizin, Abtlg. Strahlenbiologie, DLR Köln, Germany, personal communication, 1994.

[1.37] C. Sagan, B.N. Khare, J.S. Lewis, Organic matter in the Saturn system, in: Saturn, T. Gehrels , M.S. Matthews, eds., Univ. of Arizona Press, Tucson 1984, 788 - 807.

[1.38] M. Menzinger and R.L. Wolfgang, Angew. Chem. (Frankfurt) 81, 446 (1969).

[1.39] G. Stöcklin, Chemie heißer Atome, Verlag Chemie, Weinheim 1969; Chimie des atoms chauds, Masson et Cie., Paris 1972.

[1.40] K. Roessler, Hot atom chemistry in space, in: Handbook of Hot Atom Chemistry, J.P. Adloff et al., eds., Kodansha, Tokyo and Verlag Chemie, Weinheim 1992, 602 - 624.

[1.41] M. Heyl, K. Roessler, Bimolecular Hot Chemistry Reaction Rates in Gas phases, in: Handbook of Hot Atom Chemistry, J.P. Adloff et al., eds. Kodansha, Tokyo and Verlag Chemie, Weinheim 1992, 226 - 231.

[1.42] M. Heyl, Chemische Reaktionen suprathermischer Wasserstoffatome in dem Koma von Kometen, Report-JÜL - 2409 (Nov. 1990), Forschungszentrum KFA Jülich, Germany.

[1.43] T. Matsuura, ed., Hot Atom Chemistry, Kodansha, Tokyo 1984.

[1.44] J.-P. Adloff et al. (eds.), Handbook of Hot Atom Chemistry, Kodansha, Tokyo and Verlag Chemie, Weinheim, 1992.

[1.45] C. MacKay and R. Wolfgang, Reactions of atomic carbon with simple hydrocarbons: evidence for C-H bond insertion, J.Am.Chem.Soc. 83, 2399 - 2400 (1961).

[1.46] C. MacKay, M. Pandow, P. Polak, and R. Wolfgang, The elementary chemistry of atomic carbon, in: Chemical Effects of Nuclear Transformations, IAEA, Vienna 1961, Vol. II., 17 - 26.

[1.47] G. Stöcklin, H. Stangl, D.R. Christman, J.B. Cumming, and A.P. Wolf, The reactions of energetic carbon atoms in methane; oxygen and phase dependence; radiation damage effects, J. Phys. Chem. 67, 1735 - 1737 (1963).

[1.48] M. Marshall, C. MacKay, and R. Wolfgang, The reactions of atomic carbon with ethylene. I. Production of allene and methylacetylene, J. Am. Chem. Soc. 86, 4741 - 4747 (1964).

[1.49] J. Dubrin, C. MacKay, and R. Wolfgang, Studies of reactions of atomic carbon by a double tracer technique, J. Am. Chem. Soc. 86, 959 - 960 (1964).

[1.50] G. Stöcklin and A. P. Wolf, Phase dependence of carbon-11 recoil products in ethane and propane, evidence for methylene insertion, J. Am. Chem. Soc. 85, 229 - 230 (1963).

[1.51] G. Stöcklin, Zur Chemie nuleogener Kohlenstoffatome, Report-JÜL-228-RC (Juli 1969), Forschungszentrum KFA Jülich, Germany.

[1.52] A. Patnaik, K. Roessler, and E. Zadór, Modification of simple organic solids in space: energetic carbon interactions with solid methane, Adv. Space Res. 9 (6), 49 - 52 (1989).

[1.53] A. Patnaik, K. Roessler, and E. Zádor, Reactions of suprathermal carbon atoms in solid methane, Radiochim. Acta 50, 75 - 85 (1990).

[1.54] K. Roessler, G. Eich, A. Patnaik, and E. Zadór, Polycyclic aromatic hydrocarbons via multicenter reactions induced by solar radiation, Lun. Plan. Sci. Conf. XXI (1990), 1035 - 1036.

[1.55] R.I. Kaiser, Chemische Prozesse durch Zyklotronionen in festem Methan - Simulation der Wechselwirkung kosmischer Strahlung in einfachen extraterrestrischen Eiskörpern, Report JÜL-2492 (Juli 1991), Forschungszentrum KFA Jülich, Germany.

[1.56] R.I. Kaiser, R.M. Mahfouz, and K. Roessler, Emission of organic products from the surface of frozen methane under MeV ion irradiation, Nucl. Instr. Meth. B65, 468 - 471 (1992).

[1.57] R.I. Kaiser, J. Lauterwein, P. Müller, and K. Roessler, Energy density effects in the formation of organic residues in frozen methane by MeV ions, Nucl. Instr. Meth. B65, 463 - 467 (1992).

[1.58] R.I. Kaiser and K. Roessler, Cosmic ray modification of organic cometary matter as simulated by cyclotron irradiation, Ann. Geophys. 10, 222 - 225 (1992).

[1.59] R.I. Kaiser, MeV-Ionen induzierte chemische Reaktionen in festem Methan, Ethen und Ethin, Report JÜL-2856 (Dez. 1993), Forschungszentrum KFA Jülich, Germany.

[1.60] M. Pandow, C. MacKay, and R. Wolfgang, J. Inorg. Nucl. Chem. 14, 153 (1960).

[1.61 J. Dubrin, C. MacKay, M.L. Pandow, and R. Wolfgang, Reactions of atomic carbon with π-bonded inorganic molecules, J. Inorg. Nucl. Chem. 26, 2113 - 2122 (1964).

[1.62] C.A. Goy, D.H. Shaw, and H.O. Pritchard, The reactions of CN radicals in the gas phase, J. Phys. Chem. 69, 1504 - 1507 (1965).

[1.63] W.C. Perkins and W.S. Koski, ^{13}N-labelled products from ^{12}C(d,n) reaction in alcohols, J. Phys. Chem. 66, 474 - 477 (1962).

[1.64] J. Dubrin, C. MacKay, and R. Wolfgang, Reactions of atomic nitrogen in the quadruplet and doublet states, J. Chem. Phys. 44, 2208 - 2209 (1966).

[1.65] R.S. Tilbury, J.R. Dahl, W.G. Monahan, and J.S. Laughlin, The production of ^{13}N labeled ammonia for medical use, Radiochem. Radioanalyt. Lett. 8, 317 - 323 (1971).

[1.66] G. Stöcklin and A.P. Wolf, Competitive gas-phase reactions of C^{11} in binary oxygen alkane systems, in: Chemical Effects of Nuclear Transformations, IAEA, Vienna 1965, Vol. 1, 121 - 132.

[1.67] B. Nebeling, Reaktionen von ^{11}C-Rückstoßatomen in den Systemen H_2O-NH_3, H_2O-CH_4 und NH_3-CH_4, Report JÜL-2245 (Nov. 1988), Forschungszentrum KFA Jülich, Germany.

[1.68] H. Ache and A.P. Wolf, Reactions and mechanisms involving hot carbon atoms and N_2-H_2, N_2-alkane and N_2-alkane-moderator systems including their relationship to other simple systems, in: Chemical Effects of Nuclear Transformations, IAEA, Vienna 1965, Vol. 1, 107 - 120.

[1.69] H.J. Ache and A.P. Wolf, Reacions of energetic carbon atoms with nitrogen molecules, Radiochim. Acta 6, 32 - 39 (1966).

[1.70] D.R. Davies, W.F. Libby, and W.E. Menschein, J. Chem. Phys. 45, 4481 - 4492 (1966).

[1.71] M.E. Sheridan, E. Greer, and W.F. Libby, J. Phys. Chem. 71, 2614 - 2618 (1967).

[1.72] N.J. Sack, R. Schuster, A. Hofmann, A. Khelim, and A. Koppmann, Astrophys. J. 360, 305 - 312 (1990).

[1.73] D. Toublanc, J.P. Parisot, J. Brillet, and D. Gautier, Modelling of the diurnal variations of the atmosphere of Titan, in ref. [1.3], 131 - 136.

[1.74] L.M. Lara, R. Rodrigo, A. Coustenis, J.J. Lopez-Moreno, and E. Chassefière, in ref. [1.3], 137 - 146.

[1.75] F. Raulin, C. Frère, L. Do, M. Khlifi, P. Paillous, and E. de Vanssay, Organic chemistry on Titan versus terrestrial prebiotic chemistry: exobiologial implications, in ref. [1.3], 149 - 160.

[1.76] J.C. Guillemin and J.P. Ferris, Photochemistry of unsaturated nitriles on Titan, in ref. [1.3], 177 - 181.

[2.1] G. Leibried, Bestrahlungseffekte in Festkörpern, Teubner, Stuttgart 1965.

[2.2] P. Sigmund, Rev. Roum. Phys. 17, 823 (1972).

[2.3] M.T. Robinson, Radiation Induced Voids in Metals, C.J.W. Corbett, L.C. Ianniello, eds., VSAEC, CONF-710601, U.S. GPO, Washington 1972, 397.

[2.4] J.B. Gibson, A.N. Goland, M. Milgram, and G. Vineyard, Phys. Rev. 120, 1229 (1960).

[2.5] G. Erginsoy, G.M. Vineyard, and A. Englert, Phys. Rev. 133, A 595 (1964).

[2.6] A. Scholz and C. Lehmann, Phys. Rev. 136, 813 (1972).

[2.7] D.E Harrison Jr., N.S. Levy, J.P. Johnson III, H.M. Effron, J. Appl. Phys. 39, 3742 (1968).

[2.8] J.R. Beeler Jr. and D.G. Besco, J. Appl. Phys. 34, 2873 (1963).

[2.9] J.H. Barrett, Phys. Rev. 133, 1527 (1971).

[2.10] I.M. Torrens, M.T. Robinson, in ref. [2.3], 739.

[2.11] M.T. Robinson and I.M. Torrens, Phys. Rev. 139, 5008 (1974).

[2.12] M.T. Robinson and O.S. Oen, Appl. Phys. Lett. 2, 30 (1963).

[2.13] K. Guttner, H. Ewald, and H. Schmidt, Rad. Eff. 13, 111 (1972).

[2.14] H. Goldstein, Classical Mechanics, Addison-Wesley, Cambridge, Mass., 1950, 58.

[2.15] Z. Kopal, Numerical Analysis, 2nd ed., Wiley, New York 1961, 367.

[2.16] M.T. Robinson, U.S. Atomic Energy Commission Report No. ORNL-4556, 1970 (unpublished).

[2.17] I.M. Torrens, Interatomic Potentials, Academic, New York 1972.

[2.18] I.M. Torrens and M.T. Robinson, in: Interatomic Potentials and Simulation of Lattice Deffects, P.G. Gehlen, J.R. Beeler Jr., and R.I. Yaffee, eds., Plenum, New York, 1972, 423.

[2.19] G. Molière, Z. Naturforsch. A2, 133 (1947).

[2.20] O.B. Firsov, Zh. Eksp. Teor. Fiz. 33, 696 (1957) (Sov. Phys. - JETP 6, 534 (1958).

[2.21] W. Westmeier and K. Roessler, Range calculations for high energy heavy atoms in complex media, Rad. Eff. 64, 61 (1982).

[2.22] W. Westmeier and K. Roessler, Range calculations for spallation recoils ThF_4 by use of the computer code "MARLOWE", JÜL-Report 1563 (December 1978), Forschungszentrum KFA Jülich, Germany.

[2.23] V.S. Nikolaev and I.S. Dimitriev, Phys. Rev. 28A, 277 (1968).

[2.24] H.D. Betz, Rev. Mod. Phys. 44, 465 (1972).

[2.25] K. Roessler, Computer simulation of collision cascades in solids, in ref. [1.44], 265 - 285.

[2.26] P. Gombas, Statistische Behandlung des Atoms, in: Encyclopedia of Physics, S. Flügge, ed., Vol. 36: Atoms II, Springer, Berlin 1956, 109.

[2.27] M.T. Robinson, Oak Ridge National Laboratory, USA, personal communication.

[2.28] J. Lindhard and M. Scharff, Phys. Rev. 124, 128 (1961).

[2.29] J. Lindhard, M. Scharff, and H.E. Schiott, Mat-Fys. Med. K. Dan. Vidensk. Selsk. 33, 14 (1963).

[2.30] F. Seitz, Disc. Farad. Soc., 5, 271 (1949).

[2.31] H. Kinchin and R.S. Pease, Rep. Prog. Phys. 18, 1 (1955).

[2.32] J.F. Ziegler, The stopping and ranges of ions in Matter, Vol. 5 of Handbook of Stopping Cross Sections for Energetic Ions in All Elements, J.F. Ziegler, ed., Pergamon, New York 1980.

[2.33] J.P. Biersack and L.C. Haggmark, Nucl. Instr. Meth. A4, 254 (1980).

[2.34] J.P. Biersack and W.G. Eckstein, Appl. Phys. 34, 73 (1984).

[2.35] W. Eckstein, Computer Simulation of Ion Solid Interaction, Springer, Berlin 1991.

[2.36] J.J. Thomson, Phil. Mag. 23, 901 (1912).

[2.37] G.G. Darwin, Phil. Mag. 23, 901 (1912).

[2.38] N. Bohr, Phil. Mag. 25, 10 (1913).

[2.39] H.A. Bethe, Z.f. Physik 76, 293 (1932).

[2.40] H.A. Bethe, Ann. Physik 5, 325 (1930).

[2.41] C. Moller, Ann. Physik 14, 531 (1932).

[2.42] N.F. Mott, Proc. Comb. Phil. Soc. 27, 553 (1931).

[2.43] A. Sommerfield, Z.f. Physik 72, 283 (1932).

[2.44] W. Lenz, Z.f. Physik 77, 713 (1932).

[2.45] H. Jensen, Z.f. Physik 77, 722 (1932).

[2.46] F. Bloch, Ann. Physik 16, 287 (1933).

[2.47] F. Bloch, Z.f. Physik 81, 383 (1933).

[2.48] F. Bloch, Z.f. Physik 81, 362 (1933).

[2.49] U. Fano, Ann. Rev. Nucl. Sci. 13, I (1963).

[2.50] R.L. Platzman, Symp. Radiobiol., Oberlin Coll., 1950 (1952).

[2.51] F.W. Martin and L.G. Northcliffe, Phys. Rev. 128, 1166 (1962).

[2.52] T.J. Thompson, Effect of chemical structure on stopping power for high-energy protons, Univ. Calif. Radiation Lab. Rept. No. 1910 (1952).

[2.53] J.R. Brolley and F.L. Ribe, Phys. Rev. 98, 1112 (1955).

[2.54] R.L. Fleischer, in: Progress in Material Science, T.B. Massalski, ed., Pergamon, New York 1981, 97 - 122.

[5.1] B. Nebeling, K. Roessler, and G. Stöcklin, Reaction of recoiling carbon atoms with water vapour, Radiochim. Acta 38, 15 - 20 (1985).

[5.2] B. Nebeling, Reaktionen von ^{11}C-Rückstoßatomen mit H_2O, Report JÜL-1973 (Febr. 1985), Forschungszentrum KFA Jülich, Germany.

[5.3] K.A. Keller, J. Lange, H. Münzel, and G. Pfennig, Q-Values and Excitation Functions of Nuclear Reactions, Part b: Excitation Functions for Charged Particles, Landoldt-Börnstein 5, Springer, Berlin 1973.

APPENDIX

Table 8.1 : Total number of all N, C, and H hot atoms produced by energetic secondaries in target I (full cascade calculation)

secondary atom ion	energy	N		C		H	
			average		average		average
N	10000	315		2.1		11.8	
			178		1.17		6.69
	1000	40.1		0.23		1.53	
			31.2		0.17		1.17
	500	22.2		0.11		0.82	
			13.1		0.067		0.48
	100	4		0.022		0.14	
			2.9		0.016		0.107
	50	1.9		0.010		0.072	
			0.95		0.005		0.036
	10	0.025		0		0	
			0.0125		0		0
	5	0		0		0	
H	10000	27.81		0.143		1.22	
			18.76		0.094		0.91
	1000	9.71		0.046		0.59	
			7.65		0.034		0.52
	500	5.59		0.022		0.45	
			3.13		0.012		0.33
	100	0.66		0.0018		0.20	
			0.37		0.0009		0.16
	50	0.075		0		0.12	
			0.0375		0		0.07
	10	0		0		0.019	
			0		0		0.001
	5	0		0		0	
C	10000	301		1.75		11.36	
			170		0.99		6.4
	1000	39.4		0.22		1.5	
			29.8		0.17		1.17
	500	20.3		0.11		0.7	
			12.12		0.07		0.44
	100	4		0.018		0.14	
			2.86		0.011		0.11
	50	1.8		0.005		0.075	
			0.90		0.0025		0.04
	10	0.03		0		0	
			0.01		0		0
	5	0		0		0	

Table 8.2 : Total number of all N, Ar, C, and H hot atoms produced by energetic secondaries in target III (full cascade calculations)

secondary atom ion	energy	N		Ar		C		H	
			average		average		average		average
N	10000	227	128	283	159.	9.6	5.4	74.6	28.6
	1000	29.4	22.4	35.9	27.4	1.3	0.9	9.5	7.1
	500	15.4	18.5	18.9	11.5	0.6	0.37	4.7	2.8
	100	3.1	2.3	4	3.1	0.1	0.075	0.96	0.69
	50	1.4	0.73	2.1	1.3	0.046	0.023	0.42	0.21
	10	0.020	0.01	0.55	0.28	0	0	0	0
	5	0		0		0		0	
Ar	10000	278	156	330	184	11.9	6.7	91.6	51.3
	1000	33.4	25.5	37.1	28	1.5	1.1	10.9	7.9
	500	17.5	10.5	18.9	11.6	0.7	0.41	4.9	2.8
	100	3.4	2.5	4.2	3.3	0.12	0.082	0.59	0.32
	50	1.5	0.77	2.3	1.5	0.045	0.0225	0.051	0.025
	10	0	0	0.66	0.33	0	0	0	0
	5	0		0		0		0	
C	10000	215	122	151	98.8	9.1	5.2	71.5	40.6
	1000	28.6	21.7	46	32.4	1.2	0.93	9.6	7.2
	500	14.8	8.9	18.5	11.2	0.65	0.38	4.8	2.9
	100	2.9	2.1	3.9	3	0.11	0.073	0.95	0.7
	50	1.3	0.66	2.1	1.3	0.037	0.021	0.45	0.
	10	0.009	0.005	0.54	0.27	0	0	0	0
	5	0		0		0		0	
H	10000	19.7	13.2	22.8	16.7	1.3	0.78	7.1	5.3
	1000	6.7	5.2	10.6	10.4	0.24	0.19	3.4	3
	500	3.8	2.1	10.2	6.5	0.13	0.072	2.5	1.8
	100	0.47	0.26	2.9	2.2	0.011	0.006	1.05	0.86
	50	0.038	0.019	1.5	0.79	0	0	0.663	0.38
	10	0	0	0.1	0.05	0	0	0.093	0.05
	5	0		0		0		0	

Table 8.3 : Total number of all N, Ar, C, and H hot atoms produced by energetic secondaries in target II (full cascade calculation)

secondary atom ion	energy	N		Ar		C		H	
			average		average		average		average
N	10000	273	154	117	65.8	5.7	3.2	39.7	22.4
	1000	35.1	26.6	14.8	11.2	0.73	0.6	5.2	4
	500	18	10.8	7.5	4.6	0.36	0.21	2.7	1.6
	100	3.6	2.6	1.7	1.2	0.063	0.046	056	034
	50	1.6	0.84	0.83	0.53	0.03	0.015	0.12	0.06
	10	0.027	0.014	0.24	0.12	0	0	0	0
	5	0		0		0		0	
Ar	10000	329	184	136	75.7	6.8	3.8	48.3	26.8
	1000	39	29.5	15.1	11.4	0.81	0.59	5.4	5.2
	500	20.1	12.1	7.6	4.6	0.4	0.22	5	2.7
	100	4	3	1.6	1.25	0.065	0.042	0.31	0.16
	50	1.9	0.94	0.89	0.6	0.018	0.009	0.015	0.008
	10	0	0	0.29	0.14	0	0	0	0
	5	0		0		0		0	
C	10000	259	147	82.6	48.6	5.2	3	38.6	21.8
	1000	34.4	26.2	14.6	11.1	0.66	0.51	4.9	3.7
	500	17.9	10.1	7.6	4.2	0.36	0.2	2.5	1.4
	100	2.4	2	0.7	0.8	0.04	0.03	0.33	0.18
	50	1.6	0.82	0.9	0.56	0.024	0.012	0.035	0.018
	10	0.02	0.01	0.22	0.11	0	0	0	0
	5	0		0		0		0	
H	10000	24	16.1	10.7	7.8	0.43	0.29	4	3
	1000	8.2	6.5	4.9	4.8	0.14	0.11	2	1.7
	500	4.7	2.6	4.8	2.9	0.07	0.036	1.5	1
	100	0.56	0.31	1.1	0.9	0.004	0.002	0.62	0.5
	50	0.064	0.032	0.6	0.35	0	0	0.37	0.21
	10	0	0	0.06	0.03	0	0	0.05	0.026
	5	0		0		0		0	

Acknowledgments

Thanks are due to the Director of the Jülich Institut für Nuklearchemie, Prof. Dr. Gerhard Stöcklin, to the Head of Physics Department of Suez Canal University in Ismiliya, Prof. Dr. Yehia Abbas and Dr. Moustafa Abu Assy from the same department for their continued interest.

The authors thank the Egyptian Channel System for a two years grant (File 823, 1991-1993) for A.M. El-S.M. and a visitors grant for H.A.K. In particular they are indebted to Prof. Dr. Kamal Radwan and Prof. Dr. Hashem Hussein from Study Mission and Cultural Department of the Embassy of the Arabic Republic of Egypt in Bonn, Germany for their friendly and helpful advice.

Likewise the thanks go to Internationales Büro of KFA Jülich (Mr. Dieter Nentwich and Mrs. Marie-Theres Königs), for a 6 month's prolongation grant (1993-1994) for A.M. El-S.M.

The authors express their cordial thanks to those who assisted the work both experimentally and by advices for the computer work : Dr. M. Hou of Université Libre de Bruxelles, Belgium, Dr. M. Heyl of Institut für Radioastronomie der Universität Bonn, Dr. E. Langenscheidt, Mr. Günter Eich, Dr. R. I. Kaiser, and Dr. B. Scholten of Institut für Nuklearchemie, the operator team of the Compact Cyclotron CV28 of KFA Jülich for the irradiations and Mrs. M. Claßen for assistance in preparing the text.

ملخص الرّسالة

تتناول هذه الرّسالة دراسة نظرية ومعملية لعمليات التّصادم الجزئى من الأشعة الكونية والفوتونات الشّمسية إلى جزيئات غلاف سطح التّيتان (ضغط ١,٦ بار) .

أولّا : دراسة إنتاج الذّرات الثّانوية المختلفة نتيجة تفاعلات الأشعة الكونية بطاقة تتراوح بين ١٠ و $^{٨}١٠$ ألكترون فولت مع أنوية غلاف سطح التّيتان (نيتروجين ـ أرجون ـ ميثان) ممثلة فى ثلاث نسب مختلفة لغازات سطح التّيتان .

وقد بنيت هذه الدّراسة على نظرية مونت كارلو الممثلة فى برنامج مارلو .

ثانيا : تطبيق هذا النّموزج على سطح التّيتان الفعلى وذلك بإستخدام نموذج قياس لكثافة الجزيئات المركزة فى سطح التّيتان . وقد تمّ إنتاج تغيرات توزيع الطّاقات بالنّسبة لإرتفاع سطح التّيتان ممثلة فى ١٠ كم بهدف إستخلاص الحقائق من دراسة التّغيرات الفعلية لمكونات سطح التّيتان ومدى تأثره بالظّواهر الشّمسية والجيوفيزيقية .

وقد تممت الدّراسة النّظرية بدراسة معملية لتمثيل فعلى لسطح التّيتان الإيجاد تأثير الأيونات ذات الطّاقات العالية وتحليل ناتج المركبات النّاتجة .

وقد أمكن من هذه الدّراسة إثبات أن الإشعة الكونية ذات الطّاقات العالية لها تأثير فعلى فى تغير سطح التّيتان .

FORSCHUNGSZENTRUM JÜLICH GmbH

KFA

Jül-3002
December 1994
ISSN 0944-2952